Comprehensive Characterization and Modelling of Operation Mechanisms in Third Generation Solar Cells

Dissertation

zur Erlangung des akademischen Grades
Dr. rer. nat.

eingereicht an der
Mathematisch-Naturwissenschaftlich-Technischen Fakultat
der Universitat Augsburg

vorgelegt von
Martin T. Neukom

Augsburg, August 2019

Universität Augsburg
University

Zürcher Hochschule für Angewandte Wissenschaften
School of Engineering
ICP Institute of Computational Physics

FLUXiM
scientific software · www.fluxim.com

1. Gutachter: Prof. Dr. Wolfgang Brütting
2. Gutachter: Prof. Dr. Armin Reller
Tag der mündlichen Prüfung: 17.10.2019

Abstract

Solar energy is one of the key enabling technologies for the transition to a zero-carbon society – a necessity to mitigate global climate change. Emerging photovoltaic technologies based on novel semiconductor materials offer new disruptive applications since they can be made light-weight, flexible and in arbitrary shape and colour. In so-called tandem structures novel materials like perovskite furthermore have the **potential to overcome the efficiency limits** of silicon solar cells. The first generation of solar materials was crystalline silicon. The second generation were inorganic thin-film solar cells. The emerging photovoltaic technologies studied in this thesis are therefore called **third generation solar cells**.

This thesis is **focused on understanding the physics** underlying third generation photovoltaics. The understanding of the physical processes and the quantification of loss mechanisms are crucial to improve the power conversion efficiency and the lifetime of these devices.

To gain insight into the physical processes measurement results from a variety of experimental characterization methods are compared with results from numerical solar cell simulation. The characterization methods consist of various optical and electrical measurements on solar cells in **steady-state, transient and frequency domain**. The developed simulation software solves the coupled differential equations describing charge transport by drift-diffusion as well as charge recombination in semiconductors.

Whereas other simulation studies have focussed on individual measurement techniques, this thesis presents a physical model and resulting **simulation data that reproduces the full variety of measurements with one set of parameters**. This approach allows a more accurate extraction of material parameters and a deeper insight into the physical processes of these solar cells. Such a comprehensive study is applied to an organic and a perovskite solar cell, both belonging to the category of third generation solar cells.

Additionally, a broad overview of solar cell characterization techniques and their interpretation is presented. For that purpose, various characterization techniques are simulated with systematically varied device and material parameters for a sample solar cell. The systematic simulation results provide a **guide for the interpretation of observed experimental results**.

In perovskite solar cells a hysteresis is often observed between the forward and reverse current-voltage scans. The simulation model can reproduce this behaviour and provide an explanation why this hysteresis is often dependent on the interface materials on both sides of the perovskite layer. This study further explains **why highly efficient solar cells often show less hysteresis**.

Finally, it is shown that only the **consideration of mobile ionic charges in conjunction with electronic charges** in the semiconductor drift-diffusion model allows to explain transient and frequency domain data of planar perovskite solar cells. A novel step response technique illustrates that the retraction of ionic charges from layer interfaces enables charge transport.

CONTENTS

Part I

INTRODUCTION

1

CLIMATE AND ENERGY MARKET

The future of humanity depends crucially on its ability to keep global environmental conditions within certain boundaries. Rockström and co-workers proposed nine planetary boundaries that should not be exceeded in order to keep a safe operating space for humanity [1]. According to Rockström *et. al.* the current rate of biodiversity loss, human interference with the nitrogen cycle and climate change already exceed these boundaries. Furthermore, ocean acidification and the change in the phosphorus cycle are also about to exceed their limits.

Stabilizing the global climate is one of the most important issues of this century. Reducing greenhouse gas emissions a little, will not be sufficient to achieve climate stability: According to the IPCC-report *on the impacts of a global warming of* 1.5 *degree* greenhouse emissions need to reach net-zero by the middle of the century [2]. Thus, a rapid transformation from a carbon-intense society to a carbon-free society needs to take place. In order to achieve this transformation, a vision first needs to be drafted of a society and economy based on a 100% renewable energy. Once this goal has been set, steps can be taken to realise this transformation.

In order to accomplish this transition, a combination of social and regulatory changes, as well as technological developments, will be required. Solar energy is one of the key enabling technologies for the transition to a zero-carbon society. Improving the power and stability of solar modules while further reducing production costs are the main challenges within this field of technology. This thesis is focused on understanding the physics underlying third generation photovoltaics like organic-inorganic perovskites, a class of novel solar materials. In combination with classical silicon-based photovoltaics, perovskites have the potential to increase the power conversion efficiency of solar cells.

1.1 ENERGY MARKETS AND PHOTOVOLTAICS

Electricity production by solar energy was negligible two decades ago. Triggered by political support the solar industry has grown rapidly and solar energy has become a competitive power source. In 2018 a total capacity of 100 GW_p was newly installed worldwide, more than 40% of which was installed in China [3]. Figure 1.1 shows the cumulative evolution of installed solar power. By the end of 2018 the total installed electricity generation capacity worldwide was 500 GW_p. SolarPower Europe estimates that the cumulative installed power could reach one terawatt by 2022 [3].

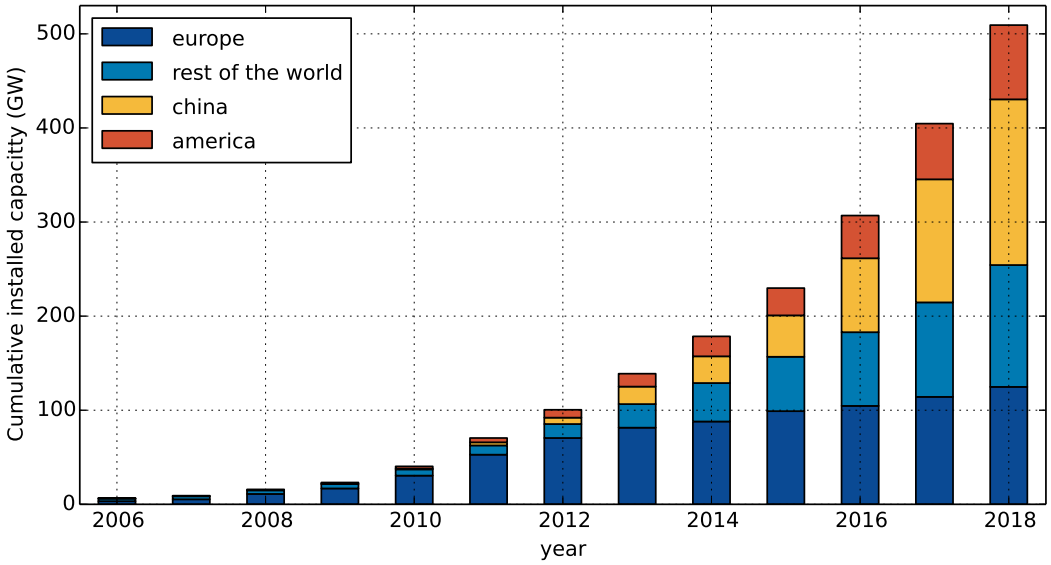

Figure 1.1: Cumulative installed photovoltaic peak power worldwide.
Data source: SolarPowerEurope [3].

Figure 1.2 shows the evolution of hydro, nuclear, wind and solar electricity generation since 1971 worldwide. The total electrical energy production each year for the different technologies is compared. While nuclear energy production has been stagnating over the past 20 years, wind and solar have grown strongly. The dashed line shows the combined energy production for wind and solar. Its growth in 2018 is comparable with the growth in nuclear energy in its boom-phase in the 1980s. Assuming that this growth trend continues, wind and solar will overtake nuclear energy production by 2021.

It is clear that wind and solar are on the rise and are becoming major sources of electricity production. Globally however, coal power remains the largest source of electrical energy, with 9600 TWh per year worldwide [7]. Decarbonization of our electricity systems therefore remains a major challenge.

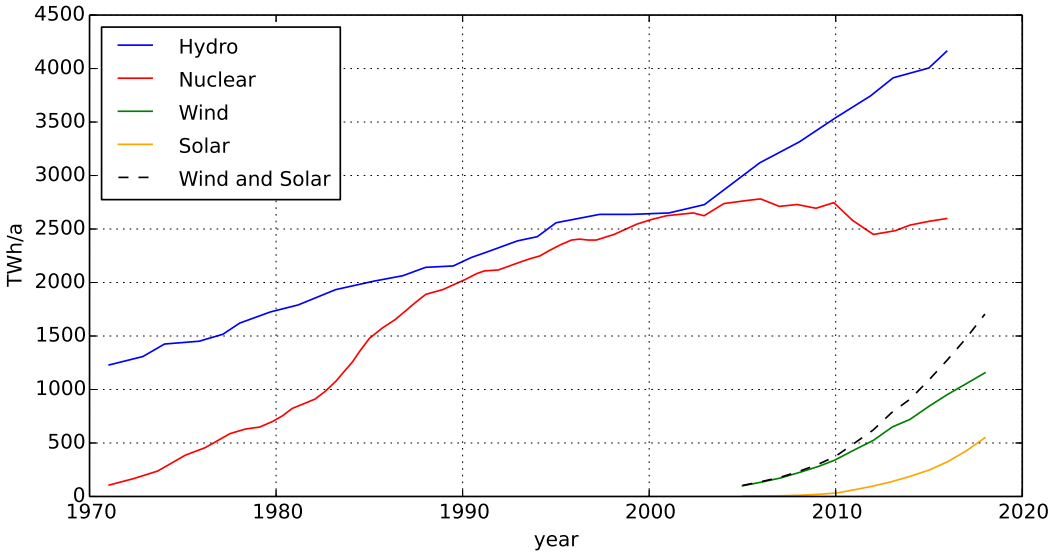

Figure 1.2: Annual worldwide electricity production by technology.
Data Source: IEA Key World Energy Statistics [4]. Wind and solar data for the years 2017 and 2018 is estimated according to the growth of solar and wind installations [5, 6].

1.2 THE ECONOMICS OF SOLAR ENERGY

The growth in electrical power generation capacity of solar and wind is strongly related to its reduction in production costs. This section is focused on the cost development of photovoltaic energy production.

Average solar module costs had decreased from around 20 *Euro/Watt* in the 1980s to 0.30 *Euro/Watt* in 2018. This rapid decay in production costs over the past three decades is shown in Figure 1.3a.

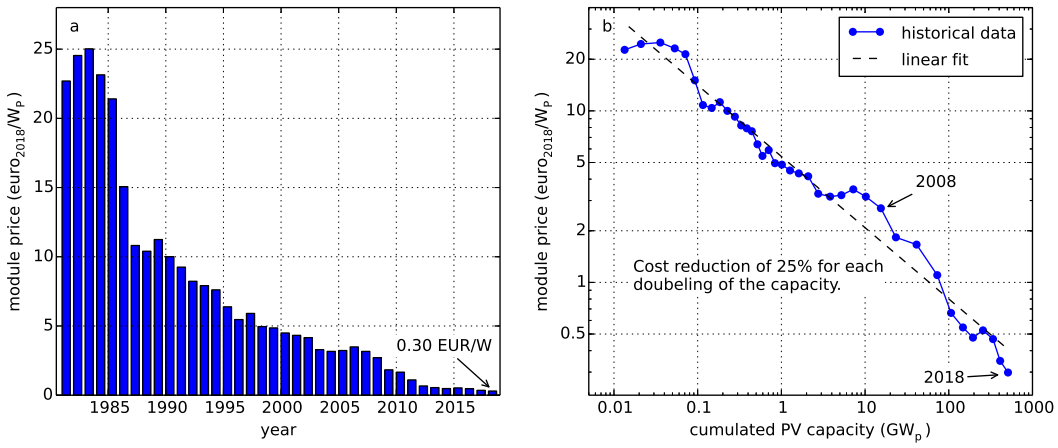

Figure 1.3: a) Historic development of module prices. b) Price experience curve of PV modules with a price experience factor of 25 %.
Data source: ISE PV report [8].

Figure 1.3b shows the module price versus the cumulated installed power for photovoltaics (PV) as shown in Figure 1.1 on a log-log scale. This data representation is called *price experience curve*. For each doubling of the globally installed PV capacity the average module price droped by around 25%.

This price decrease has been driven by economies of scale in production as well as large improvements in power conversion efficiency [8]. Provided that they are not accompanied by a significant increase in production costs, further efficiency improvements in PV modules could lead to even lower module costs in future.

2 SOLAR CELL TECHNOLOGY OVERVIEW

In this chapter solar cell materials and technologies are discussed and compared.

Crystalline silicon: The vast majority of solar modules on the market are based on crystalline silicon. Silicon is earth-abundant and non-toxic. The record power conversion efficiency for crystalline silicon solar cells is 26.7% [9], close to the physical limit of a single junction solar cell [10]. Improvements can be expected on the average module efficiency in the coming years. Compared to many other solar materials however, the optical absorption of silicon is relatively weak and an absorber layer thickness of over 100 μm is required to absorb most of the light. Silicon solar cells are therefore considered to be *thick*. PV materials that utilize much thinner absorber layers ($< 4\,\mu m$) are therefore termed *thin film solar cells*. While a small fraction of the current market share are amorphous silicon solar cells, research and development on amorphous silicon has now stopped owing to the poor efficiency/cost balance of the technology.

CdTe and CIGS: In 2017 the market share of cadmium tellurium (CdTe) and copper, indium, gallium and selenium (CIGS) thin film technologies was below 5% [11]. In both technologies the absorber material compound is coated on glass resulting in a film with a thickness of a few micrometers. Record power conversion efficiencies of above 21% have been achieved for CdTe and almost 23% for CIGS [12]. While cadmium is very toxic, its compound with tellurium is not. The growth potential for both technologies may be limited however owing to their reliance on non-earth-abundant materials i.e. indium, gallium, and tellurium. A related absorber material class are kesterites that use the abundant materials zinc and tin to replace indium and gallium in the CIGS structure. These copper zinc tin sulfide (CZTS) solar cells have achieved comparitively low record efficiencies of 11.3% however [12].

Concentrator PV and III-V Solar Cells: The highest PV power conversion efficiency currently on record is 46%, and was achieved using a quadruple junction III-V solar cell under concentrated light [12]. As the name implies, III-V materials are compounds of materials from element group III (e.g. gallium, indium) and materials from element group V (e.g. phosphorus, arsenic) of the periodic table. These material systems can be carefully designed for multijunction solar cells to enable high efficiencies by tuning the bandgap of each subcell. Commercially, these solar cells are employed in concentrator structures in which concentration factors of up to 500 can be reached using Fresnel lenses. Concentrators have a number of advantages; on one hand light concentration allows for higher efficiency, and on the other, very small area solar cells reduce costs. The major disadvantage of concentrated photovoltaics however is

that only direct sunlight can be captured, making dual axis tracking a requirement.

New Materials: A great deal of research is currently being undertaken on new materials and cell concepts to improve the power conversion efficiency or design solar cells that are lightweight, flexible or semi-transparent. The range of materials employed in these so-called *third generation solar cells* is very large. In bulk-heterojunction solar cells two materials (an electron transporter and a hole transporter) are intermixed. Small organic molecules, polymers or quantum dots (nanometer-sized particles) are typically used in this application. These materials are of particular interest to materials scientists and chemists owing to the ability to design and tune their properties by chemical modification. Huge progress has been achieved in recent years with organic solar cells reaching 17.3% [13] and quantum dot solar cells reaching 16.6% [14].

The class of PV materials gaining the most attention in recent years has been perovskites. These materials can be deposited by solution and are remarkably tolerant towards impurities. The standard perovskite consists of methylammonium, lead, and iodide. To date, the record efficiency for perovskites is 24.2% [12]. Recently, in tandem configuration with a silicon bottom cell a record efficiency of 28.0% was achieved [12].

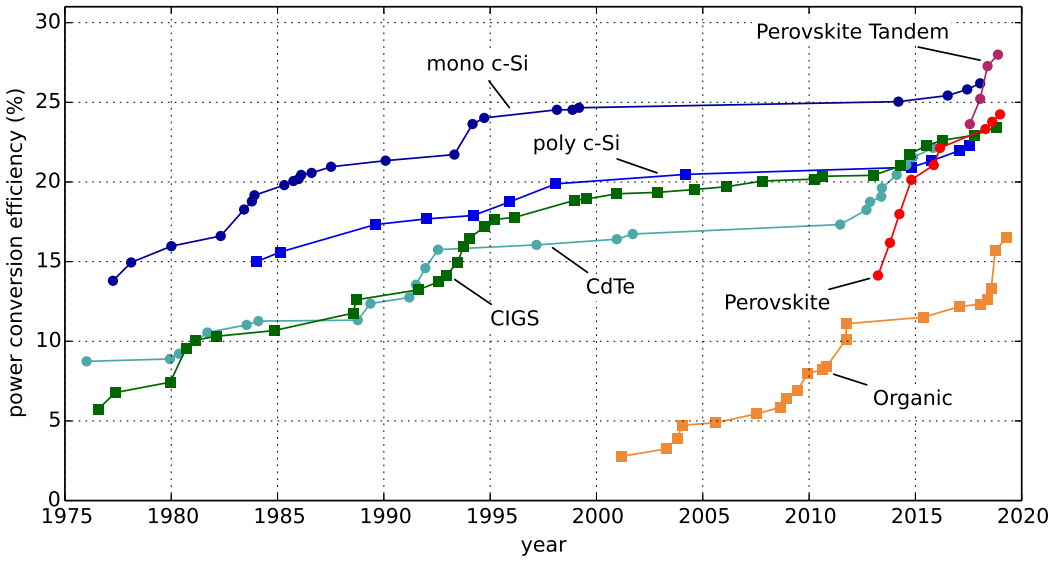

Figure 2.1: Development of the record power conversion efficiencies since 1975.
Data source: NREL best research cell efficiencies. [14]

The development of the record efficiencies of established solar cell technologies, perovskites and organic solar cells is shown in Figure 2.1. Crystalline silicon solar cells are divided into monocrystalline silicon (mono c-Si) and polycrystalline silicon (poly c-Si). Polycrystalline modules are cheaper to produce but have lower efficiency compared to their monocrystalline counterparts. Within a decade the record efficiencies of perovskite solar cells reached the ones of CIGS, CdTe and monocrystalline silicon. The development of organic solar cells seemed stuck after 2012 but with the discovery of the nonfullerene acceptors (see subsection 5.1.2)

the efficiency increased above 15%.

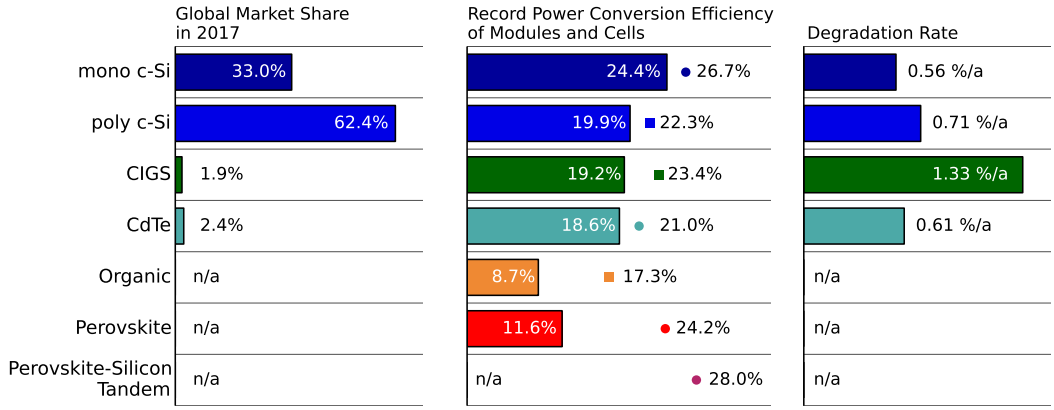

Figure 2.2: Overview of PV materials and technologies. Dots indicate the record power conversion efficiency for lab-scale cells while the bars indicate the module records. It should be noted that for organic solar cells and perovskites there is no reliable degradation data and the technologies are not commercially available yet. *Data source: Market share from ISE PV report [11]. Record efficiencies from solar cell efficiency tables version 54 [12]. Degradation data from Jordan [15].*

In Figure 2.2 a technology overview is presented with market share, record cell and module efficiency and the average degradation rate. The record efficiencies (dots) are typically measured on small-area lab-scale devices. When scaling up to square-meter-sized module areas, additional losses reduce the overall efficiency. Upscaling organic and perovskite solar cell production is challenging, making the difference between record efficiencies on small area devices and modules larger compared to the established technologies.

On average crystalline silicon solar cells degrade at a rate of less than one precent per year [15]. With a degradation rate of $0.71\%/a$ (poly-crystalline silicon solar cells) the solar module will still deliver 80% of its initial performance after 31 years. Organic and perovskite solar cells are not yet as stable as their silicon counterparts. Both material classes are sensitive to oxygen and moisture and require careful encapsulation [16].

2.1 THE ROLE OF NEW MATERIALS AND THEIR APPLICATIONS

At the beginning of the 21st century wafer-based crystalline silicon solar modules were expensive. At that time research on new materials was driven by the desire to lower cost. While PV devices based on amorphous silicon were less efficient, they were much less expensive to produce since they used less of the costly silicon raw material. A lower module efficiency was therefore acceptable as long as the total cost could be kept down.

This paradigm changed around 2010 when the cost of the silicon raw material dropped, production capacities increased and the production costs decreased. The process of cutting silicon ingots or bricks into single wafers was continuously

optimized enabling thinner wafers and less kerf[1] losses. By 2018 silicon solar modules were as cheap as 0.30 *Euro/Watt* (see Figure 1.3). Few would have believed in the year 2000 that production cost could decrease so rapidly within 18 years. Since silicon solar cells are continuously getting better and cheaper, it seems unrealistic that any other PV technology will be able compete on price in the near future.

Today's research on new solar cell materials therefore has another focus. One approach is to focus on new markets like mobile applications, applications that require lightweight, semi-transparent or flexible solar cells. The other approach is to reach higher power conversion efficiencies compared to crystalline silicon by applying new materials in tandem structures.

2.1.1 *New Markets*

One disadvantage of crystalline silicon solar modules is that they are brittle, inflexible and heavy. This presents an opportunity for solar cells made using new absorber materials since they can be made light-weight, flexible, partially transparent and in various shapes and colours.

Building-integrated photovoltaics (BIPV): In addition to rooftops, the facades of buildings can be used for solar energy production. This leads to higher yields in the wintertime due to both an improved angle of incidence and an absence of snow coverage. Custom-shaped and colourful modules can also be used as a design element in modern architecture as has been demonstrated in the SwissTech convention centre in Lausanne (Figure 2.3). The German companies OPVIUS [17] and Heliatek [18] produce commercially-available organic solar modules for building integration.

Mobile devices: Solar cells can be integrated into surfaces on mobile devices such as mobile phones or laptops to extend their battery life. One example of a commercially available mobile photovoltaic product is a charger sold by infinityPV [19] as shown in Figure 2.4. The flexibility of this organic solar cell module allows it to be rolled away for compact storage.

Automotive PV: Solar cells may also be integrated into the surfaces of electric cars or trucks. They could charge the battery when parked or while driving extending the driving range of the vehicle (see automotive paper of OPVIUS [20]).

1 Kerf is the width of material lost during the cutting process.

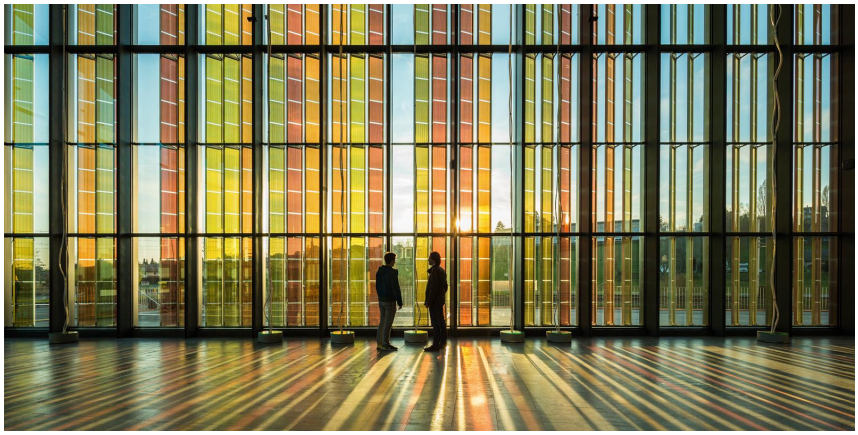

Figure 2.3: Solar facade of the SwissTech convention centre in Lausanne, Switzerland. Image: Richter Dahl Rocha and associes architectes [21].

Figure 2.4: Mobile phone charger HeLi-on by infinityPV [19].

2.1.2 *Lowering Cost via Higher Module Efficiency*

The total cost of a photovoltaic installation consists of the module cost and the so-called balance of system (BOS). The BOS cost includes everything except the module, namely that of the inverter, installation labour, grid connection, fees, and taxes etc. Whereas the module price can be monitored globally and follows a cost reduction trend as shown in Figure 1.3, the BOS costs vary regionally [22].

In almost all cases the BOS accounts for the majority of the total cost of a PV installation [22]. Figure 2.5 shows results from the National Renewable Energy Laboratory (NREL) *photovoltaic system cost benchmark* [23].

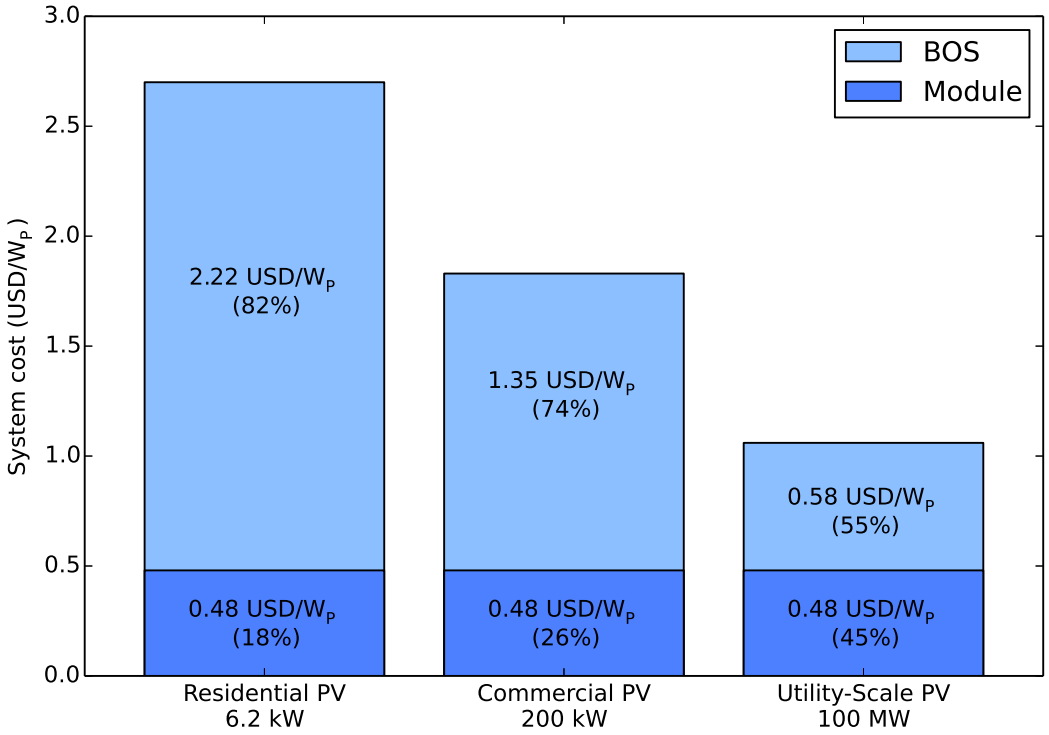

Figure 2.5: Photovoltaic system cost in the US 2018 split between PV module cost and balance of system cost (BOS).
Data source: photovoltaic system cost benchmark from NREL [23].

Dependent on the size of the installation, the module costs accounted for between 18% and 45% of the total system cost in the US market in 2018. This statistic demonstrates that module costs are becoming less relevant with respect to the total system cost, a continuing trend that is also seen globally. The cost reduction curve of the BOS, however, is not as steep as for that of the module. Elshurafa and co-workers have shown that, for a sample of different countries, costs drop by 11% on average whenever the cumulative installation doubles. [22].

Further cost reductions to the total system cost can be achieved by improving the module efficiency [23, 24]. A PV power plant utilising high efficiency modules requires less cabling, land, and installation labour as compared to a plant using lower efficiency modules producing the same power output. Hence, the fixed and

area-related costs are reduced relatively when the module efficiency is increased. Further improvements to module power conversion efficiencies therefore provide an important route to further cost reductions.

2.1.3 *Increasing Module Efficiencies*

For utility-scale PV installations in the US the average module efficiency was 19% in 2017 [23]. The current module efficiency record for crystalline silicon is 24.4% [12], while the physical limit for a single-junction solar cell, as determined by Shockley and Queisser, is 31% [10].

There are a number of approaches to surpass the Shockley-Queisser limit [25]. The most successful of these is the tandem solar cell in which two photovoltaic materials with different band-gaps are stacked on top of each other. The top cell absorbs the higher energy photons (for example blue and red visible light) whereas the bottom cell absorbs the lower energy photons (for example infrared light) enabling a greater proportion of the solar spectrum to be utilized. This approach is successfully employed in multi-junction III-V solar cells for concentrated photovoltaics as described previously.

In combination with a silicon or CIGS bottom cell, perovskites present a promising candidate for use in tandem top cells. While the theoretical limit for a double junction solar cell is approximately 46%, optical simulation studies of this configuration suggest that power conversion efficiencies above 30% are feasible [26, 27]. In a two terminal tandem, where two solar cells are stacked directly on top of each other, the current of both subcells needs to be equal. This requirement for current matching demands a high degree of stack optimization. Whereas established technologies like crystalline silicon, CdTe or CIGS have a fixed band gap, the band gap of perovskites can be adjusted by compositional changes. Perovskites with band gaps between 1.18 eV and 2.3 eV have been demonstrated [28]. This flexibility can be used to match perovskite top cells to existing bottom cells. The requirement for current-matching can be avoided in 4-terminal configurations where both subcells are contacted individually. The draw-back is that transparent electrodes are required on both sides of the top cell leading to additional ohmic losses and parasitic absorption losses.

The following is a non-exhaustive list of efficiency results from perovskites tandem configurations:

- 2-terminal perovskite-silicon tandem with 28.0% efficiency by OxfordPV [29].
- 4-terminal perovskite-silicon tandem with 26.7% efficiency by Quiroz *et. al.* [30].
- 2-terminal perovskite-perovskite tandem with 18.0% efficiency by Forgacs *et. al.* [31].
- 4-terminal perovskite-perovskite tandem with 22.9% efficiency by Zhao *et. al.* [32].

The 2-terminal perovskite-silicon tandem solar cell has great economic potential since adding the perovskite deposition step to existing silicon solar cell production lines would require only a small adaptation to existing processes. The cost of deposition of the additional layers was estimated to be lower than $10\,USD/m^2$ [28].

A silicon module with costs of $0.3\,Euro/W$ and an efficiency of 22% has area costs of $66\,Euro/m^2$. Adding an additional percentage point in efficiency can therefore not cost more than $3\,Euro/m^2$ to keep the $0.3\,Euro/W$ constant. To be economically viable the perovskite top cell with extra costs of $10\,USD/m^2$ needs to add at least 3%-points to the efficiency compared to the single silicon cell. Perovskite-silicon tandem solar cells present a opportunity to increase efficiency and thereby decrease the total system costs. Meeting the cost target will however be challenging as silicon module prices continue to decrease.

The principle challenges for this technology lie in the improvement of the power conversion efficiency, the upscaling of the perovskite layer deposition and the improvement of the long-term stability of perovskite solar cells.

3 THE SCOPE OF THIS THESIS

A comprehensive understanding of the physical processes underlying solar cell devices is key for future power conversion efficiency improvements. Over the past 30 years a profound understanding of the relevant materials has facilitated progress in solar cell research. An understanding and quantification of losses in the solar cell allows strategies to mitigate them.

The physics of silicon solar cells is well understood. Crystalline silicon is an indirect band gap semiconductor with a relatively low absorption coefficient but good charge transport. Its electrical performance is mainly determined by the surface-quality and the material purity. Free charges (electrons and holes) live long enough to diffuse through the bulk across the pn junction. The minority carrier lifetime is the most important material parameter and it can be measured by quasi steady-state photo-conductance (QSSPC) [33].

The physics of third generation solar cells is more challenging. These thin film devices often have a high electric field that facilitates charge transport. Many different material parameters influence charge generation (exciton dissociation), transport, recombination and extraction. These parameters depend on both the properties of the material itself and on the specific choice of deposition process. For example, changing the spin coating speed for the deposition of the donor-acceptor blend for an organic solar cell, can completely change the charge carrier mobility, the recombination coefficient and other parameters. Opto-electronic characterization is therefore important for these devices and materials. In many cases material parameters can not be determined by individual experiments since they are entangled. [34].

This thesis is focussed on the characterization and simulation of organic and perovskite solar cells and aims to provide improved insight into their operating principles with the ultimate aim of improving the power conversion efficiency and stability of these devices.

chapter 4 explains the basic concepts of solar cell physics including charge transport, band diagrams, charge recombination and excitons. In this thesis organic solar cells as well as perovskite solar cells are investigated. These two material classes are introduced in chapter 5.

The experimental setup applied to characterize the solar cell devices is described in chapter 6. The drift-diffusion simulation model and the numerical methods are described in chapter 7 and 8.

chapter 9 presents a comprehensive overview on electro-optical characterization methods for third generation solar cells. Various experiments are simulated with systematically varied device and material parameters for a sample organic solar cell. Characterization methods in steady-state, transient and frequency domain are investigated. The systematic simulation results provide a guide for the interpretation of observed experimental results. A selection of the presented characterization methods are performed on an organic solar cell based on the active material PCDTBT:$PC_{70}BM$. The same experimental techniques are fitted by numerical simulation. The resulting fit shows that the main physical effects are understood and that relevant material and device parameters can be extracted accurately. A drift-diffusion model with discrete energy levels, constant charge mobilities, ohmic contacts, charge trapping and Shockley-Reed-Hall (SRH) recombination is applied in this study.

In perovskite solar cells a hysteresis is observed between the forward and reverse current-voltage (IV) scans [35]. There is strong evidence that mobile ions are present in these materials and their motion during the IV-scan can cause IV-curve hysteresis. In chapter 10 the drift-diffusion model is extended to include mobile ions. The ion redistribution is calculated according to the applied voltage, then the transport of electron and holes is calculated using a fixed ion concentration profile. This model is applied to investigate and explain the effects of mobile ions in the perovskite material. It is shown that mobile ions cause hysteresis if either surface- or bulk-recombination is high enough. If surface-recombination is very low (well passivated surfaces) and the bulk-recombination is also low enough charge carriers can diffuse to the correct contact even if mobile ions screen the electric field. This study explains why highly efficient solar cells often show less hysteresis.

In chapter 11 the drift-diffusion model is solved with fully coupled mobile ions. Several of the measurement techniques presented in chapter 9 are performed on vacuum deposited methylammonium lead iodide perovskite solar cells. The simulation model is applied to reproduce the full complement of measurements with one set of parameters. Where other simulation studies have focussed on individual measurement techniques, this study presents simulation data for a variety of experiments and allows deeper insight into the physical processes of these devices. The limits of the current device model are illustrated and possible model extensions are discussed. A parameter variation is performed in order to understand the performance limiting factors of the device under investigation.

The scientific work of this thesis was done at the institute of computational physics (ICP) at the Zürich University of Applied Sciences (ZHAW) in Winterthur in strong collaboration with the company Fluxim AG. Fluxim's tools, the simulation software *Setfos* as well as the measurement system *Paios* were applied and further developed within this work.

Part II

BASIC CONCEPTS OF THIRD GENERATION SOLAR CELLS

4

SOLAR CELL PHYSICS

This chapter is partially based on the section "solar cell physics" of the author's previous publication [36]. The basic physical principles of solar cells are discussed.

4.1 GENERAL OPERATING PRINCIPLES

In solar cells the absorption of a photon with energy equal to or above the bandgap leads to the excitation of an electron from the valence band (or HOMO-level[1]) to the conduction band (or LUMO-level[2]). The excited electron leaves behind a positively charged hole in the valence band. The hole in the valence band and the electron in the conduction band attract each other due to the Coulombic interaction. This bound state of electron and hole can be described as quasi-particle that is called exciton. Thermal energy, an electric field or a material interface is required to dissociate an exciton into a free electron and a free hole. The exciton binding energy depends on the specific material and is discussed in section 4.6 Excitons. When an electron falls back into a hole, a process known as recombination, its energy is emitted either thermally (phonon-emission) or optically (photon-emission).

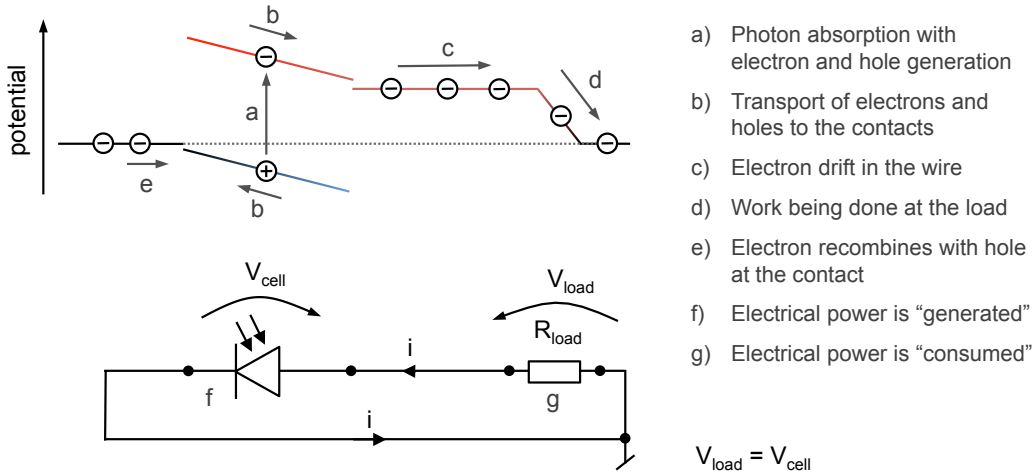

Figure 4.1: General working principle of a solar cell illustrated with an extended band diagram (upper graph) and an electric circuit including a load (lower graph). Please note that the current *i* is defined as positive, resulting in electrons moving in the opposite direction to the arrows.

Figure 4.1 shows the main operating principles of a solar cell. In step *a* light is absorbed and the exciton separated as described above. According to the driving forces explained in the next section the electrons and holes move to the contacts (step *b*). The wires connected to the solar cell are metallic and consequently have

1 The HOMO-level is the energy level of the highest occupied molecular orbit.
2 The LUMO-level is the energy level of the lowest unoccupied molecular orbit.

many free electrons facilitating the current (step *c*). In step *d* the electron performs work on the load by going from the high potential to the low potential. In this illustration the cell is at its maximum power point (MPP) somewhere between the short-circuit and the open-circuit. To reach this state the load R_{load} must be appropriately matched to the cell's current voltage characteristics.

In the electric circuit in Figure 4.1 the sign of the voltage of the solar cell V_{cell} is in the opposite direction to that of the current i (see *f*). From an electrical point of view, power is generated in the solar cell, whereas power is dissipated in the load resistor R_{load} (see *g*).

4.2 DRIVING FORCES

The driving force for electrons and holes is the gradient of their respective quasi Fermi levels [25]. The total particle currents j_e and j_h are described in Equation 4.1 and 4.2.

$$j_e = n_e \cdot \mu_e \cdot grad(E_{fe}) \tag{4.1}$$
$$j_h = -n_h \cdot \mu_h \cdot grad(E_{fh}) \tag{4.2}$$

where n_e and n_h are the electron and hole densities, μ_e and μ_h are the electron and hole mobilities and E_{fe} and E_{fh} are the quasi Fermi levels for electrons and holes, respectively.

The quasi Fermi level is equal to the electrochemical potential[3] η that consists of the electrical potential φ and the chemical potential γ as shown in Equation 4.3 and 4.4.

$$E_{fe} = \eta_e = \gamma_e + q \cdot \varphi \tag{4.3}$$
$$E_{fh} = -\eta_h = -\gamma_h - q \cdot \varphi \tag{4.4}$$

The chemical potential of electrons and holes (γ_e and γ_h) is dependent on their charge carrier density (n_e and n_h), and assuming Boltzmann statistics, can be expressed according to Equation 4.5 and 4.6,

$$\gamma_e = -\chi_e + k_B \cdot T \cdot ln\left(\frac{n_e}{N_C}\right) \tag{4.5}$$
$$\gamma_h = -\chi_h + k_B \cdot T \cdot ln\left(\frac{n_h}{N_V}\right) \tag{4.6}$$

where χ_e is the electron affinity[4], χ_h the ionization potential[5], N_C and N_V are the conduction and valence band effective density of states respectively, k_B is the Boltzmann constant and T is the temperature.

3 The electrochemical potential is in contrast to its name not a potential but an energy.
4 The electron affinity is equal to the LUMO-level.
5 The ionization potential is equal to the HOMO-level.

Combining Equation 4.1, 4.3 and 4.5 results in Equation 4.7 for electrons. Replacing the gradient with a one dimensional spatial derivative results in Equation 4.9 - the electron drift-diffusion equation as described in chapter 7.1 The Charge Carrier Drift-Diffusion Equations.

$$j_e = n_e \cdot \mu_e \cdot grad\left(-\chi_e + k \cdot T \cdot ln\left(\frac{n_e}{N_C}\right) + q \cdot \varphi\right) \tag{4.7}$$

$$j_e = n_e \cdot \mu_e \cdot k \cdot T \cdot \frac{\partial}{\partial x}\left(ln\left(\frac{n_e}{N_C}\right)\right) + n_e \cdot \mu_e \cdot q \cdot \frac{\partial \varphi}{\partial x} \tag{4.8}$$

$$j_e = \mu_e \cdot k \cdot T \cdot \frac{\partial n_e}{\partial x} + n_e \cdot \mu_e \cdot q \cdot \frac{\partial \varphi}{\partial x} \tag{4.9}$$

The analogous equation for holes is shown in Equation 4.10.

$$j_h = \mu_h \cdot k \cdot T \cdot \frac{\partial n_h}{\partial x} - n_h \cdot \mu_h \cdot q \cdot \frac{\partial \varphi}{\partial x} \tag{4.10}$$

To cut a long story short: The gradient of the quasi Fermi levels is the driving force for charge transport, combining the principles of diffusion (chemical potential) and drift (electrical potential). In solar cell physics the Fermi level and band structures are often illustrated to understand the device operating mechanisms. Band diagrams are explained in the next section.

4.3 BAND DIAGRAMS AND BASIC SOLAR CELL OPERATION

Let us consider a simple solar cell with good charge transport, low recombination and a built-in voltage that drives the charge carriers to the electrodes. The device is not doped and has no traps. The current-voltage (IV) curve of such an idealised device is shown in Figure 4.2a.

In a band diagram, electron energy is plotted against position in the device. In this case the device is illuminated from the left. The anode, at which the holes are extracted, is on the left-hand side of the device at $x = 0\,nm$. On the right at $x = 100\,nm$ is the cathode where electrons are extracted.

At **short-circuit in the dark** (Figure 4.2b) no current flows. There is a single Fermi level for both electrons and holes and its gradient is zero. The bands are inclined resulting in a constant electric field throughout the device.

Under **illumination at short-circuit** (Figure 4.2c) charge generation leads to an increase in electron and hole densities and the respective quasi Fermi-levels split. Since the two contacts (indicated with thick lines) are at the same potential, there is no voltage drop on the cell. As there is a gradient in both quasi Fermi levels an electron and a hole current flows.

At an **applied forward voltage in the dark** (Figure 4.2d) the internal field is reduced and the bands become flatter. The difference between the quasi Fermi level of holes on the left and the quasi Fermi level of electrons on the right is defined by the applied voltage. A forward current flows. As the charge carrier

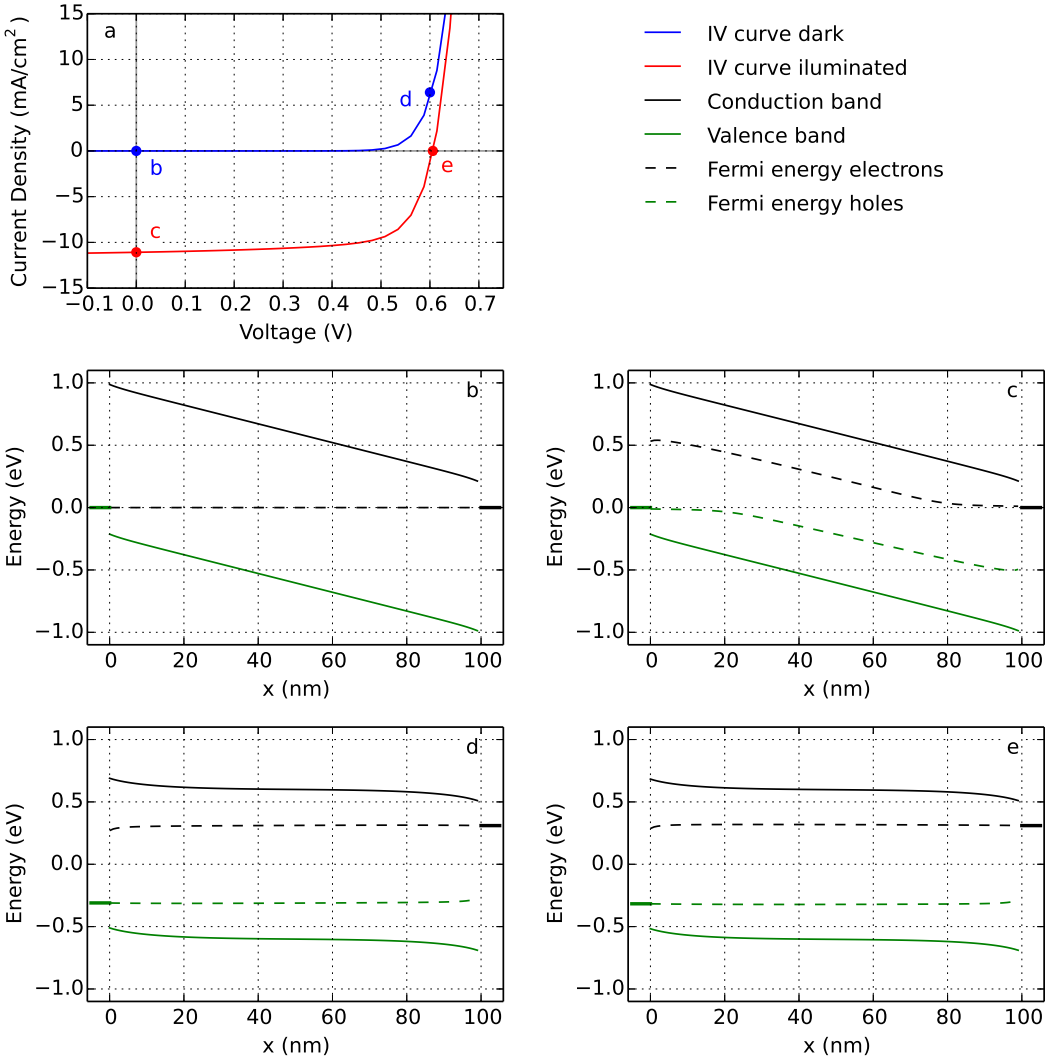

Figure 4.2: a) Simulated current-voltage (IV) curve in the dark and illuminated. b) Band diagram at 0 V in the dark. c) Band diagram at 0 V under illumination. d) Band diagram with forward bias in the dark. e) Band diagram at open-circuit.

density is very high, a very small gradient in the quasi Fermi-levels is sufficient to create large currents.

At **open-circuit under illumination** (Figure 4.2e) no current flows - all charges recombine. As can be seen in the band diagram, the charge carrier density is high resulting in quasi Fermi-levels much closer to the bands as compared to short circuit under illumination in case c.

4.4 MAJORITY VERSUS MINORITY CARRIER DEVICES

Solar cells can be categorised in many different ways: in this section the distinction is made between the main driving forces into *minority carrier devices* governed

by diffusion and *majority carrier devices* governed by drift. While this way of categorising devices may be unfamiliar to many solar cell specialists as they only deal with one or the other type, it provides a useful framework for understanding the principle device physics of third generation solar cells.

Figure 4.3 shows a comparison of the two device types. The majority carrier device is shown as *pin*-structure[6] and the minority carrier device with the same structure but the intrinsic region *i* replaced with an n-type doped layer. Both band diagrams are shown at zero applied voltage under illumination. In the simulations presented here, charge carriers are generated homogeneously throughout the device.

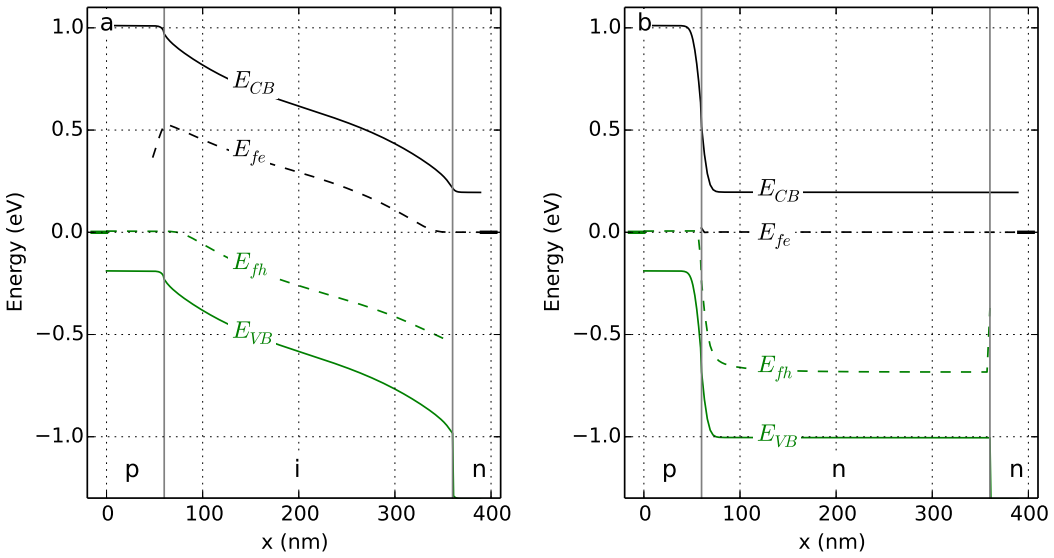

Figure 4.3: a) Majority carrier device in pin-structure. Steep bands indicate a high electric field. b) Minority carrier device in pn-structure where the bands are flat within the majority of the device. The applied voltage is zero volt and the device is under illumination.

4.4.1 *Minority Carrier Devices*

Minority carrier devices are doped which leads to an imbalance of charge carriers in a large part of the device. The transport is then limited by the diffusion of minority carriers to the junction.

An example of the band structure in a minority carrier device is shown in Figure 4.3b. At the pn-junction the electric field is very high, whereas in the n-type region it is screened (close to zero). In the n-type region the electron quasi Fermi-level (E_{fe}) is much closer to the conduction band (E_{CB}) than the hole quasi Fermi-level (E_{fh}) to the valence band (E_{VB}) indicating that fewer holes are present than electrons. In this example the minority carriers are the holes. To be extracted, holes must diffuse from the n-type region to the junction since transport by drift

6 The pin stands for p-type doped, intrinsic (undoped) and n-type doped sequence of layers.

in the bulk is negligible. Electron transport via diffusion is not limiting due to the high electron density in the n-type region.

Most of the established solar cell technologies including crystalline silicon, cadmium-telluride (CdTe) and copper-indium-gallium-selenide (CIGS) employ pn-junction minority carrier mechanics.

4.4.2 *Majority Carrier Devices*

The absorber layer of majority carrier devices is undoped and as such the densities of electrons and holes are of a similar order of magnitude. In the majority carrier device shown in Figure 4.3a an electric field is created in the intrinsic region due to the difference in Fermi energies of the n-type and p-type regions. Alternatively, such a field can be created using metals with different workfunctions as contacts. Please note that minority carrier devices also have a built-in potential: This potential drops at the pn-junction, leaving the rest of the device field-free.

In many types of majority carrier devices the diffusion length is too short and an electric field is required to transport charge carriers to the electrodes before they recombine. Common majority carrier devices are amorphous silicon, organic solar cells or perovskite solar cells.

4.4.3 *Charge Carrier Lifetime*

In *minority carrier devices* the charge carrier lifetime for electrons τ_e is defined as

$$\tau_e = \frac{n_e}{R} \tag{4.11}$$

where R is the recombination and n_e is the electron density (minority carriers in this case). For radiative recombination $R = \beta \cdot n_e \cdot n_h$ and the lifetime is independent of the minority carrier density. Assuming a heavily p-doped device, where $n_h = N_A$, the lifetime results in

$$\tau_e = \frac{n_e}{\beta \cdot n_e \cdot n_h} = \frac{1}{\beta \cdot N_A} \tag{4.12}$$

where β is the recombination prefactor, n_h is the hole density and N_A is the doping density. Assuming $n_h >> n_e$ (which is the case in a doped device) the hole density is largely unaffected by recombination and can be considered as constant. Hence the charge carrier lifetime can be considered as a constant material parameter.

If both the diffusion constant D_e and the lifetime τ_e are known, the diffusion length $L_{D,e}$ can be calculated according to

$$L_{D,e} = \sqrt{D_e \cdot \tau_e} = \sqrt{\mu_e \cdot k_B \cdot T \cdot \tau_e} = \sqrt{\frac{\mu_e \cdot k_B \cdot T}{\beta \cdot N_A}} \tag{4.13}$$

where μ_e is the electron mobility, k_B the Boltzmann constant and T the temperature. Similar to above, the minority carrier diffusion length can be regarded as

constant material parameter if the material is heavily doped. For a device to operate efficiently the diffusion length needs to be significantly longer than the device thickness.

In *majority carrier devices* the concept of charge carrier lifetime cannot be applied directly. The assumption $n_h >> n_e$ does not hold in these devices as the absorber layer is undoped. The electron lifetime τ_e depends on the hole density n_h and the hole lifetime τ_h depends on the electron density n_e as shown in Equation 4.14.

$$\tau_e(n_h) = \frac{1}{\beta \cdot n_h} \qquad \tau_h(n_e) = \frac{1}{\beta \cdot n_e} \tag{4.14}$$

The electron density n_e and hole density n_h can vary over orders of magnitude depending on both the position within the device and the time. Charge carrier lifetime can not, therefore, be regarded as constant material parameter in a majority carrier device like a perovskite or organic solar cell. Consequently, the product of the diffusion constant D and lifetime τ as shown in Equation 4.13 is not physically meaningful. A charge carrier travelling through the device will have different lifetimes depending on its position. Furthermore, in these types of devices, charge carriers are mainly transported by drift[7].
Although the physical meaning may be questionable, the mobility-lifetime-product is sometimes used in publications to discuss majority carrier devices [37–44]. The physical meaning of carrier lifetimes in pin-structured solar cells should therefore be critically discussed in the scientific community.

4.4.4 *Traps and Doping*

Semiconductor doping can be intentional, as in the case of a silicon solar cell, or unintentional, as is sometimes the case in organic photovoltaics. As shown by Kirchartz *et. al.* doping is typically detrimental to the performance of organic solar cells since the electric field is screened and charges cannot be transported to the electrodes [45].

Doping usually refers to the creation of free charge carriers activated at room temperature leaving static ions of opposite charged polarity. Figure 4.4a and 4.4c illustrate this process. An atom or molecule is placed in a semiconductor such that the atom's occupied energy level is close to the unoccupied conduction band of the semiconductor. If thermal energy at room temperature is sufficient the atom or molecule is ionized. In Figure 4.4c a free electron leaves behind an immobile positive charge (hole).

Charge trapping can however lead to the same effect and is sometimes referred to as photo-doping [46]. Figure 4.4b shows a semiconductor with an additional energy level somewhere in the band-gap acting as hole-trap. Without any activation it is neutral as in the case of Figure 4.4a. If a photon is absorbed a free

7 A notable exception are pin-structured perovskite solar cells, where charge transport is most probably governed by diffusion as shown in this thesis.

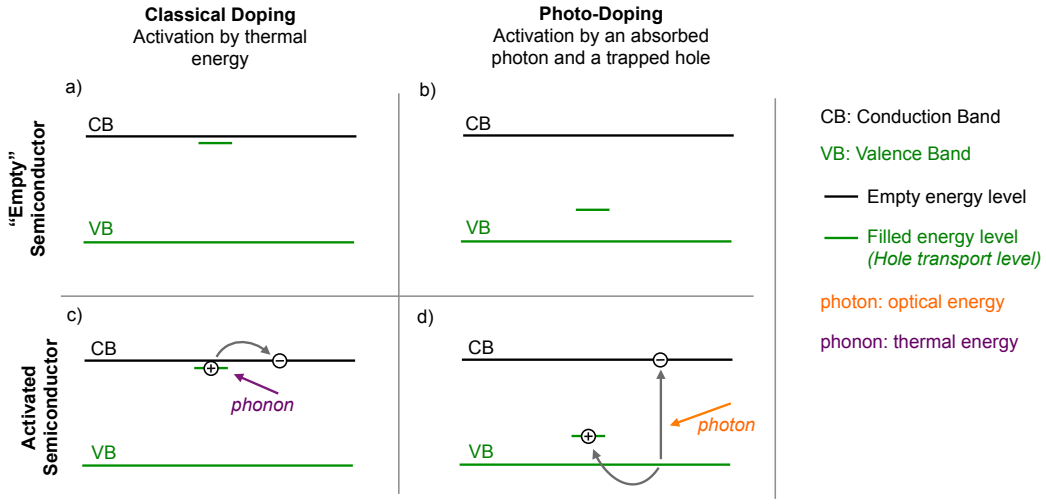

Figure 4.4: a) An "empty" semiconductor containing a filled energy level close to the conduction band. b) An "empty" semiconductor containing a filled energy level somewhere in the band-gap (this is also called a hole-trap). c) By thermal energy the electron is moved from its energy level to the conduction band (ionized dopant). d) An electron and a hole are created by photon-absorption. After a short time the hole gets trapped (photo-doping).

electron and hole are created. If the hole falls into the hole-trap it is immobile. The two situations (classical doping and photo-doping) lead to the same result: a free electron and a fixed hole (or vise-versa).

In numerical drift-diffusion modelling doping is added as fixed charge in the Poisson equation as shown in Equation 7.12 in section 7.1 The Charge Carrier Drift-Diffusion Equations.

4.5 RECOMBINATION AND OPEN-CIRCUIT VOLTAGE

Recombination is the annihilation of an electron and a hole. During a recombination event the potential energy of the electron in the conduction band is transferred resulting in phonon and/or photon emission. Figure 4.5 shows the four recombination types that can be present in semiconductors.

Radiative recombination is physically inherent in absorbing materials and cannot be avoided. The recombination rate is proportional to both charge carrier densities and depends on the Fermi level splitting as shown in Equation 4.15.

$$R_{rad} = \beta \cdot n_e \cdot n_h = \beta \cdot e^{\frac{E_{fe} - E_{fh}}{k_B \cdot T}} \tag{4.15}$$

As indicated in Figure 4.5 a photon is emitted during radiative recombination. Radiative recombination can, therefore, be directly monitored by measuring the electro-luminescence (EL) signal. A high EL efficiency indicates that other, avoidable, recombination types are not dominant. Hence, a good solar cell with a

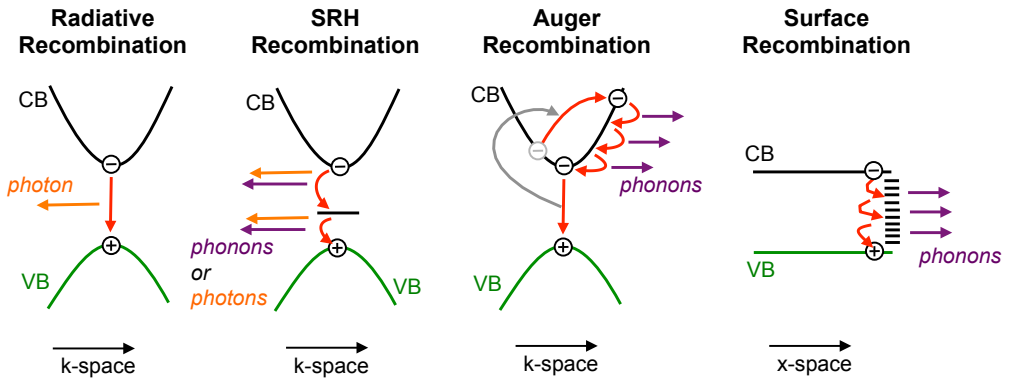

Figure 4.5: Schematic illustration of recombination types in semiconductors.

high open-circuit voltage will also exhibit a high EL efficiency.

Langevin recombination: When an electron and a hole in an organic semiconductor get closer than the Coulomb radius they form an exciton and recombine. This recombination is mostly non-radiative. Mathematically, it has however the same form as the radiative recombination described above. The probability that electrons and holes meet and recombine is proportional to their densities and their charge carrier mobilities as described by the Langevin theory. The recombination prefactor β is calculated according to $\beta = \eta \cdot (\mu_e + \mu_h) \cdot q/\epsilon$ where η is the Langevin prefactor controlling the recombination efficiency, μ is charge carrier mobility, q the unit charge and ϵ the permittivity.

Shockley-Read-Hall (SRH) recombination (also known as trap-assisted recombination) requires an energy level within the band-gap. The energy is either emitted by a phonon or a photon as shown in Figure 4.5. Such mid-gap states occur due to dangling bonds or impurities. In a perfect material SRH recombination is absent. For a cell in steady-state, SRH recombination can be expressed as

$$R_{SRH} = n_{imp} \cdot \frac{n_e \cdot n_h - n_i^2}{\frac{n_e + N_C \cdot e^{-\frac{E_{CB} - E_{imp}}{k \cdot T}}}{c_h} + \frac{n_h + N_V \cdot e^{-\frac{E_{imp} - E_{VC}}{k \cdot T}}}{c_e}} \tag{4.16}$$

where n_{imp} is the density of the impurities, n_i is the intrinsic carrier density, E_{imp} is the energy level of the impurity, c_h and c_e are the capture rates of electrons and holes and N_C and N_V are the effective density of states of the conduction band and valence bands, respectively.

Auger recombination can be considered as the reverse of impact ionization. An electron transfers its energy to another electron which is subsequently elevated to a higher energy state in the conduction band. The second electron then thermalises down to the conduction band edge by emitting phonons as shown in Figure 4.5. The mathematical expressions for electron and hole Auger recombination are given in Equation 4.17

$$R_{Aug,e} = C_e \cdot n_e^2 \cdot n_h \qquad R_{Aug,h} = C_h \cdot n_e \cdot n_h^2 \tag{4.17}$$

where C_e and C_h are Auger recombination constants. As Auger recombination scales with the cube of the charge carrier density, it is large for devices with high levels of doping. While in silicon solar cells it largely determines the efficiency limits of the record devices [25], it is practically irrelevant for majority carrier devices.

Surface recombination happens via one or more states that are present at the surface of an interface between two materials. Dangling bonds and defects present at interfaces can create states within the band-gap. A charge carrier reaching a surface hops from state to state loosing its energy by phonon emission as shown in Figure 4.5. Surface recombination is described as

$$R_{Sur,e} = \nu_e \cdot n_e \qquad R_{Sur,h} = \nu_h \cdot n_h \tag{4.18}$$

where ν is the surface recombination velocity. Metals have an infinite surface recombination velocity ν: there are so many states available that charges effectively recombine immediately when reaching the surface.

The term surface passivation means applying measures to lower the surface recombination velocity. This can be done by coating additional buffer layers that are blocking one charge carrier type or by additional local doping at the contact[8].

Minority carrier devices require passivated surfaces. In majority carrier devices surface recombination is generally less detrimental to devices as charge selectivity is ensured by the electric field.

4.5.1 *Recombination Order*

The concept of a recombination order requires a zero-dimensional model of the solar cell. For its explanation similar electron and hole densities are assumed. The recombination order k is defined as

$$R = n^k \tag{4.19}$$

where R is the recombination and n is the charge carrier density. Given the previous mathematical descriptions of recombination types, if the recombination order can be successfully identified, it can provide information about the dominant recombination type in any given device.

8 In silicon solar cells this concept is called back surface field BSF. The p-type wafer is doped with p+ at the contact to reduce the electron concentration and passivate the surface.

Assuming the simplification $n = n_e = n_h$ the expression for radiative recombination becomes

$$R_{rad} = \beta \cdot n_e \cdot n_h = \beta \cdot n^2 \tag{4.20}$$

The recombination order for radiative recombination is therefore 2. For SRH recombination the recombination order results in 1 as shown in Equation 4.21. For the Auger recombination the recombination order is 3 as shown in Equation 4.22.

$$R_{SRH} = n_{imp} \cdot \frac{n_e \cdot n_h}{C_1 \cdot n_e + C_2 \cdot n_h + C_3} = C_4 \cdot n \tag{4.21}$$

$$R_{Aug,e} = C_e \cdot n_e^2 \cdot n_h = C_e \cdot n^3 \tag{4.22}$$

4.5.2 *Ideality Factor*

The ideality factor n_{id} is used in the Shockley (or diode) equation to describe an IV curve analytically

$$j(V) = j_S \cdot \left(exp\left(\frac{V \cdot q}{k_B \cdot T \cdot n_{id}}\right) - 1\right) - j_{ill} \tag{4.23}$$

where j_S is the reverse saturation current and j_{ill} is the current due to illumination. If the ideality factor n_{id} is 1, the cell is *ideal*. The real ideality factor is always larger than one.

Similar to the reaction order and under the above assumptions, measurement of the ideality factor can allow the dominant recombination processes in devices to be identified. The ideality factor n_{id} and the recombination order k are related to each other:

$$n_{id} = \frac{2}{k} \tag{4.24}$$

With pure radiative recombination the recombination order is 2 and the ideality factor is 1. If SRH recombination is dominant the recombination order is 1 and the ideality factor is 2. This is however a simplified view: depending on carrier concentrations and the energy level of the trap also SRH-recombination can have an ideality factor of 1 [47].

Dark and light ideality factors are described in more detail in section 9.4.1 Dark current-voltage characteristics and 9.4.2 Open-circuit voltage versus light intensity.

4.6 EXCITONS

When a material absorbs a photon, an exciton is created. Excitons are bound electron-hole pair quasi-particles in which the Coulomb force binds the electron and hole together. They are charge neutral and are transported via diffusion processes. Dissociation of an exciton into a free electron and a free hole requires energy equal to or greater than the binding energy.
The exciton binding energy E_C is described by Equation 4.25

$$E_C = \frac{q^2}{4 \cdot \pi \cdot \epsilon_0 \cdot \epsilon_r \cdot r} \tag{4.25}$$

where q is the unit charge, ϵ_0 is the vacuum permittivity, ϵ_r is the relative dielectric constant and r is the distance between the charges usually around $1\,nm$.

According to Equation 4.25 the exciton binding energy is inversely proportional to the dielectric constant. A high dielectric constant is therefore desirable in photovoltaic materials. Crystalline silicon has a dielectric constant of 11.8 resulting in an exciton binding energy small enough such that the thermal energy kT is sufficient to dissociate the exciton at room temperature. Organic materials have a dielectric constant of around 4 leading to strongly bound excitons. As discussed in the following chapter, organic solar cells therefore require a material interface to facilitate exciton dissociation.

5 SOLAR CELL MATERIALS

There are a number of semiconductor material properties that are particularly relevant to photovoltaics. Solar cell materials can be categorized into:

- **Crystalline / amorph**
  Crystalline materials have a long range order. The overlapping electron wavefunctions lead to the formation of bands with efficient charge transport. Amorphous materials have comparatively random atomic structures and are usually highly defective leading to a lower charge carrier mobility and higher recombination rates.

- **Excitonic / non-excitonic**
  As discussed in section 4.6, whether or not a material generates strongly bound electron-hole pairs (excitons) depends to a large extent on its electric permittivity. Materials with a high dielectric constant are considered non-excitonic since excitons dissociate into free charge carriers rapidly at room temperature. Excitonic materials have strongly bound electron-hole pairs that require additional energy to dissociate.

- **Direct / indirect band gap**
  A material with an indirect band gap requires a photon and a phonon to excite an electron from the valence to the conduction band, while materials with direct band gaps only require a photon. The probability of simultaneous phonon and photon absorption is low. The absorption coefficient of indirect band gap materials is therefore typically much lower than direct band gap materials.

5.1 ORGANIC SEMICONDUCTOR MATERIALS

Organic materials consist of molecules with at least one carbon atom. When the molecule has alternating single and double bonds between carbon atoms (conjugation) the molecule becomes semiconducting. Organic semiconducting materials are successfully employed and commercialized as organic light emitting diodes (OLED) in TV and mobile phone displays. Organic bulk-heterojunction solar cells recently achieved a record efficiency of 17.3% in a two-terminal tandem structure [13].

In inorganic materials the electronic wave-functions overlap such that continuous bands are formed. By contrast, in organic materials the electrons are localized on single molecules. Charge transport instead works by charge carrier hopping. Charge carrier mobilities of between $10^{-6}\,cm^2/Vs$ and $10^{-2}\,cm^2/Vs$ are normally observed in organic materials [48–50]. This range is many orders of magnitudes lower than the charge carrier mobility of crystalline silicon ($300\,cm^2/Vs$). The absorption coefficient of organic materials can be very high, thus enabling the absorber film to be made very thin (often around $100\,nm$).

5.1.1 *The Bulk Heterojunction Concept*

As previously discussed, organic materials usually have low dielectric constants and as a consequence, high exciton binding energies. In contrast to inorganic materials thermal energy at room temperature is not sufficient in organic materials to create a free electron and hole from an exciton.
In order to dissociate excitons in organic materials a material interface is required with an energetic offset. Excitons in the material diffuse either until the electron and hole recombine or else until they reach an interface with a second material. The energy offset allows either the electron or the hole to be transferred to the other material. At this point a charge transfer (CT) exciton is created. The CT-exciton can be dissociated more easily into free carriers. The material in which the electron is transported is called *acceptor*, the material where the hole is transported is called *donor*.

While an absorber thickness of around $100\,nm$ is usually required to absorb enough light in organic photovoltaics, exciton diffusion lengths are usually between 1 and $10\,nm$ [51]. Hence in a planar configuration with a donor and acceptor of $50\,nm$ only a small fraction of excitons would reach the donor-acceptor interface.
A breakthrough in solving this problem was the *bulk heterojunction* concept whereby the donor and acceptor materials are mixed into a blend. It is called *heterojunction* since the junction where electrons and holes separate is realised with two different materials. This interface between the two materials is present throughout the *bulk*.

Morphology: The morphology of the donor-acceptor structure needs to be optimized to reach a compromise between exciton dissociation and charge transport. If the donor-acceptor mixing is very coarse charge transport will be efficient but excitons may recombine before reaching an interface. If the mixing is very fine, the majority of excitons will dissociate but charge transport will be inefficient since there may not be connected paths for electrons and holes to travel through (percolation pathways) [52, 53].

Materials: A commonly used material combination is that of the polymer donor and the fullerene acceptor. In chapter 9 an example of such a material system, $PCDTBT{:}PC_{70}BM$, is investigated.
Due to the difficulty in creating high performance polymer acceptors, all-polymer solar cells have met with less research success. Advances have been made in recent years however and a record power conversion efficiency of 9% has been reached [54].
As the name suggests, in *small molecule* solar cells both donor and acceptor consist of small molecules rather than polymers.

Organic solar cells are fabricated either by physical vapour deposition or by solution processing.

5.1.2 *Non-Fullerene Acceptors and Ternary Blends*

For over two decades acceptors based on fullerene derivatives were used in organic solar cell research. Fullerenes are ball-like molecules of fully conjugated carbon atoms and denoted as C_{60} or C_{70}, where the subscript denotes the number of carbon atoms in each molecule.
Recently non-fullerene acceptors (NFA) have been developed. These new materials exhibit great tunability in both their absorption spectra and band energy levels [55]. NFAs absorb more light than fullerenes, thereby contributing to the device photocurrent. To date single junction power conversion efficiencies of 15% have been reached [56].

Traditionally it was believed that a certain energy budget was required to dissociate excitons in organic materials. Due to this additional energy loss the maximum achievable efficiency was predicted to be much lower in organic as compared to inorganic photovoltaics. [57]. In NFAs however, excitons can be separated efficiently with negligible energy level offset [55]. As a result NFA solar cells show both higher open-circuit voltage and higher currents. The mechanism underlying exciton dissociation in these devices is not yet well understood.

Ternary blends: Since it is difficult to design organic materials with spectrally broad absorption, more than two materials can be mixed together to increase the total absorption. This architecture is called a *ternary blend* [58].

In contrast to perovskite solar cells the underlying physical processes in organic solar cells are comparatively well understood. In the chapter 9 of this thesis simulation results are presented that describe the charge transport of a $PCDTBT : PC_{70}BM$ solar cell during various experimental techniques. Simulation and experiment match well for a single set of parameters and the drift-diffusion model appears to be capable of reproducing all of the key device physics.

5.2 METAL ORGANIC HALIDE PEROVSKITES

The discovery of perovskite as solar cell material has triggered enormous scientific interest. The reported power conversion efficiencies have increased from 3% in 2009 [59] to above 24% in 2019 [12]. This pace of development is unprecedented in solar cell research. In this section the perovskite material, its properties and perovskite solar cell architectures are discussed.

5.2.1 *Perovskite Materials*

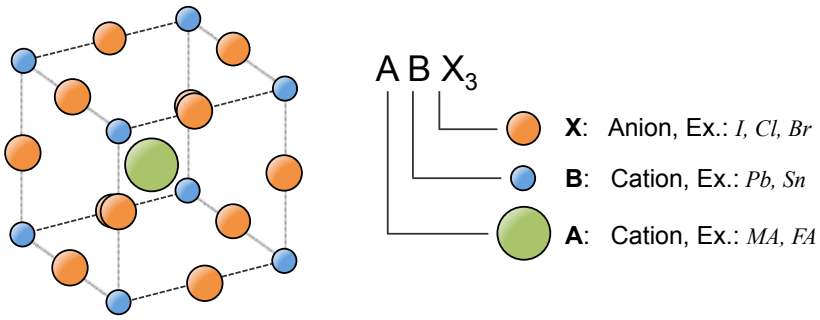

Figure 5.1: Unit-cell of a perovskite structure.

Perovskite is a crystal structure with the form ABX_3 as shown in Figure 5.1 where:

- **A** is a cation. In most cases an organic molecule is used like methylammonium (MA) $CH_3NH_3^+$ or formamidinium (FA) $HC(NH_2)_2^+$. Alternatively caesium (Cs) or rubidium (Rb) can be used.
- **B** is a cation that is normally either lead (Pb) or tin (Sn).
- **X** is an anion for which iodide (I), chloride, (Cl) and/or Bromide (Br) are used.

The materials for each site A, B and X can also be mixed to better stabilize the crystal structure or tune material properties like the band gap.

The most commonly used perovskite material is methylammonium lead iodide ($CH_3NH_3PbI_3$, often denoted MAPI), which has a band gap of $1.5\,eV$ [60]. When iodine (I) is replaced with bromine (Br) the band gap is $2.2\,eV$. By mixing iodine and bromine (mixed halide perovskite $CH_3NH_3PbI_{3-x}Br_x$) the band gap can be continuously tuned between $1.5\,eV$ and $2.2\,eV$ [60, 61], which is highly advantageous for designing materials for tandem devices.

MAPI perovskite is very sensitive to moisture and easily decomposes to MAI and PbI_2, a process which turns the material yellow. By mixing several cations like methylammonium (MA), formamidinium (FA), caesium (Cs) and rubidium (Rb) the material stability, device reproducibility, and power conversion efficiency can

be improved [62].

To date, all high efficiency perovskites contain **lead**, the toxicity of which may present a hurdle for commercialization. Consequently, attempts have been made to replace lead with tin. Record efficiencies for tin perovskite-based devices however remain at 9% [63]. Furthermore tin-based perovskites are very unstable due to the formation of Sn^{4+} leading to strong p-doping and lower device performance [64]. While other material combinations using germanium (*Ge*), bismuth (*Bi*), antimony (*Sb*) or magnesium (*Mg*) have been studied, efficiencies are low at below 2% [64].

5.2.2 *Perovskite Fabriaction*

There are several methods to create perovskite films. The majority of research groups currently produce perovskite films from solution. Here, either one step or two step deposition processes can be used. In one step deposition the precursors materials are dissolved in a single solution. In the two step deposition, two separate solutions of MAI and PbI_2 are prepared and perovskite formation takes place upon deposition. Film fabrication is achieved by one or more of the following methods: ultrasonic spray coating, spin coating, doctor blading, printing, dipping, and slot die coating [63].

Alternatively, films can be deposited by physical vapor deposition leading to highly uniform films with small grains. Power conversion efficiencies up to 20% have been reached with vapor-deposited perovskite solar cells [65]. Vapor-deposition allows complex layer structures to be created as no solvent-orthogonality is required as is the case in solution processing. This is particularly advantageous for fabricating two-terminal perovskite-perovskite tandems [31, 66].

The precise properties of the perovskite layer depend strongly on how the material crystallizes, a process which, in turn, is determined by the deposition temperature, moisture, the substrate, the timing, and the chosen deposition method [67, 68]. Reproducibility of results between scientific groups is therefore highly variable.

5.2.3 *Perovskite Solar Cell Architectures*

Three of the commonly used structures for perovskite solar cells are shown in Figure 5.2. The meso-structure uses a mesoporous titanium dioxide (TiO_2) layer into which the perovskite is infiltrated. It has been proposed that the porous TiO_2 enhances the interfacial area between perovskite and the TiO_2 electron transporter enabling rapid electron transfer from MAPI to TiO_2 [69]. Both other structures are planar. In *regular* perovskite solar cells electrons are extracted to the front contact and holes to the back contact and vise-versa in *inverted* perovskite solar cells. Please note that this is the opposite of the nomenclature for organic solar cells.

Most perovskite devices are fabricated on top of glass with a transparent conducting oxide (TCO). The low processing temperatures also allow for deposition

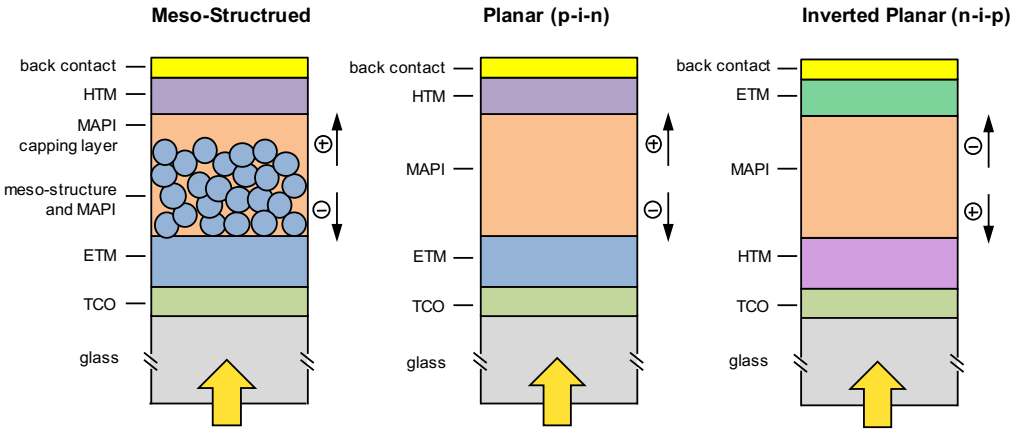

Figure 5.2: Different solar cell architectures employing perovskite.

on plastic foils enabling flexible solar cells [63].
The perovskite absorber is sandwiched between an electron transport material (ETM) and a hole transport material (HTM). Both p-i-n and n-i-p configurations have been fabricated. Gold (Au) or silver (Ag) are commonly employed for the top electrode material.

Contact materials: Charge injection and device performance as well as the character of the frequently-observed IV curve hysteresis are all strongly influenced by the choice and quality of the contact layers [70–72]. The following materials have been used as contact layers [63]:

- Electron transport materials: TiO_2, ZnO, SnO_2, $C60$, $PCBM$, $IDIC$, BCP
- Hole transport materials: *spiro-OMeTAD*, $P3HT$, *PEDOT:PSS*, *PCBTDPP*, *PDCBT*, *PTAA*, *TaTm*, *CuSCN*

Many contact materials employed in perovskite solar cells, such as $PCBM$ or $P3HT$, were originally developed for use in organic solar cells. Ideally the energy levels of the contact material should be well-aligned with the appropriate band energy of the perovskite. Furthermore, the perovskite-contact interfaces must be well-passivated in order to minimise interface recombination. It has been observed by several groups that fullerenes ($PCBM$ or C60) passivate the perovskite leading to increased device efficiencies and a reduction in IV hysteresis [73–76].

5.2.4 *Perovskite Properties*

Perovskites have many properties suitable for producing efficient photovoltaics such as low exciton binding energies, low bulk recombination coefficients and high carrier mobilities relative to organic materials. There are however a number of disadvantageous properties related to the soft nature of the material such as the presence of mobile ions and the tendency toward halide segregation. In this section, the key material properties are reviewed.

High absorption: Most organometallic halide perovskites have a comparatively high absorption coefficient of around $10^5\,cm^{-1}$ with a strong absorption onset [77] enabling maximum absorption to be achieved with thin layers of around $500\,nm$.

Low recombination: Density functional theory (DFT) calculations predict that perovskites are exceptionally defect tolerant. Most defects (such as vacancies) do not create states within the band gap and therefore do not create recombination centres [78]. The point defects that do exist with deep levels within the band gap are those with high formation energies [79]. Experimentally, low recombination rates and a very high photoluminescence (PL) efficiency are observed [80] leading to high open-circuit voltages.

High charge carrier mobilities: In MAPI charge carrier mobilities between $2\,cm^2/Vs$ and $1000\,cm^2/Vs$ have been measured in single crystals [81]. In multicrystalline MAPI perovskites mobilities between $0.1\,cm^2/Vs$ and $20\,cm^2/Vs$ have been reported [81]. The large spread of reported values stems from sample variability in addition to different interpretations of the experimental results.
The estimated mobilities are, however, high enough to facilitate efficient charge transport within a $500\,nm$ thick layer. Furthermore, the electron and hole mobilities appear to be balanced [82]. This is advantageous for avoiding charge accumulation, a process detrimental to efficient extraction.

Low exciton binding energy: Several studies have reported exciton binding energies well below $50\,meV$ [80, 83, 84] suggesting that excitons in perovskites readily dissociate to free charge carriers under thermal excitation at room temperature.

Reversible photo-induced trap formation: In mixed halide perovskites it has been postulated that traps are dynamically created upon light excitation [85].

Ferroelectric domains: Ferroelectric domains have been measured by piezoresponse force microscopy (PFM). The influence on the device performances remains unclear however [86].

IV curve hysteresis: In many perovskite devices a hysteresis is observed between the forward and reverse current-voltage (IV) scans [35, 87]. This IV curve hysteresis can be problematic for the correct determination of the power conversion efficiency. Maximum power point (MPP) tracking over several minutes to obtain a stabilized value therefore represents a better method to obtain an accurate power conversion efficiency [88].
While the exact origin of the IV curve hysteresis has remained a topic of debate, it is now widely accepted that mobile ions are the principle cause [89–94].

Mobile ionic defects: Metal organic halide perovskites are soft ionic materials with a high density of defects [90, 95]. First principle calculations have predicted that iodine vacancies have relatively low activation energies, enabling them to

move inside the crystal [96, 97]. Measurements by glow discharge optical emission spectroscopy (GD-OES) provided direct experimental evidence of mobile iodine [93]. It has been shown that mobile ions can cause an IV curve hysteresis [89, 98–100]. These findings are further confirmed in this thesis.
Various activation energies for ion migration have been published reaching for iodine vacancies from 0.08 eV to 0.58 eV and for MA vacancies from 0.46 eV to 1.12 eV [92].

The migration of extrinsic ions from the contact layers has also been shown [101]. Mobile ions from the perovskite layer may also migrate into the contact layers. Furthermore, ions may migrate preferably along the grain boundaries [102]. The slow transient optoelectronic behaviour of perovskite solar cells is likely to be related to the migration of ionic defects [87, 103–107]. For example it has recently been shown the high capacitance under illumination at low frequency [108] can be explained by ion migration [91, 109].

Part III

METHODS

6 EXPERIMENTAL SETUP

All experiments presented in this thesis were performed with the all-in-one measurement system *Paios 4.1* [110] that was originally developed by the author and further extended within this thesis. An image of the system is shown in Figure 6.1.

Figure 6.1: Paios: platform for all-in-one characterization of solar cells.

Paios is a measurement system that performs steady-state, transient and frequency domain measurements. A predefined measurement protocol is performed sequentially leading to highly systematic measurement results. The following is a list of the principle experimental techniques available with *Paios*:

- Current-voltage scans (see subsection 9.4.1)
- Transient photocurrent (see subsection 9.4.9)
- Transient photovoltage (see subsection 9.4.6)
- Charge extraction with linearly increasing voltage (see subsection 9.4.3)
- Charge extraction (see subsection 9.4.11)
- Deep level transient spectroscopy (see subsection 9.4.8)
- Impedance spectroscopy (see subsection 9.4.12)
- Intensity-modulated photocurrent spectroscopy (see subsection 9.4.15)
- Intensity-modulated photovoltage spectroscopy (see subsection 9.4.16)

Users can define their own measurement protocols to design new experiments based on analytical formulas. For most techniques sophisticated post-processing tools are also available in the software interface of *Paios*, called *Characterization Suite*.

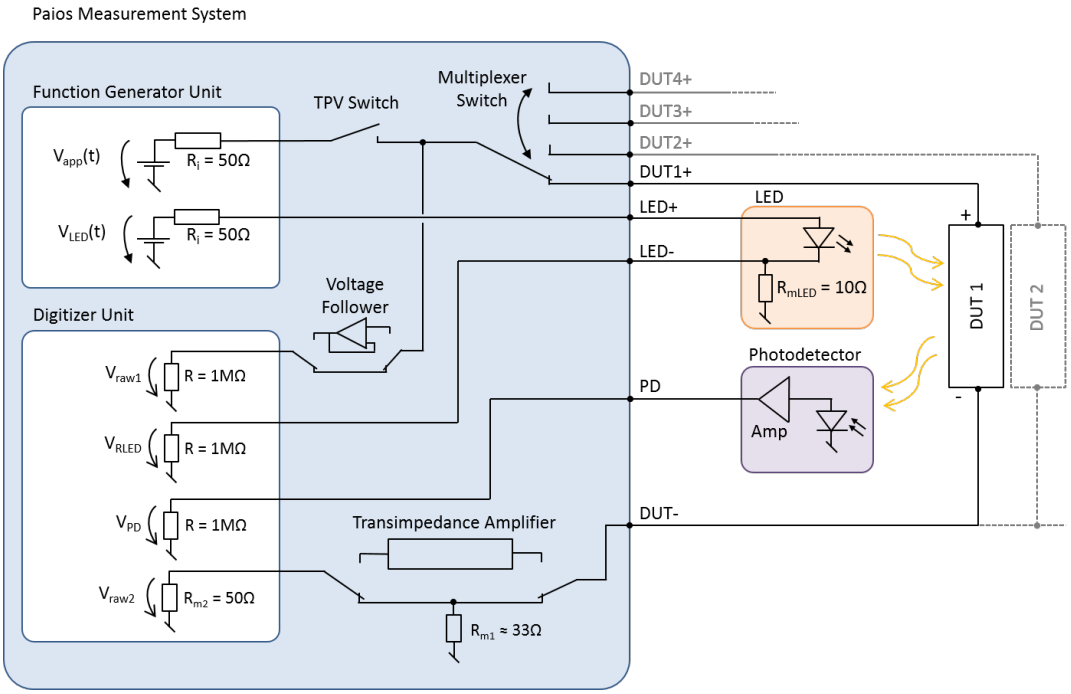

Figure 6.2: Schematic of the measurement setup layout of *Paios*.

Inside *Paios* two function generators control the voltage signal applied to the device and the LED light source as shown in Figure 6.2. A white LED is used with a rise-time of approximately 100 *ns*. The current and voltage of the solar cell device are measured with a digitizer.

Current measurements: The current of the solar cell is measured either by the voltage drop over the resistor or by the transimpedance amplifier. The transimpedance amplifier has different gains and is employed to measure small currents. *Paios* switches automatically between gains of the transimpedance amplifier and the measurement resistor R_{m1}.

Photovoltage measurements: For transient photovoltage (OCVD, TPV) and intensity-modulated photovoltage spectroscopy (IMVS) measurements the open-circuit voltage of a solar cell is measured under illumination. Here, the TPV switch is opened and the voltage is measured over a 1 $M\Omega$ resistor. For all other measurements the TPV switch is closed.

Calibration: In order to ensure high measurement precision *Paios* is calibrated with an automatic algorithm measuring different high precision resistors. For each measurement gain two resistors are measured over a frequency range of 10 MHz to 1 Hz. From this data a frequency-dependent correction function is calculated

for each measurement gain.

Flex-Res: Transient signals can be measured with a very high time resolution – a feature named *flex res*. In Figure 6.3 the current response to a voltage pulse applied to a perovskite solar cell is shown with and without *Flex-Res*. The left graph shows the entire current response to the 1 second voltage pulse. The Flex-Res data (red line) has lower noise because many points are averaged. Due to the long signal length the sampling rate is very low without Flex-Res (black curve, $\Delta t \approx 12\,ms$). With Flex-Res the fast RC-peak at the beginning can still be resolved nicely. *Paios* can resolve 8 orders of magnitude in time in a single measurement. This feature is well illustrated in Figure 6.3b where the current data has been plotted on a logarithmic time axis. Without Flex-Res only three orders of magnitude can be resolved.

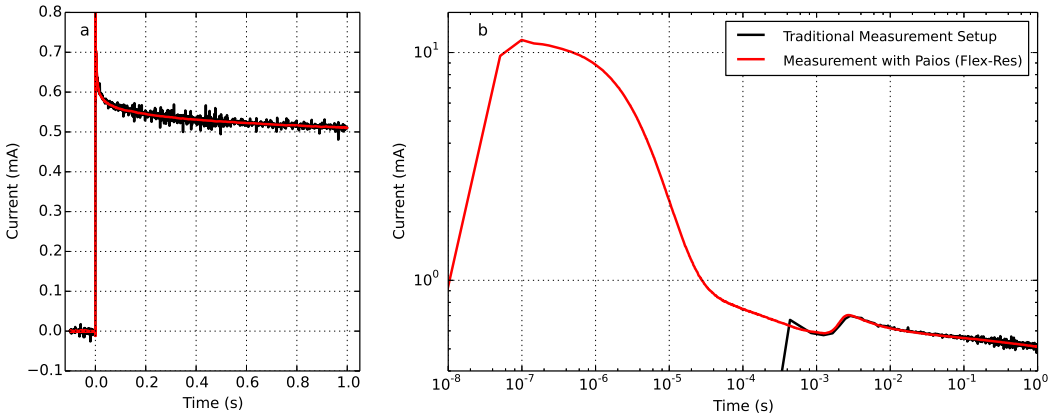

Figure 6.3: Voltage step response of a perovskite solar cell measured with Flex-Res and compared with a traditional measurement setup. The same data-set is shown in linear time-scale (a) and logarithmic time-scale (b).

Simulation: A numerical drift-diffusion simulation is seamlessly integrated in the *Paios* software. Simulations can be defined and started directly in the software interface of *Paios* and the simulation results can be directly compared with the measurement results. Optimization of the simulation parameters to match simulation with measurement results can also be directly performed in the *Paios* software. Fitting algorithms, the details of which are explained in section 8.2 Fitting procedure and parameter correlation, have been extensively used in this thesis. The details of the simulation model are explained in the chapter 7 PHYSICAL MODEL.

7 PHYSICAL MODEL

The physical model used in this thesis is implemented in the numerical simulation software *Setfos 4.6* [111]. The model solves the charge carrier drift-diffusion equations on a one-dimensional grid. It incorporates Langevin recombination, trapping and de-trapping, Shockley-Read-Hall (SRH) recombination, mobile ions and doping. Transport levels for electrons and holes as well as trap levels were chosen discrete in this thesis. Charge carrier densities are fixed at the contacts and calculated according to Boltzmann statistics using the energetic offset between HOMO or LUMO level and the metal workfunction. Both series and parallel resistances are also included in the simulation. Light absorption is calculated by a transfer matrix method [112, 113].
This 1D-model can only describe devices that are spatially homogeneous in the second and third dimensions, which is a reasonable assumption for thinfilm devices with a high width-to-thickness aspect ratio.

This device model has been validated with both organic solar cells [114, 115, 34, 116, 113] and perovskite solar cells [36].

This section introduces the equations of the drift-diffusion model, while the parameters and variables are described in the next section (7.2 Physical Quantities).

7.1 THE CHARGE CARRIER DRIFT-DIFFUSION EQUATIONS

7.1.1 *Electronic Drift-Diffusion*

The continuity equations for electrons and holes govern the change in charge carrier density due to current flow, electron or hole exchange with traps, recombination and generation.

$$\frac{\partial n_e}{\partial t}(x,t) = \frac{1}{q} \cdot \frac{\partial j_e}{\partial x}(x,t) - R_{te}(x,t) - R(x,t) + G_{opt} \cdot g(x) \tag{7.1}$$

$$\frac{\partial n_h}{\partial t}(x,t) = -\frac{1}{q} \cdot \frac{\partial j_h}{\partial x}(x,t) - R_{th}(x,t) - R(x,t) + G_{opt} \cdot g(x) \tag{7.2}$$

For the calculation of the charge generation profile $g(x)$ *Setfos* uses the measured illumination spectrum, the complex refractive indices of the materials and the thickness of each layer in the cell stack.

Radiative recombination is described by

$$R(x,t) = \beta \cdot n_e(x,t) \cdot n_h(x,t) \tag{7.3}$$

In case of Langevin recombination β is defined as

$$\beta = \eta \cdot (\mu_e + \mu_h) \cdot \frac{q}{\epsilon} \tag{7.4}$$

The currents of electrons and holes consist of drift in the electric field and diffusion due to the charge carrier density gradients.

$$j_e(x,t) = n_e(x,t) \cdot q \cdot \mu_e \cdot E(x,t) + \mu_e \cdot k_B \cdot T \cdot \frac{\partial n_e}{\partial x}(x,t) \tag{7.5}$$

$$j_h(x,t) = n_h(x,t) \cdot q \cdot \mu_h \cdot E(x,t) - \mu_h \cdot k_B \cdot T \cdot \frac{\partial n_h}{\partial x}(x,t) \tag{7.6}$$

7.1.2 *Ionic Drift-Diffusion*

The continuity equations for anions and cations govern the change in ion density due to ionic current flow. In the model ions don't interact with eachother and cannot be created or annihilated. Ions are present with a defined density and arrange within the layer.

$$\frac{\partial n_a}{\partial t}(x,t) = \frac{1}{q} \cdot \frac{\partial j_a}{\partial x}(x,t) \tag{7.7}$$

$$\frac{\partial n_c}{\partial t}(x,t) = -\frac{1}{q} \cdot \frac{\partial j_c}{\partial x}(x,t) \tag{7.8}$$

Ionic charge transport is described by drift-diffusion.

$$j_a(x,t) = n_a(x,t) \cdot q \cdot \mu_a \cdot E(x,t) + \mu_a \cdot k_B \cdot T \cdot \frac{\partial n_a}{\partial x}(x,t) \tag{7.9}$$

$$j_c(x,t) = n_c(x,t) \cdot q \cdot \mu_c \cdot E(x,t) - \mu_c \cdot k_B \cdot T \cdot \frac{\partial n_c}{\partial x}(x,t) \tag{7.10}$$

7.1.3 *Total Current, Poisson and Device Voltage*

The total current is the sum of electron current j_e, hole current j_h, anion current j_a, cation current j_c, displacement current and the current through the parallel resistance. This total current j is constant in x at any time.

$$\begin{aligned} j(x,t) =& j_e(x,t) + j_h(x,t) + j_a(x,t) + j_c(x,t) + \\ & \frac{\partial E}{\partial t}(x,t) \cdot \epsilon + \frac{V_{dev}(t)}{R_p} \end{aligned} \tag{7.11}$$

Poisson's equation relates the electric field with the charges inside the layer.

$$\begin{aligned} \frac{\partial E}{\partial x}(x,t) = -\frac{q}{\epsilon} \cdot [& n_h(x,t) - n_e(x,t) + n_c(x,t) - \\ & n_a(x,t) - n_t(x,t) - n_{n-doping} + n_{p-doping}] \end{aligned} \tag{7.12}$$

The voltage at the device without the series resistance is named device voltage V_{dev} in our model. It is defined by the integral of the electric field E over position x plus the built-in voltage V_{bi}. It is the applied voltage $V_{applied}$ minus the voltage drop over the series resistance.

$$V_{dev}(t) = \int_0^d E(x,t) \cdot dx + V_{bi} = V_{applied}(t) - R_S \cdot j(t) \cdot S \tag{7.13}$$

The electric potential ϕ is evaluated according to

$$\phi(x_1,\ t) = \int_0^{x_1} E\,(x,t) \cdot dx \tag{7.14}$$

7.1.4 *The Built-In Voltage*

The built-in voltage is defined as the difference in workfunctions of the electrodes. The workfunctions are calculated using the boundary charge carrier densities n_{h0} and n_{e0}.

$$V_{bi} = \frac{\Phi_A - \Phi_C}{q} \tag{7.15}$$

$$\Phi_C = E_{LUMO} - ln\left(\frac{n_{e0}}{N_0}\right) \cdot k_B \cdot T \tag{7.16}$$

$$\Phi_A = E_{HOMO} + ln\left(\frac{n_{h0}}{N_0}\right) \cdot k_B \cdot T \tag{7.17}$$

7.1.5 *Boundary Conditions*

The electron density at the anode and the hole density at the cathode are set to fixed values n_{e0} and n_{h0} to form the charge carrier boundary conditions

$$n_h\,(0,t) = n_{h0} \tag{7.18}$$

$$n_e\,(0,t) = N_0^2 \cdot \exp\left(-\frac{E_g}{k_B \cdot T}\right) \cdot \frac{1}{n_{h0}} \tag{7.19}$$

$$n_e\,(d,t) = n_{e0} \tag{7.20}$$

$$n_h\,(d,t) = N_0^2 \cdot \exp\left(-\frac{E_g}{k_B \cdot T}\right) \cdot \frac{1}{n_{e0}} \tag{7.21}$$

As ions shall not leave the perovskite layer the ionic current is set to zero at the HTM-MAPI interface (position d_1) and at the MAPI-ETM interface (position d_2).

$$j_a\,(d_1,t) = 0 \qquad j_c\,(d_1,t) = 0 \tag{7.22}$$

$$j_a\,(d_2,t) = 0 \qquad j_c\,(d_2,t) = 0 \tag{7.23}$$

The total ion density is the integral over the perovskite layer. The total ion density is conserved over time.

$$N_a = \frac{1}{d} \cdot \int_0^d n_a(x,t) \cdot dx \tag{7.24}$$

$$N_c = \frac{1}{d} \cdot \int_0^d n_c(x,t) \cdot dx \tag{7.25}$$

7.1.6 *Trapping*

Trapping and de-trapping of electron traps is described by the electron trap rate equation. The electron trap can either exchange electrons with the LUMO level at the rate R_{te} or exchange holes with the HOMO level at the rate R_{th}.

$$\frac{\partial n_t}{\partial t} = R_{te} - R_{th} \tag{7.26}$$

Free electrons in the LUMO can be captured by traps. Trapped electrons can be thermally activated into the LUMO.

$$R_{te} = c_e \cdot n_e \cdot (N_t - n_t) - c_e \cdot N_0 \cdot \exp\left(\frac{E_t - E_{LUMO}}{k_B \cdot T}\right) \cdot n_t \tag{7.27}$$

Trapped electrons can recombine with free holes. An empty trap can capture an electron from the HOMO level by thermal activation (leaving behind a hole).

$$R_{th} = c_h \cdot n_h \cdot n_t - c_h \cdot N_0 \cdot \exp\left(-\frac{E_t - E_{HOMO}}{k_B \cdot T}\right) \cdot (N_t - n_t) \tag{7.28}$$

The three equations above describe SRH-recombination in a two-step process. Free electrons are captured in the trap and subsequently recombine with a free hole. Alternatively, an electron can be thermally activated from the HOMO to the trap level and from the trap level to the LUMO. The latter two routes occur with lower probability.

7.2 PHYSICAL QUANTITIES

Table 7.1 lists all parameters and all other quantities occurring in the equations of the previous section.

Symbol	Parameter	Unit
n_e	Electron density	cm^{-3}
n_h	Hole density	cm^{-3}
n_c	Cation density	cm^{-3}
n_a	Anion density	cm^{-3}
n_t	Density of trapped electrons	cm^{-3}
j_e	Electron current	mA/cm^2
j_h	Hole current	mA/cm^2
j_c	Cation current	mA/cm^2
j_a	Anion current	mA/cm^2
j	Total current	mA/cm^2
E	Electric field	V/m
φ	Electric potential	V
R	Recombination rate	$s^{-1}cm^{-3}$
R_{te}	Electron trap – electron exchange rate	$s^{-1}cm^{-3}$
R_{th}	Electron trap – hole exchange rate	$s^{-1}cm^{-3}$
$g(x)$	Charge generation profile	$s^{-1}cm^{-3}$
x	Dimension in layer direction	nm
t	Time	s
d	Full simulation domain width	nm
d_1	Position of the interface HTM-MAPI	nm
d_2	Position of the interface MAPI-ETM	nm
S	Device area	cm^2
μ_e	Electron mobility	cm^2/Vs
μ_h	Hole mobility	cm^2/Vs
μ_c	Cation mobility	cm^2/Vs
μ_a	Anion mobility	cm^2/Vs
β	Recombination coefficient	cm^3/s
η	Langevin recombination efficiency	1
V_{dev}	Voltage at the device without series resistance.	V
$V_{applied}$	Voltage at the device with series resistance	V
V_{bi}	Built-in voltage	V

table continues on the next page

Symbol	Parameter	Unit
R_S	Series resistance	Ω
R_P	Parallel resistance	Ω
Φ_A	Workfunction of the anode	eV
Φ_C	Workfunction of the cathode	eV
E_{HOMO}	Energy of highest occupied molecular orbital	eV
E_{LUMO}	Energy of lowest unoccupied molecular orbital	eV
E_t	Trap energy	eV
n_{e0}	Electron density at the right electrode (x=d) as boundary condition of the simulation.	cm^{-3}
n_{h0}	Hole density at the left electrode (x=0) as boundary condition of the simulation.	cm^{-3}
N_0	Effective density of states	cm^{-3}
N_t	Trap density	cm^{-3}
N_c	Total cation density	cm^{-3}
N_a	Total anion density	cm^{-3}
c_e	Capture rate for electrons	cm^3/s
c_h	Capture rate for holes	cm^3/s
G_{opt}	Photon-to-charge conversion efficiency This factor accounts for non-dissociated excitons.	1
ε	Electrical permittivity ($\varepsilon = \varepsilon_0 \cdot \varepsilon_r$)	F/m
q	Unit charge	C
k_B	Boltzmann constant	J/K
T	Temperature	K

Table 7.1: Parameters and quantities used in equations in section 7.1 The Charge Carrier Drift-Diffusion Equations.

7.3 RC-EFFECTS

In this section the effects of the series resistance, parallel resistance and the geometric capacitance are explained.

Solar cells for the purposes of research typically have an active area of less than $0.1\,cm^2$. The transparent conducting oxide (TCO) is coated on the glass sample such that it can be contacted with a probe. Since the TCO is usually thin ($\sim 100\,nm$) it has a significant series resistance R_S. Together with the geometric capacitance C_{geom} an RC-circuit is formed with a time constant $\tau = R_S \cdot C_{geom}$.

While using small-area solar cells helps to minimise the RC time constant, capacitive currents can not be completely avoided. In transient and frequency domain measurements the RC-effects are included within the measurement. Features in the current caused by semiconductor device physics cannot be resolved if they are faster than the RC-effects. It is therefore important to quantify RC-effects in these measurements.

A shunt in the solar cell leads to an additional current that flows in parallel to the regular device current. It can be modeled adding a parallel resistance R_P. This is a simplification as shunts are often non-Ohmic in reality [117].

Figure 7.1 is a schematic showing the series resistance R_S, parallel resistance R_P, and device under test (DUT). The DUT contains the geometric capacitance C_{geom}.

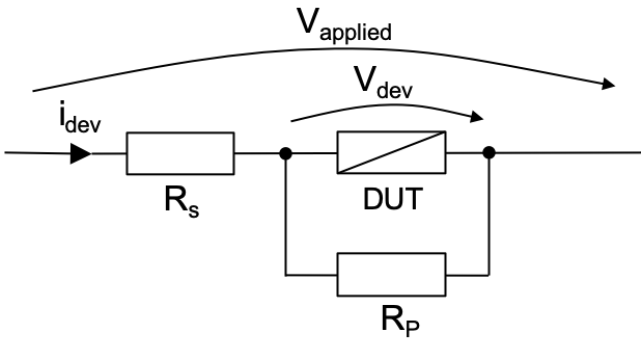

Figure 7.1: Equivalent circuit model for a device with series resistance R_S and parallel resistance R_P.

7.3.1 *RC Effects in Steady-State Measurements*

RC-effects do not play a role in steady-state measurements. The series resistance R_S does however lead to an additional voltage drop and the parallel resistance R_P leads to an additional current. If both resistances are known, the current-voltage characteristics can be corrected according to Equation 7.29 and Equation 7.30.

$$V_{corr} = V_{dev} = V_{applied} - R_S \cdot I_{dev} \tag{7.29}$$

$$I_{corr} = I_{dev} - \frac{V_{corr}}{R_P} \tag{7.30}$$

Figure 7.2 shows an example IV-curve that has been corrected for the series resistance. The effective voltage at the device terminals is smaller due to the voltage drop over R_S. In this example R_p is 1 $G\Omega$ and has no effect.

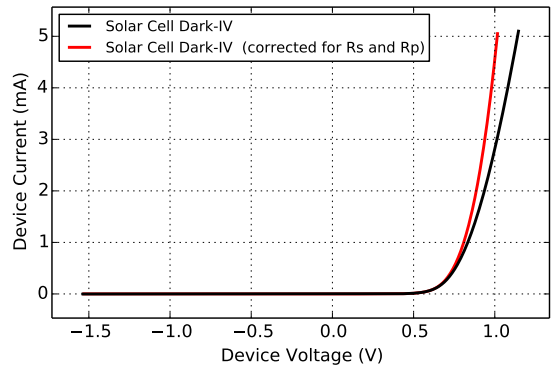

Figure 7.2: Example of an organic solar cell with and without voltage curretion with R_S.

7.3.2 *RC Effects in Transient Measurements*

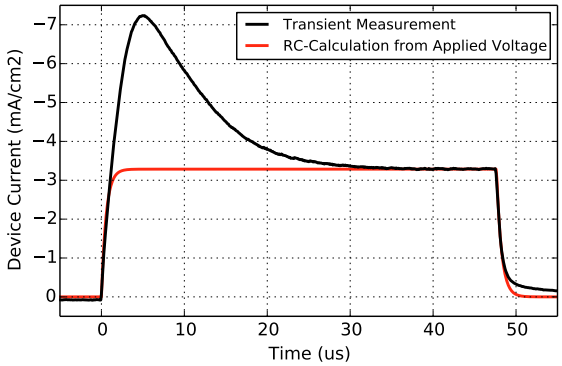

Figure 7.3: CELIV measurement with corresponding RC-current calculated from the applied voltage, the geometric capacitance and the series resistance.

To estimate the RC-effects in a particular transient measurement the pure RC-current can be calculated assuming the device is a parallel plate capacitor C_{geom}.

The RC-current I_{RC} is calculated using the applied voltage $V_{applied}$. Here the total series resistance of the full electric circuit needs to be used for the calculation. The total series resistance R_{tot} is calculated according to Equation 7.31 and consists

of the series resistance of the device R_S, the internal resistance of the function generator R_i and the measurement resistor R_m.

$$R_{tot} = R_S + R_i + R_m \approx R_S + 70\ \Omega \tag{7.31}$$

The RC-current is calculated using R_{tot} by solving Equation 7.32

$$I_{RC} = C_{geom} \cdot \frac{d}{dt}(V_{applied} - R_{tot} \cdot I_{dev}) + \frac{1}{R_p} \cdot (V_{app} - R_{tot} \cdot I_{dev}) \tag{7.32}$$

An example RC-current calculated with this formula is shown in Figure 7.3. It shows the current of a CELIV experiment in which the voltage is linearly changing (see subsection 9.4.3 for more information on CELIV). Between 0 and 20 μs charge carriers are extracted from the solar cell. After 25 μs only the displacement current due to the geometric capacitance is observed. The device current reaches the level of the calculated RC-current. This RC-calculation helps with the interpretation of experimental results.

7.3.3 *RC Effects in Impedance Measurements*

For the interpretation of impedance measurements it is advantegeous to plot the impedance of the pure RC-elements together with the measurement data. The impedance of the RC-element $Z_{RC} = R_S + (C_{geom}||R_P)$ is calculated by evaluating Equation 7.33.

$$\overline{Z_{RC}(f)} = R_S + \frac{R_p}{1 + j \cdot 2\pi f \cdot C_{geom} \cdot R_p} \tag{7.33}$$

Please note that $\overline{Z_{RC}}$ is complex and frequency-dependent. An example is shown in Figure 7.4. The capacitance C is calculated from the impedance $\overline{Z}$ by $C = 1/\omega \cdot Imag(1/\overline{Z})$. Here it is evident that the impedance above 200 kHz is dominated by RC-effects. Showing impedance measurement data together with the RC impedance helps with their interpretation.

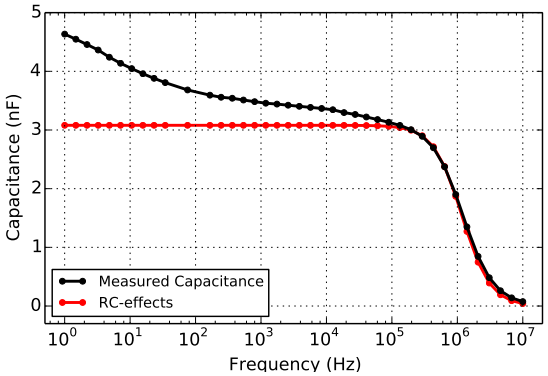

Figure 7.4: Capacitance measurement with corresponding RC-effects.

8 NUMERICAL METHODS

8.1 CALCULATION METHODS

The equations described in chapter 7 PHYSICAL MODEL are solved on a one-dimensional grid either in steady-state, in the transient or frequency domain. The charge carrier densities are discretized with logarithmic elements (Scharfetter–Gummel distretization [118]). Dirichlet boundary conditions are used to fix the charge carrier densities at the spatial domain boundaries. The equations are solved either with a Gummel [119] approach or using a Newton solver. For transient simulation implicit time steps are implemented. Further details can be found in references [120, 121, 113].

8.1.1 *Calculating frequency domain data from step-response*

In linear systems there is a fundamental relation between the step-response in the time-domain and the transfer function in the frequency-domain: The Fourier transform of the time-derivative of the step-response signal is equal to the system response in the frequency domain. This relation can be exploited to calculate impedance spectroscopy data from the results of a transient numerical solver [122].

This approach is applied in this thesis to calculate the impedance spectroscopy results presented in chapter 11. The simulation software *Setfos 4.6* [111] can perform small signal analysis to simulate impedance spectroscopy. In contrast to the transient solver, at the time of writing, the solver for small signal analysis cannot yet handle mobile ions. The calculation of impedance spectroscopy data from the results of the transient solver therefore presents a viable and robust alternative.

First, the step response of the system is calculated. At $t = 0$ the applied voltage jumps from V_{offset} to $V_{offset} + \Delta V$. The chosen voltage step ΔV needs to be small enough such that the system behaves linearly. If the voltage step is too small, however, numerical problems arise. For the calculations presented in this thesis a value of between $1\,mV$ and $10\,mV$ was chosen for ΔV. The current $j_{SR}(t)$ is calculated by the transient solver using logarithmic, implicit time-steps.

The admittance Y is calculated according to Equation 8.1 and 8.2.

$$Y_{real}(\omega) = \frac{\Delta j}{\Delta V} + \frac{\omega}{\Delta V} \cdot \int_0^{N/f} j_{SR}(t) \cdot sin(\omega \cdot t) \cdot dt \tag{8.1}$$

$$Y_{imag}(\omega) = \frac{\omega}{\Delta V} \cdot \int_0^{N/f} j_{SR}(t) \cdot cos(\omega \cdot t) \cdot dt \tag{8.2}$$

where ω is the angular frequency ($2 \cdot \pi \cdot f$), N is the number of periods (this must be a natural number) and Δj is the current step ($\Delta j = j_{SR}(\infty) - j_{SR}(t < 0)$).

For each time step of the numerical solution of the transient current $j_{SR}[k]$ the integrals of Equation 8.1 and 8.2 are solved analytically assuming a constant current during the time step. The admittance Y is calculated from the current $j_{SR}[k]$ according to Equation 8.3 and 8.4

$$Y_{real}(\omega) = \frac{\Delta j}{\Delta V} + \frac{1}{\Delta V} \cdot \sum_{k=0}^{n-2} j_{SR}[k] \cdot (cos(t[k] \cdot \omega) - cos(t[k+1] \cdot \omega)) \tag{8.3}$$

$$Y_{imag}(\omega) = \frac{1}{\Delta V} \cdot \sum_{k=0}^{n-2} j_{SR}[k] \cdot (sin(t[k+1] \cdot \omega) - sin(t[k] \cdot \omega)) \tag{8.4}$$

where $j_{SR}[k]$ is the current array and $t[k]$ is the time array.

To increase numerical precision the step-response without series resistance can first be calculated and series resistance is then added in postprocessing. In this case the geometric capacitance C_0 needs to be added to the impedance after the calculation [122]. The capacitance C_0 can be calculated using the current spike after the first time step according to Equation 8.5.

$$C_0 = \frac{(j_{SR}[1] - j_{SR}[0]) \cdot (t[1] - t[0])}{\Delta V} \tag{8.5}$$

To validate the step-response method the impedance spectrum of an organic solar cell was simulated using the small signal analysis and compared to the calculation with the step response. The result is shown in Figure 8.1. The example solar cell has trapping activated resulting in two distinct features in the step response as shown in Figure 8.1a. Initially RC charging is observed, after which traps are filled. Figure 8.1b and c show the capacitance and the conductance calculated from the step response and compared with the solution from the small signal analysis. Both simulations are congruent, validating the presented approach. The trapping feature in the step response current ($t \sim 10^{-3}\,s$) translates into features in the capacitance and conductance at $f \sim 10^3\,Hz$.

Both intensity-modulated photocurrent and photovoltage spectroscopy (IMPS and IMVS) can also be calculated using a similar step-response approach. Instead of a voltage step a step in light intensity is applied.

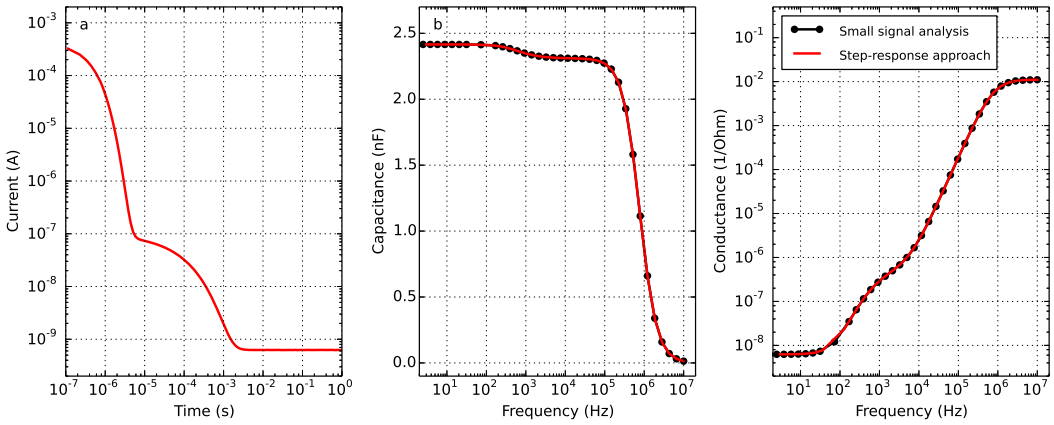

Figure 8.1: Example of an impedance calculation with the step-response approach for an organic solar cell. a) Transient current in response to a voltage step. b) Capacitance-frequency plot from small signal analysis and calculated by the step-response approach. c) Conductance-frequency plot.

8.2 FITTING PROCEDURE AND PARAMETER CORRELATION

The parameter extraction presented in this thesis is performed by fitting simulation results to experimental data. Two different fitting algorithms were implemented: a gradient-based approach (Levenberg-Marquardt) and a stochastic method (simulated annealing).

In both cases a minimization function f_i is defined as the difference between the simulated values s_i and the measured values m_i as

$$f_i = w_i \cdot (s_i - m_i) \tag{8.6}$$

where w_i are the weights for each point. The convergence of the fitting algorithm depends critically on the choice of measurement values m_i. These measurement values are the targets for the simulation. We define several current-targets for different voltages on the JV-curve, current-targets at different times in transient experiments, and amplitude and phase targets for each frequency point in impedance spectroscopy. Furthermore, we add additional targets such as the open-circuit voltage in the JV-curve and the current-peak time in photo-CELIV. The weights w_i are chosen to set priorities for the fitting algorithm.

8.2.1 *Simulated Annealing*

In simulated annealing parameters are varied randomly. Starting with an initial set of parameters the algorithm jumps to a new set of parameters. The jump direction is random and the step-size is reduced during the optimization process. If the sum of f_i is reduced with the new parameter set then the new parameter set becomes the new base set.

Simulated Annealing is advantageous for global parameter optimization. It is less prone to convergence to local minima compared to gradient methods and the method is robust: even if a given simulation fails to converge, the optimization can continue.

8.2.2 *Levenberg-Marquardt*

Levenberg-Marquardt is a nonlinear least square algorithm [123, 124]. The full derivative of the target function f_i over each fit-parameter is calculated in each optimization step. The algorithm moves in the descending direction and evaluates the function with its derivative again.

The advantage of this method is good convergence provided that the initial set of parameters is not far from the final solution. The disadvantage is that it can converge to local minima rather than the global minimum.

To calculate a step in the optimization, the Jacobian matrix J of the function f_i is calculated according to

$$J_{ik} = \frac{\partial f_i}{\partial p_k} \tag{8.7}$$

where p are the simulation parameters to be optimized. The calculation of the Jacobian matrix is the computationally expensive step during the optimization.

The parameter set h for the next step in the optimization is calculated by solving

$$\left(J^T \cdot J + \mu \cdot I\right) \cdot h = -J^T \cdot f \tag{8.8}$$

where μ is a damping parameter and I is the identity matrix [123, 124]. This procedure is repeated until the system has converged.

8.2.3 *Parameter correlation*

A correlation matrix can be used to judge the quality of a fit. The correlation matrix shows the linear correlation for all parameter combinations. It is normalized such that 1.0 means full positive correlation and -1.0 means full negative correlation. In case of full positive correlation increasing parameter 1 has the exact same influence as increasing parameter 2. The closer the value is to zero, the more independent are the parameters and the more unique the solution. A example correlation matrix is shown in section 9.6.4 Parameter correlation.

The correlation matrix M is calculated using the Jacobian matrix J from the previous section according to

$$C = J^T \cdot J \qquad\qquad M_{ik} = \frac{C_{ik}}{\sqrt{C_{ii} \cdot C_{kk}}} \tag{8.9}$$

where C is the covariance matrix. A more detailed explanation about the calculation of the correlation matrix can be found in the author's previous publication [34].

The correlation matrix is calculated by linearizing a system at a particular working point (a set of simulation parameters). It is therefore only a local property of the system somewhere in the N-dimensional parameter space. At a different working point, the matrix might be different.

If there is strong correlation, as is the case in Figure 9.26, the extracted parameters are most probably inaccurate. The opposite is however not true; a low parameter correlation, as shown in Figure 9.25, is an indication for a good quality fit, but not a proof. While this indicates that a stable local minimum has been found, no conclusions about a global minimum can be made.

Part IV

RESULTS

9

OPTO-ELECTRONIC CHARACTERIZATION OF THIRD-GENERATION SOLAR CELLS

This chapter is based on the author's publication *Opto-electronic characterization of third-generation solar cells* [125].

9.1 ABSTRACT

We present an overview of opto-electronic characterization techniques for solar cells including light-induced charge extraction by linearly increasing voltage, impedance spectroscopy, transient photovoltage, charge extraction and more. Guidelines for the interpretation of experimental results are derived based on charge drift-diffusion simulations of solar cells with common performance limitations. It is investigated how nonidealities like charge injection barriers, traps and low mobilities among others manifest themselves in each of the studied cell characterization techniques. Moreover, comprehensive parameter extraction for an organic bulk-heterojunction solar cell comprising PCDTBT:$PC_{70}BM$ is demonstrated. The simulations reproduce measured results of 9 different experimental techniques. Parameter correlation is minimized due to the combination of various techniques. Thereby a route to comprehensive and accurate parameter extraction is identified.

9.2 INTRODUCTION

The past decade witnessed an impressive development in power conversion efficiencies of novel thin film solar cells based on organic materials, quantum dots, hybrid and perovskite materials. All these new concepts are denoted by the term *third generation photovoltaics* and have in common that the variety of possible materials and device structures is very large. Accurate characterization is therefore crucial for material screening and device optimization.

Developing a physical understanding of mechanisms governing the operation of third generation solar cells is much more demanding than for silicon solar cells. Crystalline silicon solar cells are doped and thicker than 100 μm. Both factors combined lead to the screening of the electric field such that the largest part of the device is field-free. Therefore, charge transport is governed by diffusion of minority carriers within the doped region. Consequently, the minority carrier lifetime and diffusion length characterize the quality of crystalline silicon [126–128, 25].

In contrast to crystalline silicon, photogeneration and transport of charges in third generation solar cells are more difficult to understand and requires more complex characterization techniques. Organic solar cells, for example, are between

50 and 300 *nm* thick and comprise of p-i-n structure (A bulk-heterojunction solar cell can be considered as p-i-n type as the bulk is usually undoped). Electrodes with different workfunctions and doped injection layers create a built-in potential that drops inside the intrinsic region. Charge transport is facilitated by drift in this built-in electric field. Inside the intrinsic region the electron and hole densities vary spatially – there are no clear *minority carriers* like in the bulk of crystalline silicon. Quantifying a diffusion length in a p-i-n structured solar cell is therefore not meaningful. Characterizing and quantifying charge transport in p-i-n structures requires measuring the electron and hole mobilities, the recombination coefficient, the built-in potential, charge injection barriers and further parameters associated with charge trapping. It is, however, very difficult to assess these parameters individually, as they are highly entangled in a solar cell device.

Furthermore, material parameters often depend on the processing, the solvents, thermal treatment and the substrate [52]. Material parameters can even depend on the batch [129, 130]. Metal workfunctions measured by photoelectron spectroscopy might be subject to change when an organic material is deposited on top, due to chemical reactions at the interface [131]. Individual characterization of the "ingredients" of a solar cell is therefore not feasible and comprehensive device characterization is mandatory. There are numerous experimental techniques available to study electrical material and device parameters of solar cells. In this review we aim to give an overview of some of the most prominent experimental techniques. We use numerical simulation to explain and quantify the effects that are observed in each of these measurements.

To obtain quantitative solar cell and material parameters the combination of several experimental techniques with numerical simulation is required [34]. The numerical simulation is fitted to the experimental results. In the last section of this review we present measurement and simulation data for an organic solar cell comprising PCDTBT:$PC_{70}BM$ as the active layer (see section 9.6 Comprehensive parameter extraction with numerical simulation). We reproduce 9 experimental techniques with one set of parameters.

We aim to provide a guide for the interpretation of experimental results. These experiments help to gain qualitative understanding of the underlying physical processes. While in the following we focus on organic solar cells, the characterization techniques discussed here are not restricted to them but can also be applied to other devices as quantum dots or perovskite solar cells.

9.3 CASE STUDY

In order to explain the various effects to be observed in the different experimental techniques we first define 11 cases of solar cells each corresponding to a specific loss mechanism. We first define a *base* case from which all other cases are derived. The *base* case is an organic bulk-heterojunction solar cell as depicted in Figure 9.1 with a realistic set of parameters similar to the PCDTBT:$PC_{70}BM$ device investigated in the last section. All the cases are defined and described in Table 9.1.

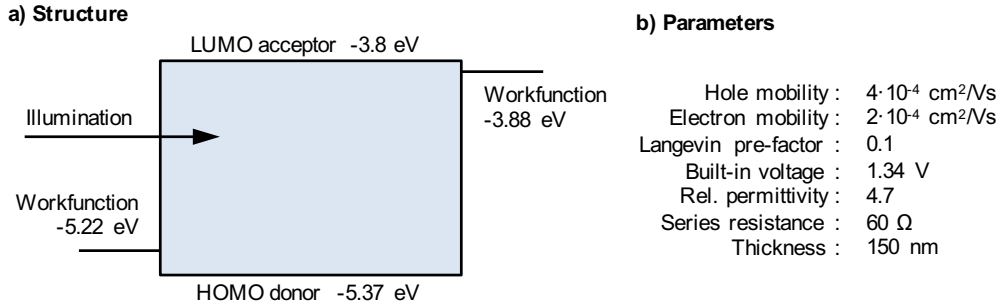

Figure 9.1: a) Device structure of the *base* case used in this study. LUMO and HOMO stand for lowest unoccupied and highest occupied molecular orbitals, respectively. b) Simulation parameters of the *base* case. Full simulation parameters of all cases are listed in the supplemental information of reference [125].

Case	Description
Base	This is the standard single-layer device without charge traps or doping. It is 150 nm thick and has Ohmic contacts with low barriers on both sides. All other devices are derived from this base device.
Extraction barrier	This device features an extraction barrier for electrons. Such a barrier can occur if an oxide layer forms at the electrode. It is modelled by an additional 3 nm thin layer between active material and electron contact with 0.35 eV energy offset. Such oxide formation has for example been shown in P3HT:PCBM solar cells comprising an aluminium electrode [130, 116, 132].

Case	Description
Non-aligned contact	This device has an injection barrier for electrons of $0.45\,eV$. This is the case if the workfunction of the metal is too high to match the LUMO level of the active material [133].
Low mobility	The active material has a mobility that is only 10% of the mobility of the base device. Both electron and hole mobilities are reduced, such that the ratio μ_e/μ_h remains as in the base device. Low mobilities can for example occur due to a unfavourable donor/acceptor morphology in organic solar cells [52].
High Langevin recombination	The active material has a Langevin recombination efficiency that is 10 times larger than for the base device. The Langevin recombination efficiency depends on the material and on the morphology of bulk-heterojunction solar cells [52]. Phase segregation for example can lead to a lower recombination pre-factor [39]. Langevin recombination is described in section 4.5 Recombination and Open-Circuit Voltage.
Shallow traps	The active material has an electron trap density of $3 \cdot 10^{17}\,cm^{-3}$ with a trap-depth of $0.3\,eV$. In organic solar cells the trap density can depend on material purity [134].
Deep traps	The active material has the same trap density of $3 \cdot 10^{17}\,cm^{-3}$ like *shallow traps* but with a depth of 0.8 eV. This trap is located in the middle of the band-gap and leads to enhanced Shockley-Read-Hall (SRH) recombination [135].
Low shunt resistance	This device has an Ohmic shunt resistance of $50\,k\Omega$ ($2.25\,k\Omega cm^2$). Shunt resistances can occur due to non-uniformity of the film, particle contaminations, spikes of the ITO leading to short-circuits, pinholes or others [136]. Shunt resistances can also be non-Ohmic and show SCLC behaviour [117]. For simplicity Ohmic shunting is used here.

Case	Description
High series resistance	The device has an ohmic series resistance of $350\,\Omega$ ($15.7\,\Omega cm^2$). A high series resistance can be caused by the low lateral conductivity of the transparent electrode [137].
High bulk doping density	The bulk of the device is n-doped with $1 \cdot 10^{17}\,cm^{-3}$. Unintentional doping can occur due to impurities that ionize. Very deep traps can have the same effect. Photo-oxidation of single molecules during degradation can also lead to doping [138].
Low charge generation	In this device the photon-to-charge conversion efficiency is reduced to 1/3. The physical origin can be reduced light absorption or hindered exciton dissociation. The latter can be the case if the phase-mixing is too coarse in an organic bulk-heterojunction solar cell [52, 53].

Table 9.1: Definition of 11 cases of solar cells. Each case is a set of parameters describing a solar cell with a particular loss mechanism like charge trapping, doping or a shunt resistance. These cases are later used in the simulation of the various experimental techniques.

Each case describes a solar cell with a particular performance reduction. The cases are then compared with the *base* case. These cases correspond to sets of parameters of the drift-diffusion model that are used for the simulation of the various experimental techniques. Another common performance limitation is an imbalance in electron and hole mobilities. The slower charge carrier type accumulates leading to space-charge and screens the electric field. We show simulations of this additional case in Figure 9.23 in the section 9.5 Imbalanced electron/hole mobilities.

9.3.1 *Simulation model*

The simulation model used for this study is explained in detail in chapter 7 PHYSICAL MODEL. In this study mobile ions were deactivated in the simulation model.

We have validated this device model with organic solar cells [34, 116, 113] and perovskite solar cells [36] in the past. The same device model is used in the last section of this review to describe several measurements of a PCDTBT:PC_{70}BM bulk-heterojunction solar cell to extract relevant electrical device and material parameters.

9.3.2 *Current-voltage characteristics of all cases*

First of all, we simulate current-voltage (JV) curves under illumination using the cases defined in Table 9.1. Figure 9.2 shows the simulation results of all cases in comparison to the *base* case. In Figure 9.2f the fill-factor of all cases is compared. Bartesaghi *et. al.* showed that the fill-factor in organic solar cells is mainly determined by the ratio of charge extraction versus charge recombination [139].

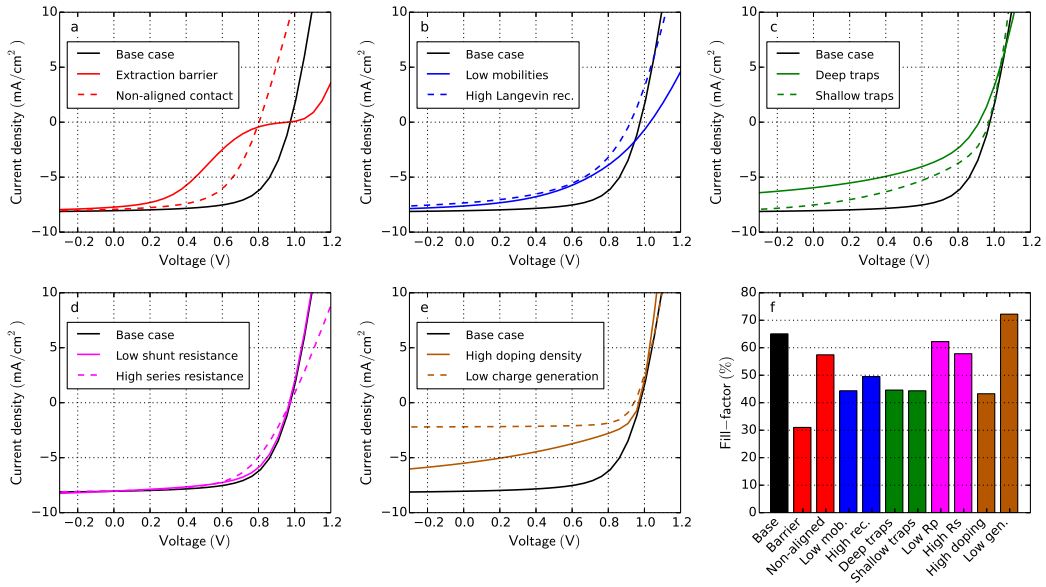

Figure 9.2: JV-curve simulations for all cases defined in Table 9.1. f) The bar-plot shows the fill-factor of all simulated cases. All the described cases impact the fill-factor. It is difficult to identify a specific physical effect if a JV-curve has a low fill-factor. An additional case with imbalanced mobilities is shown in Figure 9.23 in the section 9.5 Imbalanced electron/hole mobilities.

The case *extraction barrier* shows a pronounced S-shaped JV-curve. S-shapes are often associated with interface effects [130, 133, 140], which is confirmed here. A non-aligned contact leads to a lower built-in and open-circuit voltage. The JV-curve is therefore shifted to the left.

The open-circuit voltage increases in the case *low mobilities*. With Langevin recombination a lower mobility leads to less recombination and thereby to an increase in open-circuit voltage. The charge transport, however, is less efficient leading to a low fill-factor. In the case *high Langevin rec.* the open-circuit voltage and the fill-factor are reduced. A very similar effect occurs in the case *deep traps*. The traps are located in the middle of the band-gap leading to efficient SRH-recombination [135]. In contrast to the case *high Langevin rec.* the short-circuit current density is also reduced. *Shallow traps* have no impact on the steady-state short-circuit current in our model, but reduce the fill-factor. Shallow traps lead to a decrease of the

effective charge carrier mobility due to capture and release events. If charges are slower their density increases and so does the recombination.

The shunt resistance in this example has only a minor effect on the JV-curve. The fill-factor is slightly reduced since some of the current goes through the parallel resistance instead of the external circuit. A change in series resistance leads to a change in the current slope in forward direction and to a lower fill-factor. A high series resistance is detrimental to device performance since current-flow leads to a voltage-drop over the resistance. The open-circuit voltage is unaffected by the series resistance because the current is zero at this point.

Charge carrier doping can be very detrimental to the efficiency of solar cells as shown by Dibb *et. al.* [45]. Doping introduces extra charge inside the bulk that screens the electric field. This hinders charge extraction and leads to a reduction in photocurrent. This is observed in the case *high doping density*. The effect is more prominent for thicker devices [130, 45]. In the case *low charge generation* the short-circuit current is decreased as expected and the fill-factor is increased. The forward injection current is unchanged in our example.

We note that several of the investigated cases lead to a similar modification of the JV-curve compared to the *base* case, as shown in Figure 9.2. Therefore, by measuring JV-curves only it is hardly possible to identify which non-ideal case is present. In real measurements different effects often occur combined, which renders it even harder to distinguish between them by a single JV-curve. Still, in literature conclusions on charge transport are often drawn by looking at illuminated JV-curves only [113, 141–144]. This can be prone to errors. Performing further measurement techniques in the steady-state, transient and frequency domain gives more insight into charge transport physics as will be presented in the next sections.

9.4 CHARACTERIZATION TECHNIQUES

9.4.1 *Dark current-voltage characteristics*

Information about the recombination type (so-called ideality) and the shunt resistance can be obtained from current-voltage (JV) curves measured in the dark. In classical semiconductor physics the JV characteristics of a p-n junction in the dark is described by the Shockley equation

$$j(V) = j_s \cdot \left(exp\left(\frac{q}{n_{idd} \cdot k_B \cdot T} \cdot V \right) - 1 \right) \tag{9.1}$$

where j is the current density, j_s is the dark saturation current density, q is the unit charge, V is the voltage, n_{idd} is the dark ideality factor, k_B the Boltzmann constant and T the temperature. When the transport resistance R_T and the parallel resistance R_P are included the JV-curve is described by the following implicit equation

$$j = j_s \cdot \left(exp\left(\frac{q}{n_{idd} \cdot k_B \cdot T} \cdot (V - R_T \cdot j \cdot S) \right) - 1 \right) + \frac{V - R_T \cdot j \cdot S}{R_P} \tag{9.2}$$

where S is the area of the device. Equation 9.2 needs to be evaluated numerically as no analytical solution can be found. The equation can be fitted to measured dark JV-curves to extract the dark saturation current j_s, the dark ideality factor n_{idd} and the parallel resistance R_P. We clearly distinguish between transport resistance R_T and series resistance R_S. The series resistance causing the RC-effects visible in impedance spectroscopy or light-induced charge extraction by linearly increasing voltage (photo-CELIV) measurements is an Ohmic external resistance. It is often caused by the lateral conductivity of the transparent electrode [137]. The transport resistance used in Equation 9.2 is a resistance that represents the charge transport in the device [48]. The transport resistance is therefore higher than the pure series resistance.

In reverse direction the diode is ideally blocking and the current is determined by the parallel resistance R_P. A low parallel resistance is usually caused by shunts in the device [136] and can also be non-Ohmic [117]. Very high trap densities can however also lead to an increase in the reverse current [134]. In forward direction charge carriers are injected and recombine. Charge carriers either recombine in the bulk or travel to the opposite electrode and recombine at the interface. If only one charge carrier type is injected (for example in unipolar devices), the device is either injection limited or space-charge limited [131]. In the latter case the charge carrier mobility can be determined using the Mott-Gurney equation [145]. In solar cells often the dark ideality factor n_{idd} is determined from the exponential current-slope in forward direction. It is usually a factor between 1.0 and 2.0. In p-i-n solar cells, an ideality factor of 1.0 is interpreted as bimolecular recombination, a value near 2.0 is a signature of SRH recombination. The ideality factor is discussed in more detail in the next section.

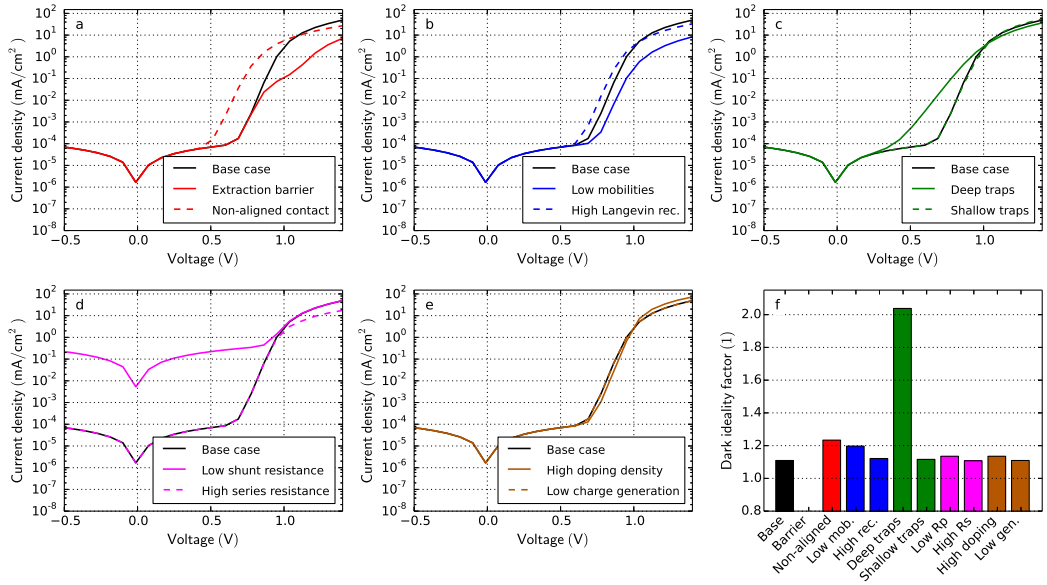

Figure 9.3: Dark JV-curve simulations for all cases in Table 9.1. f) Dark ideality factors extracted using Equation 9.2

Figure 9.3 shows dark JV-curve simulations of all cases. In these simulations reverse charge injection is negligible. The reverse current is solely determined by the parallel resistance. The case *low shunt resistance* (d) shows much higher reverse current. The parallel resistance can be determined accurately from the differential resistance in reverse.

In the case *non-aligned contact* (a) the exponential current increase is shifted to lower voltage due to the smaller built-in voltage. A low mobility leads to a smaller forward current as observed in Figure 9.3b. The slope of the current in the exponential regime is similar in all cases except for the case *deep traps* (c). The dark ideality factor, extracted using Equation 9.2, is around 1.1 for most cases and around 2.0 for the case *deep traps*.

It has been shown that the dark ideality factor can be inconsistent with the light ideality factor (next section) and the interpretation can be difficult [146, 147]. A high series resistance or low parallel resistance can influence the extraction of the dark-ideality factor [147]. Nevertheless, our simulation results show a clear difference in the dark ideality for the case *deep traps* – the only case with SRH recombination.

9.4.2 *Open-circuit voltage versus light intensity*

Measuring the open-circuit voltage versus the light intensity can be used to extract the light ideality factor. The ideality factor is a measure whether the recombination type is SRH ($n_{idL} = 2$) or bimolecular ($n_{idL} = 1$). In an ideal device the light ideality factor n_{idL} is identical with the dark ideality factor n_{idd} from dark JV-curves. In real devices dark- and light ideality factor can deviate. Since the light

ideality factor is not influenced by the series resistance it is easier to analyse [147].

An expression for the open-circuit voltage V_{oc} is obtained by setting the current to zero in the Shockley equation (Equation 9.1) leading to

$$V_{oc} = n_{idL} \cdot \frac{k_B \cdot T}{q} \cdot \ln\left(\frac{j_{ph}}{j_s} + 1\right) \tag{9.3}$$

where n_{idL} is the light ideality factor, k_B the Boltzmann constant, T the temperature, q the unit charge, j_{ph} the photocurrent and j_s the dark saturation current. Under the assumption that the photocurrent scales linearly with the light intensity and $j_{ph}/j_s >> 1$ we obtain

$$V_{oc} = n_{idL} \cdot \frac{k_B \cdot T}{q} \cdot \ln(L) + C_1(T) \tag{9.4}$$

where L is the normalized light intensity and C_1 is a temperature factor that does not depend on L. Please note that C_1 is constant with illumination but not constant with the temperature. The open-circuit voltage decreases with temperature and increases with light intensity. The slope of the open-circuit voltage versus light intensity depends only on the light ideality factor and the temperature. The light ideality factor is calculated according to

$$n_{idL} = \frac{q}{k_B \cdot T} \cdot \frac{dV_{oc}}{d(\ln(L))} \tag{9.5}$$

The light ideality factor n_{idL} can further depend on the light intensity. SRH recombination for example is more prominent at low light intensities. Often the average is calculated to obtain a single number for the ideality. It is however also interesting to study and compare the ideality factor versus the open-circuit voltage [147].

Generally, an ideality factor of 1.0 is attributed to bimolecular recombination (radiative recombination) whereas an ideality factor of 2.0 is attributed to dominant SRH recombination [40]. We however want to point out that the concept is based on a single zero-dimensional device model. In a real device the charge carrier distribution varies in space and energy which can influence the ideality factor even if no traps are present. In organic solar cells the photocurrent j_{ph} can depend on the voltage due to Onsager-Braun dissociation of excitons into free carriers [148]. In devices with field-dependent charge generation the analysis of the light ideality factor might be prone to errors [149].

Figure 9.4 shows simulated open-circuit voltages versus light intensity for the different cases. In Figure 9.4f the light ideality factor is shown, calculated from the average slope of the V_{oc} versus the light intensity according to Equation 9.5. The *base* case has an ideality factor of exactly one. Apart from the case *low shunt*

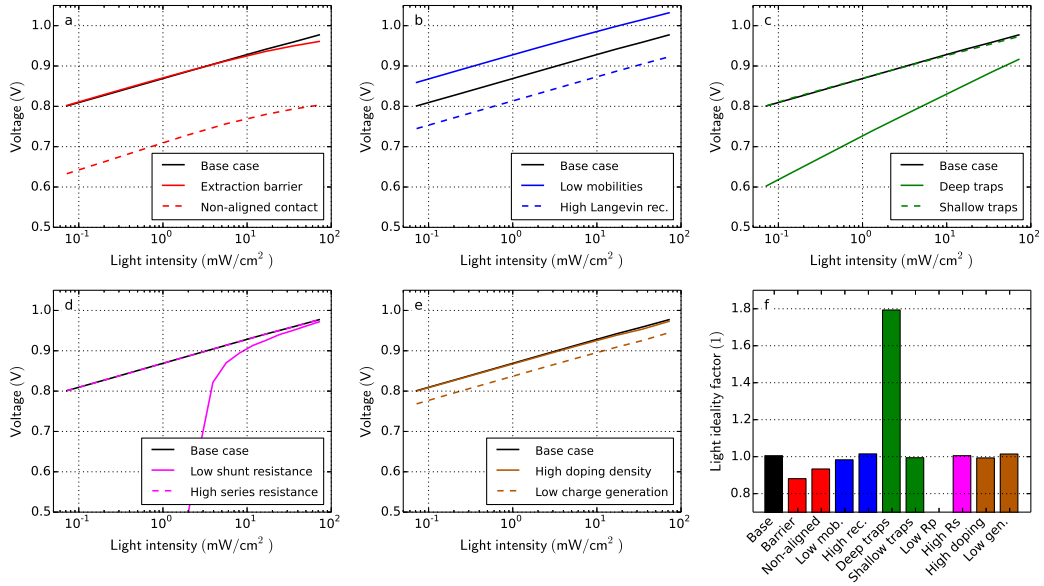

Figure 9.4: Simulation of the open-circuit voltage dependent on the light intensity for all cases in Table 9.1. f) Light ideality factors obtained from the simulation results with Equation 9.5 – an average is used.

resistance and *deep traps* the ideality factor is around 1.0. If the recombination prefactor is increased (b) the V_{oc} is lower, but the V_{oc}-slope remains constant. In the case of *deep traps* (c) the slope (V_{oc} vs L) is significantly steeper leading to an average ideality factor of 1.8. In the case *low shunt resistance* (d) the V_{oc} collapses at lower light intensity and the calculation of an average ideality factor does not make sense.

Thus, our simulation results show that the light ideality factor can be useful to investigate whether SRH-recombination is significant in a device, as we found for the case *deep traps*. The analysis works only if the effect is not concealed by a low shunt resistance.

9.4.3 *Charge extraction by linearly increasing voltage*

Charge extraction by linearly increasing voltage (CELIV) is a popular technique to estimate charge carrier mobilities in thin-film solar cells. It was introduced by Juska *et. al.* [150] in 2000 and many adaptions or extensions were proposed [151–153, 37]. Figure 9.5 shows the principle of CELIV schematically. A linearly increasing voltage in reverse direction is applied to the device $V(t) = A \cdot t$, where A is the ramp rate.

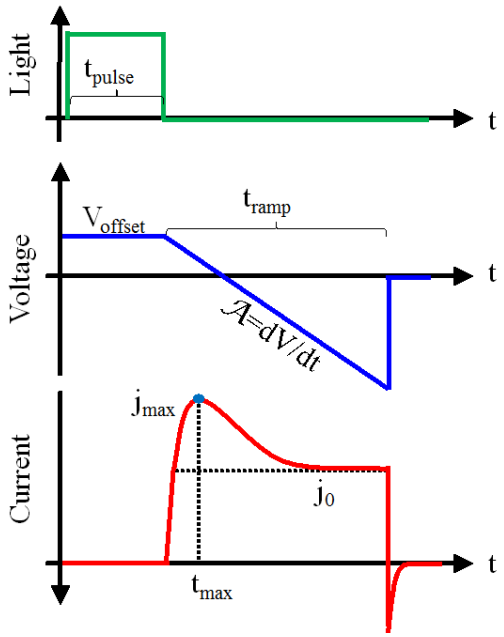

Figure 9.5: Schematic illustration of a photo-CELIV experiment. The linearly increasing voltage extracts charge carriers and leads to a peak (j_{max}) in current. The charge carrier mobility is calculated using t_{max}.

The linearly changing voltage induces a constant displacement current density j_{disp}, which is calculated according to

$$j_{disp} = \frac{1}{S} \cdot \frac{dV}{dt} \cdot C_{geom} = \frac{1}{S} \cdot \frac{d}{dt}(A \cdot t) \cdot \frac{S \cdot e_0 \cdot e_r}{d} = \frac{A \cdot e_0 \cdot e_r}{d} \tag{9.6}$$

where S is the device area, C_{geom} is the geometric capacitance, ϵ_0 is the vacuum permittivity, ϵ_r is the relative dielectric permittivity and d is the active layer thickness.

If charge carriers are present in the device, they are extracted and lead to a peak in the transient current. According to the time of the current-peak (t_{max}) the charge carrier mobility can be estimated.

The charges that are extracted by the voltage ramp can be intrinsic (dark-CELIV), be generated by illumination prior to extraction (photo-CELIV) or be injected by a positive voltage prior to extraction (injection-CELIV).

Performing the latter with metal-insulator-semiconductor (MIS) devices allows distinguishing between extracted electrons and extracted holes (MIS-CELIV).

Here the charge dynamics are different and another formula is applied to extract the charge carrier mobility [154–156]. Because the deposition of a thin, high-quality dielectric layer is difficult we demonstrated MIS-CELIV using polar tris(8-hydroxyquinolinato)aluminium (Alq_3) [157, 158].

9.4.4 *Dark-CELIV*

Dark-CELIV can be used to extract the relative dielectric permittivity and estimate the doping density. The relative dielectric permittivity can be calculated from the displacement current j_{disp} by rearranging Equation 9.6:

$$\epsilon_r = \frac{j_{disp} \cdot d}{A \cdot e_0} \tag{9.7}$$

The doping density of the device can be estimated by integrating the current. The charges on the electrodes ($Q = C \cdot V$) need to be subtracted. The doping density can be estimated according to

$$n_{doping} = \frac{1}{d \cdot q} \cdot \Big(- \int_0^{t_{ramp}} j(t) \cdot dt - \frac{C_{geom} \cdot V(t_{ramp})}{S} \Big) \tag{9.8}$$

where d is the active layer thickness, q is the unit charge, t_{ramp} is the time when the ramp ends, j is the current, C_{geom} is the geometric capacitance, V is the applied voltage and S is the device area.

Figure 9.6 shows the simulation results of dark-CELIV using the cases defined in Table 9.1. The only device that shows a current peak is the case with a high doping density. The homogeneous immobile doping induces oppositely charged carriers, which are mobile and can be extracted by CELIV. The parallel resistance leads to an increase in current over time. In such a case neither the integration of the current nor the estimation of the electric permittivity works.

In the other cases mostly RC-effects are observed. We apply Equation 9.7 to the simulation results. The relative permittivity is obtained with an error of less than 1% in all cases except *low shunt resistance* and *high doping density*. The capacitance of the device can change over time, for example due to mobile ions as observed in perovskite solar cells [95, 89, 93, 96]. In such a case the calculation of the relative permittivity is less accurate.

The extracted doping density is shown in the bar-plot in Figure 9.6f. For the case with high doping a charge carrier density of $1.2 \cdot 10^{16}\ cm^{-3}$ is extracted. It is almost an order of magnitude lower than the doping density defined as simulation input ($1 \cdot 10^{17}\ cm^{-3}$). The reason is that not all charge carriers can be extracted due to the finite ramp-time. The doping density extracted from dark-CELIV should therefore be interpreted as a lower limit for the doping density. We recommend to perform the experiment with varying the ramp-rates and to use the highest density value.

An alternative method to extract the doping density from dark-CELIV currents was presented by Sandberg *et. al.* analysing the shape of the current-decay, based

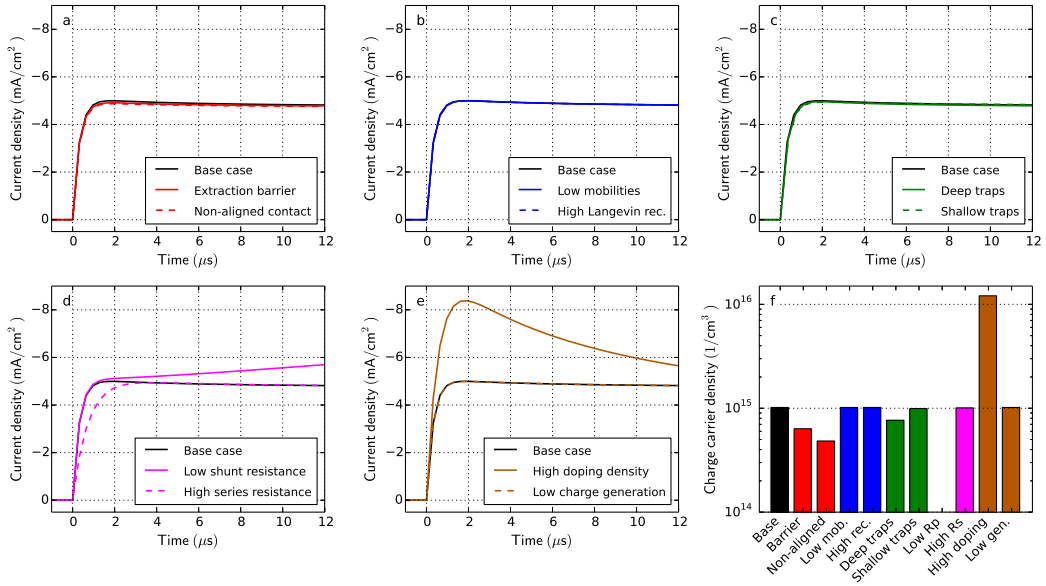

Figure 9.6: Dark-CELIV simulations of all cases in Table 9.1. The ramp starts at $t = 0$ with a ramp rate of $171\,V/ms$. f) The bar plot shows the extracted charge carrier density.

on the Mott-Schottky formalism [159]. Seemann and co-workers demonstrated the evolution of unintentional doping during device degradation by using dark-CELIV measurements [138]. In organic solar cells doping is usually detrimental to device performance [45].

9.4.5 *Photo-CELIV*

In photo-CELIV free charge carriers are generated by a light pulse and are subsequently extracted by a voltage ramp. As a light source either a light emitting diode (LED) or a laser is used. When the charge carriers are extracted from the bulk they create a current overshoot $\Delta j = j_{max} - j_0$. According to Juska *et. al.* [150] the time where the current peaks (t_{max}) can be used to calculate the charge carrier mobility by

$$\mu = \frac{2 \cdot d^2}{3 \cdot A \cdot {t_{max}}^2} \cdot \frac{1}{1 + 0.36 \cdot \Delta j / j_{disp}} \tag{9.9}$$

where μ is the charge carrier mobility, d is the active layer thickness, A is the ramp rate, t_{max} is the time where the current peaks, j_{disp} is the displacement current and Δj is the peak current minus the displacement current. The factor $1 + 0.36 \cdot \Delta j / j_{disp}$ in the formula is an empirical correction accounting for the redistribution of the electric field. Bange *et. al.* presented a new equation for the CELIV mobility evaluation validated using drift-diffusion calculations [152]. Lorrmann *et. al.* presented a parametric equation that needs to be evaluated computationally [153]. These adaptions did however not lead to an overall improvement of the

accuracy of the estimated mobility when applied to our simulation results.

The analytical approach is based on a simple model that considers one charge carrier type to be mobile and the other one to be static. The initial distribution of the charges is considered to be uniform in the bulk and diffusion is neglected. As these approximations are usually inadequate to describe thin film devices, it is apparent that the charge carrier mobility determined based on this model is less accurate compared to full drift-diffusion parameter extraction. In a previous publication we have studied the CELIV experiment in detail and concluded that the formula (Equation 9.9) obtains the charge carrier mobility with an accuracy of a factor of 4. The RC-effects lead to a strong underestimation of the mobility [115]. In such a case it is advised to increase the thickness of the transparent conducting oxide (TCO) and metallise the TCO stripes. This effectively reduces the series resistance and thereby the RC time constant. Furthermore, it is advised to use devices with a small area leading to a small capacitance and a low RC time.

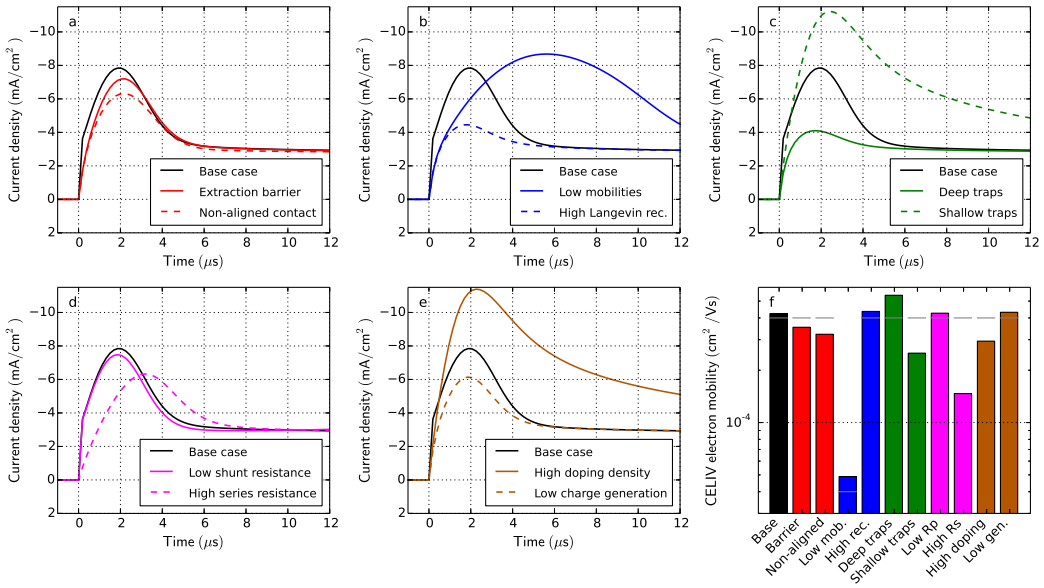

Figure 9.7: Photo-CELIV simulations for all cases in Table 9.1. The light is turned off at $t = 0$ and the voltage ramp starts at $t = 0$ with a ramp rate of $100\,V/ms$. The voltage offset prior the ramp is set such that the current is zero at $t < 0$. f) The bar plot shows the charge carrier mobility calculated from the peak position (t_{max}) using Equation 9.9. The grey lines indicate the electron mobility used as simulation input.

Figure 9.7 shows photo-CELIV simulation results of all cases defined in Table 9.1. All devices show a current overshoot with peak-times ranging between 2 and $6\,\mu s$. Figure 9.7f shows mobilities calculated using Equation 9.9. The extracted mobility agrees within a factor of 2 with the input electron mobility (grey line), except for the case with the high series resistance. It leads to a slower charge extraction and to an underestimation of the mobility. In the case of low mobility (Figure 9.7b) the current extraction is slower and the extracted mobility is lower.

Traps significantly influence the charge extraction as visible in Figure 9.7c. Deep traps create additional recombination channels (SRH), therefore less charge is extracted. Shallow traps however save charges from recombination. Therefore, more charge is extracted and the apparent mobility is lower. A similar effect of a slower charge extraction is observed in case of imbalanced mobilities as shown in Figure 9.23 in section 9.5 Imbalanced electron/hole mobilities.

Photo-CELIV can also be used to estimate the recombination coefficient. Hereby the experiment is performed several times with varied delay-time between the light pulse turn-off and the voltage ramp start. Then the extracted charge carrier density is plotted versus the delay-time. The recombination coefficient is obtained by fitting a simple zero-dimensional rate equation ($dn/dt = -k_2 \cdot n^2 - k_1 \cdot n$) [151, 38].

If the applied voltage is constant during the delay-time, charge is either injected (if the voltage is too high) or charge is extracted (if the voltage is too low). To keep the cell at open-circuit during the delay-time Clarke *et. al.* used a very fast electrical switch [41]. An alternative that might be easier to realize was proposed by Baumann and co-workers and named OTRACE [37]. Thereby the photovoltage decay is measured first. This voltage signal is then applied during the delay-time of the CELIV experiment. OTRACE ensures that charge carriers remain and recombine in the device during the delay-time and therefore increases the accuracy of the experiment [37].

9.4.6 *Transient photovoltage and open-circuit voltage decay*

Under open-circuit condition the external current is zero and hence charge generation is equal to charge recombination. Techniques probing the device under open-circuit are generally suited to study recombination. Open-circuit voltage decay (OCVD, sometimes also called large-signal TPV) measurements reveal information about recombination and the shunt resistance. In OCVD measurements the device is first illuminated by an LED or a laser to create charge carriers. Then the light is turned-off and the decay of the voltage is measured over time.

Figure 9.8 shows OCVD simulation results of the defined cases. All the cases have in common, that the voltage drops significantly beyond 50 milliseconds after light turn-off. This is related to the shunt resistance. The most pronounced effect with respect to the *base* case is visible in the case *low shunt resistance* (Figure 9.8d). Instead of recombining slowly the charges flow through the shunt resistance and deplete the device. When the shunt resistance is decreased the voltage decays more rapidly. The *base* case has a shunt resistance of 160 $M\Omega$, the kink at 50 milliseconds is caused by this parallel resistance. The voltage decay before 50 milliseconds shows a logarithmic dependence on time similar as observed by Elliott and co-workers [160]. In the case of deep traps the decay rate is higher as visible in Figure 9.8c. With shallow traps the voltage decay is slower as charges are immobilized when trapped delaying the recombination. In perovskite solar cells a persistent photovoltage was observed after light turn-off [161] that might be caused by mobile ions.

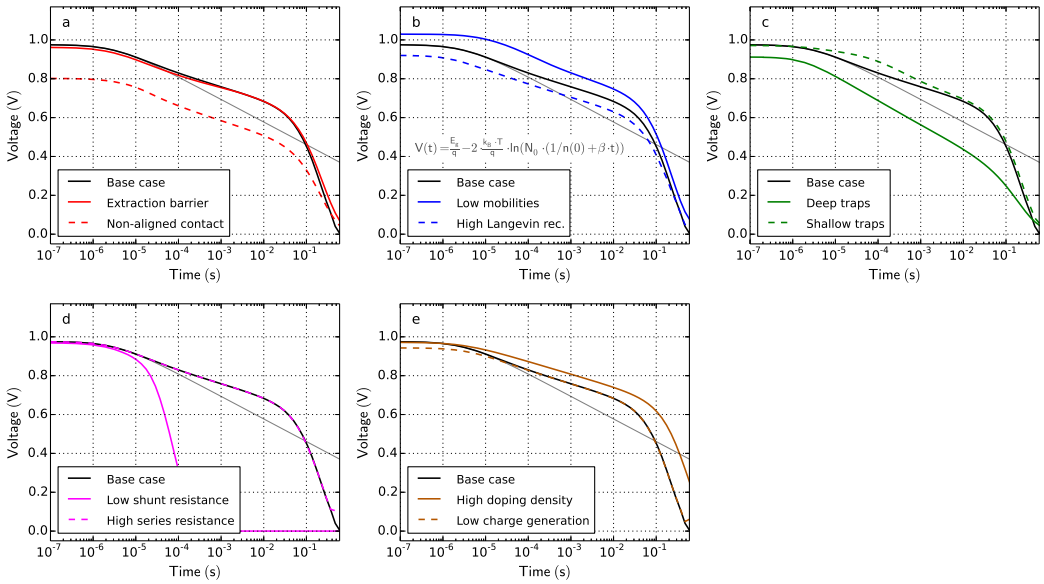

Figure 9.8: OCVD simulations for all cases in Table 9.1. The light is turned off at $t = 0$. The grey line indicates the analytic solution (Equation 9.11) assuming homogeneous charge densities and purely bimolecular recombination.

The open-circuit voltage V_{oc} in a solar cell can be described according to

$$V_{oc} = \frac{E_g}{q} - \frac{k_B \cdot T}{q} \cdot \ln\left(\frac{N_0^2}{n \cdot p}\right) \tag{9.10}$$

where E_g is the energy of the band-gap, q is the unit charge, k_B is the Boltzmann constant, T is the temperature, N_0 is the effective density of states, n the electron density and p the hole density. When the decay of a homogeneous charge carrier density ($dn/dt = -\beta \cdot n^2$ with $n = p$) is inserted into Equation 9.10 we obtain

$$V_{ocvd}(t) = \frac{E_g}{q} - 2 \cdot \frac{k_B \cdot T}{q} \cdot \ln\left(N_0 \cdot \left(\frac{1}{n(0)} + \beta \cdot t\right)\right) \tag{9.11}$$

where $n(0)$ is the initial charge carrier density at open-circuit and β is the recombination pre-factor. According to Equation 9.11 the voltage signal is expected to decay with a logarithmic dependence on time. This is shown in the plots of Figure 9.8 as grey lines. Parameter β is chosen according to the *base* case. The analytic solution (Equation 9.11) does only fit the numerical simulation at the very beginning. The reason is that the charge is not homogeneously distributed inside the device [162]. Close to the electrodes the densities are higher and charges flow slowly into the middle of the device where they recombine. Zero-dimensional models are therefore not suited to describe the open-circuit voltage decay in p-i-n structured solar cells. The same consideration also applies to recombination coefficients extracted from CELIV using the OTRACE method or to lifetimes determined from TPV or IMVS which are also described in this thesis.

From OCVD measurements no material parameters can be derived directly. It can however be useful for comparing different devices or to perform parameter extraction by fitting numerical simulations (see section 9.6 Comprehensive parameter extraction with numerical simulation).

9.4.7 *Transient photovoltage and charge carrier lifetime*

Transient Photovoltage (small-signal TPV) is frequently performed to determine charge carrier lifetimes in organic solar cells [39–44]. The concept of *charge carrier lifetimes* stems from the community of silicon solar cells and describes how long on average a minority charge carrier survives in a doped bulk material [126]. A general definition of minority charge carrier lifetime τ is

$$\tau = \frac{n}{R} \tag{9.12}$$

where n is the charge carrier density (electrons or holes) and R is the recombination current. In a device with a high and homogeneous doping density (majority charge carrier) the minority charge carrier has a lifetime that is constant in space and time.

In p-i-n structures the charge carriers are generated in the intrinsic region and transported to the electron and hole contact layers. The intrinsic region has no doping and consequently also no clear majority or minority carriers. Both electron and hole densities vary spatially even at open-circuit [162]. The charge carrier lifetime is therefore not clearly defined in a p-i-n structure and it is position-dependent. Physical conclusions based on measured *charge carrier lifetimes* can therefore be misleading. Despite these limitations lifetimes are often determined also for thin p-i-n structured devices [39–44]. A more detailed discussion about this issue is found in section 4.4.3 Charge Carrier Lifetime.

In a TPV experiment the solar cell is kept at open-circuit voltage under bias-illumination. Then an additional small laser pulse (or LED pulse) is applied to the device to create some additional charge that decays exponentially thereafter. If the light pulse is small enough the assumption that the change in density of photogenerated carriers is proportional to the photovoltage increase ($\Delta n \sim \Delta V$) holds. The voltage decays as

$$V(t) = V_{oc} + \Delta V \cdot exp(-t/\ \tau) \tag{9.13}$$

where V_{oc} is the open-circuit voltage at the bias illumination, ΔV is the voltage increase due to the laser pulse and τ is the minority carrier lifetime. By the TPV experiment the charge carrier lifetime at given bias illumination can be estimated directly from the exponential voltage decay. Charge carrier lifetimes are usually plotted versus the charge carrier density.

Lifetimes from TPV are not a direct measure of the steady-state charge carrier lifetime as shown by O'Regan *et. al.* [163]. To obtain steady-state carrier lifetimes the TPV lifetimes need to be multiplied with the reaction order (often denoted as $\lambda + 1$) [41, 163].

We perform TPV simulations and extract charge carrier lifetimes from the exponential voltage decay after light turn-off. Figure 9.9 shows charge carrier lifetimes determined from TPV simulations versus the open-circuit voltage for varied offset light intensities. The lifetimes were corrected with the reaction order of 2.0 according to O'Regan *et. al.* [163]. The points show the lifetimes extracted from IMVS simulations (see section 9.4.16 Intensity-modulated photovoltage spectroscopy) for two different offset light intensities. Also these lifetimes were corrected with the reaction order. Apart from minor numerical deviations in Figure 9.9c the lifetimes from TPV and IMVS agree completely. TPV and IMVS are therefore suited to cross-check measured charge carrier lifetimes.

The ideal charge carrier lifetime τ under the assumption of bimolecular recombination and equal densities of electrons and holes can be described as

$$\tau = \frac{1}{\beta \cdot N_0} \cdot \exp\left(-\frac{V_{oc} \cdot q - E_g}{2 \cdot k_B \cdot T}\right) \tag{9.14}$$

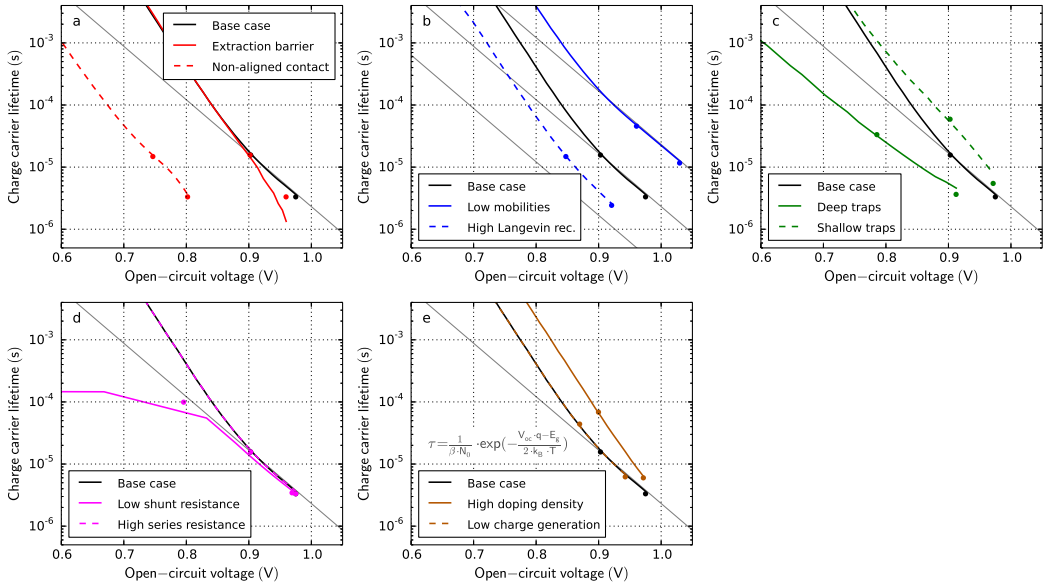

Figure 9.9: Transient photovoltage simulations for all cases in Table 9.1. From an exponential decay fit to the simulation result the charge carrier lifetime is calculated. The points mark lifetimes calculated from IMVS at offset light intensities $65\,mW/cm^2$ and $3.6\,mW/cm^2$. All lifetimes are corrected with a reaction order of 2. The grey line shows the analytical solution for purely bimolecular recombination in a zero-dimensional model with equal electron and hole densities.

where β is the recombination pre-factor, N_0 is the density of states, V_{oc} the open-circuit voltage, q the unit charge, E_g the band-gap, k_B the Boltzmann constant and T the temperature. The lifetime calculated from this equation is shown in grey using the recombination pre-factor of the *base* case. In the *base* case the charge carrier lifetime reaches exactly the analytical solution. The charge carrier densities are homogenous and therefore the lifetimes agree with the zero-dimensional analytical solution. At lower light intensity the charge carrier lifetime is underestimated by the simple formula. The reason is that the charge carriers are spatially inhomogeneous [162].

In the case *non-aligned contact* (a) the V_{oc} is lower compared to the *base* case but the charge carrier lifetime is the same. It does not agree with the analytical solution although it has only bimolecular recombination as in the *base* case.

The case *low mobilities* (b) agrees as well with its analytical solution at high light intensity. However, the case *high Langevin recombination* does not reach the analytical solution. With higher recombination the inhomogeneity of the charge carrier distribution increases and the lifetime approach fails.

While the *shallow traps* (c) lead to a higher V_{oc}, the *deep traps* (c) lead to a reduced V_{oc} due to SRH-recombination. The shunt resistance (d) leads to a collapse of the V_{oc} but fairly similar lifetimes.

In Figure 9.10 we show the same lifetime data plotted versus the charge carrier density extracted from simulated charge extraction (see section 9.4.11 Charge

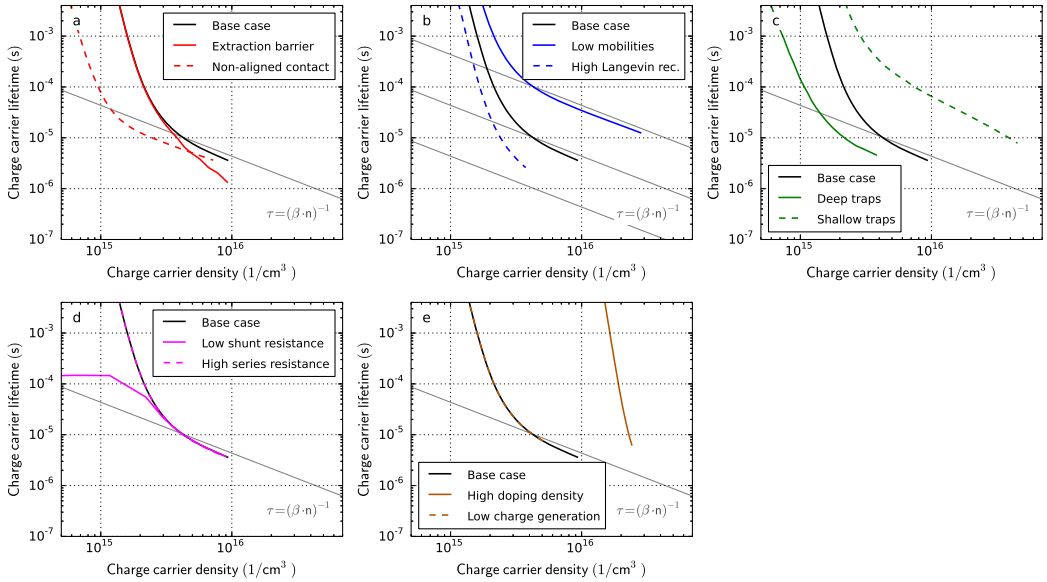

Figure 9.10: Transient photovoltage simulations for all cases in Table 9.1 in combination with the charge carrier densities determined from charge extraction simulations. The grey line shows the analytical solution for purely bimolecular recombination in a zero-dimensional model with equal electron and hole densities.

extraction). Also here the analytical solution for the lifetime is drawn with a grey line. The assumption is an equal electron and hole density that is spatially homogenous with bimolecular recombination only. Also here it is shown that in the *base* case the simulated TPV lifetimes only agree with the analytical solution at high light intensities. At low light intensities the charge carrier distribution becomes too inhomogeneous and the lifetime analysis fails. One might interpret such measurement results by a reduced recombination order at low light intensity – but in fact it is only a spatial separation that causes this effect. This conclusion agrees partly with Kiermasch *et. al.* stating that apparent charge carrier lifetimes in thin solar cells are mainly caused by capacitive discharging [164].

We conclude that lifetimes plotted versus charge carrier density show the expected trends, but detailed conclusions about recombination and charge transport from such measurements are difficult. In general the agreement is better at high light intensities since the charge carrier distributions are more uniform. We recommend to interpret measured charge carrier lifetimes from p-i-n structures carefully. In thick devices the problem is less severe as the charge carrier gradients are smaller [162].

9.4.8 *Deep level transient spectroscopy*

Deep level transient spectroscopy (DLTS) is a technique that was developed to study trapping in semiconductor devices. In DLTS a capacitance, a current (i-DLTS) or charge (Q-DLTS) is measured over time after the application of a voltage step at various temperatures. DLTS was introduced by Lang in 1974 measuring capacitance transients of GaAs semiconductor devices at varied temperature [165]. The technique promises to determine trap spectra (trap density versus energetic trap depth) of majority and minority carrier traps as well as capture cross-sections. It is frequently applied to study defect distributions in inorganic semiconductors [165–169]. DLTS is of limited use for organic semiconductors since their mobility is too low and RC-effects are usually too high [170].

Great care must be taken to accurately determine trap spectra in organic or quantum dot semiconductors. When measuring capacitance-based DLTS the probing frequency must be small enough to measure the space-charge capacitance [170]. When measuring current-based DLTS it is important to properly subtract the displacement current [171] and measure with high current resolution [172]. DLTS has also been performed on perovskite solar cells to determine trap energies and densities [173]. Such results should however be carefully interpreted as the presence of mobile ions may disturb the measurement.

In this review we simulate current-based DLTS [167, 171, 172, 174]. A negative voltage step ($0\,V$ to $-5\,V$) is applied to the device in the dark and the transient current response is analysed. Apart from the displacement current caused by RC-effects there is a small current from trap emission. The trap emission current j_{te} from a discrete energy trap can be described as

$$j_{te}(t) = \frac{1}{\tau_{te}} \cdot q \cdot d \cdot N_t \cdot \exp\left(-\frac{t}{\tau_{te}}\right) \tag{9.15}$$

where τ_{te} is the trap emission time constant, q is the unit charge, d the device thickness (or depletion width in thick devices) and N_t is the trap volume density. The trap emission time τ_{te} is the inverse of the trap emission rate e_t and is described as

$$\tau_{te} = \frac{1}{e_t} = \frac{1}{c_t \cdot N_0} \cdot \exp\left(\frac{\Delta E}{k_B \cdot T}\right) \tag{9.16}$$

where c_t is the trap capture rate, N_0 is the number of chargeable sites (density of states), ΔE the trap depth, k_B the Boltzmann constant and T the temperature. The trap capture rate c_t can be considered as material constant that includes the capture cross-section. For inorganic semiconductors the trap emission time includes another factor $1/T^2$ to account for the temperature dependence of the thermal velocity and the temperature dependence of the density of states [169].

We distinguish between two distinct shapes of the current decay from thermal emission of trapped carriers. The emission current from single energy trap levels

(Equation 9.15) is exponentially decaying. The emission current from an exponential band tail shows a power-law decay.

Street analysed current decays after illumination turn-off with thermal emission of carriers from exponential band tails [175]. Such a TPC current decay is consistent with the DLTS current decay after the transit time. The emission current j_{em} from the exponential band tail $N(E) = N_D \cdot exp(-E/E_0)$ is described as

$$j_{em}(t) = q \cdot d \cdot N_D \cdot k_B \cdot T \cdot \omega^{-\frac{k_B \cdot T}{E_0}} \cdot t^{(-\frac{k_B \cdot T}{E_0}-1)} \tag{9.17}$$

where $N(E)$ is the density of states as a function of energy, N_D is the density at $0\,eV$ with unit $cm^{-3}\,eV^{-1}$, E is the energy from the band edge ($E = 0$) into the band-gap, E_0 is the band tail slope, q the unit charge, d the device thickness, k_B the Boltzmann constant, T the temperature and ω is the attempt-to-escape factor (on the order of $10^{12}\,s^{-1}$) [175].

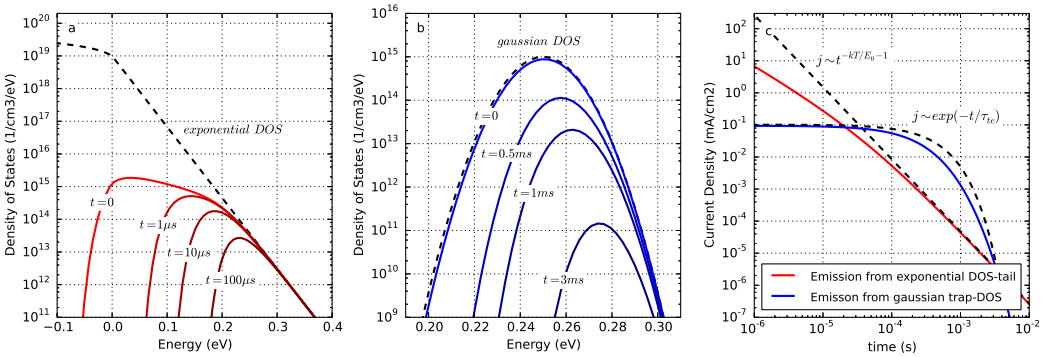

Figure 9.11: Calculation of the thermal emission of charge carriers from the density of states. a) The dashed line is the density of states with square-root dependence above the band edge and exponential dependence inside the band. The solid lines represent the charge carrier distributions at different times. The LUMO-level is located at $0\,eV$, positive energy values reach into the band-gap. b) Same as in a) but for a Gaussian DOS. c) Calculated currents from carrier emission of a) and b) including analytical fits according to Equation 9.15 and Equation 9.17.

To illustrate the different current decay shapes, we calculate the emission current from two different densities of states. First the density of states is filled with charges using Fermi-Dirac-statistics, then the emission current over time is calculated. Charge transport inside the device is neglected. In Figure 9.11 the carrier distribution and emission current from an exponential trap-DOS and a Gaussian trap-DOS are shown. The initial Fermi-level was chosen as $0.2\,eV$. The traps DOS in Figure 9.11b is therefore completely filled. The exponential tail is filled below $0.2\,eV$. The emission current over time from the exponential DOS follows a power-law decay (Figure 9.11c) and is described well for longer times using Equation 9.17. The emission from the Gaussian trap DOS is exponential and reflected by Equation 9.15. In reality a combination of both may be observed. Furthermore, emission currents from both electrons and holes will make the analysis more difficult. For simplicity we use single energy traps and discrete

band energies for the simulations of DLTS below.

Figure 9.12 shows DLTS simulations at room temperature. In contrast to the results of the rate equation model in Figure 9.11c, the results in Figure 9.12 were obtained with the drift-diffusion software *Setfos* [111] that considers the position-dependence of carrier transport in the device. The current peak within the first $1\,\mu s$ is caused by RC-effects and is not of interest here. The recombination pre-factor and the mobility have no influence on the resulting current (Figure 9.12b). For *shallow traps* an additional current flow from trap emission is observed (Figure 9.12c). The deep traps lead to SRH-recombination – trapped charges recombine instead of being re-emitted. An extraction barrier as shown in Figure 9.12a can however lead to a current tail that might be mistaken for trap emission. When the device has a low shunt resistance as shown in Figure 9.12d the trap emission current is hidden by the leakage current through the shunt. If the device is doped some of the equilibrium charge is extracted that leads to an additional current (Figure 9.12e).

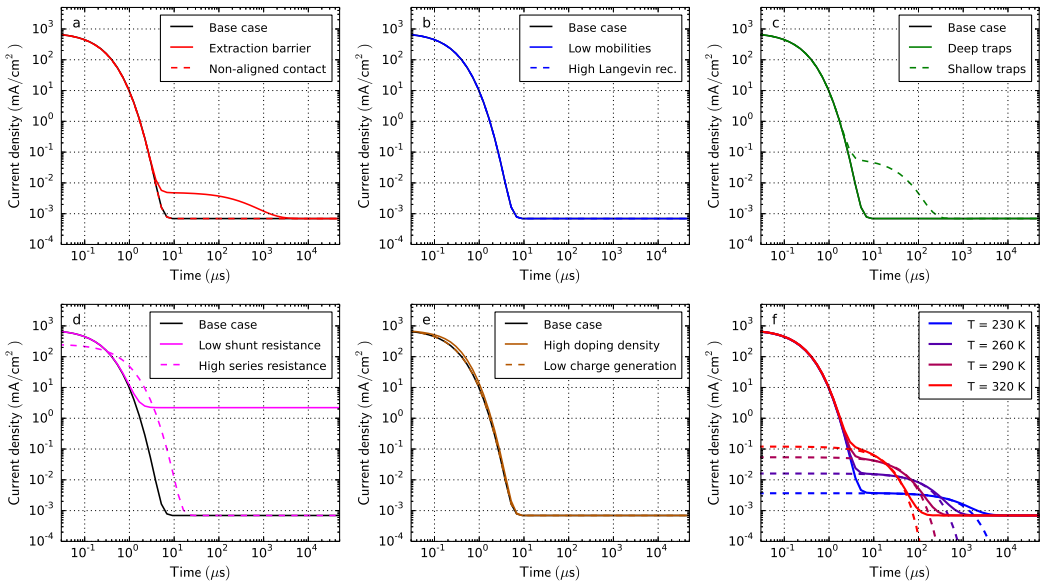

Figure 9.12: DLTS simulations for all cases in Table 9.1. The voltage is $0\,V$ for $t < 0$. At $t = 0$ the voltage jumps to $-5\,V$. f) DLTS simulations of case *shallow traps* at different temperatures (solid lines). The dashed lines are exponential fits according to Equation 9.15.

Figure 9.12f shows the simulation results of case *shallow traps* at different temperatures. The dashed lines represent exponential fits using Equation 9.15. Using the extracted trap emission time τ_{te} the trap-depth can be calculated using Equation 9.16 in an Arrhenius plot. The trap depth of $0.4\,eV$ can be accurately determined when analysing the simulation results and is thus consistent with this model input parameter. For the number of occupied traps values between $7 \cdot 10^{14}$ and $1.6 \cdot 10^{15}\,cm^{-3}$ were extracted. The effective density of occupied traps at room temperature in the dark is $2 \cdot 10^{16}\,cm^{-3}$ for the case *shallow traps*. The analytical fit

from the emission current thus underestimates the trap density by a factor of 10 in this case. The reason is that also at -5 volt not all the traps are empty. The effective trap density is therefore likely to be underestimated with this method.

In our simulation there is no limit for the current resolution. In measurements it can however be difficult to resolve 6 orders of magnitude of currents in this time-regime. Trap emission might be hidden in measurement noise.

9.4.9 *Transient photocurrent*

In transient photocurrent (TPC) experiments the current response to a light step is measured at constant offset-voltage. The current rise and decay reveal information about the charge carrier mobilities, trapping and doping. TPC is usually performed with varied offset-voltage, offset-light or light pulse intensity. The rise time in organic solar cells usually lies between 1 μs and 100 μs. In perovskite solar cells the current rise starts in the microsecond regime and can take several seconds until steady-state is reached [36].

Christopher McNeill and co-workers observed a photocurrent overshoot in polymer solar cells and explained it by charge trapping and detrapping using drift-diffusion simulations [176]. If the charge trapping is slow enough it leads to a current overshoot caused by space charge effects. As more and more charges get trapped they screen the electric field and hinder charge transport. Fast trapping however leads to a slower current rise [177]. In some cases, a current overshoot occurs only at negative bias voltage [42].

The current decay can be described in the same manner as in DLTS. Using Equation 9.15 trap emission currents from discrete energies can be calculated. Using Equation 9.17 trap emission from an exponential DOS tail is calculated. Street calculated the density of states of the band tail of PCDTBT:PCBM and P3HT:PCBM solar cells by analysing the TPC current decay [175].

By integrating the current decay over time, the extracted charge is obtained [176]. In our simulations the extracted charge is one or two orders of magnitude lower than the effective charge inside the device. During extraction most of the charge recombines. The fraction depends on the relative time scale of recombination with respect to charge extraction.

Figure 9.13 shows TPC simulations with light pulses of 15 μs duration and normalized current. The shape of the current rise does not change for the cases: *extraction barrier* (a), *non-aligned contact* (a), *high Langevin recombination* (b), *low shunt resistance* (d) and *low charge generation* (e). A smaller charge carrier mobility clearly leads to a slower rise and decay as shown in Figure 9.13b. The shallow traps fill slowly (capture and re-emission) and lead to a slower equilibration of the current (c). The trap emission leads to a slow exponential current decay after light turn-off. The case *deep traps* shows a current overshoot (c) consistent with the analysis of McNeill [176]. Space-charge is built up by the charged traps reducing the current on a longer timescale. If TPC is performed with offset-light the current overshoot and the long decay vanish because the offset-light keeps the traps filled

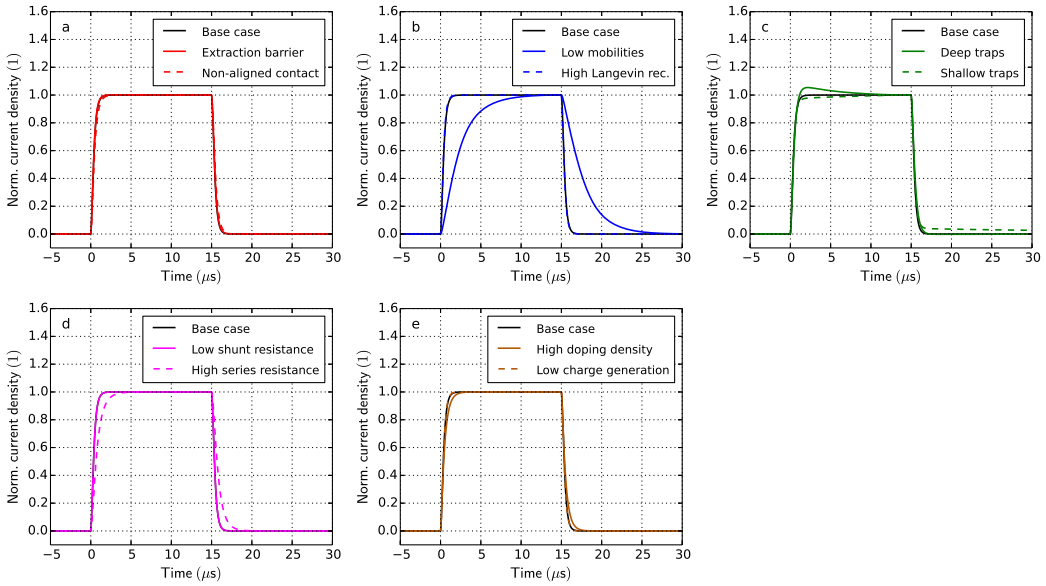

Figure 9.13: Transient Photocurrent simulations for all cases in Table 9.1. At $t = 0$ the illumination is turned on. At $t = 15\,\mu s$ the illumination is turned off. The applied voltage is 0 volt. The current is normalized by the current at $15\,\mu s$.

[176]. In our simulations this effect is already visible with offset-light intensities of 0.1% of the pulse illumination intensity. A high series resistance can also lead to a slower current rise and decay as shown in Figure 9.13d. The case *high doping density* shows a slightly longer current rise and decay caused by space charge effects. With imbalanced mobilities two time-constants arise corresponding to the fast and the slow carrier type as shown in Figure 9.23 in section 9.5 Imbalanced electron/hole mobilities.

In contrast to CELIV there is no simple formula to extract the charge carrier mobility from TPC data. TPC is however a powerful technique to study charge transport, identify trapping and to extract parameters using numerical modelling.

9.4.10 *Transient Photocurrent Decay*

In the previous section transient photocurrent simulations with rise and decay are presented. Here we analyse the same TPC decay in detail. Figure 9.14 shows simulation results of the transient photocurrent decay for all cases defined in Table 9.1. With a lower mobility (b) the decay is slower because it takes longer until the device is empty. In the case *deep traps* (c) the current shows an undershoot (the photocurrent becomes positive). Charges flow back into the device. This reverse current can be explained by looking at the trap occupation. In the dark more traps are filled than under illumination. Illumination leads to a depletion of traps via SRH-recombination. The *shallow traps* (c) lead to an exponentially decaying current caused by thermal emission of the carrier from the traps. Interestingly, the case with an extraction barrier (a) shows a very similar behaviour, as also here an

energetic activation governs the slow part of the charge collection.

The tail current is integrated and divided through the device volume to obtain the charge carrier density as shown in Figure 9.14f. The grey lines represent the effective charge carrier density calculated from integrating the simulated charge carrier profiles at short-circuit. The charge carrier density at 0 volt in the dark is subtracted. Similarly, as in the case of charge extraction also here the charge carrier density is underestimated by a factor of 10 or more due to charge carriers that recombine before they can be collected.

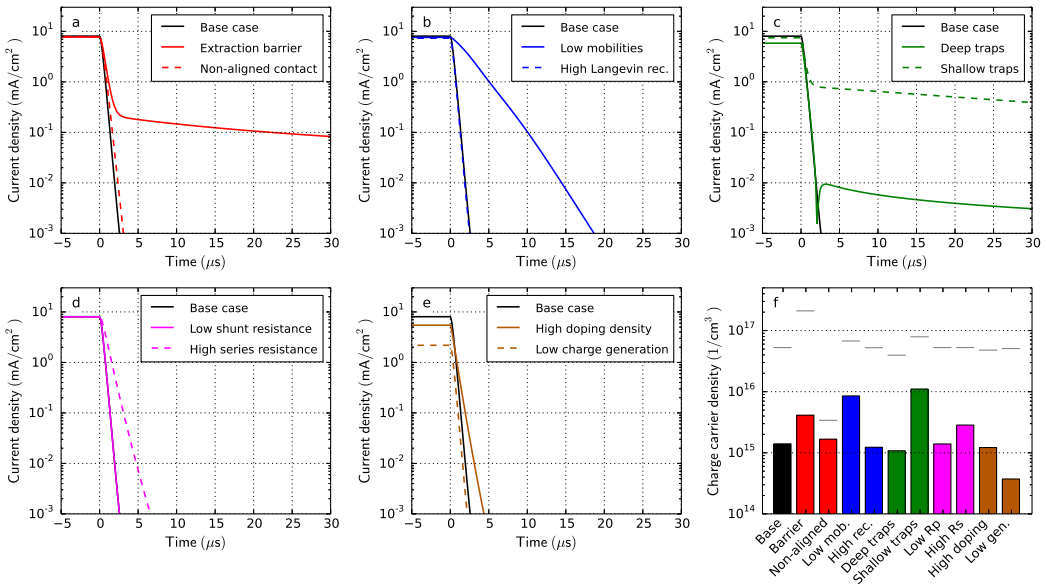

Figure 9.14: Transient photocurrent decay simulations for all cases in Table 9.1. The light is turned off at $t = 0$. f) Charge carrier density obtained from integration of the decay-current over time. The grey lines represent the effective charge carrier density from the simulated charge carrier profiles at short-circuit.

9.4.11 *Charge extraction*

Charge extraction (CE) was introduced by Duffy *et. al.* [178] in 2000 to measure the charge carrier density in dye-sensitised solar cells. It was applied to organic solar cells by Shuttle *et. al.* [179] and is frequently utilized to measure charge carrier density at varied light intensity [40, 41, 43, 180]. It is sometimes also referred to as photo-induced charge extraction (PICE) or time-resolved charge extraction (TRCE) [41]. When a negative extraction voltage is used it is referred to as bias amplified charge extraction (BACE) [181].

In the charge extraction experiment the solar cell is illuminated and the open-circuit voltage is applied such that no current flows (V_{oc}). In this state all charge carriers generated by light recombine. At $t = 0$ the light is switched off and simultaneously the voltage is set to zero (or reverse bias [181, 182]). The charge carriers are extracted by the built-in field and lead to a current. Integrating the extraction current over time yields the extracted charge. The charge carrier density n_{CE} is then calculated according to

$$n_{CE} = \frac{1}{d \cdot q} \cdot \left(\int_0^{t_e} j(t) \cdot dt - (V_a - V_e) \cdot C_{geom} \right) \tag{9.18}$$

where d is the device thickness, q is the unit charge, t_e is the extraction time (usually $1\,ms$ is sufficient), $j(t)$ is the transient current density, C_{geom} is the geometric capacitance, V_a the voltage applied prior extraction (in most cases V_{oc}) and V_e is the extraction voltage. The charge on the capacitance needs to be subtracted [182] because only the charge carrier density inside the bulk is of interest.

When the experiment is performed with varied delay time between light turn-off and charge extraction, CE can also be used to study recombination [41, 178, 182]. The technique is then very similar to CELIV with OTRACE [37] described in section 9.4.3 Charge extraction by linearly increasing voltage.

Figure 9.15 shows simulation results of charge extraction with varied light intensity for all cases. Changing the mobility or the recombination pre-factor changes the open-circuit voltage V_{oc} but has no major influence on the relation charge carrier density versus the V_{oc} (b). The thin grey line is the theoretical open-circuit voltage from a zero dimensional model assuming equal electron and hole densities (see Equation 9.10 in subsection 9.4.6). At high light intensity the trend agrees well with the simple model. At low light intensity the zero-dimensional model fails due to stronger spatial separation of electrons and holes.

The case *deep traps* (c) has a similar n vs V_{oc} curve. The *shallow traps* (c) however lead to a higher density of extracted charges. Trapped charge carriers are "protected" from recombination. Therefore, a higher charge density can accumulate at V_{oc}. The V_{oc} in the case *non-aligned contact* (a) is lower. More charge is required to reach the same V_{oc}. It is far away from the ideal curve shown in grey. The series resistance (d) has no influence on the extracted charge. The extraction current is slowed down, but the current-integral remains constant. Interestingly, the charge carrier density is much higher in the case *high doping density*. The device is p-doped, so there are less electrons under illumination compared to the un-doped

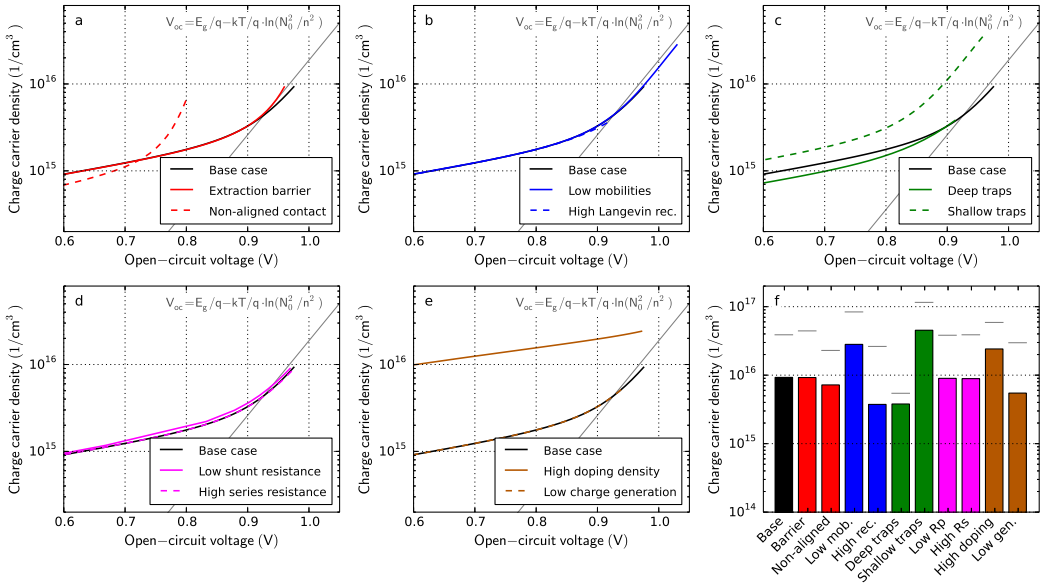

Figure 9.15: Charge extraction simulations for varied light intensity (and thus V_{oc}) for all cases defined in Table 9.1. The current is integrated over time according to Equation 9.18 to obtain the charge carrier density (the charge on the capacitance is subtracted). The light intensity is varied by five orders of magnitude. The grey-line is the theoretical V_{oc} for $n = p$ in a zero-dimensional model. f) Extracted charge carrier density at the highest light intensity. Grey lines represent the effective amount of photogenerated charge at open-circuit obtained from the simulated charge carrier profiles.

case. Under illumination the depletion region gets smaller and more holes can accumulate compared to the un-doped case.

In Figure 9.15f the extracted charge at the highest light intensity is compared to the effective photogenerated charge in the device at open-circuit. The extracted charge carrier density is in all cases lower than the effective charge carrier density at open-circuit. In our simulations between 15% to 70% of the charge is extracted (see grey line in Figure 9.15f). Applying a negative extraction voltage V_e reduces recombination losses [181, 182]. Indeed, in our simulations more charge is extracted (between 20% and 90% at $-3\,V$) using a negative extraction voltage.

Our case study is based on a device with a rather high Langevin recombination efficiency of 0.1. If Langevin recombination is turned down to 10^{-3} in our simulation more than 90% of the charge is indeed extracted. The accuracy of the charge extraction results therefore critically depends on the recombination.

9.4.12 *Impedance spectroscopy*

Impedance spectroscopy is a popular technique to investigate solar cells. It is abbreviated as IS or EIS (electro-chemical impedance spectroscopy). It is also called admittance spectroscopy (admittance is the inverse of the impedance). In impedance spectroscopy a small sinusoidal voltage $V(t)$ is applied to the solar cell according to

$$V(t) = V_0 + V_{amp} \cdot \sin(\omega \cdot t) \tag{9.19}$$

where V_0 is the offset voltage, V_{amp} is the voltage amplitude and ω is the angular frequency $2 \cdot \pi \cdot f$. If the voltage amplitude V_{amp} is small enough the system can be considered as linear therefore the current density $j(t)$ is also sinusoidal. The amplitude and the phase-shift of the current are analysed. Impedance spectroscopy is performed at various frequencies and/or offset voltages (see next section) and/or offset illuminations. Using the transient voltage and the transient current signal the complex impedance Z is calculated according to

$$Z = \frac{1}{Y} = \frac{\int_0^{N \cdot T} V(t) \cdot \exp(i \cdot \omega \cdot t) \cdot dt}{\int_0^{N \cdot T} j(t) \cdot \exp(i \cdot \omega \cdot t) \ \cdot dt} \tag{9.20}$$

where Y is the admittance, N is the number of periods, T is the period $1/f$, i is the imaginary unit and ω is the angular frequency. For the analysis of the impedance often the capacitance C and the conductance G are plotted versus frequency or offset voltage and are calculated according to

$$C = \frac{1}{\omega} \cdot Im\left(\frac{1}{Z}\right) \tag{9.21}$$

and

$$G = Re\left(\frac{1}{Z}\right) \tag{9.22}$$

where ω is the angular frequency, $Im()$ denotes the imaginary part and $Re()$ the real part.

Usually impedance spectroscopy data is plotted in the so-called Cole-Cole plot. Here the real and imaginary part of the impedance Z are plotted in the complex plane for the different frequencies. Alternatively, the capacitance C is plotted versus the frequency.

One of the main advantages using impedance spectroscopy is that effects occurring on different timescales can be separated. Trapping and de-trapping for example occurs usually on longer timescale (lower frequency) compared to transport of free carriers.

Most commonly impedance spectroscopy data is analysed using equivalent circuits. Thereby electric circuits are constructed from resistors, capacitors, inductors and further electric elements such that the measured frequency-dependent impedance can be reproduced [183–187]. The disadvantage of equivalent circuits is that the results can be ambiguous and the parameters cannot be directly associated with macroscopic material parameters.

Knapp and Ruhstaller solved the drift-diffusion equations with a small signal analysis to simulate impedance spectroscopy data [121, 188]. Here physical parameters are used as simulation input that allow direct interpretation of the results. The same approach is implemented in the software *Setfos* [111] that we apply in this study.

Measuring the capacitance is a way to probe the occupation of trap sites due to space charge effects [189]. Slow traps can increase the capacitance at low frequencies as shown by numerical simulation [121, 188]. Also slow ionic charges which might be present in perovskite solar cells can lead to an increase of the capacitance at low frequencies [95, 186]. Recombination of charge carriers leads to a decrease in the capacitance – it can even become negative. Also self-heating of a device can lead to a negative capacitance as analysed by Knapp and Ruhstaller [190]. A positive capacitance means that the phase-shift between voltage and current is positive (voltage leading the current), a negative capacitance means that the phase-shift becomes positive (current leading the voltage).

The real part of the impedance at low frequency coincides with the inverse of the current slope in the JV-curve at the same offset-voltage. If the probing frequency is low enough one basically measures the DC properties. Thus, an JV-curve can be used as consistency check of the impedance measurement. From low-frequency impedance data the JV-curve can be reconstructed without using equivalent circuits [183].

Figure 9.16 shows impedance simulations of all cases. In the *base* case mainly RC-effects are observed. Due to the background illumination the capacitance is however slightly higher than the geometric capacitance of $27\,nF/cm^2$. A large amount of charge in the bulk leads to a reduced depletion region – and consequently to a higher capacitance. The extraction barrier (a), the low mobility (b), traps (c) or doping (e) therefore lead to an increase in the capacitance under illumination. In the case *deep traps* and *shallow traps* (c) this capacitance rise occurs only at low frequency. If the probing frequency is too high charges cannot be trapped and de-trapped during one period. These slow traps are therefore invisible at high frequencies (for example at $100\,kHz$ in plot Figure 9.16c). With shallow traps the de-trapping is much faster – therefore the capacitance-rise happens already at faster timescale.

In all cases the capacitance decreases at frequencies above $1\,MHz$ due to RC-effects. In the case with a higher series resistance (d) the capacitance-decrease shifts

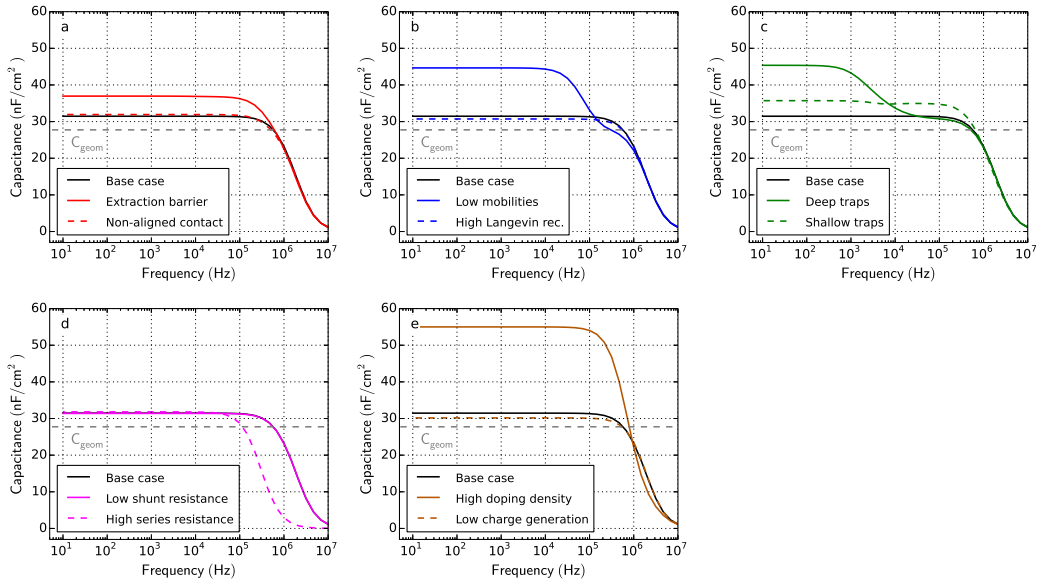

Figure 9.16: Impedance simulations for all cases in Table 9.1. The capacitance C is calculated according to Equation 9.21. The offset-voltage is 0 and offset-light is turned on. The dashed grey line represents the geometric capacitance.

to lower frequencies due to a higher RC-time. The impedance of the RC-effects Z_{RC} can be calculated according to

$$Z_{RC}(\omega) = R_S + \frac{1}{i \cdot \omega \cdot C_{geom}} \tag{9.23}$$

where R_S is the series resistance, i the imaginary unit, ω the angular frequency and C_{geom} the geometric capacitance. Using Equation 9.23 the series resistance and the geometric capacitance can be determined from a capacitance-frequency plot in the dark.

Cole-Cole Representation: In Figure 9.17 the same impedance spectroscopy data as in Figure 9.16 is shown in the Cole-Cole representation where the real part of the impedance is plotted on the x-axis and the imaginary part on the y-axis. In most cases one or more semicircles arise in this representation. Often the size of the semicircle is attributed to recombination in the device. The case *high Langevin recombination* (b) shows however a larger semicircle than the *base* case. The size of the semicircle depends apparently on more factors than just the recombination. With traps, with the extraction barrier or with doping two semicircles show up in our simulations.

From our simulation results we conclude that many effects influence the size of the semi-circle in the complex plane. We therefore advise to interpret such results carefully.

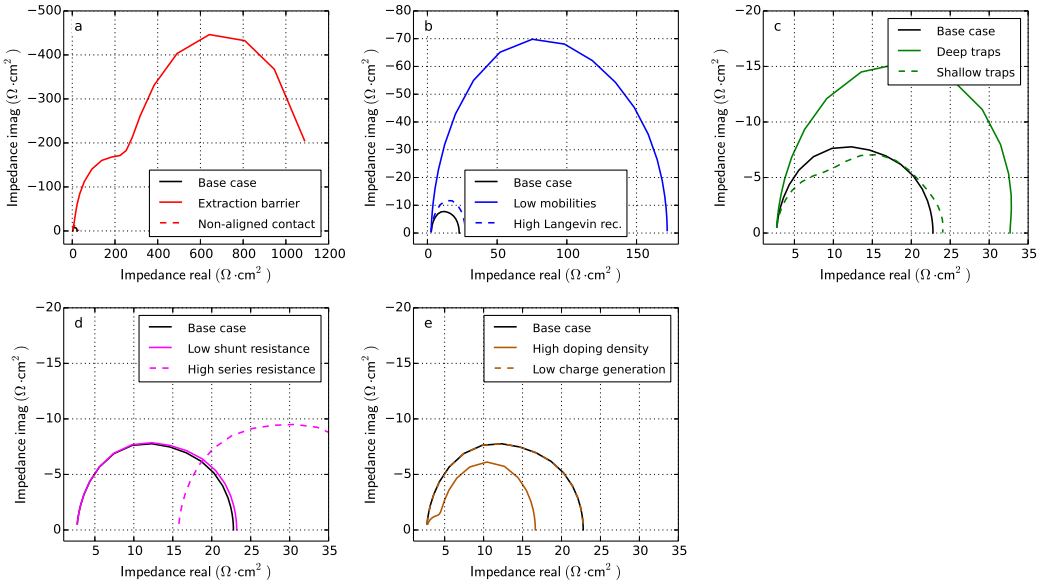

Figure 9.17: Impedance spectroscopy simulation for all cases in Table 9.1 in Cole-Cole representation.

9.4.13 *Capacitance-voltage*

In capacitance-voltage (CV) measurements the impedance is measured at constant frequency and the offset-voltage is varied. The capacitance is calculated according to Equation 9.21. To measure CV usually frequencies below $50\,kHz$ are used. In most diode-like devices, CV shows a peak at forward voltage. The position of this peak is usually independent of the probing frequency and independent of the device thickness [191]. The peak voltage is usually smaller than the built-in voltage [192] and it can be regarded as an effective value for the conduction onset [193]. The height and the voltage of the capacitance-peak is related to carrier injection [194] (the injection barriers and the built-in voltage). In bipolar devices like solar cells the capacitance-peak cannot be directly related with an analytical expression as shown for unipolar devices [192].

The increase of the capacitance is caused by a space-charge effect. When the voltage increases charges are injected and the depletion width decreases – leading to an increase in capacitance. After a certain voltage conduction starts and the capacitance decreases again and can even get negative. Negative capacitances can be caused by recombination or self-heating [190].

CV can be used to monitor the change of injection barrier for example during degradation [116, 132, 195, 196]. In bilayer devices CV can result in a plateau instead of a peak as observed for Alq_3/NPB devices [131, 196]. At a certain voltage charge carriers are injected into one of the two layers. When one layer is flooded with carriers only the *parallel plate* capacitance of the remaining layers is observed leading to a higher capacitance plateau until charges are injected into the second layer as well. The effect is observable as long as the injection into the two layers occurs at different voltages. Materials with a permanent dipole moment facilitate different electron and hole injection voltages in bilayer devices. Using CV the macroscopic polar sheet charge of such materials can be determined [197].

Figure 9.18 shows CV simulations of all cases. Significant changes in the peak voltage are only observed in the cases where the charge injection is changed. The case *non-aligned contact* (a) has a lower built-in voltage which leads to a decrease of the peak-voltage. The case *extraction barrier* (a) has the same built-in voltage but an additional barrier to overcome and thus the CV peak is shifted to higher voltages. In all other cases only a slight change in CV peak voltage is observed. CV seems therefore suited to investigate charge injection and the built-in voltage.

9.4.14 *Mott-Schottky analysis of capacitance-voltage measurements*

Mott-Schottky analysis is a popular technique applied to CV data to extract the doping density and the built-in voltage using the relation

$$\frac{1}{C^2} = \frac{2}{S^2 \cdot \epsilon \cdot q} \cdot \frac{1}{N_A} \cdot (V_{bi} - V) \tag{9.24}$$

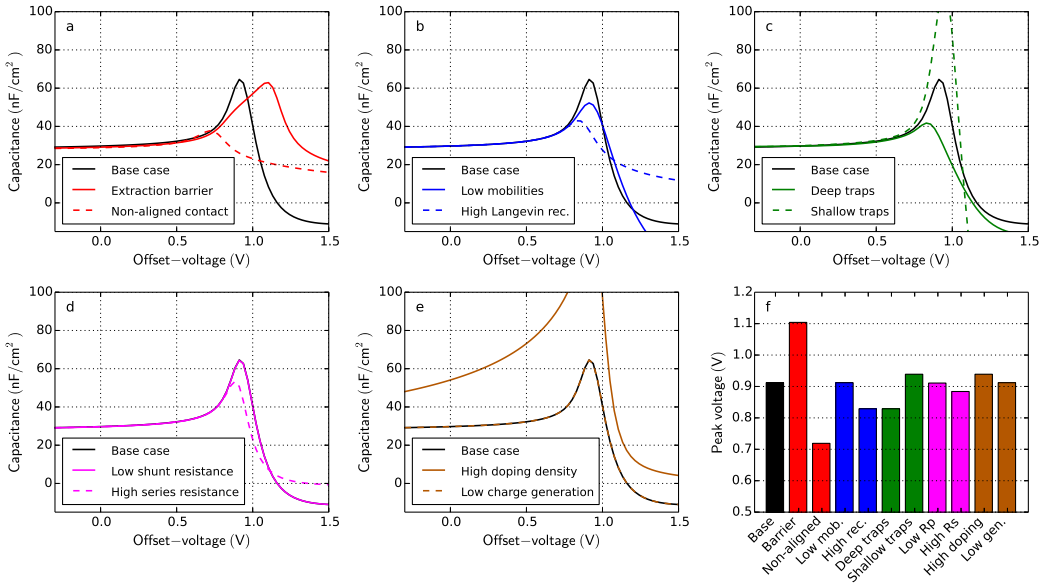

Figure 9.18: Capacitance-voltage simulations for all cases in Table 9.1 without offset illumination. The capacitance C is calculated according to Equation 9.21. The frequency is kept constant at $10\,kHz$. f) Voltage where the capacitance reaches a maximum.

where C is the capacitance, S is the device area, ϵ is the permittivity, q is the unit charge, N_A is the doping density in the bulk and V_{bi} is the built-in voltage. The quantity $1/C^2$ is linear with the voltage and allows one to determine the doping density N_A and the built-in voltage. It has however been shown that the analysis returns erroneous results in thin semiconductors. Kirchartz *et. al.* simulated an un-doped device with $100\,nm$ thickness. The Mott-Schottky analysis of the simulated CV data resulted in an apparent doping density of $1 \cdot 10^{16}\,cm^{-3}$ even though no doping was assumed in the simulation [198] – a clear indication that the technique should not be used for thin semiconductor layers like organic solar cells.

Tripathi and Mohapatra proposed to use the relation $C^{-2/3}$ for the analysis of organic devices [191]. Their analysis is however based on the assumption of a unipolar device and is therefore also not suited for the analysis of solar cells. We propose to use dark-CELIV to estimate the lower limit of the doping density of organic solar cells.

The determination of the built-in potential with a Mott-Schottky analysis is also erroneous as shown by Mingebach *et. al.* [199]. Mott-Schottky analysis should only be performed on devices that are thick enough and highly doped.

9.4.15 *Intensity-modulated photocurrent spectroscopy*

In intensity-modulated photocurrent spectroscopy (IMPS) the device is illuminated with a modulated light intensity and the photocurrent is measured. The voltage is kept constant. The modulated light intensity $L(t)$ is described as

$$L(t) = L_0 + L_{amp} \cdot \sin(\omega \cdot t) \tag{9.25}$$

where L_0 is the offset light intensity, L_{amp} is the amplitude of the modulation (typically $5\% - 10\%$ of L_0) and ω is the angular frequency $2 \cdot \pi \cdot f$. Like in impedance spectroscopy the theory for IMPS is based on the linearization of the device at a working point, which is valid as long as the light intensity amplitude L_{amp} is small enough. In this case also the current is sinusoidal and the phase shift and amplitude are studied. The complex IMPS quantity Z_{IMPS} is calculated according to

$$Z_{IMPS} = \frac{\int_0^{N \cdot T} j(t) \cdot \exp(i \cdot \omega \cdot t) \ \cdot dt}{\int_0^{N \cdot T} L(t) \cdot \exp\left(i \cdot \omega \cdot t\right) \ \cdot dt} \tag{9.26}$$

where N is the number of periods, T is the period $1/f$, i is the imaginary unit and ω is the angular frequency. The concept and analysis of IMPS are similar to impedance spectroscopy – in impedance spectroscopy the voltage is modulated and in IMPS the light is modulated.

In 1985 the first IMPS theory was introduced by Li and Peter to describe semiconductor-electrolyte interfaces [200]. It was later refined and frequently used to characterise dye-sensitised solar cells (DSSC) [201–204]. For the analysis of IMPS data a transport time-constant τ_{tr} is calculated according to

$$\tau_{tr} = \frac{1}{2 \cdot p \cdot f_{peak}} \tag{9.27}$$

where f_{peak} is the frequency where the imaginary part of the IMPS quantity reaches a maximum. In dye-sensitised solar cells the electron diffusion coefficient is calculated from the transport time-constant ($D_n = d^2/(2.35 \cdot \tau_{tr})$) [203]. In DSSC there is the common assumption of a fully screened electric field by the ionic charge of the electrolyte. Therefore, electron diffusion dominates transport and can be characterized by IMPS. In organic and other third generation solar cells this assumption does not hold. In this case there is no mathematical framework available yet for the analysis of IMPS measurements. In degraded organic solar cells, a negative phase shift was observed at certain frequency ranges – meaning that the current leads the illumination. Set *et. al.* used drift-diffusion simulations to show that negative IMPS phase shifts are caused by trap-assisted recombination [205]. Indeed, in our model we observe minor negative phase shifts only for the case with deep traps at low light intensity. At low frequency the real part of the IMPS signal equals the steady-state photocurrent [204].

IMPS has also been applied as imaging technique to study morphological phases in bulk-heterojunction solar cells [206]. In perovskite solar cells a second peak at 10 Hz was observed and attributed to ionic motion [207]. This finding is confirmed in chapter 11 of this thesis.

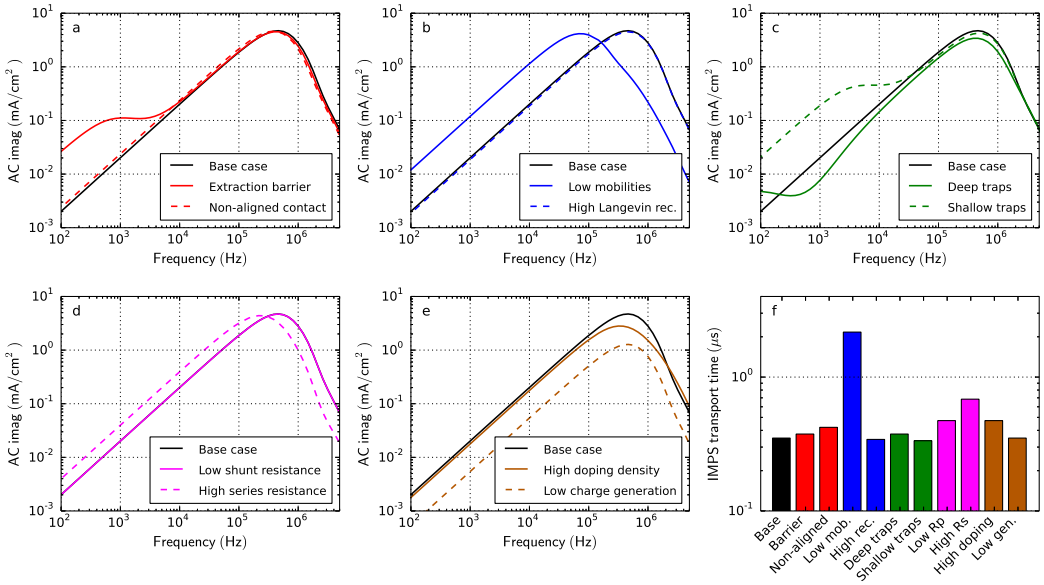

Figure 9.19: IMPS simulations for all cases in Table 9.1 with low offset light intensity (3.6 mW/cm^2). The offset voltage is zero. f) IMPS transport time-constant calculated according to Equation 9.27.

Figure 9.19 shows the imaginary part of the IMPS simulations for all cases. In all cases a peak at high frequency is observed. It can be related to charge transport – only the case *low mobilities* (b) leads to a significantly longer transport time-constant and thus the peak shifts to lower frequency. Trapping and de-trapping (c) as well as an extraction barrier (a) can lead to an additional peak/shoulder at low frequency. The series resistance slows down charge transport (d) as in all transient experiments, thus shifting the peak to lower frequency. All other cases show no distinct features.

In certain measurements two peaks in IMPS are observed. If the electron and hole mobilities are imbalanced, two peaks can arise as we show in section 9.5 Imbalanced electron/hole mobilities.

9.4.16 *Intensity-modulated photovoltage spectroscopy*

In intensity-modulated photovoltage spectroscopy (IMVS) the illumination is modulated and the device is kept at open-circuit and the photovoltage is measured. IMPS and IMVS are closely related. In IMPS the voltage is constant and the sinusoidal current is measured. In IMVS the current is zero and the sinusoidal voltage is measured.

Classically, from IMVS measurements the charge carrier lifetime is extracted using the frequency where the imaginary part reaches a minimum [204, 208, 61]. As outlined in the section on transient photovoltage (subsection 9.4.7) the quantity charge carrier lifetime is not physically meaningful in p-i-n structured devices. Our simulation results show that at open-circuit the device behaviour is not only governed by recombination (as commonly expected) but also by charge transport, which is in line with findings of Street [175]. Up to now there is no straight-forward interpretation of IMVS measurement results.

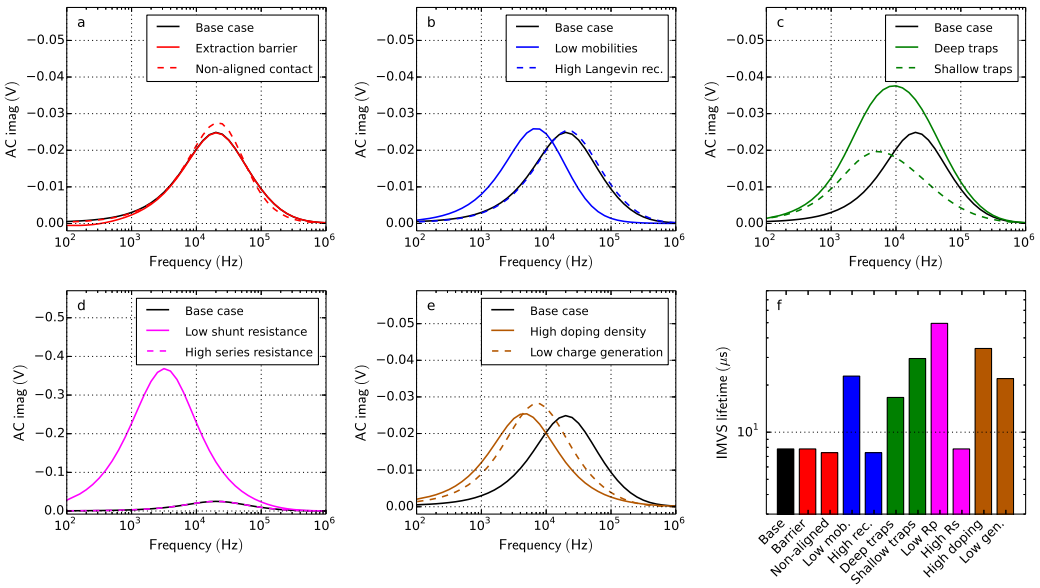

Figure 9.20: Simulation of IMVS for all cases defined in Table 9.1. The offset light intensity is 3.6 mW/cm^2 and light modulation amplitude is 20% of the offset light intensity. f) IMVS charge carrier lifetime extracted from the peak frequency.

In Figure 9.20 IMVS simulation results are shown for all cases. Figure 9.20f shows the charge carrier lifetime calculated from the frequency of the IMVS peak. It might seem surprising that the case *high Langevin recombination* (b) has a peak at the same frequency and consequently the same charge carrier lifetime. The reason is that the V_{oc} of the case *high Langevin recombination* is lower at this light intensity. Plotting the charge carrier lifetime versus the V_{oc} is more conclusive, as we show in the section 9.4.7 Transient photovoltage and charge carrier lifetime. Our simulation results show that charge carrier lifetimes extracted from IMVS and TPV are fully consistent.

9.4.17 *Double injection transients*

In double injection transients (DoI) the current response to a voltage step is measured. Compared to dark injection transients this technique is applied to ambipolar devices where electrons and holes can be injected. It leads to a slow current rise until steady-state is reached. The electron mobility, hole mobility and recombination pre-factor determine the current rise dynamics and can be estimated by formulas [49, 209].

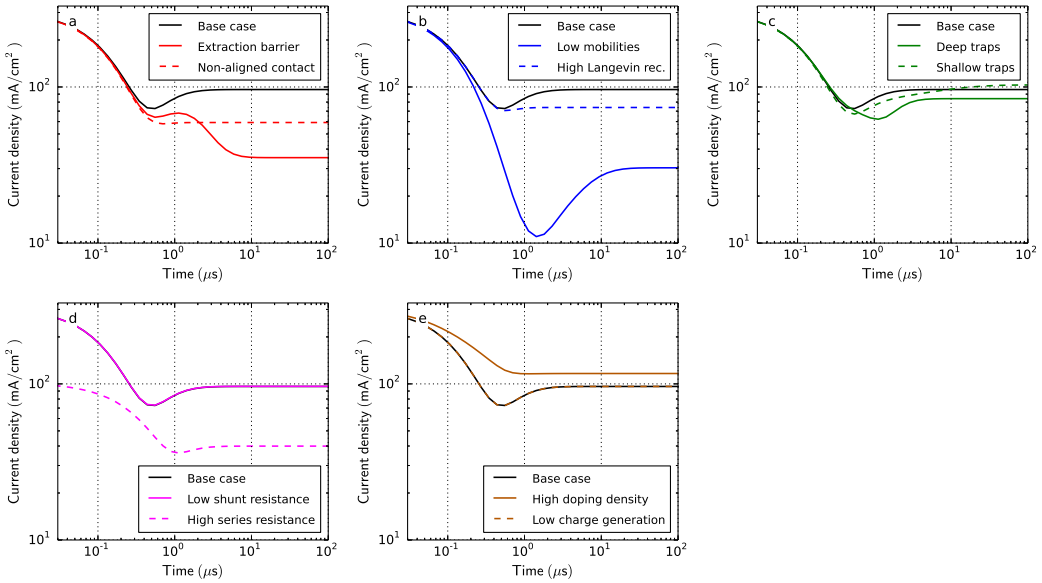

Figure 9.21: Double injection transient simulations for all cases in Table 9.1. At $t = 0$ the voltage steps from $0\,V$ to $2\,V$. The simulation is performed in the dark.

Figure 9.21 shows DoI simulations of all cases. Below $0.2\,\mu s$ the current signal is dominated by the displacement current caused by RC-effects. In most cases it is followed by a slow current rise up to steady-state. The rise-time is related to charge transport and recombination. In the case *low mobilities* the rise is therefore much slower compared to the *base* case. Also the shallow and the deep traps lead to a slower current rise. In the cases *high doping density*, *non-aligned contact* and *high Langevin recombination* the current rise it too fast and hidden in the RC-effects.

9.4.18 *Open-circuit voltage versus temperature*

Measuring the open-circuit voltage V_{oc} down to low temperatures is an effective technique to estimate the built-in voltage [199]. Figure 9.22 shows simulations of V_{oc} versus temperature. Apart from the case *extraction barrier* all curves reach exactly the built-in voltage at low temperature ($< 50\,K$). At such low temperatures the open-circuit voltage is limited by the built-in voltage only. This method however only works as long as there is no extraction barrier. In the case *extraction barrier* the V_{oc} collapses to zero because at low temperature the barrier cannot be overcome by charges.

If the contacts are perfectly aligned with the energy levels of the active layer, the V_{oc} would reach the band-gap energy at zero Kelvin. By linear extrapolation of the V_{oc} to 0 K the electrical band-gap can therefore be estimated. In Figure 9.22f we show the results of the extrapolation of the simulation data in the linear regime (250 K to 300 K). The effective band-gap of 1.57 eV (simulation input) is estimated accurately in all cases except for *extraction barrier* and *non-aligned contact*. In both cases the open-circuit voltage versus temperature is not yet in a linear regime at 300 K and higher temperatures would be required for the analysis.

We conclude that the band-gap estimation works precisely if the injection barriers are low. Furthermore, the built-in voltage can accurately be determined if a saturation of the open-circuit voltage is observed at low temperatures.

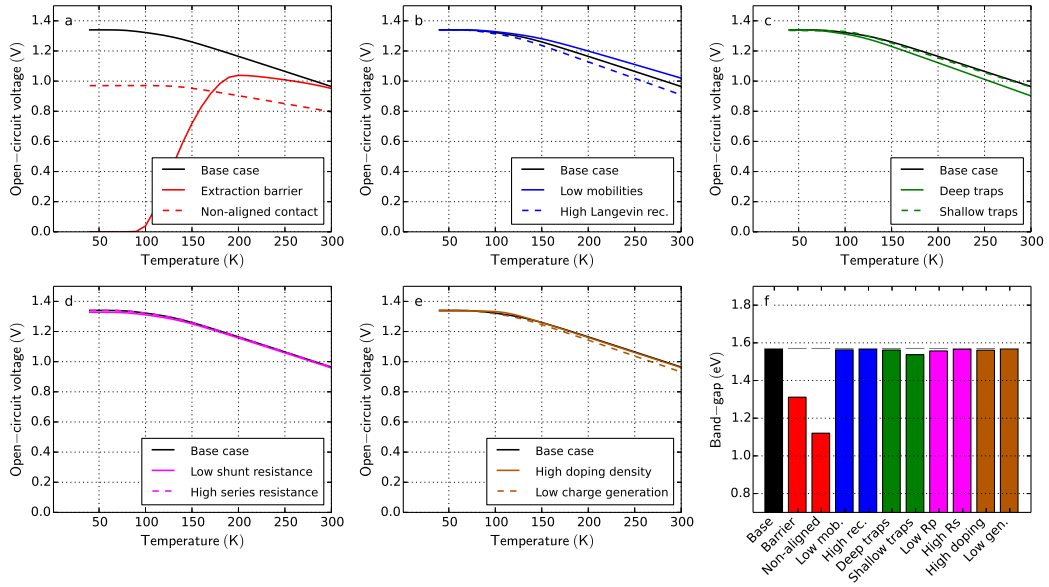

Figure 9.22: Simulation of open-circuit voltage versus temperature for all cases defined in Table 9.1. Apart of the case *extraction barrier* all cases reach exactly the built-in voltage at low temperature. f) Extrapolation of the linear regime at high temperature to 0 Kelvin. The effective band gap is 1.57 eV in all cases indicated by the grey lines.

9.4.19 *Further characterization techniques*

There are a number of further opto-electrical characterization techniques for solar cells that we describe here only briefly without being exhaustive.

Displacement current measurement (DCM) is a technique that is used to study the capacitance of multi-layered devices and estimate trap densities [195]. In DCM a triangular voltage is applied to the device in the dark in two cycles. Compared to CELIV in DCM the voltage ramp goes up and down such that both the injection and the extraction of carriers can be studied. When carriers are injected into one layer the capacitance of the multilayer system changes and so does the displacement current. Comparing the first and the second cycle allows one to estimate the trap density.

In **dark injection transients (DIT)** a voltage step is applied to a device and the transient current is measured. The device under investigation needs to be unipolar (only one charge carrier type can be injected) and good Ohmic contacts are required. A space-charge effect leads to a current overshoot. Therefore, this technique is also called transient space-charge-limited current (T-SCLC) in the literature. The time of the current overshoot is related to a transit time and allows the estimation of the charge carrier mobility and its field dependence [49, 210]. The occurrence of the current overshoot is a confirmation of good electrical contact for charge injection.

Differential charging combines small-perturbation transient photocurrent (TPC) and transient photovoltage (TPV) measurements. From the two experiments the differential capacitance $C = \Delta Q / \Delta V$ is calculated for varied light intensity. The integral reveals the charge carrier density at open-circuit [39, 44]. The charge ΔQ stems from the current-integral of TPC whereas the ΔV is the change in voltage in TPV. Both experiments are performed with offset-light and a small light pulse.

In **time-delayed collection field (TDCF)** the device is kept at a constant voltage when a short laser pulse is applied [211, 212]. After a delay-time a reverse bias is applied to extract the charge carriers. TDCF can be used to investigate the field dependence of charge generation and recombination. A low RC-time is required for this experiment.

Thermally stimulated current (TSC) is a technique to measure trap spectra in semiconductors. The device is illuminated and cooled down to very low temperatures ($< 50\,K$). Then the illumination is turned off and the device is slowly heated back to room temperature. The current resulting from trap emission is measured over time. Shallow traps are released at low temperatures and deeper traps are released at higher temperature. Trap density and trap energy levels can be estimated [213].

In **thermal admittance spectroscopy (TAS)** impedance spectroscopy is measured at different temperature levels. Similar to DLTS full trap spectra can be extracted analysing the capacitance-frequency relation [189]. It is also possible to determine activation energies for mobility and injection [158].

Transient absorption spectroscopy (TAS): This technique takes advantage of the fact that in some materials infrared light is absorbed by free charge carriers. The device is illuminated by infrared light (usually at a wavelength around $1000\,nm$) and the transmitted or reflected light is measured with a photo-detector. An additional optical light pulse creates charge carriers that are then monitored over time by the infrared light to investigate recombination dynamics [41, 44, 163].

Time-of-flight (TOF) is a technique to measure the charge carrier mobility in semiconductors [49, 209, 214]. A short laser pulse generates a small amount of charge carriers on one side of the semiconductor layer. Due to an applied voltage the charge carrier package drifts through the layer. From the transit time of the current the mobility is calculated. The advantage of the technique is that electron and hole mobilities can be measured separately. A disadvantage is that the technique requires thick samples ($> 1\,\mu m$) and blocking contacts. Therefore, it cannot easily be applied to regularly prepared solar cells [49].

9.5 IMBALANCED ELECTRON/HOLE MOBILITIES

A common limitation in organic solar cells is an imbalance of the electron and hole mobilities. In such a case the slower carrier accumulates and leads to space-charge. In Figure 9.23 we show simulations of a solar cell with imbalanced mobilities and compare them with the *base* case. In both cases the hole mobility is $4 \cdot 10^{-4}\, cm^2/Vs$. The electron mobility is $2 \cdot 10^{-4}\, cm^2/Vs$ in the *base* case and $2 \cdot 10^{-5}\, cm^2/Vs$ in the case *imbalanced mobilities*. In the case *imbalanced mobilities* the electron mobility is lower by a factor of 20 compared to the hole mobility.

As seen in the JV-curve (Figure 9.23a) the fill factor is reduced in the case *imbalanced mobilities*. The slow electrons accumulate whereas the fast holes are quickly extracted. The resulting space-charge screens the electric field and hence the driving force for charge extraction. Therefore, the performance of the device decreases.

In Figure 9.23b the transient photocurrent response (TPC) is shown. The initial current rise and decay is governed by the fast carrier type (holes). In the case *imbalanced mobilities* the current rise and decay shows a second, much slower component that is caused by the slower electrons. Two time-constants in TPC are an indication of imbalanced mobilities. A high charge carrier doping can however lead to a similar effect as shown in section 9.4.9 Transient photocurrent.

Figure 9.23c shows photo-CELIV simulations of both cases. In the case *imbalanced mobilities* the electrons are extracted later leading to a lower current peak and to a longer current tail. Whereas in the *base* case most charges are extracted after $6\,\mu s$, the charge extraction lasts longer than $12\,\mu s$ in the case *imbalanced mobilities*.

Figure 9.23d shows IMPS simulations of both cases. The different mobilities lead to two peaks with different time constants.

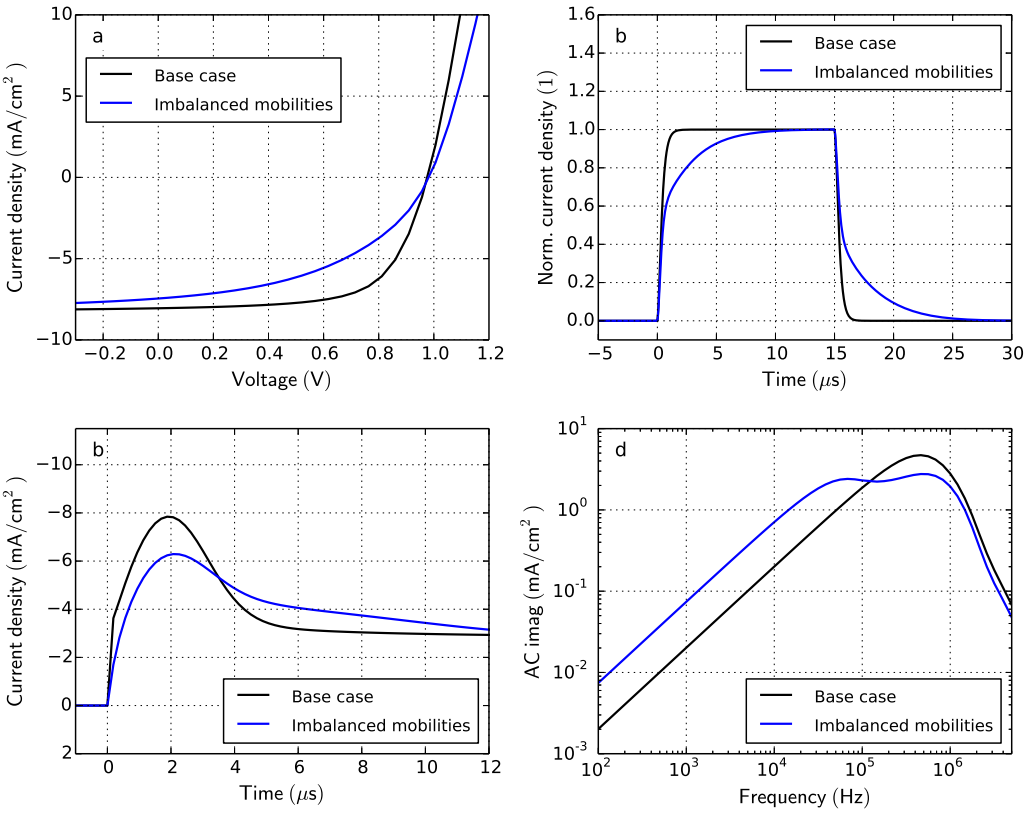

Figure 9.23: Simulation results of the *base* case and an additional case *imbalanced mobilities*. In both cases the hole mobility is $4 \cdot 10^{-4}\, cm^2/Vs$. The electron mobility is $2 \cdot 10^{-4}\, cm^2/Vs$ in the *base* case and $2 \cdot 10^{-5}\, cm^2/Vs$ in the case *imbalanced mobilities*. a) JV-curve simulations under illumination. b) Transient photocurrent simulations at 0 Volt. Light is turned on at $t = 0$ and turned off at $t = 15\,\mu s$. The photocurrent is normalized to 1. c) Photo-CELIV simulations. The light is turned off at $t = 0$ and the voltage ramp starts at $t = 0$ with a ramp rate of $100\, V/ms$. The voltage offset prior to the ramp is set such that the current is zero at $t < 0$. d) IMPS simulations. The offset light intensity is $3.6\, mW/cm^2$ and the light modulation amplitude is 20% of the offset light intensity.

9.6 COMPREHENSIVE PARAMETER EXTRACTION WITH NUMERICAL SIMULATION

In the previous sections we presented an overview over various measurement techniques for solar cells. Their interpretation allows mainly qualitative conclusions: devices can be compared and trends can be observed. When monitoring device ageing conclusions can be drawn regarding the physical origin of the degradation [116, 132, 138].

Organic and other third generation solar cells are devices with complex charge transport physics. Simple analytical device descriptions are often not capable to capture all relevant physical effects. Parameters can not easily be determined by simple methods. The analysis with analytical expressions as for photo-CELIV or for Mott-Schottky can lead to inaccurate results [115, 198, 199]. Fits with equivalent circuits to impedance spectroscopy data are ambiguous and physical interpretation can be arbitrary.

Extracting physically meaningful material parameters from these experimental techniques requires therefore numerical simulation. Numerical simulation provides a deeper understanding of the underlying physical processes.

Often JV-curves are fitted by simulation to extract charge transport parameters [113, 141–144]. We showed in a previous publication that fitting JV-curves is clearly insufficient to unambiguously determine physical parameters [34]. Our conclusions are consistent with Set *et. al.* demonstrating that parameter extracted from JV-curve fits are arbitrary [215]. The parameters are correlated – parameter 1 can have the same influence on the JV-curve as parameter 2. The influence of the different parameters on the result is highly entangled. Parameter correlation can be reduced by combining several experimental techniques [34]. The combination of a variety of experiments leads to a broader understanding, a higher accuracy and a quantitative description of a semiconductor device. The following study follows the approach of combining several experimental techniques for accurate parameter extraction for an organic polymer-fullerene solar cell.

9.6.1 *Device under investigation*

We perform measurements on an organic bulk-heterojunction solar cell comprising PCDTBT:$PC_{70}BM$ (weight ratio 1 : 4) as active material to demonstrate parameter extraction by numerical simulation. The device has the structure: ITO (130 nm) / MoO_3 (10 nm) / PCDTBT:$PC_{70}BM$ (85 nm) / LiF / Al (100 nm) and has a power conversion efficiency of 3.3%. The device was fabricated at Karlstad University [216]. Below we give further information on the used materials and sample preparation.

Materials: PCDTBT ($M_n = 19\,kg/mol$ and $M_w = 39\,kg/mol$) was purchased from Ossila Ltd, $PC_{70}BM$ (purity $> 99\%$) was purchased from Solenne BV. MoO_3 (99.98%) was purchased from Sigma-Aldrich. Chlorobenzene (analytical grade) was purchased from Merck KGaA and used as received. Patterned ITO-coated

glass substrates ($100\,nm$, $20\,\Omega/sq$) and light-curable encapsulation epoxy were purchased from Ossila Ltd.

Sample preparation: The solar cells were prepared on ITO-coated glass substrates that had been cleaned in isopropanol in an ultrasonic bath for $60\,min$ and subsequently UV-ozone treated for $20\,min$. An $8\,nm$ MoO_3 layer was deposited by thermal evaporation with a deposition rate of $0.04\,nm/s$ at $10^{-6}\,mbar$. A blend solution of PCDTBT:PC_{70}BM in a 1 : 4 weight/weight ratio, at a total concentration of $20\,mg/ml$, was prepared in chlorobenzene and filtered through a $0.45\,\mu m$ polytetrafluoroethylene (PTFE) filter directly before being deposited on top of the MoO_3 by spin coating at $750\,rpm$ for $100\,s$ in a protected N_2 atmosphere ($< 0.1\,ppm$ O_2, $< 0.1\,ppm$ H_2O) inside a glove box (M. Braun Inertgas-Systeme GmbH). The active layer thickness was measured by scanning across a scratch in the film with the tip of an AFM (Nanoscope IIIa Multimode, Veeco Metrology group, now Bruker Corporation). After spincoating the active layer, the samples were transferred to the vacuum chamber of a thermal evaporator (Univex 350 G, Oerlikon Leybold Vacuum GmbH) integrated in the glove box, where $0.3\,nm$ LiF and $100\,nm$ Al was deposited with a deposition rate of $0.05\,nm/s$ (LiF) and $0.1\,nm/s$ (Al) at $10^{-6}\,mbar$. Inside the glove box, the solar cells were encapsulated using encapsulation epoxy and glass coverslips. The epoxy was cured by exposure to UV-light (LV 202E, Mega Electronics) for $30\,min$ [216].

9.6.2 *Measurements and Simulation*

All measurements were performed on the very same solar cell, fully automated within 35 minutes such that unintentional degradation between different measurements or changes in ambient conditions can be minimized. The automated measurement without changing the contacting probes and measurement within a short period of time is important to obtain a fully consistent set of experimental data. We measured 4 nominally identical devices and found very good reproducibility. Here we show measurement data of one device. An IV-curve was measured at the beginning and at the end of the procedure to confirm that no degradation occurred during the measurement. All measurements were performed using the all-in-one measurement system Paios [110]. For the illumination in all experiments a white LED (Cree XP-G) is used.

The simulation model and all equations are described in the chapter 7 PHYSICAL MODEL. We use a rather *simple* model (discrete transport and trap energies) to keep the number of unknown parameters low. For the fitting the Levenberg-Marquardt [123, 124] algorithm is applied (see section 8.2.2 Levenberg-Marquardt for details).

We use the following procedure to obtain the simulation parameters:

1. The relative dielectric constant ϵ_r and the series resistance R_S are extracted from the capacitance-frequency plot. The values are cross-checked with the displacement current in dark-CELIV.

2. The parallel resistance R_P is determined from the reverse current of the dark JV-curve and can be cross-checked with the conductance of impedance spectroscopy data.

3. The photon-to-charge conversion efficiency η_{p2c} is estimated from the short-circuit current.

4. Electron and hole mobilities are fitted to the normalized transient photocurrent rise and decay.

5. The injection barriers and the built-in voltage are fitted to the illuminated JV-curve and CV measurements.

6. The recombination pre-factor is adjusted to the CELIV-peak current.

7. Global fitting is performed for fine-tuning the parameter set. The parameters from step 1-3 (ϵ_r, R_S, R_P and η_{p2c}) were fixed during the global fitting routine.

9.6.3 *Measurement and Simulation Results*

Figure 9.24 shows an overview of 9 experimental techniques with measurement and simulation. For all simulations the same material and device parameters are used, as summarized in Table 9.2. The simulation results (red curves) match the measurement data (black curves) very well. To the best of our knowledge it is the first time that such a comprehensive description of an organic solar cell is published.

The illuminated JV-curve (Figure 9.24a) shows a slightly stronger voltage-dependence of the photocurrent than reproduced by simulation. This could be caused by field-assisted exciton dissociation (Onsager-Braun) [148, 211] which was not included in the simulation but could be activated in the model for further refinement [113]. The dark JV-curve (Figure 9.24b) is well-described by the simulation. The open-circuit voltage dependence on light intensity (Figure 9.24c) shows an ideality factor of 1.2 to 1.5. Namkoong *et. al.* [217] determined an ideality factor of 2.0 for a device with the same active layer. Such ideality factors can only be reproduced by introducing traps with SRH-recombination in the simulation model.

In the dark-CELIV (Figure 9.24d) no current-overshoot is observed indicating little or no doping. The current is mainly determined by RC-effects that are well-reproduced by the simulation. The photo-CELIV (Figure 9.24d) signal shows only a small overshot due to the high Langevin recombination in this system. The shape of the open-circuit voltage decay (OCVD), shown in Figure 9.24f, is influenced by the amount of SRH-recombination and is reproduced well by the simulation for high ($L = 72\,mW/cm^2$) and low ($L = 0.7\,mW/cm^2$) light intensity (note the logarithmic time-scale). The voltage decay starting at $1\,ms$ is caused by the measurement resistance of $1\,M\Omega$ which is also considered in the simulation. Figure 9.24g shows transient photocurrents for two different light intensities. The shape of current rise and decay is mainly influenced by the electron and hole

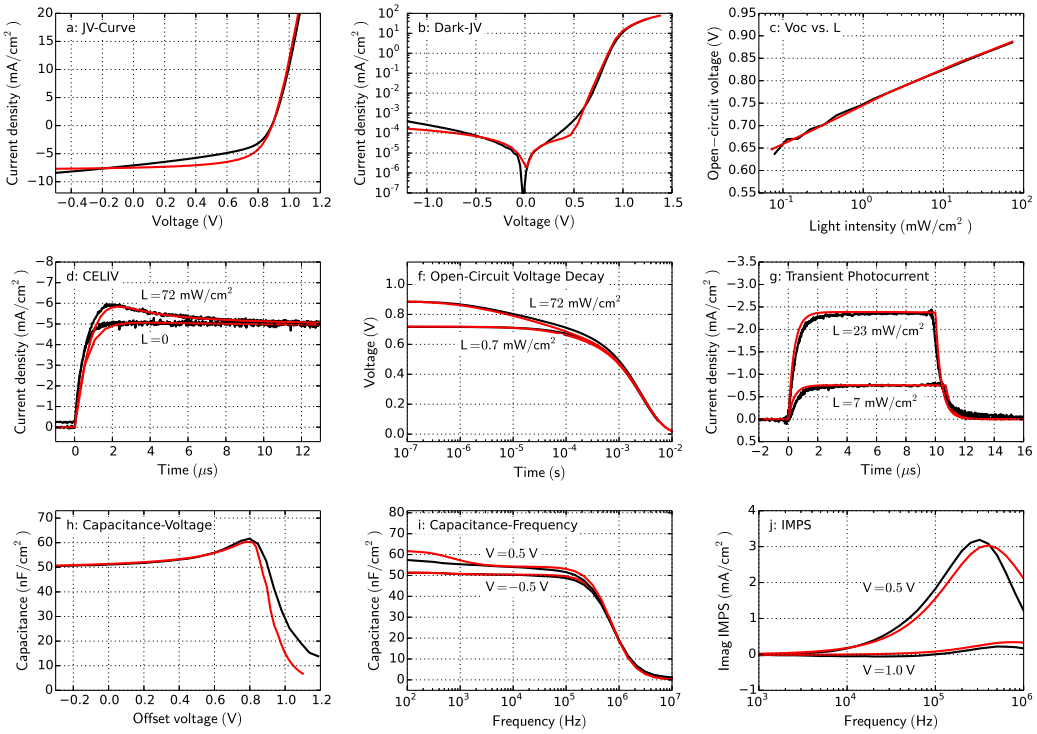

Figure 9.24: Measurements of an organic PCDTBT:$PC_{70}BM$ solar cell (black) and drift-diffusion simulation results (red). a) JV-curve under illumination ($L = 72\,mW/cm^2$). b) dark JV-curve. c) Open-circuit voltage for varied light intensity. d) Dark-CELIV ($L = 0$) and photo-CELIV ($L = 72\,mW/cm^2$) with ramp rate $100\,V/ms$. Light is turned off at $t = 0$. f) Open-circuit voltage decay for two light intensities. Light is turned off at $t = 0$. g) Transient photocurrent for two light intensities. Light is turned on at $t = 0$ and turned off at $t = 10\,\mu s$. h) Impedance spectroscopy at $10\,kHz$ with varied offset-voltage. i) Impedance spectroscopy at constant voltage with varied frequency. j) Intensity-modulated photocurrent spectroscopy (IMPS) with constant offset voltage. Simulation parameters are summarized in Table 9.2.

mobility and are well reproduced by the simulation. The peak in capacitance-voltage (Figure 9.24h) is reproduced well by the simulation. There is however a small deviation in the injection regime ($> 0.8\,V$) that we cannot clearly attribute to a certain effect. Impedance spectroscopy data is shown in Figure 9.24i for two offset-voltages. The capacitance decay at high frequency ($> 300\,kHz$) is caused by the series resistance. The simulation reproduces the difference in capacitance for offset-voltages of $-0.5\,V$ and $+0.5\,V$. The trapping leads to an increased capacitance at low frequency in the simulation that is slightly overestimated compared to the measurement. Discrete energy levels are used to describe the traps. A broader trap-distribution could reproduce the capacitance increase at low frequency more accurately [189]. Figure 9.24j shows intensity-modulated photocurrent spectroscopy (IMPS) data for two different offset-voltages. The IMPS data was not included in the fitting. The parameters determined from the fit were used to simulate IMPS data as a cross-check. Indeed, the measurement and simulation of

the IMPS signal fit reasonably well – a further indication for the validity of the approach for parameter extraction presented here.

9.6.4 *Parameter correlation*

To quantify the parameter correlation of the simulation result a correlation analysis is performed. The calculation of the correlation matrix is described in section 8.2.3 Parameter correlation. If the correlation is 1.0 or -1.0 parameters are fully correlated. If the correlation is zero they are not correlated and fully independent.

The correlation matrix of the simulation in Figure 9.24 is shown in Figure 9.25. The diagonal of the correlation matrix is always one, since each parameter fully correlates with itself. Most parameters show only a very weak correlation with other parameters. The average correlation is 0.13. There are a few exceptions that show significant correlation. For example, the electron capture rate of the trap c_e correlates with the density of chargeable sites N_0. This can be explained looking at the governing equations in chapter 7 PHYSICAL MODEL: Trap release to the LUMO-level is proportional to $c_e \cdot N_0$. Both parameters therefore have the same influence on the trap release current.

For comparison, we calculated the correlation matrix of only the illuminated JV-curve (Figure 9.24a). The correlation matrix is shown in Figure 9.26. Here most parameters are highly correlated with other parameters and not a single parameter is independent. The average correlation is 0.50. Such a result indicates that the extracted parameters are not unique and a fit would therefore not be reliable. Comparing the two correlation matrices (Figure 9.25 and Figure 9.26) it is clear that combining several experimental techniques reduces the correlation significantly.

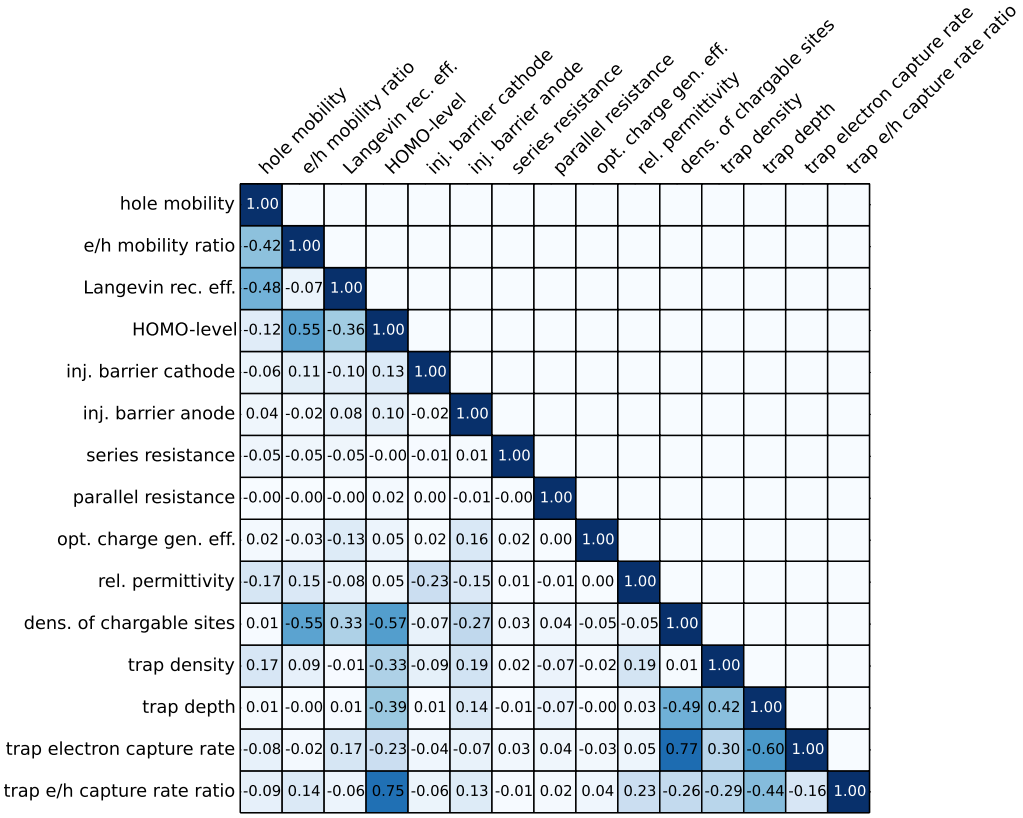

Figure 9.25: Correlation matrix of the simulation results of Figure 9.24. Experiments included in the calculation of the correlation matrix are: JV under illumination, dark-JV, V_{oc} versus light intensity, dark-CELIV, photo-CELIV, OCVD, TPC, CV and C-f.

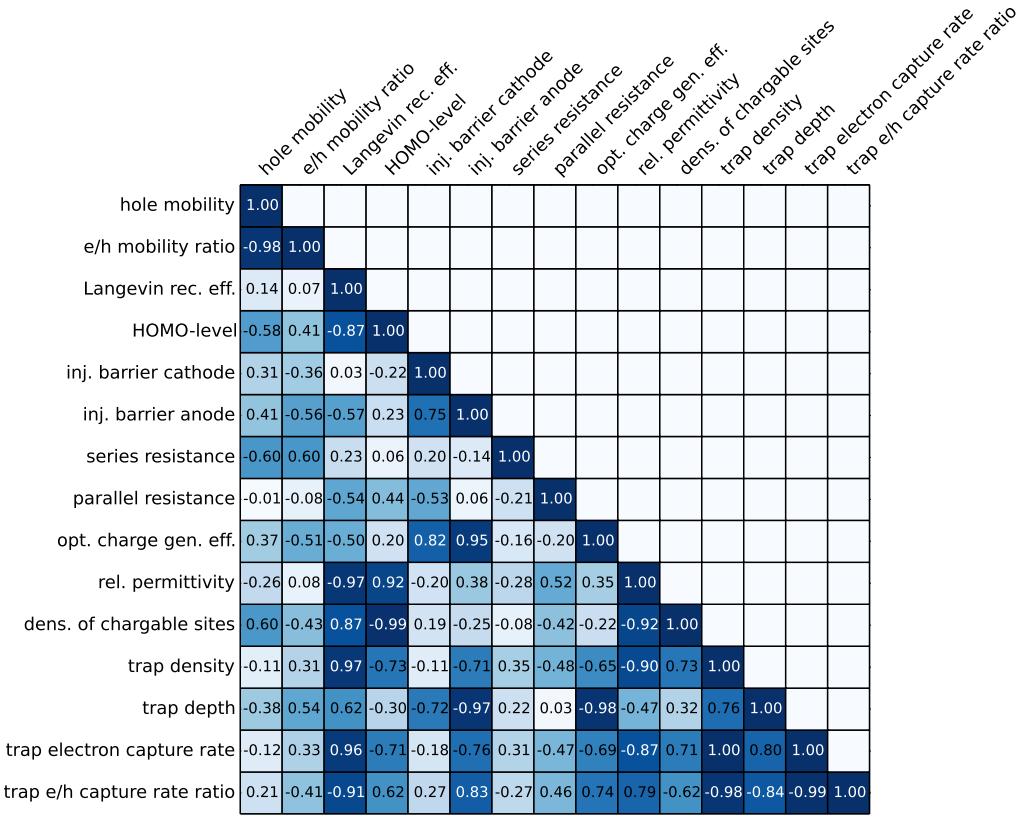

Figure 9.26: Correlation matrix of the simulation results in Figure 9.24 using only the illuminated JV-curve.

9.6.5 *Extracted Parameters*

Parameter	Symbol	Value	Obtained by
Device thickness	d	$85\,nm$	Measured by AFM
Device area	S	$0.045\,cm^2$	-
Series resistance	R_S	$90\,\Omega$	High frequency range of capacitance-frequency plot
Parallel resistance	R_P	$160\,M\Omega$	Reverse current of dark JV-curve
Relative permittivity	ϵ_r	4.7	Capacitance level in capacitance-frequency plot and dark-CELIV
LUMO	E_{LUMO}	$3.8\,eV$	-
HOMO	E_{HOMO}	$5.37\,eV$	fit
Band-gap energy	E_g	$1.57\,eV$	-
Workfunction MoO_3	Φ_A	$5.22\,eV$	fit
Workfunction Al	Φ_C	$3.88\,eV$	fit
Built-in voltage	V_{bi}	$1.34\,V$	-
Effective density of states	N_0	$1.5 \cdot 10^{21}\,cm^{-3}$	fit
Electron mobility	μ_e	$1.6 \cdot 10^{-3}\,cm^2/Vs$	fit
Hole mobility	μ_h	$8 \cdot 10^{-4}\,cm^2/Vs$	fit
Langevin recombination efficiency	η	1.0	fit
Photon to charge conversion efficiency	η_{p2c}	0.37	Adjusted to match the short-circuit current
Electron trap density	N_t	$1 \cdot 10^{17}\,cm^{-3}$	fit
Electron trap depth	E_t	$0.4\,eV$	fit
Electron trap – electron capture rate	c_e	$1 \cdot 10^{-11}\,cm^3/s$	fit
Electron trap – hole capture rate	c_h	$3.2 \cdot 10^{-10}\,cm^3/s$	fit

Table 9.2: Parameters that were used to simulate all experiments in Figure 9.24.

The parameters determined from the fit are shown in Table 9.2 and allow conclusions about the material system under investigation. The system has high and balanced charge carrier mobilities leading to efficient transport. The mobilities observed here are higher than reported for similar material systems ($5 \cdot 10^{-5}\,cm^2/Vs$ by CELIV and TOF [50] and $3 \cdot 10^{-4}\,cm^2/Vs$ by SCLC and DIT

[210]). The reason might be the different morphology due to different processing. The Langevin pre-factor is 1.0, resulting in efficient recombination. It is consistent with the findings of Clarke *et. al.* who determined a Langevin pre-factor between 0.3 and 1.0 for PCDTBT:PCBM which is common in polymer-fullerene material combinations [50]. An exception is P3HT:PCBM that shows a strongly reduced Langevin recombination with a pre-factor lower than 0.001 [39, 209]. There seems to be no doping but a considerable density of electron traps leading to efficient recombination paths. Significant trap-assisted recombination has also been reported by Li and McNeill [218] and Clarke *et. al.* [50] for PCDTBT:fullerene solar cells.

The photon-to-charge conversion efficiency is very low in this study. It can however also be caused by inaccuracies in the determination of the light intensity in our setup. There is evidence for field-dependent exciton dissociation that lowers the photocurrent. The energy alignment of the contact materials to the HOMO and LUMO levels is very good leading to a high built-in voltage of $1.34\,V$ and consequently to a high V_{oc}.

The simulation and measurement results presented in this section show that material systems like PCDTBT:$PC_{70}BM$ can be described well even with a rather simple drift-diffusion model employing discrete transport and trap levels and Ohmic injection. All the main features observed in the experimental techniques can be reproduced. The simulation results provide physical insight and help to gain a better understanding of novel material systems and device concepts.

9.7 SUMMARY

We present an overview of opto-electrical characterization techniques for solar cells, namely dark-CELIV, photo-CELIV, open-circuit voltage decay (OCVD), transient photovoltage (TPV), deep-level transient spectroscopy (DLTS), transient photocurrent (TPC), charge extraction (CE), impedance spectroscopy (IS), capacitance-voltage (CV), intensity-modulated photocurrent spectroscopy (IMPS), intensity-modulated photovoltage spectroscopy (IMVS), dark JV-curves, open-circuit voltage versus light intensity and open-circuit voltage versus temperatue measurements.

Simulation results of all these techniques are presented on the basis of 10 common limitations and defects of solar cell devices. We provide rich information for judgement and interpretation of experimental results of these characterisation techniques. Doping might be best extracted from dark-CELIV measurements. Recombination clearly influences the peak-height of the photo-CELIV current whereas the charge carrier mobility influences the rise-time in TPC. From the TPC decay and the DLTS decay, trap densities and trap depths may be estimated using temperature dependent measurements. The charge extraction experiment underestimates the effective charge carrier density by up to a factor of 5 in our simulations. The series-resistance and the electrical permittivity can be determined from capacitance-frequency plots of impedance spectroscopy data

and from dark-CELIV. A capacitance-rise at low frequency is an indication of slow trapping. With capacitance-voltage measurements the injection behaviour can be studied. We recommend not to use Mott-Schottky analysis of CV data for thin devices like organic solar cells. The ideality factors from dark JV-curves and V_{oc} versus light intensity measurements are a clear indicator for trap-assisted recombination. Only the case with deep traps leads to an ideality factor of 2.0 in our simulations. The shunt resistance is extracted from the reverse current of the dark JV-curve or OCVD. The accuracy of the parameter extracted from these techniques using analytical approaches is discussed.

We further demonstrate comprehensive parameter extraction from experimental data by global parameter fitting on the example of an organic bulk-heterojunction solar cell comprising PCDTBT:$PC_{70}BM$. Our simulation results match the data of 9 different experimental techniques in the steady-state, transient and frequency domain very well. Problematic parameter correlation is minimized by the combination of several techniques. All relevant parameters that govern charge transport are determined including the electron and hole mobilities, recombination pre-factor, trap density, trap depth, built-in potential, injection barriers, shunt resistance, series resistance and the relative dielectric constant.

We provide assistance in interpretation of experimental results and demonstrate comprehensive parameter extraction. Understanding and quantifying physical effects is a prerequisite for further progress in research of efficient and stable third-generation solar cell technologies.

10

WHY PEROVSKITE SOLAR CELLS WITH HIGH EFFICIENCY SHOW SMALL IV-CURVE HYSTERESIS

This chapter is based on the author's publication *Why perovskite solar cells with high efficiency show small IV-curve hysteresis* [219].

10.1 ABSTRACT

There is increasing evidence that the presence of mobile ions in perovskite solar cells can cause a current-voltage curve hysteresis. However, it is still subject of ongoing debates how exactly mobile ions influence the device operation. We use drift-diffusion simulations incorporating mobile ions to describe IV-curves of preconditioned methylammonium lead iodide perovskite solar cells and compare them with experimental results.

Our simulation results show that the hysteresis depends on the extent of surface recombination and on the diffusion length of charge carriers. We provide a detailed explanation for the reduced hysteresis of perovskite solar cells with high power conversion efficiencies. We find that in high-efficiency solar cells ion migration is still present, but does not cause a hysteresis effect. In these devices charge extraction is mainly driven by diffusion of free electrons and holes.

10.2 INTRODUCTION

The device physics of metal-organic halide perovskite solar cells is still under debate. The hysteresis in the current voltage-curve [35] occurring at different voltage scan-rates has been attributed to the slow movement of mobile ions in the perovskite film [89, 87]. Using density functional theory (DFT) it has been shown that formation energies for iodine vacancies and methylammonium (MA) vacancies are sufficiently low such that both vacancies are present at high concentrations at room temperature [90]. Furthermore, it was found that iodine vacancies can migrate through the device [96]. The hypothesis of mobile iodine vacancies has been further confirmed by TOF-SIMS measurements that have revealed changes in chemical composition before and after illumination on microscopic spots [220]. There is also evidence for other species migrating through the perovskite layer such as gold [221] or hydrogen [222].

Van Reenen *et. al.* [98], Richardson *et. al.* [99] and Calado *et. al.* [100] have presented drift-diffusion models incorporating mobile ions in order to study transient phenomena consistent with the hysteresis effect. Their transient simulations show that mobile ions indeed can lead to a hysteresis in the IV-curve as observed in

measurements.

Although the presence of mobile ions seems to be confirmed and their influence on the IV-curve hysteresis has been simulated, important questions remain open. The strength of the IV-curve hysteresis depends strongly on the contact materials used to extract electrons and holes [35, 87, 72, 73, 223, 71]. Perovskite solar cells employing PEDOT:PSS and PCBM as contact layers for example have almost no hysteresis whereas perovskite solar cells with compact TiO_2 and Spiro-OMeTAD show very pronounced hysteresis [71]. It was shown that surface optimization can eliminate the hysteresis [72, 73, 224]. There is evidence that inverted devices (holes extracted at the front-side, electrons on the rear-side) have generally less hysteresis [71, 225]. If mobile ions inside the bulk perovskite layer are responsible for the hysteresis, the question arises why the hysteresis depends on the contact materials used for charge extraction.

Furthermore it is generally observed that highly efficient perovskite solar cells suffer less from hysteresis [224, 225, 207, 226, 142, 227, 228]. How can this be related to ion migration?

Calado and co-workers presented evidence for mobile ions also in hysteresis-free devices and concluded that electronic passivation[1] of the contact surfaces reduces the hysteresis [100]. This is consistent with the work of van Reenen *et. al.* that states the necessity of the presence of interface traps and mobile ions for the occurrence of the hysteresis [98]. Richardson and co-workers however presented simulation data without surface recombination still resulting in a hysteresis [99].

In this chapter we investigate the influence of surface-recombination and diffusion length on the IV-curve hysteresis of perovskite solar cells. We use a drift-diffusion model incorporating mobile ionic species to simulate preconditioned IV-curves and compare it with experimental results. We provide an explanation why highly efficient devices have generally small hysteresis and why the contact materials play an important role.

10.3 METHODS

10.3.1 *Experimental methods*

To study the influence of mobile ions it is helpful to use experiments that distinguish ionic from electronic processes. When an IV-curve is measured with a voltage-ramp up and down, processes of ionic charge transport and electronic charge transport are both involved. With commonly used scan-rates it is not possible to study ions and electrons or holes separately.

In order to distinguish ionic from electronic charge transport we thus perform IV-curve measurements with very high ramp-rates (full IV-curve measured in 70 milliseconds, up and down) after preconditioning the device for 10 seconds

1 Electronic passivation of a surface means the reduction of surface states (interface traps) that leads to a lower surface recombination rate.

at a constant voltage, as proposed by Tress *et. al.* [89]. The long preconditioning time allows the ions to move and equilibrate in the device. Therefore we achieve a separation of electronic and ionic processes in our measurements. Jacobs and co-workers concluded that preconditioned rapid IV-scans are more effective at manifesting the hysteretic behaviour than classical slow IV-scans [229].

The preconditioned IV-curves are acquired with the all-in-one measurement system Paios [110]. For illumination a white LED is used with fast turn-on time. The preconditioning and the IV-curve acquisition are performed in a one-shot measurement. A voltage signal is applied that is constant for 10 seconds and subsequently drives the IV-curve down to -0.6 volt and up to 2.3 volt within 70 milliseconds. The measurement system is described in more detail in chapter 6 EXPERIMENTAL SETUP.

10.3.2 *Numerical model*

To simulate preconditioned IV-curves, we profit from the fact that ionic motion and motion of electron and holes occur on different time scales and can be investigated separately, as already described in the section 10.3.1 Experimental methods. This allows us to simulate first the ion distribution as a result of preconditioning and then the charge transport of electrons and holes in the presence of the fixed ion distribution. Compared to a fully coupled solver this two-step approach can be faster while preserving good convergence.

The prerequisite of this approach is that ions do not move significantly during the fast IV-ramp and that the electronic charge carrier concentration is much smaller than the concentration of ions during the preconditioning, such that the electrons and holes do not significantly alter the electric field. With our parameter set this is the case. We also have tested a fully coupled dynamic electronic-ionic modelling approach for certain parameter sets, compared it with the two-step approach and did not find relevant differences as long as the charge carrier density is significantly lower than the ion density.

The device structure and the simulation domain are shown in Figure 10.1. The mesoporous structure with TiO_2 is neglected in the model. The absorbing layer is modelled as one effective material with one transport level for electron and one for holes, respectively.

It is energetically favourable for photogenerated electrons to transfer to TiO_2. This process has been estimated to happen within picoseconds. We therefore assume that the electrons are mainly transported in the mesoporous TiO_2. As TiO_2 has a lower electron mobility, an imbalance between electron and hole mobility is assumed as proposed by Ponseca *et. al.* [69]. The compact TiO_2 as electron transport layer and the Spiro-OMeTAD as hole transport layer are modelled as metallic. It is assumed that their doping density is high enough to fix the

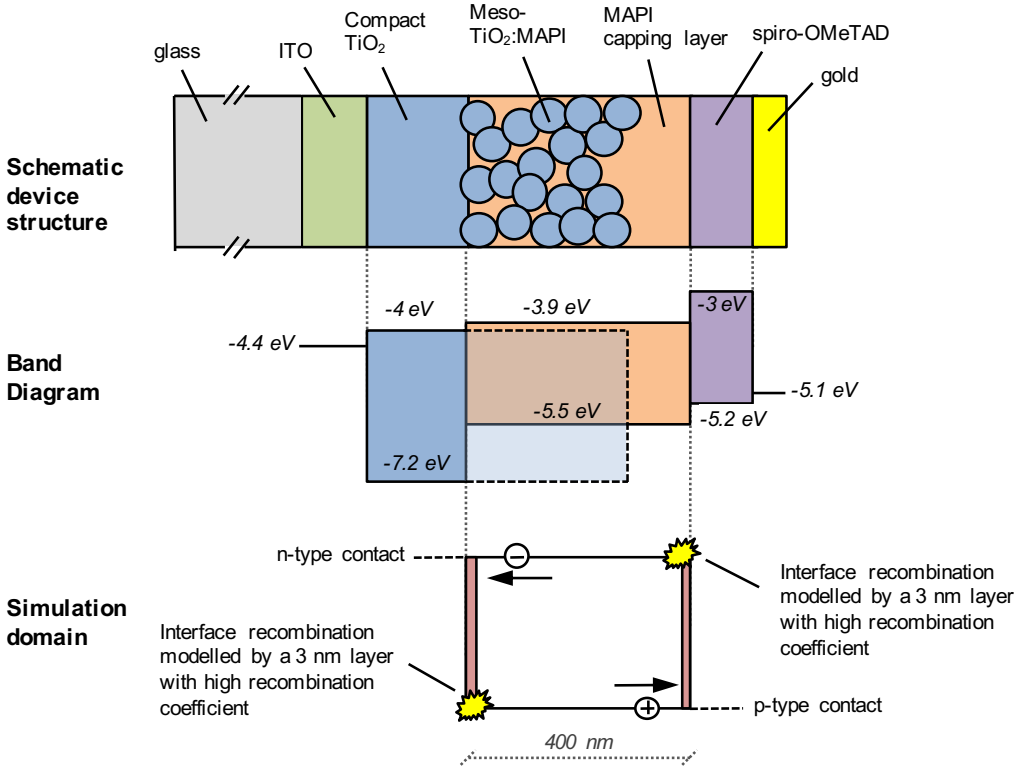

Figure 10.1: Device structure, schematic band diagram and simulation domain of the perovskite solar cell.

Fermi-level at the interface with the perovskite.

The simulation domain is discretized into 100 elements in the bulk. With high ion densities very steep density gradients can occur at the boundaries leading to numeric instability as observed by Richardson *et. al.* [99]. To address this issue we refine the grid close to the boundaries with additional 20 points each.

The drift-diffusion equations for the mobile ions are solved first. Neumann boundary conditions of zero flux (no ions can enter or leave the perovskite layer) and an initial ion density with uniform distribution are used. Walsh and co-workers showed with quantum mechanical calculations that the charge carrier concentration is regulated by ionic compensation (self-regulation mechanism) [90]. The Schottky-defect formation results in an equal amount of positively and negatively charged ions. We therefore assume the same density for both ion species.

Eames *et. al.* calculated that iodine as well as MA are mobile within perovskite, the later however with a much lower mobility [96]. We therefore consider both ion types to be mobile. The steady-state solution of the ion distribution is however independent of the ion-mobility. Note that there is a large difference between the solutions for an ion mobility of zero and extremely low ion mobility. Ions with non-zero mobility accumulate on one side of the electrodes at steady-state, independent of their mobility. The mobility only determines how long it takes to reach

steady-state. We therefore suggest not to employ fixed charges with uniform distribution for slow ions like MA vacancies as used by Richardson and Calado [99, 100].

The resulting steady-state ion distribution at the preconditioning voltage is then used in the second drift-diffusion simulation as fixed charges. These fixed ionic charges enter the Poisson equation and thereby influence the electric field profile in the device. The second drift-diffusion simulation solves for the electronic charge distributions in the bulk and uses fixed electronic charge carrier densities as boundary conditions, namely a fixed electron density at the TiO_2-interface and a fixed hole density at the Spiro-OMeTAD-interface. The drift-diffusion simulation is performed using the simulation software *Setfos* [111].

To simulate surface recombination 3-nanometre thin recombination layers are used at the interfaces with the transport layers on both sides. Changing the recombination coefficient of each of these thin layers effectively controls surface recombination at the perovskite layer interface. The physical cause of the interface recombination could be energetic states (interface traps) at the interface leading to Shockley-Read-Hall recombination.

The simulation of the illuminated device considers the illumination spectrum and a thin film optics model of the complete multi-layer stack as previously presented for the simulation of organic solar cells [34, 113] and perovskite solar cells [230, 36].

The detailed description of the simulation model is found in chapter 7 PHYSICAL MODEL. The model used in this study is however less complex as it does not include Shockley-Read-Hall (SRH) and the mobile ions are not fully coupled. Furthermore only a single layer is simulated.

10.3.3 *Device fabrication*

All chemicals were purchased in a high purity grade and were used as received. Fluorine doped tin oxide-coated glass substrates (Solaronix, resistivity $7\,\Omega/sq$) were patterned by etching with Zn powder and HCl (conc.) and were then sequentially cleaned in Hellmanex (Hellma, Germany), de-ionized water, acetone and 2-propanol.

For the deposition of the compact TiO_2 blocking layer, $25\,ml$ of $TiCl_4$ (Sigma Aldrich) was hydrolyzed in $90\,ml$ of deionized water at $0^\circ\,C$, then spin coated on cleaned FTO at $5000\,rpm$ for $30\,s$. The mesoporous $TiO_2$was deposited on top of FTO/TiO_2 by spin coating a paste of TiO_2 nanoparticles (Ti-Nanoxide T/SP from Solaronix diluted with ethanol 0.22% wt/wt) at $5000\,rpm$ for 30 seconds followed by heating to $380^\circ\,C$ for $10\,min$ and then to $500^\circ\,C$ for $30\,min$ in air. Before deposition of the perovskite layer, the substrates were heated inside the glovebox at $140^\circ\,C$ for $10\,min$.

A solution of the precursors PbI_2 (CTI Japan, 99.9%) and methylammonium iodide (Sigma Aldrich) in dimethyl sulfoxide (DMSO, Sigma Aldrich) (DMSO, 1:1 M ratio, concentration 45% wt/wt) was spin coated inside the glovebox on the

mesoporous TiO_2 at 1000 rpm for 10 s followed by 5000 rpm for 30 s. During the last 10 s of spin coating, 1 ml of chlorobenzene (Sigma Aldrich, 99.8%) was dropped on the spinning substrate. The perovskite films were then annealed at 100° C for 60 min.

A hole transport layer solution of 2,2′,7,7′-tetrakis- (N,N-di-p-methoxyphenylamine)-9,9′-spirobifluorene (Spiro-OMeTAD, Sigma-Aldrich 99%) with a dopant (FK209 from Dyesol) and additives (4-tert-butylpyridine and lithium bis(trifluoromethylsulfonyl)imide, Sigma Aldrich) was prepared as previously described [231] and coated on the perovskite film at 4000 rpm for 30 s. Finally, 80 nm of Au (Kurt J. Lesker, 99.999%) were deposited by thermal evaporation at $< 5 \cdot 10^{-6}$ $mbar$ through a shadow mask. Four solar cells were defined on each substrate with an active area of 0.138 cm^2.

An SEM cross-section image of the device is shown as Figure 1a in reference [82]. The thickness of the mesoporous TiO_2/MAPI layer is approximately 400 nm. Devices were fabricated by Dr. Mohammed Makha at EMPA in Dübendorf, Switzerland.

10.4 RESULTS

Devices are fabricated according to the procedure described in section 10.3.3 Device fabrication. In Figure 10.2 the IV-curves of the device measured under AM1.5 is shown. The hysteresis of this IV-curve is small because the device was measured with a slow scan rate of 0.1 V/s. The power conversion efficiency is around 12%.

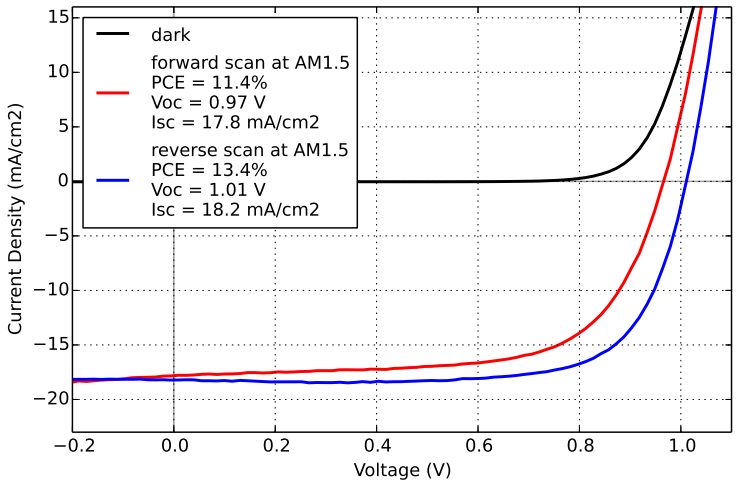

Figure 10.2: IV-curves measured under AM1.5 with forward and reverse scan and a reverse dark-scan.

Figure 10.3 shows IV-curves measured with different scan-rates. The hysteresis shape depends significantly on the scan-rate. At low scan-rates (Figure 10.3a and 10.3b) the downward scan results in higher open-circuit voltage and higher fill factor. This is the type of hysteresis that is often published and is comparable with the hysteresis of the IV-curve in Figure 10.2. The IV-curve at higher scan-rate

(Figure 10.3c) shows a crossing point and an S-shape in the forward scan. At the highest scan-rate two crossing-points occur and the hysteresis is most pronounced.

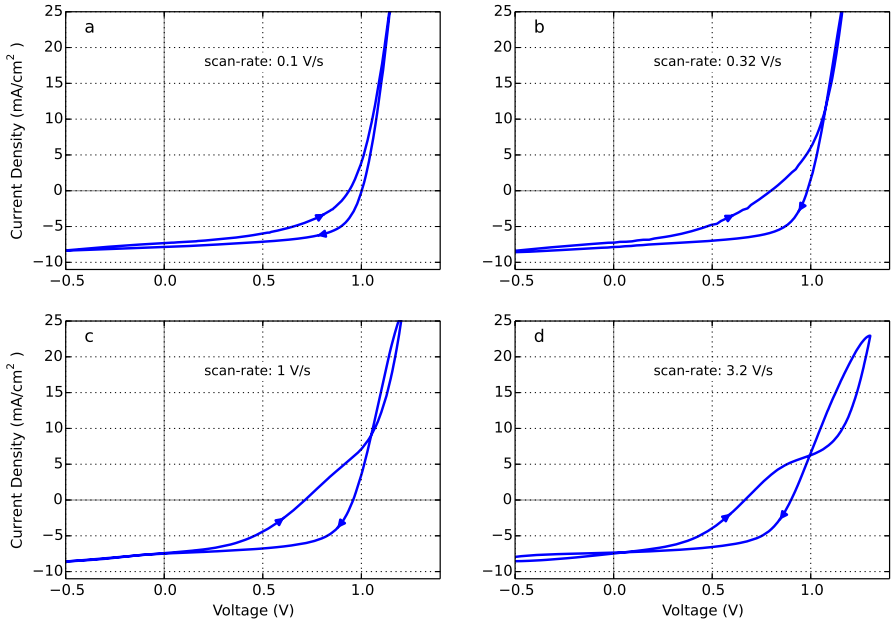

Figure 10.3: IV-curves measured with different scan-rates. Arrows indicate the scan-direction.

10.4.1 *Preconditioned IV-curves*

Preconditioned IV-curves allow separating the influence of mobile ions and electronic charges. Electrons and holes in perovskite have charge carrier mobilities between 0.01 and 20 cm^2/Vs [80, 46, 232] whereas iodine vacancies are expected to have a mobility in the order of $10^{-11}\,cm^2/Vs$ [96]. Other ionic species like MA vacancies are even slower with a mobility of around $10^{-15}\,cm^2/Vs$ [96]. Although the IV-curve is measured within 70 milliseconds, the electrons and holes can be considered in steady-state at each voltage-point due to their high mobility. The ions however are too slow to follow the voltage-ramp, thus we consider the ion distribution in the perovskite layer as unchanged during the IV-sweep.

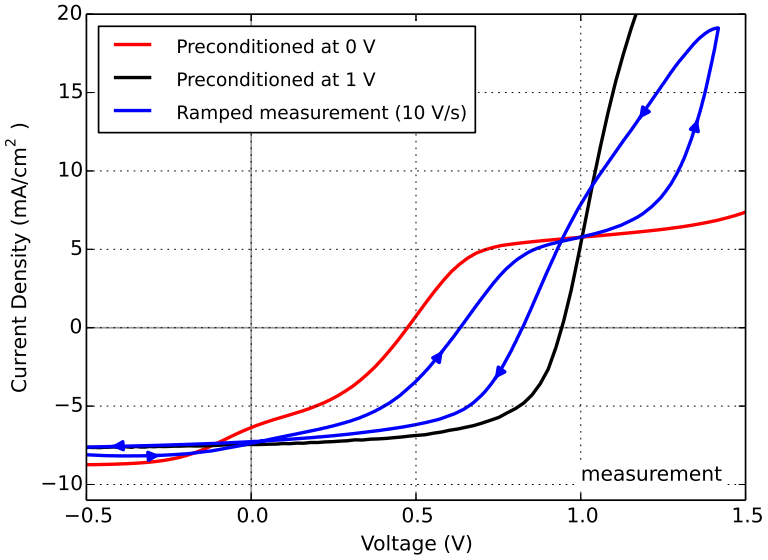

Figure 10.4: Comparison between IV-curves measured with different preconditioning (acquired with a fast upward-ramp after 10 seconds preconditioning at 0 volt or 1 volt) and an IV-curve measured with a ramp-up and down. The arrows indicate the sweep direction.

The difference between the two preconditioned IV-curves can be directly related to the hysteresis of IV-curves measured with a voltage-ramp up and down. In Figure 10.4 the preconditioned IV-curves are compared to an IV-curve measured with a regular voltage ramp (ramp from low to high voltage and back). The upward sweep is comparable to the IV-curve preconditioned at 0 volt and the downward sweep is comparable to the IV-curve preconditioned at 1 volt. The IV-curve measured with the voltage ramp lies somewhere between the two extreme cases of preconditioning at 1 volt or 0 volt. The ramp of $10\,V/s$ is slow enough such that the ions have time to partially adjust in the electric field during the scan. By analysing the preconditioned IV-curves at 0 and 1 volt we can make direct conclusions about the hysteresis observed with finite scan rates.

10.4.2 *Measurement and Simulation*

Preconditioned IV-curves of the perovskite solar cells are measured as described in section 10.3.1 Experimental methods

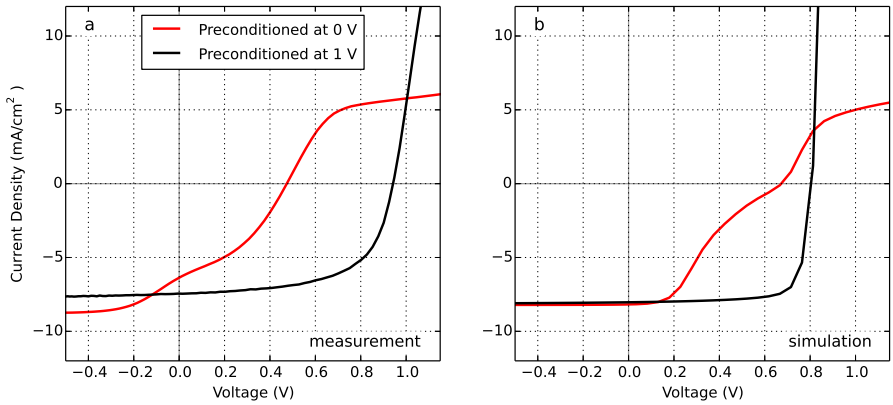

Figure 10.5: a) Measured IV-curves of a methylammonium lead iodide (MAPI) perovskite solar cell that was preconditioned at 0 and 1 volt for 10 seconds. b) Simulation results including mobile ions and surface recombination.

Figure 10.5a shows preconditioned IV-curves at 0 volt and 1 volt of a mesoporous perovskite solar cell with the structure ITO | TiO_2 | meso-TiO_2:MAPI | MAPI | Spiro-OMeTAD | Gold. The curve with preconditioning at 0 volt shows about half the open-circuit voltage and has a low current in forward direction. A white LED is used for the illumination, therefore the photocurrent is lower compared to one sun AM1.5 illumination.

We use the drift-diffusion simulator *Setfos* [111] extended by an ion charge transport solver to provide a possible explanation for the observed effects. Figure 10.5b shows the simulation result for the two preconditioned IV-curves reproducing the significant features. The shift in open-circuit voltage is less pronounced compared to the measurement.

A mobile ion density of $1 \cdot 10^{18}\, cm^{-3}$ was used. High vacancy densities up to $2 \cdot 10^{20}\, cm^{-3}$ could be expected from theoretical calculations [90]. It is however not clear how many MA vacancies and iodine vacancies are compensated by an electric charge and are neutral. We emphasize that finding methods to determine the density of mobile ions is important for quantitative simulations. The simulation parameters are summarized and explained in Table 10.1.

Parameter	Value	Details
Device thickness (d)	$400\,nm$	-
Electron mobility (μ_e)	$1 \cdot 10^{-2}\ cm^2/Vs$	Electrons are transferred to TiO_2 within picoseconds [80]. We therefore assume that electrons are transported inside the mesoporous TiO_2 [233] with a mobility of $1 \cdot 10^{-2}\,cm^2/Vs$ [234].
Hole mobility (μ_h)	$1\ cm^2/Vs$	Charge carrier mobility has been estimated to be around $20\,cm^2/Vs$ by terahertz and microwave conductivity [69]. These two techniques measure short range mobility. For device modelling long range mobilities (across grain boundaries) are more adequate. We therefore use results from time-of-flight measurements, that showed mobilities between 0.06 and $1.4\,cm^2/Vs$ [82].
Radiative recombination coefficient (β)	$1 \cdot 10^{-9}\ cm^3/s$	The radiative recombination coefficient has been measured to be between $1 \cdot 10^{-10}$ and $1 \cdot 10^{-9}\,cm^3/s$ by time-delayed collection field experiments [235].
Effective density of states (N_0)	$1 \cdot 10^{27}\ m^{-3}$	-
LUMO (E_{LUMO})	$3.9\,eV$	-
HOMO (E_{HOMO})	$5.4\,eV$	-
Relative Permittivity (ε_r)	35	Capacitance-frequency plots from impedance measurements gave a relative permittivity of 35. This is close to the theoretical calculations from Frost *et. al.* resulting in permittivities between 24 and 33 [95].

table continues on the next page

Parameter	Value	Details
Equilibrium density of mobile positive ions ($N_{anion,0}$)	$1 \cdot 10^{18}\ cm^{-3}$	Molecular dynamics calculations by Walsh *et. al.* predict ion concentrations up to $2 \cdot 10^{20}\ cm^{-3}$ [90]. In recent approaches to model mobile ions densities between $1 \cdot 10^{17}$ and $1 \cdot 10^{19}\ cm^{-3}$ have been used [99, 98, 100]. Ion densities of $1 \cdot 10^{18} cm^{-3}$ show in our case the best results. The density of mobile ions needs to be investigated in more detail in future. It is also not clear yet, how many vacancies are ionized at room temperature.
Equilibrium density of mobile negative ions ($N_{cation,0}$)	$1 \cdot 10^{18}\ cm^{-3}$	Both positive and negative ion densities are equal according to the theory of Schottky defects.
ETM n-doping (n_{ETM})	$1 \cdot 10^{15}\ cm^{-3}$	Fitting value
HTM p-doping (p_{HTM})	$1 \cdot 10^{15}\ cm^{-3}$	Fitting value
ETM recombination layer: radiative recombination coefficient (β_{ETM})	$1 \cdot 10^{-9}\ cm^3/s$	Fitting value
HTM recombination layer: radiative recombination coefficient (β_{HTM})	$8 \cdot 10^{-4}\ cm^3/s$	Fitting value

Table 10.1: Simulation parameters for the simulation of the IV-curves shown in Figure 10.5b.

Figure 10.6a shows the calculated ion distribution after preconditioning at 0 volt and 1 volt. At 0 volt the negative ions (anions) move to the electron contact, positive ions (cations) to the hole contact, driven by the built-in potential. The ions compensate the built-in field in this state hindering charge extraction. However, for preconditioning at 1 volt the ions move to the opposite side and enhance the built-in potential.

Figure 10.6b shows the electric field during the fast IV-scan at 1 volt after preconditioning. In the case where the ions were preconditioned at 0 volt the ionic space charge creates a positive electric field close to both contacts. This field acts as a barrier for injection of electronic charges. The forward current is therefore lim-

ited as no charge can be injected. Therefore only the photocurrent is extracted in forward direction (Figure 10.5b). In the case with preconditioning at 1 volt the electric field is negative close to the contacts leading to a regime with efficient injection.

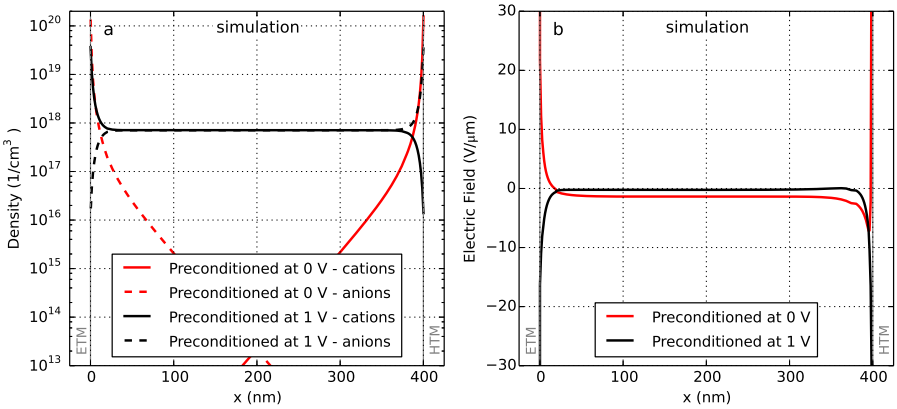

Figure 10.6: a) Simulated ion distribution after preconditioning at 0 volt and 1 volt. b) Simulated electric field profiles at 1 volt forward bias for both ion distributions shown in a). The same simulation parameters are used as in Figure 10.5b

The example in this section illustrates that the simulation result compares favourably with the experimentally observed IV curves (Figure 10.5) and that the underlying electronic and ion charge distributions (Figure 10.6) are responsible for the distinct behaviour of preconditioning at different prebias.

10.4.3 *Preconditioned IV-Curves under Illumination and in the Dark*

To further validate our simulation approach we fabricated planar perovskite devices with the same layer structure. Also in these devices the current is injection limited if preconditioned at 0 volt as shown in Figure 10.7a. In forward and in reverse direction only the photocurrent of $20\,mA/cm^2$ is extracted. Charge injection is blocked by the ions close to the contact. The simulation reproduces this behaviour as shown in Figure 10.7c.

In these devices also dark-IV curves were measured with varied preconditioning (Figure 10.7b). In case of a preconditioned device at 0 volt the ions are close to the contacts and inhibit charge carrier injection. Compared to the IV-curve under illumination there are however no charges in the bulk that could be extracted. Therefore, the current is very low. If preconditioned at 1 volt the ions have moved away from the layer interfaces (see Figure 10.6). In this state charges can be injected into the perovskite layer. Electrons and holes recombine in the bulk and a forward current flows. This IV-curve shows regular diode behaviour.

In the simulation the same behaviour is reproduced using the same parameters for light and dark IV. Please note that the series resistance of this planar device is higher than the one in the mesoporous device used in this study. This effect is considered in the simulation. The short circuit current is higher compared to

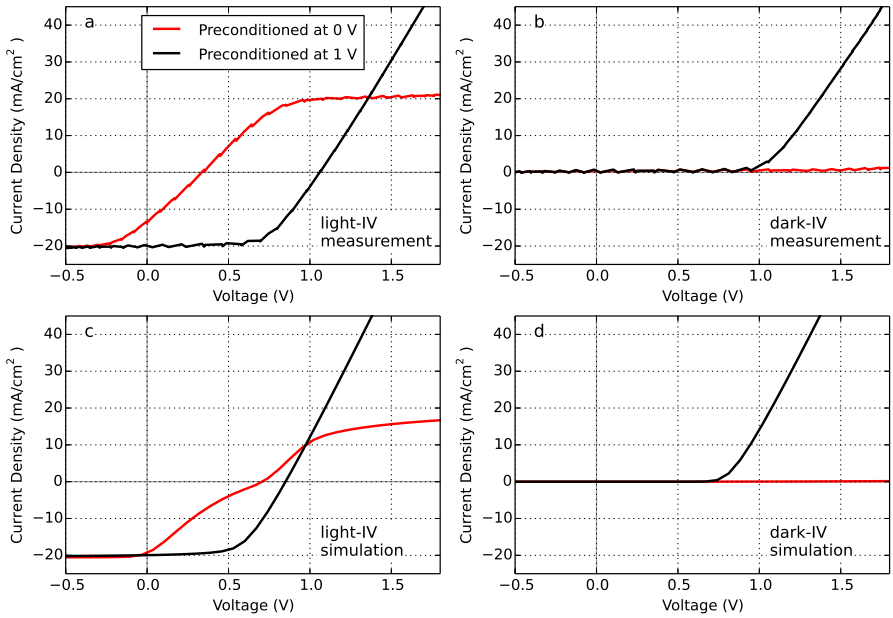

Figure 10.7: a) Preconditioned IV-curves under illumination of a planar perovskite solar cell. b) Preconditioned IV-curves in the dark. c) Simulated IV-curves under illumination with ion distribution at 0 and 1 volt. d) Simulated IV-curves in the dark with ion distributions at 0 and 1 volt.

the mesoporous device. We use a higher charge generation in the simulation to account for this fact. All other parameters of the simulation remained the same, as shown in Table 10.1.

10.4.4 *Influence of diffusion length and surface recombination*

To better understand hysteresis caused by mobile ions we analyse the influence of surface recombination and the carrier diffusion length on the IV-curve hysteresis.

The carrier diffusion length L is defined as

$$L = \sqrt{D \cdot \tau} = \sqrt{\tau \cdot \mu \cdot \frac{kT}{q}} \tag{10.1}$$

where D is the diffusion constant, τ is the charge carrier lifetime, μ is the mobility and kT/q is the thermal voltage. The charge carrier lifetime for electrons (τ_e) and holes (τ_h) is defined as

$$\tau_e = \frac{n_e}{R} = \frac{1}{\beta \cdot n_h} \tag{10.2}$$

$$\tau_h = \frac{n_h}{R} = \frac{1}{\beta \cdot n_e} \tag{10.3}$$

where n_e is the electron density, n_h is the hole density, R is the recombination and β is the radiative recombination coefficient. The two equations show that the electron lifetime is dependent on the hole density and the hole lifetime is dependent on the electron density. In an intrinsic region of a p-i-n junction the electron and hole densities vary spatially. Consequently, also the lifetime varies within the device. Therefore, neither the lifetime nor the diffusion length are physically meaningful in the intrinsic region of a p-i-n junction device [236, 237]. The situation is different in a doped device like a crystalline silicon solar cell. There the minority carrier lifetime and the diffusion length are spatially constant and therefore a physically meaningful quantity to describe how far minority carriers can travel on average by diffusion.

As our perovskite solar cell has a p-i-n structure the apparent diffusion length cannot be considered as a quantity that describes how far charges diffuse. It can however be employed as a measure of how well charges are transported to the contact layers under illumination. As the quantity diffusion length is already well established also in the perovskite community, we use it in this study to quantify the charge extraction properties. We name it pseudo diffusion length to emphasise that it cannot be directly compared with diffusion lengths extracted from experiment such as transient photo-voltage (TPV). The pseudo diffusion length does not describe how far charges diffuse on average but is rather a quantification for how well charges are extracted.

To control the pseudo diffusion length we change the bulk recombination coefficient β which is an input to the simulation. The pseudo diffusion length is then calculated from the simulation results.

Interfaces between two materials often have energy levels in the band gap that trigger trap-assisted recombination. The passivation of interface surface states is

therefore an important step to reach high efficiencies in solar cells. We model the surface recombination by setting a higher recombination coefficient β in the perovskite material in a 3-nanometre thick layer adjacent to the contacts.

In Figure 10.8 we illustrate four extreme cases of simulated preconditioned IV-curves using combinations of short and long diffusion lengths with low and high surface recombination. In the case of a small diffusion length and a high surface recombination the hysteresis is most pronounced (Figure 10.8c). In the opposite case (Figure 10.8b) with long diffusion length and low surface recombination the hysteresis is very low. If the diffusion length is short (Figure 10.8a) or the surface recombination is high (Figure 10.8d) a pronounced hysteresis is observed. We conclude that both, large diffusion length and low surface recombination are required to obtain IV curves with small hysteresis.

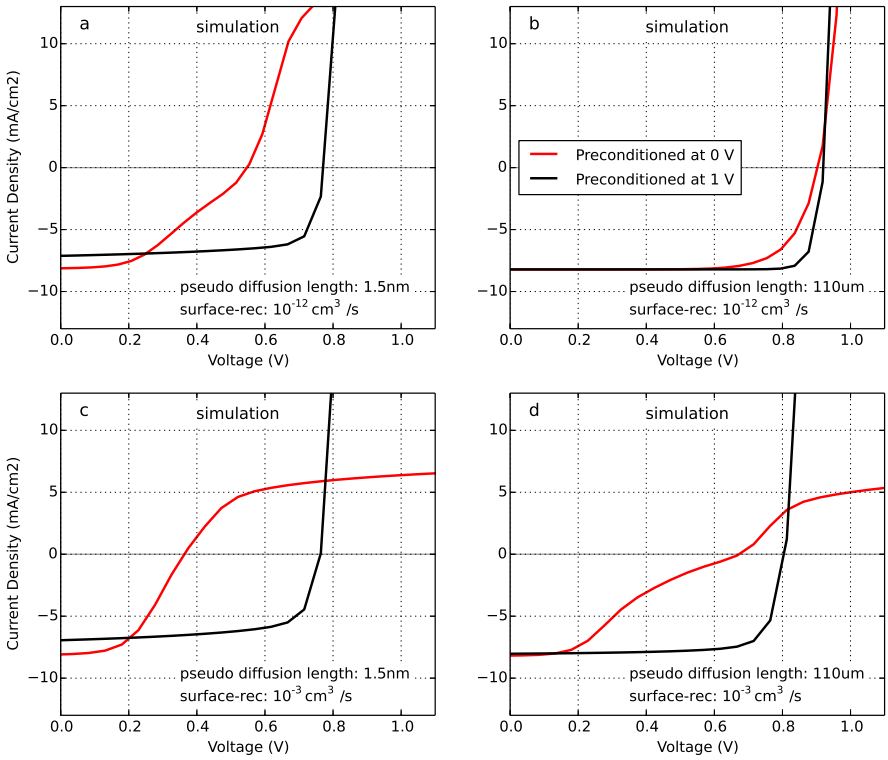

Figure 10.8: Simulation of IV-curves with different preconditioning voltage and therefore different ion distributions. The same simulation parameters are used as in Figure 10.5 except for the diffusion length and surface recombination which are given in the insets of a, b, c and d.

These results explain the difference between the simulations of Richardson *et. al.* [99] and van Reenen *et. al.* [98]. Richardson used no surface recombination but a short diffusion length (high SRH-recombination rate in the bulk) which corresponds to case a) of Figure 10.8. Van Reenen used long diffusion lengths (low bulk recombination, high mobilities) and high surface recombination (SRH

recombination assisted by traps at the interface) that corresponds to case d) of Figure 10.8.

Methylammonium lead iodide perovskite has a low radiative recombination coefficient [46, 235]. The grain boundaries have favourable energies to prevent SRH recombination as shown by DFT simulations [78]. High charge carrier mobilities up to $20\,cm^2/Vs$ have been measured [69, 80]. Both of these factors lead to a long diffusion length, which results in an efficient charge extraction. Therefore a high surface recombination is probably the dominant cause for the IV-curve hysteresis in perovskite solar cells. Calado and co-workers show in their simulation that the hysteresis vanishes if passivated surfaces (low surface recombination rates) are used. Our simulations confirm these findings and provide a classification in terms of diffusion length and surface recombination.

We explain the effect as follows: When the ions are preconditioned at 0 volt the built-in field is compensated (see Figure 10.6). At forward bias (example 0.8 volt) during the fast IV-scan the electric field hinders charge extraction – the field points in the *wrong* direction. If the recombination at the surface is high the charges are driven to the *wrong* contact and recombine there. If recombination at the surface is sufficiently low then charges can *pile-up* at the *wrong* contact. Charges are therefore driven to the *wrong* contact until a density gradient is established that enables diffusion across the device to the extraction contact. In the next chapter (chapter 11) a similar set of IV curves is calculated with a solver with fully-coupled mobile ions. The conclusion from Figure 10.8 is confirmed with the more advanced solver, see Figure 11.10 section 11.4.7 IV-curve hysteresis.

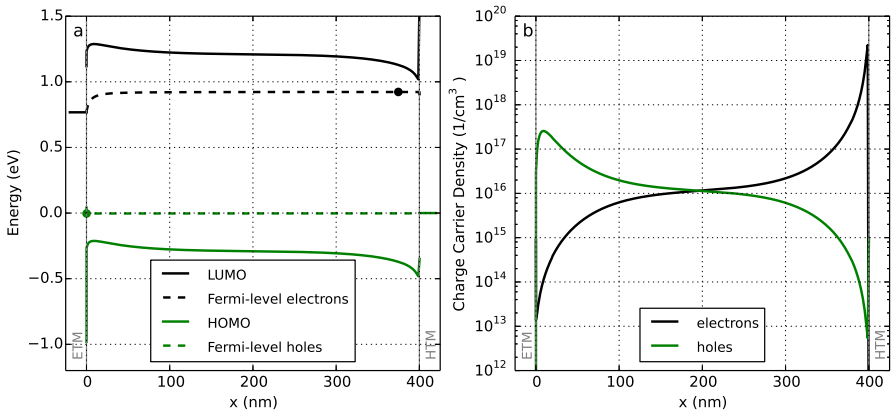

Figure 10.9: Band diagram a) and charge carrier densities b) at 0.8 volt of a perovskite solar cell with high diffusion lengths and low surface recombination (corresponding to case b in Figure 10.8). Ion distribution preconditioned at 0 volt. The circles in the band diagram mark the maximum of the electron quasi-Fermi level and the minimum of the hole quasi-Fermi level.

Figure 10.9a shows the corresponding energy band diagram for the cell of Figure 10.8b at 0.8 volt bias (ions preconditioned at 0 volt). The bands are tilted to

the right leading to an electric field hindering charge extraction. Charges however are still collected efficiently since there is a density gradient throughout the whole layer. Thus, the charges are extracted due to diffusion as driving force even against the electric field. For clarity we plot the electron and hole concentration in Figure 10.9b.

10.4.5 *High efficiency and small hysteresis*

In Figure 10.8 we have demonstrated simulated IV-curves for cells with distinct combinations of surface recombination rates and diffusion lengths for both cases of pre-conditioning. We argue that these simulation results are directly linked to the hysteresis observed in IV-curve measurements with finite voltage ramp rates. To further analyse the expected hysteresis behaviour we define as a quantitative measure for the hysteresis the integrated current difference between the two IV-curves (preconditioned at 0 volt and 1 volt). This quantity represents the area between the two IV-curves in the graph and is an indication on how severe the hysteresis is.

Figure 10.10 depicts the normalised hysteresis indicator dependent on surface recombination and diffusion length. As already shown in Figure 10.8 the hysteresis is weak when the surface recombination is low and the diffusion length is long.

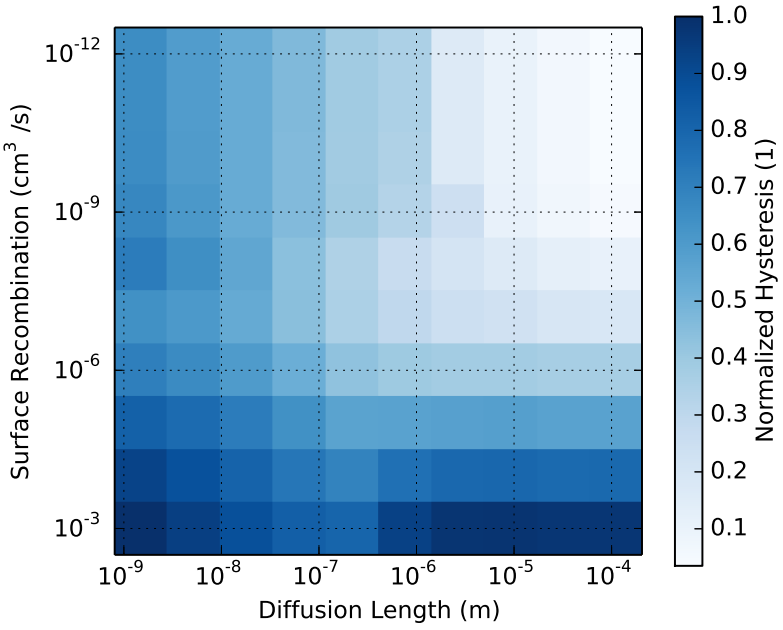

Figure 10.10: Simulation of the extent of the hysteresis dependent on surface recombination and the charge carrier diffusion length. The hysteresis strength is the integrated difference of the IV-curves and normalized by the maximum hysteresis.

Solar cells with high power conversion efficiencies can only be realized if the diffusion length is sufficiently long and the surface recombination is not dominant. Aiming for high efficiencies by increasing the diffusion length and decreasing the surface recombination has the positive side effect that the hysteresis is reduced - even if the density of mobile ions remains the same.

To illustrate this relationship we plot calculated power conversion efficiencies in Figure 10.11 for different surface recombination values and diffusion lengths. The region with the highest efficiency is found where both the diffusion length is long and the surface recombination is low. This high-efficiency parameter region coincides with the region where the hysteresis indicator is small.

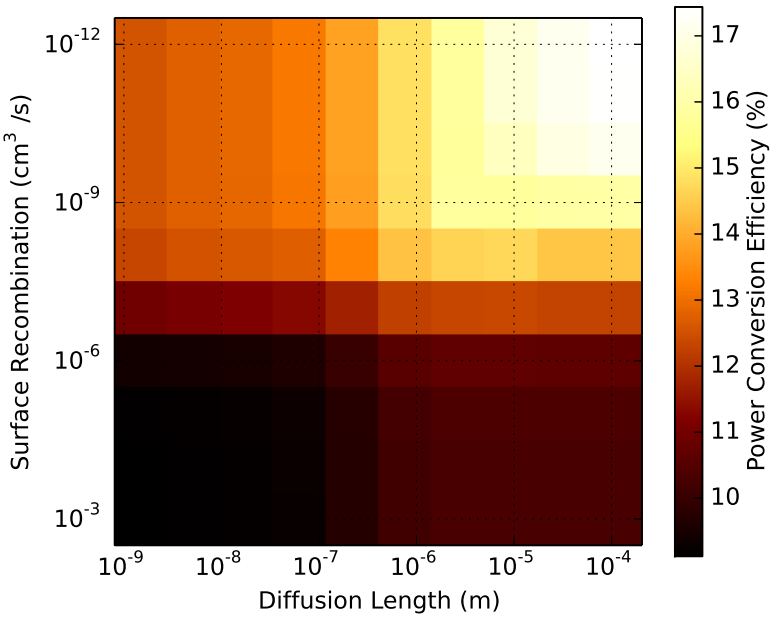

Figure 10.11: Simulation of the power conversion efficiency depending on surface recombination and charge carrier diffusion length.

Our simulation results provide an explanation why high power conversion efficiency and small hysteresis is correlated. Furthermore, it provides an explanation why hysteresis depends on contact materials, because contact materials have an influence on the surface recombination.

In our model we kept the ion density unchanged. It is conceivable that the density of mobile ions depends on the perovskite type and the processing conditions. Hysteresis is enhanced with increasing number of mobile ions. Note, that the absolute efficiency also depends on other factors like absorption coefficient and active layer thickness.

The perovskite grain size can have a strong influence on device efficiency and hysteresis [142, 186]. Grain boundaries disrupt the crystal quality and hinder charge transport (lower pseudo diffusion length) but they can also affect the

surface recombination [186]. Shao and co-workers presented compelling evidence that ions migrate preferably along the grain boundaries [102]. Grain size and grain boundaries therefore may affect material quality, interface quality or the effective ion mobility.

Notably, there is evidence for reduced hysteresis in inverted devices [71]. Most photons are absorbed near the front-side. Regarding surface recombination in inverted cells the front-contact is more relevant. Assuming that the electron contact is generally more critical in perovskite devices, it would be better to move the electron contact to the rear-side. This is a possible explanation for the reduced hysteresis in inverted device architectures that deserves further investigation.

10.5 CONCLUSIONS

We employed preconditioned IV-curves and numerical simulation to explain the hysteresis behaviour of perovskite solar cells. Our results provide an explanation for the recently observed reduced hysteresis in high efficiency perovskite solar cells.

The IV-curve hysteresis depends on the contact quality (amount of surface recombination) and on the diffusion length of the charge carriers. Hysteresis effects are weak only if both the charge diffusion length is long and the surface recombination is low. Both requirements are also necessary conditions to reach high efficiencies. We thus have established a correlation between high power conversion efficiency and weak hysteresis. Our simulations confirm previous findings and provide a classification in terms of diffusion length and surface recombination. This allows us to better understand the reported numerical studies and experimental results, too.

Our analysis is based on the assumption of no direct interaction between electric charges and mobile ions (except through the electric field in the Poisson equation). We assume that both positive and negative ions are mobile. Both assumptions need further investigation.

In this study a medium ion density of $1 \cdot 10^{18}\, cm^{-3}$ was used. In order to quantitatively understand the physics of perovskite solar cells, reliable methods to determine the densities of mobile ions need to be found.

11

CONSISTENT DEVICE SIMULATION MODEL FOR PEROVSKITE SOLAR CELLS

This chapter is based on the author's publication *Consistent Device Simulation Model Describing Perovskite Solar Cells in Steady-State, Transient and Frequency Domain* [238].

11.1 ABSTRACT

A variety of experiments on vacuum deposited methylammonium lead iodide perovskite solar cells is presented, including IV curves with different scan rates, light intensity dependent open-circuit voltage, impedance spectra, intensity-modulated photocurrent spectra (IMPS), transient photocurrents and transient voltage step responses. All these experimental data sets are successfully reproduced by a charge drift-diffusion simulation model incorporating mobile ions and charge traps using a single set of parameters.

While previous modelling studies focused on a single experimental technique, we combine steady-state, transient and frequency-domain simulations and measurements. Our study is an important step towards quantitative simulation of perovskite solar cells leading to a deeper understanding of the physical effects in these materials. The analysis of the transient current upon voltage turn-on in the dark reveals that the charge injection properties of the interfaces are triggered by the accumulation of mobile ionic defects. We show that the current rise of voltage step experiments allow conclusions about the recombination at the interface. Whether one or two mobile ionic species are used in the model, has only a minor influence on the observed effects.

A delayed current rise observed upon reversing the bias from $+3$ volts to -3 volts in the dark cannot be reproduced yet by our drift-diffusion model. We speculate that a reversible chemical reaction of mobile ions with the contact material may be the cause of this effect thus requiring a future model extension.

A parameter variation is performed in order to understand the performance limiting factors of the device under investigation.

11.2 INTRODUCTION

Metal organic halide perovskites are electronic-ionic conductors, which is believed to be the reason for the frequently observed IV curve hysteresis in perovskite solar cells[35] and other intriguing effects like the extraordinarily high low-frequency capacitance under illumination [108]. Thereby, iodine vacancies can migrate and lead to a screening of the electric field [89, 90, 96, 93]. The exact physical operation

mechanism of perovskite solar cells remains however under debate.

The physical processes in these materials are often too complex to be understood by ad-hoc explanations or simple analytical formulas. Numerical simulations offer a deeper understanding of the underlying device physics. First charge drift-diffusion models incorporating mobile ions were presented by van Reenen [98], Richardson [99] and Calado [100]. In these models the IV curve is simulated with a transient solver in forward and reverse direction, reproducing the observed IV curve hysteresis. Similar models were applied to simulate transient voltage steps [239], open-circuit voltage transients [240], transient photocurrents [94], capacitance-voltage [109] and impedance spectroscopy [109].

Despite the success of these models in qualitatively describing the observed effects, it remains under debate whether mobile ions are sufficient to describe the working mechanism of perovskite solar cells. All models presented so far were applied to simulate a single experiment. Conclusions from only one experiment can be error-prone as we show in the following paragraph.

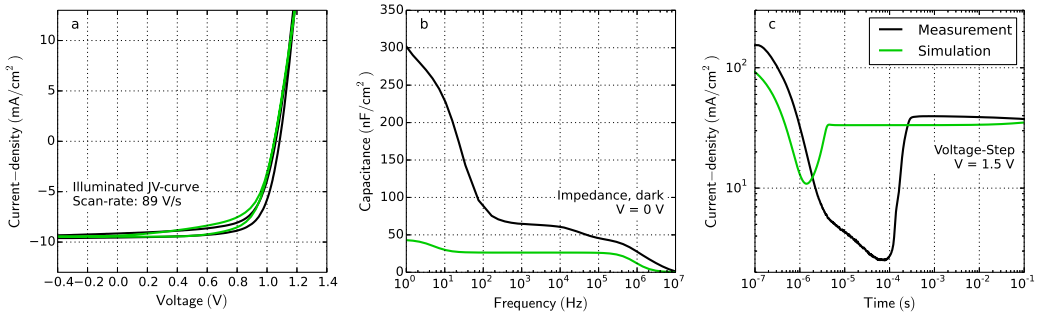

Figure 11.1: Example of simulation mismatch. Measurement (black) and simulation (green) of a planar perovskite solar cell. a) JV curve with a ramp rate of $89\,V/s$. b) Impedance spectroscopy in the dark. c) Transient current as response to a voltage step from 0 volt to 1.5 volt at $t = 0$. Despite the agreement of simulation and measurement in the JV curve, they do not match for impedance and voltage step experiments. Parameters extracted from JV curve fitting (a) are thus likely to be inaccurate.

We measure the current-voltage (JV) curve, impedance spectroscopy in the dark and a voltage step response of a methylammonium lead iodide (MAPI) perovskite solar cell (details on cell structure in section 11.3.3 Device Fabrication). Our numerical simulation model [111] is fitted to the transient JV curve. The hysteresis is well reproduced quantitatively as shown in Figure 11.1a. The same parameter set is used to simulate the impedance spectroscopy and the voltage step results. As shown in Figure 11.1b and Figure 11.1c the simulation does not reproduce the measurement results well. The parameter set describing the JV curve with hysteresis well, does not match with the impedance spectroscopy results or the transient voltage step. The parameters are inaccurate and might be misinterpreted

although the JV curve is reproduced.

In the past we have demonstrated parameter extraction of organic solar cells using numerical simulations [34, 125]. By fitting numerical simulations to measurement results of several experimental techniques the parameter correlation can be reduced significantly [34]. Moreover, we have shown that a rather simple drift-diffusion model with constant charge mobilities, discrete traps and ohmic contacts is sufficient to simultaneously reproduce JV curve, photo-CELIV, OCVD, TPC, capacitance-voltage, impedance and intensity-modulated photocurrent spectroscopy (IMPS) data for a bulk-heterojunction organic solar cell (see section 9.6 Comprehensive parameter extraction with numerical simulation).

In this study we present various measurements and simulations of a planar MAPI perovskite solar cell. Our simulation model incorporating mobile ions and charge traps is capable of describing the hysteresis of JV curves with varied scan rates, the dependence of the open-circuit voltage on the light intensity, transient photocurrent, impedance spectroscopy in the dark and under illumination and IMPS. The main signatures observed in all these experimental techniques are reproduced by the simulation model using one single parameter set for all simulations.

To the best of our knowledge this is the most comprehensive description of the device physics of perovskite solar cells up to now. We show that the major physical effects observed in perovskite solar cells can consistently be described by a device model incorporating inert mobile ions and traps. Based on our model we investigate the influence of mobile ions, traps and other parameters on the experimental results. In the last section we show a parameter analysis to determine which factors limit the device performance.

11.3 METHODS

11.3.1 *Experimental Methods*

All experiments were performed with the all-in-one measurement platform *Paios* 4.0 from Fluxim [110]. All experiments were computer-controlled and sequentially performed with minimal delay in order to minimize cell degradation between two measurements. A white LED was used as illumination source for all experiments. Eight nominally identical solar cells were characterized to test the reproducibility. Detailed information about the measurement system can be found in chapter 6 EXPERIMENTAL SETUP.

11.3.2 *Numerical Methods*

The simulation model used in this study is implemented in the simulation software *Setfos* 4.6 from Fluxim [111]. The charge generation profile within the MAPI layer is calculated by the transfer matrix method using wavelength-dependent

complex refractive indices of all layers.

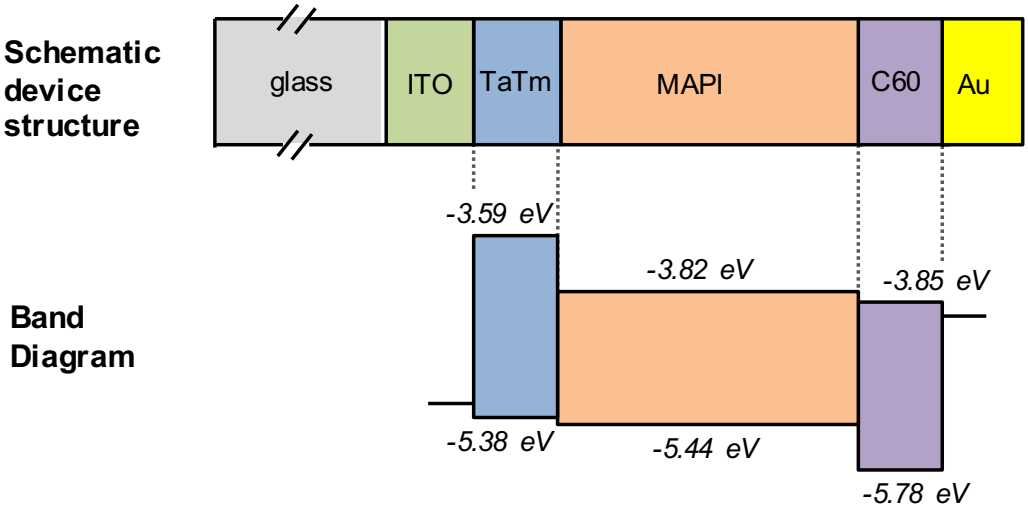

Figure 11.2: Device layout and band-diagram of the simulated device.

Drift-diffusion calculations are performed within the three layers TaTm, MAPI and C60 illustrated in Figure 11.2. All model equations are shown in chapter 7 PHYSICAL MODEL. Two mobile ionic species (one positive one negative) of the same density are allowed to move inside the MAPI layers. The interfaces to TaTm and C60 are treated as ion-blocking. In the MAPI layer $0.5\,eV$ deep traps lead to Shockley-Reed-Hall (SRH) recombination. SRH recombination is necessary to reproduce the ideality factor of approximately 2.0 as observed in the light-intensity dependence of the open-circuit voltage. An external series resistance is considered in the simulation accounting for the combined effect of the internal measurement resistor ($50\,\Omega$) of the voltage source, the measurement resistor for current measurement ($20\,\Omega$) and further parasitic resistances as for example in the transparent conducting oxide (TCO).

The impedance spectra and the intensity modulated photocurrent spectra (IMPS) are calculated from the Fourier transformation of a transient step response calculation as described by Ershov *et. al.* [122]. The calculation is explained in detail in section 8.1.1 Calculating frequency domain data from step-response.

We would like to stress the importance of taking the transport layers into account in such simulations. The voltage drop within the doped transport layers depends on their conductivity. The voltage drop inside the perovskite layer and the distribution of the mobile ions within the layer are consequently influenced by the contact layers [241]. The ion densities at the TaTm-MAPI and the MAPI-C60 interfaces are much lower when contact layers are considered in the simulation.

We assume an equal density of iodine vacancies (cations) and methylammonium (MA) vacancies (anions) to be present in the device where the MA vacancies have a much lower mobility. We show in section 11.4.4 Simulation results with one

mobile ionic specie that simulations with only iodine vacancies (cations) being mobile produce very similar results.

No direct interaction among ions is assumed and no interaction of ions with electrons, holes or traps takes place. The position of the ions however influences the electric field inside the device and thereby the charge transport.

11.3.3 *Device Fabrication*

The solar cells were fully vacuum processed using a previously reported protocol [65]. Briefly, the devices (scheme in Figure 11.2) were deposited in a p-i-n configuration onto indium tin oxide (ITO) coated glass slides. *N*4,*N*4,*N*4″,*N*4″-tetra([1,1′-biphenyl]-4-yl)-[1,1′:4′,1″-terphenyl]-4,4″-diamine (TaTm) was used as the hole transport material (HTM), either intrinsic or doped by co-sublimation with 2,2′-(perfluoronaphthalene-2,6-diylidene) dimalononitrile (F_6-TCNNQ). The fullerene C_{60} was used as the electron transport material (ETM) both intrinsic or doped by co-sublimation with *N*1,*N*4-bis(tri-*p*-tolylphosphoranylidene)benzene-1,4-diamine (PhIm). The MAPI perovskite films were prepared by dual source vacuum deposition of the two starting compounds, CH_3NH_3I and PbI_2, in a high vacuum chamber. The final device structure was ITO/TaTm:F_6-TCNNQ (40 nm)/TaTm (10 nm)/MAPI (500 nm)/C_{60} (10 nm)/C_{60}:PhIm (40 nm)/Ag (100 nm). The active cell area is 0.065 cm^2. Devices were fabricated at the university Valencia in Spain.

11.4 RESULTS AND DISCUSSION

We perform measurements on perovskite solar cells, fabricated as described in the section 11.3.3 Device Fabrication. To test the reproducibility 8 nominally identical devices were characterized. For the sake of better readability, we show only one representative device in this study. The simulation model as described in the section 11.3.2 Numerical Methods is applied to simulate the same characterization techniques as in the measurements. The parameters of the model are adjusted to reach an agreement between simulation and measurement. A combination of automated and manual fitting was used.

Figure 11.3 shows measurement and simulation data for nine distinct experiments. In Figure 11.3a-c JV curves measured forward and reverse are shown. The scan rate is varied from a) to c). The short-circuit current of 10 mA/cm^2 is low since a white LED is used for the illumination instead of a sun simulator. With scan rates below 1 V/s the hysteresis is very low. Only if very high scan rates up to 500 V/s are applied a pronounced hysteresis appears (Figure 11.3c). We simulate the same transient voltage ramp up and down to obtain an JV curve with hysteresis. At low scan rates the hysteresis is small in the simulation as well as in the measurement (Figure 11.3a). With higher scan rate a pronounced hysteresis appears in the measurement and is well reproduced by the simulation. Here we confirm that even hysteresis-free devices can have a hysteresis that is shifted to different time scales, consistent with the finding of Jacobs *et. al.* [109].

The dependence of the open-circuit voltage on the light intensity is shown in Figure 11.3d. Its ideality ($n_{id} = q/(k \cdot T) \cdot dVoc/d(ln(L))$) is clearly above 1.0 indicating dominant SRH recombination [125, 147, 40]. In the simulation an ideality factor higher than 1.0 is only achievable with trap-assisted recombination. The simulation reproduces the dependence of the open-circuit voltage on the light intensity.

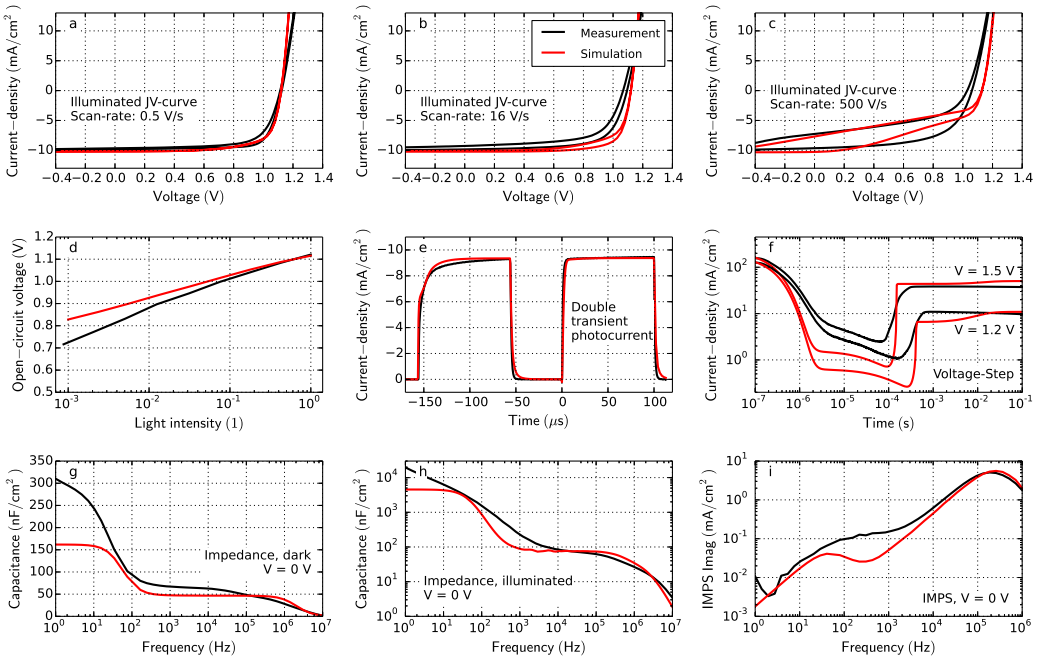

Figure 11.3: Measurement (black) and simulation (red) of the perovskite solar cell. a-c) IV curves with hysteresis and varied scan rates. The device is illuminated with a white LED. The short-circuit current is therefore lower compared to the short-circuit current under AM1.5. d) Dependence of the open-circuit voltage on the light intensity. e) Photocurrent as response to two subsequent light pulses. The first light pulse is from $-160\,\mu s$ to $-50\,\mu s$. The second light pulse from $0\,\mu s$ to $100\,\mu s$. f) Transient current as response to a voltage step in the dark in log-log representation. g) Impedance spectra in the dark in capacitance-frequency representation. h) Impedance spectra under illumination in capacitance-frequency representation. c) Intensity-modulated photocurrent spectroscopy (IMPS).

Figure 11.3e shows the transient current response to two subsequent light pulses. The measured current rise of the first pulse is significantly slower than the current rise of the second pulse. This behaviour is reproduced very well by the simulation using traps. During the first light pulse traps are filled slowly. In the subsequent pulse the traps are already filled, therefore the current rise is faster. If the delay time between the two pulses is increased to milliseconds the first and the second current rise are identical again. In this case all trapped charges are released during the delay time. Therefore, the double light pulse measurement is well suited to study trapping in perovskite solar cells.

In Figure 11.3f the transient current as response to a voltage step is shown. Richardson *et. al.* presented transient voltage step simulations on perovskite devices [239]. We use higher voltage steps than Richardson which allows us to study charge injection as we detail in the following.

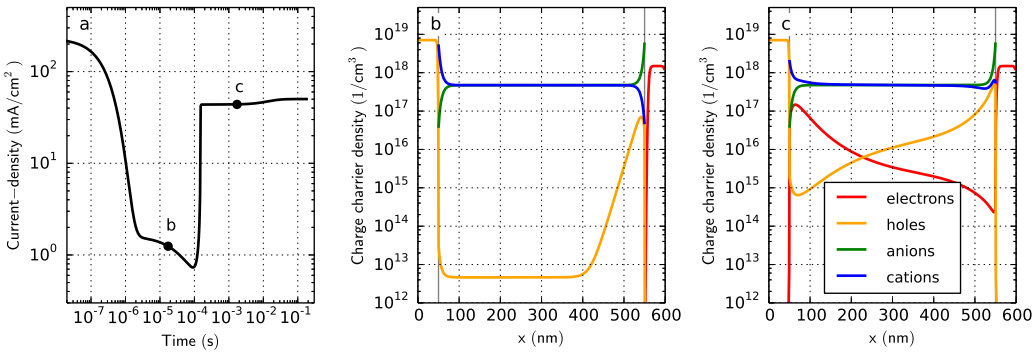

Figure 11.4: Simulation of a forward-bias voltage step from 0 to 1.5 volt. a) Transient current. b and c) Charge carrier density profiles of electrons, holes, anions and cations at two different time steps as marked in a. The HTM-perovskite and perovskite-ETM interfaces are located at 50 nm and 550 nm, respectively.

The current peak before 1 μs is the charging current of the device capacitance. Afterwards the current is small and then increases steeply at around 100 μs. To illustrate the origin of this effect we plot the spatial charge carrier density profiles in Figure 11.4. The device is preconditioned at 0 volt where the built-in voltage drives the cations (assumed to be iodine vacancies) to the hole contact layer. A few microseconds after the voltage step to 1.5 volt is applied, the ions are still at their steady-state position (Figure 11.4b). The accumulated cations hinder hole injection due to the strong electric field at the interface. After 1 millisecond the cations have moved away from the interface (Figure 11.4c) enabling charge injection. Charges recombine in the bulk or at the opposite interface and a steady-state current flows.

In the simulation (Figure 11.3 and Figure 11.4) the surface recombination is very weak. Therefore, electrons can accumulate at the hole contact and holes can accumulate at the electron contact (Figure 11.4c). The steepness of the current rise after 100 μs (Figure 11.4a) is influenced by the surface recombination. A comparison of a device with high and with low surface recombination is presented in section 11.4.6 Influence of the surface recombination.

We conclude: Voltage step experiments are well suited to study the charge injection behaviour of perovskite solar cells. A steep rise is an indication for low surface recombination.

Figure 11.3g shows the capacitance-frequency representation of an impedance measurement. The capacitance rise at low frequency ($< 100\,Hz$) is reproduced by the simulation. The transition frequency depends on the ion conductivity (ion density times the ion mobility). In Figure 11.5a simulation results with varied ion mobility are shown. The transition frequency of the capacitance varies with the mobility. Varying the ion density has the same effect. If ions are disabled in the

simulation the capacitance remains low at low frequencies.

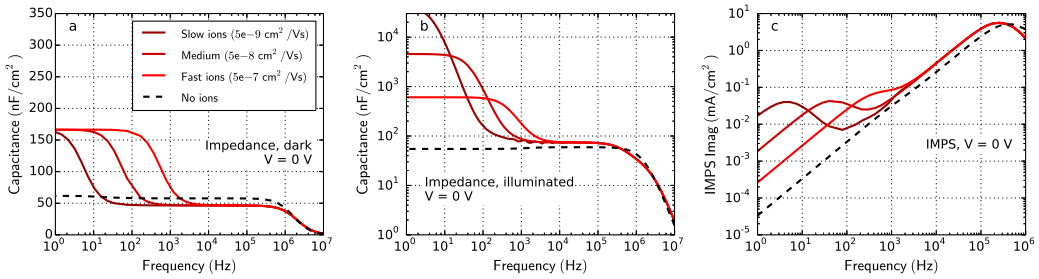

Figure 11.5: Simulation results with varied ion mobility and disabled ions (dashed line). a) Impedance spectroscopy in the dark. b) Impedance spectroscopy under illumination. c) Intensity-modulated photocurrent spectroscopy (IMPS).

Figure 11.3h shows impedance spectroscopy data under illumination. Under illumination the capacitance at low frequencies reaches extraordinarily high values, consistent with what has been reported in literature [108]. In these experiments the word *capacitance* can be misleading. Moia and co-workers described the behaviour as an *ionic-to-electronic current amplification* [91]. The idea behind this: The oscillating voltage moves the ions between the contacts. When ions are close to one contact injection is enhanced, if they are close to the other contact injection is suppressed. An increased injection enables a large electron-hole current to flow in phase with the modulated ions. The mobile ions only "open the door" for electronic charges. Since the ion accumulation is out-of-phase with the voltage modulation, also the electronic current is out-of-phase and a very high apparent capacitance is observed. The higher the bulk conductivity, the higher the observed capacitance. Hence, the observed capacitance increases with illumination. Our simulation reproduces this effect and capacitance values of more than $1\,\mu F/cm^2$ are reached at $1\,Hz$. The same mechanism is also well-explained by Jacobs *et. al.* using numerical simulation [109]. The magnitude of the capacitance as well as the frequency of the onset depend on the ion mobility as shown in Figure 11.5b. Without mobile ions the capacitance remains low.

Figure 11.3i shows intensity-modulated photocurrent spectroscopy (IMPS) data. In this technique the light intensity is modulated and the current response is measured [125, 208, 200]. The peak of the imaginary part of the IMPS signal is often attributed to a charge transport time [125]. In perovskite solar cells the second peak or shoulder at low frequency is of special interest. Correa-Baena *et. al.* observed a peak at low frequencies and speculated that mobile ions could be the cause [207]. Our measurement shows a shoulder rather than a peak in a similar frequency range. The IMPS simulation reproduces this peak. We can therefore confirm the hypothesis by Correa-Baena and co-workers, that mobile ions are responsible for the low-frequency peak. The frequency of the peak depends on the ion mobility as shown in Figure 11.5c. Without mobile ions the peak vanishes.

We conclude: The three experiments in the frequency domain are well suited to study ion conductivity.

11.4.1 *Device and material parameters*

Table 11.1 and Table 11.2 show the material and device parameters obtained from the fit and used in all simulations shown in Figure 11.3. We want to stress again that the parameter set was identical for every simulation and only the operating condition i.e. characterization technique was varied.

Parameter	**HTM, TaTm**	**MAPI**	**ETM, C60**
Thickness	$50\,nm$	$500\,nm$	$50\,nm$
Electron mobility	-	$0.2\,cm^2/Vs$	$8.9 \cdot 10^{-4}\,cm^2/Vs$
Hole mobility	$1.5 \cdot 10^{-3}\,cm^2/Vs$	$0.1\,cm^2/Vs$	-
Recombination constant	-	$1 \cdot 10^{-10}\,cm^3/s$	-
Relative Permittivity	3 [143]	35 [242]	3.9 [143]
HOMO energy	$5.38\,eV$	$5.44\,eV$	$5.77\,eV$
LUMO energy	$3.59\,eV$	$3.82\,eV$	$3.85\,eV$
Electron trap density	-	$1.2 \cdot 10^{16}\,cm^{-3}$	-
Electron trap depth	-	$0.5\,eV$	-
Electron trap electron capture rate	-	$3 \cdot 10^{-10}\,cm^3/s$	-
Electron trap hole capture rate	-	$3 \cdot 10^{-12}\,cm^3/s$	-
n-doping density	-	-	$1.5 \cdot 10^{18}\,cm^{-3}$
p-doping density	$7 \cdot 10^{18}\,cm^{-3}$	-	-
Mobile cation density	-	$5 \cdot 10^{17}\,cm^{-3}$	-
Mobile anion density	-	$5 \cdot 10^{17}\,cm^{-3}$	-
Cation mobility	-	$5 \cdot 10^{-8}\,cm^2/Vs$	-
Anion mobility	-	$1 \cdot 10^{-14}\,cm^2/Vs$	-
Effective density of states	$1 \cdot 10^{27}\,m^{-3}$	$6 \cdot 10^{25}\,m^{-3}$	$1 \cdot 10^{27}\,m^{-3}$

Table 11.1: Layer-dependent simulation parameters used for all simulations in Figure 11.3, Figure 11.4 and Figure 11.5.

Parameter	Value
External series resistance	$25\,\Omega$
Device area	$0.065\,cm^2$
Temperature	$293\,K$
Boundary condition top electrode hole-density	$6.8 \cdot 10^{18}\,cm^{-3}$
Boundary condition bottom electrode electron-density	$6.5 \cdot 10^{17}\,cm^{-3}$

Table 11.2: Layer-independent simulation parameters used for all simulations in Figure 11.3, Figure 11.4 and Figure 11.5.

We present a numerical device model for perovskite solar cells that is capable to describe consistently all major effects found in a variety of opto-electrical experiments. The electron and hole mobilities of the perovskite layer are $0.2\,cm^2/Vs$ and $0.1\,cm^2/Vs$, respectively. This is at the lower end of published mobilities for polycrystalline MAPI perovskites ($0.1 - 25\,cm^2/Vs$ [81]). In our drift-diffusion model the charge carrier mobility is an effective macroscopic quantity of the layer including grain boundaries. The low bulk mobility might be explained by the rather small crystals ($\sim 100\,nm$ [65]) of our perovskite solar cells. The recombination coefficient of $1 \cdot 10^{-10}\,cm^3/s$ lies in the expected range ($1 \cdot 10^{-9}$ to $1 \cdot 10^{-10}\,cm^3/s$ [235]). The trap depth of $0.5\,eV$ was chosen according to results of Baumann *et. al.* from thermally stimulated currents [213].

11.4.2 *Governing physical effects*

When mobile ions accumulate at an interface with a transport layer (HTM or ETM), the charge injection property of this interface is altered. With applied voltage ions migrate from one interface to the other. These two effects cause the JV curve hysteresis (Figure 11.3a-c), the high capacitance at low frequencies under illumination (Figure 11.3h) and the delayed current-rise in the voltage pulse experiments (Figure 11.3f).

The simulation results of Figure 11.3 are very sensitive to the doping density of the boundary layers TaTm and C60. If the contact layers are highly conductive most of the potential drops within the perovskite layer [241]. Ions compensate this voltage drop when they move to the interfaces. The JV curve hysteresis does therefore most probably depend on the conductivity of the boundary layers. A high conductivity would lead to a higher potential drop inside the bulk and therefore to a more pronounced JV curve hysteresis.

In solar cells with small built-in fields surface recombination plays an important role. Due to the low electric field charges may reach the opposite contact and recombine there. A passivated contact can hinder such recombination. In our material system the interface recombination is suppressed in a similar way as it is done in highly efficient OLED stacks [243]. The addition of $10\,nm$ of intrinsic

transport layer material on both sides leads to an effectively suppressed surface recombination [65]. Omitting these thin intrinsic passivation layers alters the voltage step response as discussed section 11.4.6 Influence of the surface recombination. Our model results are consistent: Decent agreement between simulation and measurement is only reached with a low surface recombination.

We have shown in chapter 10 that even in the presence of mobile ions the JV curve hysteresis vanishes if the surface recombination is sufficiently low and the charge carrier ”lifetime” is sufficiently high. In the present case the JV curve hysteresis appears due to the small bulk ”lifetime” of charge carriers. In the section 11.4.7 IV-curve hysteresis we show that improving the bulk-quality (lower SRH recombination and higher charge carrier mobility) reduces the hysteresis significantly.

11.4.3 *Simulation results with and without mobile ions*

In this section the influence of the mobile ions on all experimental techniques is investigated. Figure 11.6 shows the comparison of the simulation result with and without mobile ions. From Figure 11.6c it is evident that the IV-curve hysteresis only occurs in the presence of mobile ions in our model.

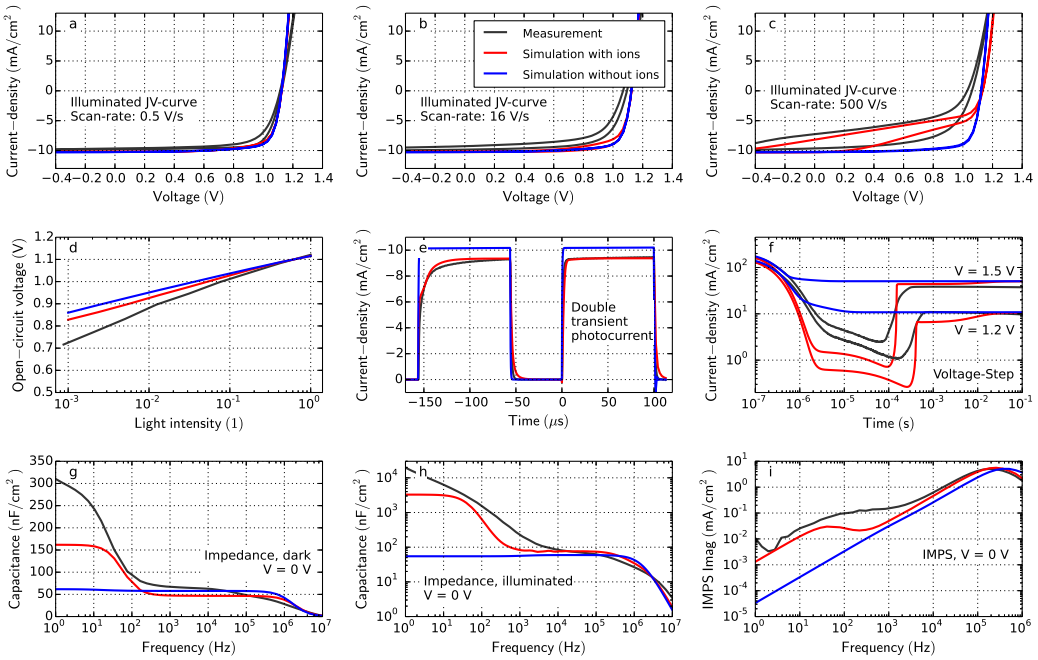

Figure 11.6: Comparison of simulation with (red) and without (blue) mobile ions. The measurement is shown in black. The figure type is identical to Figure 11.3.

The slow current-rise observed in the double light pulse (Figure 11.6e) caused by slow trapping disappears without mobile ions. The mobile ions do not move on these time-scales, but their accumulation at the interface in steady-state lowers the effective field in the device. In the case without the mobile ions the trap-filling is still a slow process, but the current can rise fast enough due to the high built-in field. The characteristic current-rise in Figure 11.6f disappears without mobile ions. Charges can be injected from the very beginning of the voltage step.

The low frequency effects in impedance spectroscopy (Figure 11.6g and Figure 11.6h) disappear when ions are disabled. The same is true for the low frequency shoulder in IMPS in Figure 11.6i.

11.4.4 *Simulation results with one mobile ionic specie*

In this section the influence of the different ionic species on all experimental techniques is investigated. There are several ionic species moving inside a methylammonium perovskite solar cell. There is convincing evidence, that iodine vacancies (positively charged) are mobile [93, 220, 96]. There is evidence that methylammonium vacancies (negatively charged) are mobile too but have a much lower mobility [96, 95, 90].

In literature numerical simulations with mobile ions have been performed with one species mobile and one species immobile [99, 239, 100] as well as with two mobile species [109, 98, 240].

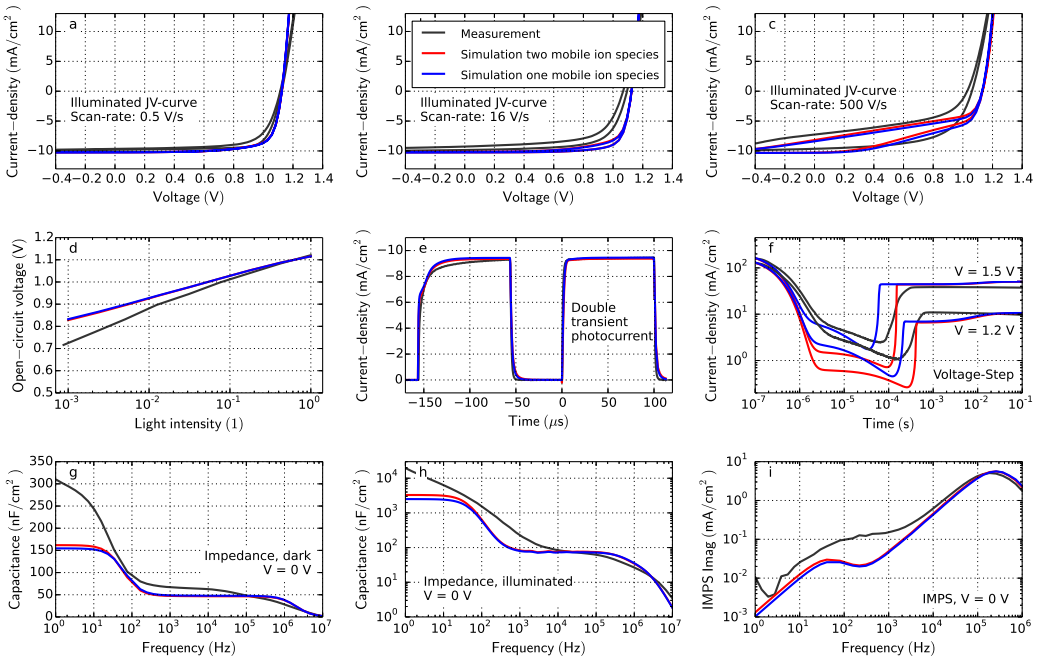

Figure 11.7: Comparison of simulation with two mobile ionic species (red) and with one mobile ionic species (blue). The measurement is shown in black. The figure type is identical to Figure 11.3.

Figure 11.7 shows a comparison between those two simulations. The red curve is the same as in Figure 11.3 using two mobile species. The blue line is the simulation result using one mobile type (positively charged iodine vacancies) and negatively charged MA vacancies of the same density as homogeneously distributed fixed negative ionic cores.

Interestingly, the results of the two simulations look almost identical. Apart of the rise-time in the transient voltage step experiment (Figure 11.7f), all major effects are also observed if only one ion type is mobile.

We conclude that it is not of great importance to the simulation result, whether one or two mobile ionic species are considered.

11.4.5 *Simulation results with and without traps*

In this section the influence of traps on the simulation results is studied. Figure 11.8 shows the comparison between simulation with traps and Shockley-Read-Hall (SRH) recombination and without traps.

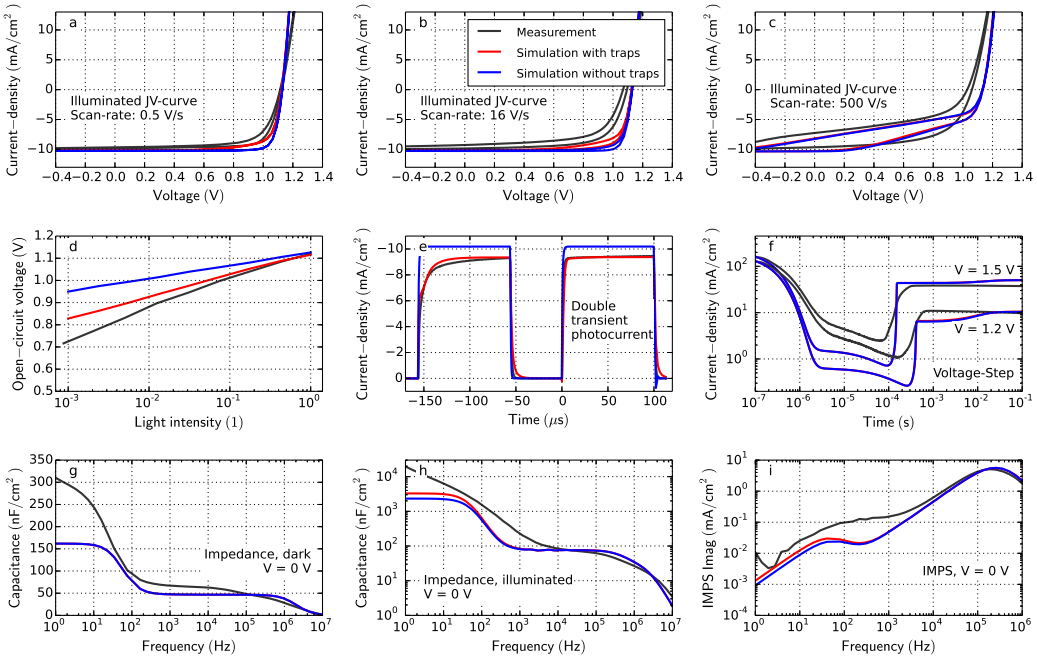

Figure 11.8: Comparison of simulation with trapping (red) and without trapping (blue). The measurement is shown in black. The figure type is identical to Figure 11.3.

Without traps and consequently without SRH-recombination the fill factor is increased (Figure 11.8a), the ideality factor is close to 1.0 (Figure 11.8d). If trapping is disabled in the simulation the current-rise in the double light pulse experiment (Figure 11.8e) is faster. Both the first and the second response look identical. All other experiments in Figure 11.8 are only marginally influenced by trapping and SRH-recombination.

11.4.6 *Influence of the surface recombination*

The shape of the current-rise as response to a voltage step depends critically on the surface recombination. The blue line in Figure 11.9a shows the simulation result of the perovskite solar cell as in Figure 11.3f. In this case the surface recombination is very low. The green line shows the simulation result with a high surface recombination. The rise-time is significantly slower compared to the case with passivated surfaces.

Surface recombination is modeled by a thin layer close to the interface where the recombination pre-factor is much larger than in the bulk.

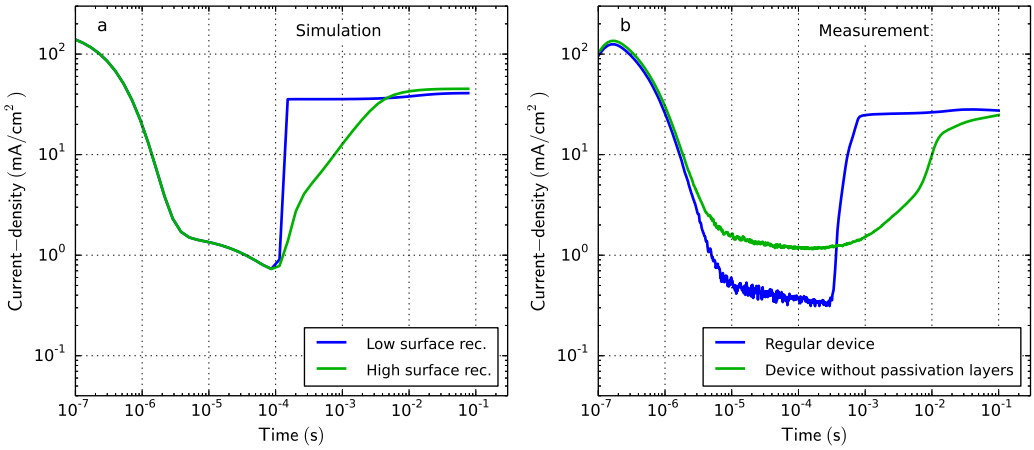

Figure 11.9: Transient current as response to a voltage step. a) Numerical simulation with varied surface recombination. b) Measurement of two different MAPI perovskite solar cells.

To further investigate this effect, we fabricated devices with and without a 10 *nm* thick intrinsic passivation layer between perovskite and the doped ETL and HTL, respectively. These extra layers are expected to supress surface recombination [65]. Voltage-step measurements on devices with and without these passivation layers are shown in Figure 11.9b. The current rise of the device without passivation layers is much slower. This behaviour is consistent with the simulation with a high surface recombination.

We conclude that a steep current-rise in the voltage step experiment is an indicator for well passivated surfaces.

11.4.7 *IV-curve hysteresis*

Even in the presence of mobile ions a perovskite solar cell can be hysteresis-free [100]. In the chapter 10 we showed that a sufficiently high charge carrier lifetime in combination with a low surface recombination is required for a minimal hysteresis. Here the more advanced model of this chapter is applied to reproduce the results from chapter 10.

The device under investigation in the current chapter has a good surface quality (low surface recombination) but a low bulk quality (low charge carrier lifetime). The simulated IV-curve with hysteresis is shown in Figure 11.10b.

In Figure 11.10a a device with low bulk quality and lower surface quality is shown. Here the hysteresis is the largest. Figure 11.10c shows a device with a high bulk quality but a low surface quality. A pronounced hysteresis is observed. Only in the case with high bulk and surface quality the hysteresis is minimal as shown in Figure 11.10d. We thereby confirm the results from chapter 10. If the surface recombination is low (high surface quality) and the charge carrier lifetime is high (high bulk quality) then charges can be extracted even against the electric field created by the mobile ions and the device shows only insignificant hysteresis in forward and reverse IV scans.

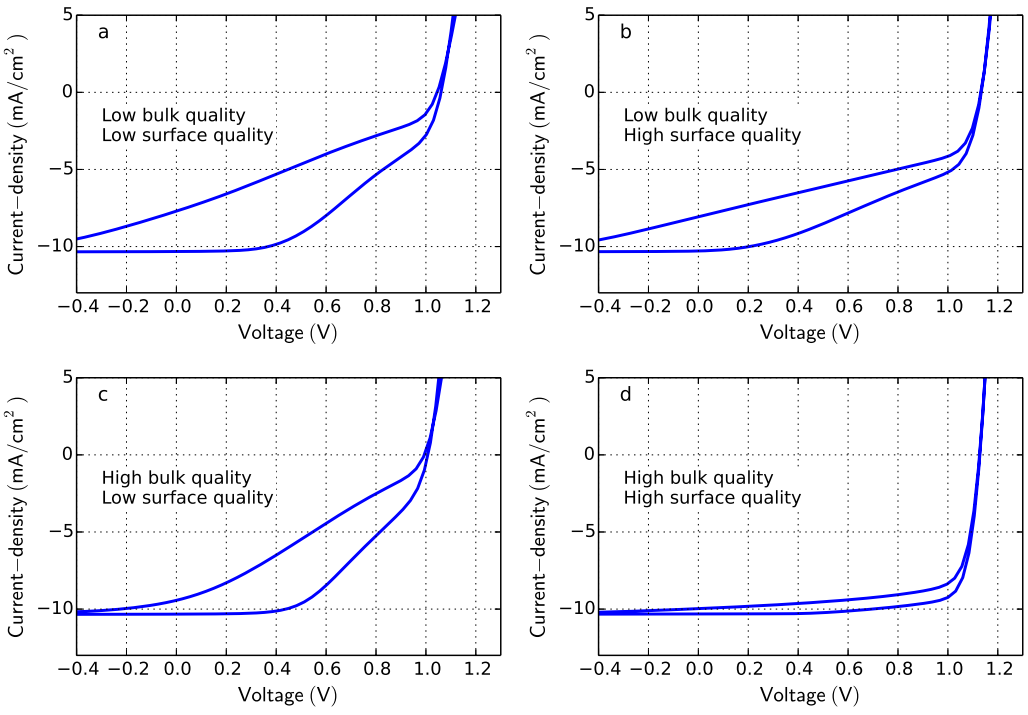

Figure 11.10: Simulations of IV-curves with hysteresis for different combinations of low and high bulk and surface qualities. A ramp-rate of 16 V/s has been used.

11.4.8 *Reverse voltage step*

To complement the set of experiments shown in Figure 11.3 we perform an additional experiment: A voltage step from forward to reverse. Figure 11.11 shows the measurement and simulation of a voltage step from $+3$ volts to -3 volts. In this case the simulation fails to describe the measurement.

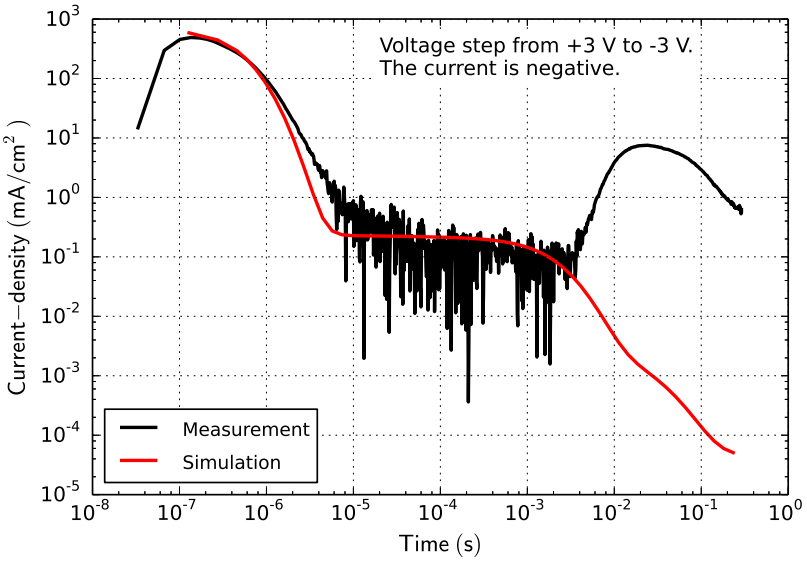

Figure 11.11: Measurement and simulation result of a MAPI perovskite solar cell. A voltage step to $+3$ volt is applied for $300\,ms$. At $t = 0$ the voltage is changed to -3 volt. The current response is shown. The simulation fails to describe the measured current.

In the measurement a reverse current is observed starting at 3 milliseconds and vanishing after 1 second. The simulated current shows a time-of-flight (TOF) [50, 210] behaviour. The ions are preconditioned in forward direction. Most of the iodine vacancies accumulate within the first nanometres close to the ETM interface. When the voltage is reversed these ions migrate through the bulk until they reach the HTM interface. The ion movement leads to a drift current of around $0.2\,mA/cm^2$. When the interface is reached after the transit time of 3 milliseconds the current goes to zero in the simulation. At this point the additional current peak, observed in the measurement, starts. The integrated current results in a sheet charge density of $4.4 \cdot 10^{13}\,cm^{-2}$. If the assumed ion density of $5 \cdot 10^{17}\,cm^{-3}$ is integrated over the MAPI thickness a comparable sheet charge of $2.5 \cdot 10^{13}\,cm^{-2}$ is obtained. We therefore speculate that a chemical reaction occurs at one of the interfaces leading to a reduction or oxidation of the contact material induced by the mobile ions. This effect does not occur in MAPI perovskite solar cells with TiO_2 and Spiro-OMeTAD contact layers, therefore it seems to be dependent on the choice of contact material. Alternatively, reverse injection may be responsible for this transient current. The effect deserves further investigation and the simulation model may need to be adapted accordingly.

11.4.9 *Model limitations*

In this section we discuss further possible model limitations.

1. In the presented model the interfaces between layers are sharp and the layers are homogeneous. The devices studied here show an interface roughness of about $10\,nm$ [65]. Ions may accumulate preferably in the valleys of the rough material interface "landscape". Their distribution therefore may not be homogenous as assumed in the one-dimensional model.

2. In our model two mobile ion species (positive and negative) are used. In reality there may be more than two active species [101, 221]. In section 11.4.4 Simulation results with one mobile ionic specie we show that a model with only one mobile species however produces very similar effects.

3. We use constant mobilities for the migration of ions. In reality ion migration may be field dependent and dispersive. Furthermore, Shao *et. al.* showed that ions migrate preferably along grain boundaries [102]. In such a case two mobilities for the same ion type might be required for its description: A bulk ion mobility and an ion mobility along the grain boundaries.

4. We do not impose an upper limit on the local ion concentration at the layer boundaries. This is a subject of our ongoing investigations and will be discussed elsewhere.

5. The ions of the perovskite layer may migrate into the adjacent electron and hole transport layers. This could lead to a degradation of these layers, a reversible chemical reaction or a dynamic doping of ETM or HTM. Such effects seem difficult to numerically describe but may be necessary to capture all relevant physical effects.

11.4.10 *Parameter Study*

In this section the influence of the model parameters on the device performance is studied. On the basis of the simulation results we perform steady-state JV curve simulations. This allows us to assess the influence of specific parameters on the power conversion efficiency. The power conversion efficiency and the fill-factors are shown in Figure 11.12.

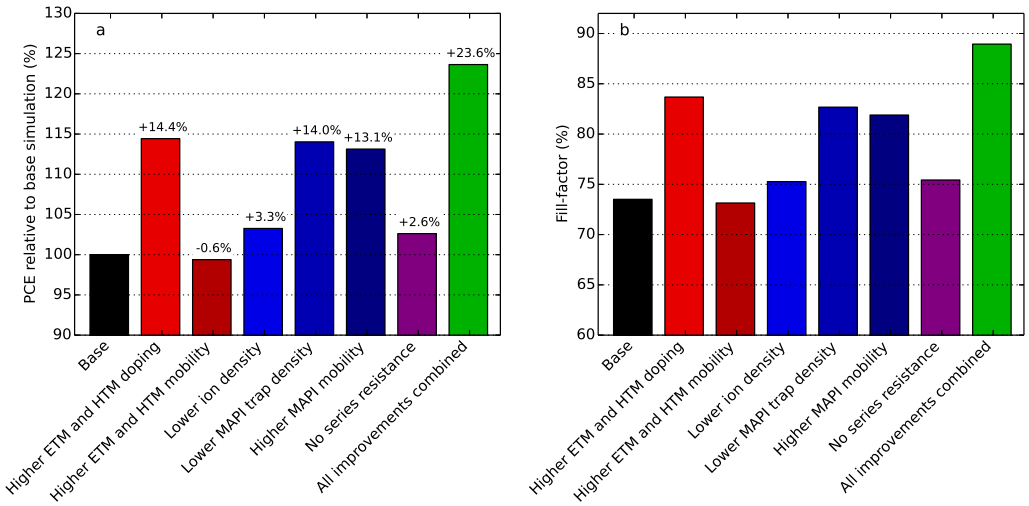

Figure 11.12: Parameter variation on the basis of the simulation results of Table 11.1 and Table 11.2. a) Power conversion efficiency improvement for different parameter variations. b) Fill-factor for different parameter variations.

A doping density of $10^{19}\,cm^{-3}$ in both transport layers improves the charge carrier extraction at the contacts and leads to a higher fill-factor. The resistive losses in the ETM and HTM are however not limiting the performance. Using 10 times higher electron and hole mobilities does not improve the performance.

A smaller density of mobile ions (10% compared to the base simulation) leads only to a minor device improvement of 3.3%. The mobile ions are not a major obstacle for efficient device operation if the mobility is high enough and the surface recombination is low enough [219]. Reducing the trap density to 10% of the base simulation leads to a large improvement by 14% due to reduced SRH-recombination. A similar improvement is reached for 10 times higher electron and hole mobilities in the perovskite material leading to better charge extraction. The external series resistance as caused by the lateral conductivity of the TCO can reduce the performance significantly [115]. Reducing it to zero leads to an improvement of only 2.6% in our case. With all the effects combined a relative performance improvement of 23% is obtained. The improvement stems mainly from a higher fill-factor (Figure 11.12b). Further performance improvements could be achieved by optimized light management [26].

11.5 CONCLUSIONS

We performed a variety of characterization experiments with vacuum deposited methylammonium lead iodide perovskite solar cells, including JV curves with different scan rates, light-intensity dependent open-circuit voltage, impedance spectroscopy, intensity-modulated photocurrent spectroscopy (IMPS), transient photocurrents and transient voltage steps.

We developed a multi-layer drift-diffusion simulation model incorporating mobile ions to simulate all experimental techniques. A decent agreement between simulation and measurement is reached for all techniques using only one parameter set in the simulation. To the best of our knowledge, this is the first study presenting a consistent device model that is capable to simultaneously describe transient, steady-state and frequency-dependent experimental results of perovskite solar cells.

Our study shows that it is necessary to consider mobile ions and Shockley-Reed-Hall (SRH) recombination in the simulation to reproduce experimental results. Whether one, two or even more different ionic species are incorporated does not play a major role for reproducing the experimental results by simulation. Further model complexity like ferroelectricity or considering individual grain boundaries is not required to understand and describe the device physics of perovskite cells.

As the physical processes in perovskite solar cells are complex, an approach combining different experimental techniques is required to achieve consistent, accurate and reliable results. We show a possible path to reach this goal and discuss the limitations of this approach. Using the device model with the derived parameters allows us to study different paths to improve the cell performance.

The delayed current peak resulting from a voltage step to a negative voltage can however not be reproduced with the drift-diffusion model. We speculate that either reverse injection or a reversible redox reaction of ions with the contact layer material may be responsible for this effect. Further effort is required to extend the device model accordingly.

Part V

SUMMARY AND OUTLOOK

12 SUMMARY AND OUTLOOK

12.1 SUMMARY

Third generation solar cells are promising technologies for helping to meet today's global energy challenges. They could be used for a variety of new applications such as on the facades of buildings or in tandem architectures with silicon solar cells to increase module power conversion efficiencies. Understanding the physical processes in third generation solar cells is essential to improve power conversion efficiency and extend device lifetime. Performance limitations may be identified and alleviated.

The key conclusion of this thesis is that several experimental methods should be combined when investigating physical processes in third generation solar cells. Analyzing single experimental results can be prone to error since the physical processes in third generation solar cells are very complex. The device and material parameters describing these processes are highly entangled and not easy to separate.

Combining measurements with numerical simulations is a powerful approach to obtain insight into the underlying physics. A comprehensive and accurate parameter extraction is demonstrated on an organic polymer-fullerene solar cell in the thesis (see section 9.6 Comprehensive parameter extraction with numerical simulation). Nine different experimental techniques were measured and simulated. The simulation and measurement results agree very well indicating that the major physical processes can be described by the model. A correlation matrix is calculated for the simulation parameters showing that parameter correlation is significantly reduced when several experiments are combined enabling accurate parameter identification. **To the best of my knowledge this is the first publication providing such a broad range of experimental measurements in combination with simulation for organic solar cells.**

The thesis further presents a broad review of solar cell device characterization techniques (see section 9.4 Characterization techniques). Simulation results for all characterization techniques show the influence of device and material parameters on each characterization technique. The overview aims to allow experimentalists to better understand experimental results and identify performance limiting factors.

In the second study the commonly observed hysteresis in the current-voltage curve of organo-metal halide perovskite solar cells is investigated. There is convincing evidence that high densities of mobile ionic defects are present in

these materials. Consequently we extended the device model to include mobile ions within the active layer. The study presents a plausible explanation for the current-voltage curve hysteresis and explains the physical processes involved. **It is shown that IV-curve hysteresis is only present in perovskite solar cells if bulk and surface recombination are high enough.** This finding presents a plausible explanation for the fact that high efficiency perovskite solar cells often have lower hysteresis than inefficient devices (see chapter 10 WHY PEROVSKITE SOLAR CELLS WITH HIGH EFFICIENCY SHOW SMALL IV-CURVE HYSTERESIS).

In organic solar cells the features in various opto-electronic experiments can be described accurately by our drift-diffusion model as demonstrated in the first study. The device physics underlying organo-metal halide perovskite solar cells are not yet well understood however. Several effects frequently observed in experiments are only partially understood by the scientific community. We further extended our drift-diffusion model with additional continuity equations describing ionic transport. These are fully coupled with the electronic drift-diffusion equation enabling optoelectronic characterization techniques to be more accurately simulated in perovskite solar cells.

Seven different experiments were performed on a methylammonium lead iodide (MAPI) perovskite solar cell and successfully modeled by drift-diffusion including mobile ions (see chapter 11 CONSISTENT DEVICE SIMULATION MODEL FOR PEROVSKITE SOLAR CELLS). The influence of different material and device parameters on experiments and device performance was investigated and discussed. This work contributes to a comprehensive physical description of perovskite solar cells.

12.2 OUTLOOK

To date drift-diffusion simulations incorporating mobile ions have not been able to fully reproduce all the observed features present in measurements of MAPI perovskite solar cells. Also in this thesis the agreement between simulation and measurement of the perovskite solar cell is not as good as in the case of the organic solar cell. Furthermore, the reverse current of the negative voltage step on the MAPI perovskite could not be reproduced by the model (see Figure 11.11). Further investigations are necessary to identify the physical origin of these effects. We speculate that a **reversible chemical reaction may take place at the interface at which mobile ionic charge has accumulated**. Alternatively, the reverse current might stem from a temporary reverse injection depending on the position of the mobile ions. Moreover, ion migration into the neighboring transport layers may be considered in a future model extension.

A further model extension may include a maximum ion density. In our current model the ion density can become arbitrarily large locally. Incorporating a maximum ion density would take into account the fact that ions have a radius and require space.

The model may be refined by incorporating a field-dependent mobility for the ions.

The algorithms for automatic parameter extraction by fitting numerical simulations to measurement data could be further optimized. Currently a good deal of manual work is still required to obtain nice results. A combination of *simulated annealing* and *Levenberg-Marquardt* fitting could be one possible route towards less expensive, robust algorithms. Applying neural networks to find good starting values for a gradient fitting algorithm could save computational time. These neural networks could be trained with random simulation data.

More experimental techniques for perovskite solar cells could be developed with the aim of better separating ionic and electronic effects. Temperature-dependent measurements on perovskite solar cells may also provide additional insight into the device physics and would further test the model's capabilities.

The next step in the understanding of the device physics is to investigate several perovskite devices by varying certain properties. For example, devices with varied active layer thickness or different contact materials could be investigated. This could lead to a better understanding of surface states responsible for surface recombination.

We found that the voltage step response in the dark is a sensitive method for assessing the passivation effect of contact materials. Observations like these may help to establish new standard techniques for perovskite cell testing.

One of the major challenges for organic and perovskite solar cells is their stability. Both materials are sensitive to moisture and air. *Litos*, a new product capable of stressing multiple solar cells in parallel over a timescale of months with well-defined temperature and atmospheric control, is currently in development at *Fluxim*. In combination with *Paios* it will be possible to perform the full compliment of experimental *Paios* techniques iteratively during the device degradation process. This promises to provide a consistent set of data that could help identify the origins of device degradation.

The methodology of this thesis may also be applied to organic light emitting diodes (OLED) and perovskite LEDs.

All these steps could lead to better understanding of the physics of third generation solar cells and provide ways to improve their lifetime and efficiency. Perovskite-silicon tandem solar cells are a promising technology to improve the power conversion efficiency of solar modules and thereby may contribute to the global energy transition. Perovskites and organic solar cells will diversify the usage of solar energy due to their versatile usage for example in the facades of buildings. Significant long-term growth of all renewable energy sources will be required to meet the climate targets of Paris and drive the transformation from a fossil fuel- to renewables-based economy.

13

ACKNOWLEDGEMENTS

I acknowledge the following people who supported this work:

- Prof. Dr. Wolfgang Brütting (University Augsburg), examiner
- Prof. Dr. Armin Reller (University Augsburg), co-examiner
- Prof. Dr. Liviu Chioncel (University Augsburg), board of examiners
- Prof. Dr. Beat Ruhstaller (Fluxim AG, ZHAW), local supervisor
- Andreas Schiller (Fluxim AG, ZHAW) for implementing mobile ions in the *Setfos* solver.
- Dr. Philip Calado (Imperial College London) for proof-reading and discussions
- Dr. Simon Züfle (ZHAW) for proof-reading and discussions
- Dr. Evelyne Knapp (ZHAW), Dr. Kurt Pernstich (ZHAW) and Dr. Sandra Jenatsch (Fluxim AG) for discussions
- Adrian Gentsch (Fluxim AG) for collaboration on the *Paios* development
- Cyrill Bolliger for providing the LaTeX template
- The research group at university Valencia for fabrication of the planar perovskite solar cells (Jorge Avila, Daniel Perez-del-Rey, Chris Dreessen, Dr. Kassio Zanoni, Dr. Michele Sessolo and Prof. Dr. Henk Bolink).
- The research group at EMPA Switzerland for fabrication of mesoporous perovskite solar cells (Dr. Mohammed Makha, Matthias Diethelm and Dr. Roland Hany).
- The research group at Karlstad University Sweden for the fabrication of the organic solar cell (Dr. Rickard Hansson and Prof. Dr. Ellen Moons)

14 PUBLICATIONS LIST

First author publications:

- **Transient photocurrent response of organic bulk heterojunction solar cells**
  Martin Neukom, Nils Reinke, Kai Brossi, Beat Ruhstaller, SPIE Photonics Europe, 77220V (2010) [114].
- **Charge extraction with linearly increasing voltage: A numerical model for parameter extraction**
  Martin Neukom, Niels Reinke, Beat Ruhstaller, Solar Energy 85, 1250–1256 (2011) [115].
- **Reliable extraction of organic solar cell parameters by combining steady-state and transient techniques**
  Martin Neukom, Simon Züfle, Beat Ruhstaller, Organic Electronics 13, 2910–2916 (2012) [34].
- **Charge Carrier Dynamics of Methylammonium Lead-Iodide Perovskite Solar Cells**
  Martin Neukom, arXiv:1611.06425v1 (2016) [36].
- **Why perovskite solar cells with high efficiency show small IV-curve hysteresis**
  Martin Neukom, Simon Züfle, Evelyne Knapp, Mohammed Makha, Roland Hany, Beat Ruhstaller, Solar Energy Materials and Solar Cells 169, 159–166 (2017) [219].
- **Opto-electronic characterization of third-generation solar cells**
  Martin Neukom, Simon Züfle, Sandra Jenatsch, Beat Ruhstaller, Science and Technology of Advanced Materials, 19:1, 291-316 (2018) [125].
- **Consistent Device Simulation Model Describing Perovskite Solar Cells in Steady-State, Transient, and Frequency Domain**
  Martin Neukom, Andreas Schiller, Simon Züfle, Evelyne Knapp, Jorge Avila, Daniel Perez-del-Rey, Chris Dreessen, Kassio Zanoni, Michele Sessolo, Henk Bolink, Beat Ruhstaller, ACS Appl. Mater. Interfaces, 11, 26, 23320-23328 (2019) [238].

Co-author publications:

- **Improved efficiency of bulk heterojunction hybrid solar cells by utilizing CdSe quantum dot–graphene nanocomposites**
  Michael Eck, Chuyen Van Pham, Simon Züfle, Martin Neukom, Martin Sessler, Dorothea Scheunemann, Emre Erdem, Stefan Weber, Holger Borchert, Beat Ruhstaller and Michael Krüger, Phys. Chem. Chem. Phys., 16(24):12251– 12260, (2014) [244].

- **Influence of Molybdenum Oxide Interface Solvent Sensitivity on Charge Trapping in Bilayer Cyanine Solar Cells**
  Sandra Jenatsch, Roland Hany, Anna Veron, Martin Neukom, Simon Züfle, Andreas Borgschulte, Beat Ruhstaller, and Frank Nüesch, The Journal of Physical Chemistry C, 118(30):17036–17045, (2014) [194].

- **An Effective Area Approach to Model Lateral Degradation in Organic Solar Cells**
  Simon Züfle, Martin T. Neukom, Stephane Altazin, Marc Zinggeler, Marek Chrapa, Ton Offermans, and Beat Ruhstaller, Advanced Energy Materials, 1614–6840 (2015) [116].

- **The use of charge extraction by linearly increasing voltage in polar organic light-emitting diodes**
  Simon Züfle, Stephane Altazin, Alexander Hofmann, Lars Jäger, Martin T. Neukom, Tobias D. Schmidt, Wolfgang Brütting, and Beat Ruhstaller, Journal of Applied Physics, 121(17):175501 (2017) [157].

- **Determination of charge transport activation energy and injection barrier in organic semiconductor devices**
  S. Züfle, S. Altazin, A. Hofmann, L. Jäger, M. T. Neukom, W. Brütting, and B. Ruhstaller, Journal of Applied Physics, 122(11):115502 (2017) [158].

- **Quantitative analysis of charge transport in intrinsic and doped organic semiconductors combining steady-state and frequency-domain data**
  S. Jenatsch, S. Altazin, P.-A. Will, M. T. Neukom, E. Knapp, S. Züfle, S. Lenk, S. Reineke, and B. Ruhstaller, Journal of Applied Physics, 124 (10):105501 (2018) [245].

- **Improved Hole Injection in Bulk Heterojunction (BHJ) Hybrid Solar Cells by Applying a Thermally Reduced Graphene Oxide Buffer Layer**
  Alfian F.Madsuha, Chuyen Van Pham, Michael Eck, Martin Neukom, Michael Krueger, Journal of Nanomaterials, 2019:1–10 (2019) [246].

Part VI

APPENDIX

15 BIBLIOGRAPHY

15.1 BIBLIOGRAPHY

[1] Johan Rockström, Will Steffen, Kevin Noone, Åsa Persson, F. Stuart Chapin, Eric F. Lambin, Timothy M. Lenton, Marten Scheffer, Carl Folke, Hans Joachim Schellnhuber, Björn Nykvist, Cynthia A. de Wit, Terry Hughes, Sander van der Leeuw, Henning Rodhe, Sverker Sörlin, Peter K. Snyder, Robert Costanza, Uno Svedin, Malin Falkenmark, Louise Karlberg, Robert W. Corell, Victoria J. Fabry, James Hansen, Brian Walker, Diana Liverman, Katherine Richardson, Paul Crutzen, and Jonathan A. Foley. A safe operating space for humanity. *Nature*, 2009 461(7263):472–475. doi: 10.1038/461472a. URL: http://www.nature.com/articles/461472a. (Cited on page 3.)

[2] Intergovernmental Panel on Climate Change. *Global warming of 1.5°C*. 2018. URL: http://www.ipcc.ch/report/sr15/. OCLC: 1056192590. (Cited on page 3.)

[3] Global Market Outlook 2019-2023. Solar Power Europe, 2019. (Cited on page 4.)

[4] International Energy Agency (IEA). Key World Energy Statistics 2018. 2018. (Cited on page 5.)

[5] Global Market Outlook 2018-2022. Solar Power Europe, 2018. (Cited on page 5.)

[6] Global Wind Energy Council (GWEC). Global Wind Report 2018. 2019. URL: www.gwec.net. (Cited on page 5.)

[7] IEA. IEA Statistics. 2019. URL: www.iea.org/statistics. (Cited on page 4.)

[8] Harry Wirth. 2019 Aktuelle Fakten zur Photovoltaik in Deutschland. URL: www.pv-fakten.de. (Cited on page 6.)

[9] Kunta Yoshikawa, Hayato Kawasaki, Wataru Yoshida, Toru Irie, Katsunori Konishi, Kunihiro Nakano, Toshihiko Uto, Daisuke Adachi, Masanori Kanematsu, Hisashi Uzu, and Kenji Yamamoto. Silicon heterojunction solar cell with interdigitated back contacts for a photoconversion efficiency over 26%. *Nature Energy*, 2017 2(5). doi: 10.1038/nenergy.2017.32. URL: http://www.nature.com/articles/nenergy201732. (Cited on page 7.)

[10] William Shockley and Hans J. Queisser. Detailed Balance Limit of Efficiency of *p-n* Junction Solar Cells. *Journal of Applied Physics*, 1961 32(3):510–519. doi: 10.1063/1.1736034. URL: http://aip.scitation.org/doi/10.1063/1.1736034. (Cited on pages 7 and 13.)

[11] Fraunhofer Ise. 2019 Photovoltaics Report. (Cited on pages 7 and 9.)

[12] Martin A. Green, Ewan D. Dunlop, Dean H. Levi, Jochen Hohl-Ebinger, Masahiro Yoshita, and Anita W.Y. Ho-Baillie. Solar cell efficiency tables (version 54). *Progress in Photovoltaics: Research and Applications*, 2019 27(7):565–575. doi: 10.1002/pip.3171. URL: http://doi.wiley.com/10.1002/pip.3171. (Cited on pages 7, 8, 9, 13 and 35.)

[13] Lingxian Meng, Yamin Zhang, Xiangjian Wan, Chenxi Li, Xin Zhang, Yanbo Wang, Xin Ke, Zuo Xiao, Liming Ding, Ruoxi Xia, Hin-Lap Yip, Yong Cao, and Yongsheng Chen. Organic and solution-processed tandem solar cells with 17.3% effi-

ciency. *Science*, 2018 361(6407):1094–1098. doi: 10.1126/science.aat2612. URL: http://www.sciencemag.org/lookup/doi/10.1126/science.aat2612. (Cited on pages 8 and 32.)

[14] Research Cell Efficiency Records, National Renewable Energy Laboratory (NREL). URL: https://www.nrel.gov/pv/cell-efficiency.html. (Cited on page 8.)

[15] Dirk C. Jordan and Sarah R. Kurtz. Photovoltaic degradation rates—an analytical review. *Progress in photovoltaics: Research and Applications*, 21(1):12–29, 2013. URL: http://onlinelibrary.wiley.com/doi/10.1002/pip.1182/full. (Cited on page 9.)

[16] Rui Wang, Muhammad Mujahid, Yu Duan, Zhao-Kui Wang, Jingjing Xue, and Yang Yang. A Review of Perovskites Solar Cell Stability. *Advanced Functional Materials*, 2019 page 1808843. doi: 10.1002/adfm.201808843. URL: http://doi.wiley.com/10.1002/adfm.201808843. (Cited on page 9.)

[17] OPVIUS, Energizing Surfaces, accessed: 02.05.2019. URL: www.opvius.com. (Cited on page 10.)

[18] Heliatek, accessed: 02.05.2019. URL: www.heliatek.com. (Cited on page 10.)

[19] InfinityPV, accessed: 02.05.2019. URL: https://infinitypv.com. (Cited on pages 10 and 11.)

[20] OPVIUS Application Paper Automotive. URL: www.opvius.com/en/automotive.html. (Cited on page 10.)

[21] Richter Dahl Rocha & Associes architectes. URL: www.richterdahlrocha.com/en/project/swisstech_graetzel_epfl. (Cited on page 11.)

[22] Amro M. Elshurafa, Shahad R. Albardi, Simona Bigerna, and Carlo Andrea Bollino. Estimating the learning curve of solar PV balance–of–system for over 20 countries: Implications and policy recommendations. *Journal of Cleaner Production*, 2018 196: 122–134. doi: 10.1016/j.jclepro.2018.06.016. URL: https://linkinghub.elsevier.com/retrieve/pii/S0959652618316652. (Cited on page 12.)

[23] Ran Fu, David Feldman, and Robert Margolis. U.S. Solar Photovoltaic System Cost Benchmark: Q1 2018. *Renewable Energy*, page 63, 2018. (Cited on pages 12 and 13.)

[24] Franz Baumgartner. Photovoltaic (PV) balance of system components. In *The Performance of Photovoltaic (PV) Systems*, pages 135–181. Elsevier, 2017. ISBN 978-1-78242-336-2. doi: 10.1016/B978-1-78242-336-2.00005-7. URL: https://linkinghub.elsevier.com/retrieve/pii/B9781782423362000057. (Cited on page 12.)

[25] Peter Würfel and Uli Würfel. *Physics of solar cells: from basic principles to advanced concepts*. Physics textbook. Wiley-VCH, Weinheim, 2nd, updated and expanded ed edition, 2009. ISBN 978-3-527-40857-3. (Cited on pages 13, 20, 28 and 65.)

[26] S. Altazin, L. Stepanova, J. Werner, B. Niesen, C. Ballif, and B. Ruhstaller. Design of perovskite/crystalline-silicon monolithic tandem solar cells. *Opt. Express*, 2018 26(10):A579. doi: 10.1364/OE.26.00A579. URL: https://www.osapublishing.org/abstract.cfm?URI=oe-26-10-A579. (Cited on pages 13 and 157.)

[27] Miha Filipič, Philipp Löper, Bjoern Niesen, Stefaan De Wolf, Janez Krč, Christophe Ballif, and Marko Topič. CH_3nh_3pbi_3 perovskite / silicon tandem solar cells: characterization based optical simulations. *Opt. Express*, 2015 23(7):A263. doi: 10.1364/OE.23.00A263. URL: https://www.osapublishing.org/abstract.cfm?URI=oe-23-7-A263. (Cited on page 13.)

[28] Tomas Leijtens, Kevin A. Bush, Rohit Prasanna, and Michael D. McGehee. Opportunities and challenges for tandem solar cells using metal halide perovskite semiconductors. *Nature Energy*, 2018 3(10):828–838. doi: 10.1038/s41560-018-0190-4. URL: http://www.nature.com/articles/s41560-018-0190-4. (Cited on pages 13 and 14.)

[29] OxfordPV perovskite solar cell achieves 28% efficiency. URL: https://www.oxfordpv.com/news/oxford-pv-perovskite-solar-cell-achieves-28-efficiency. (Cited on page 13.)

[30] César Omar Ramírez Quiroz, Yilei Shen, Michael Salvador, Karen Forberich, Nadine Schrenker, George D. Spyropoulos, Thomas Heumüller, Benjamin Wilkinson, Thomas Kirchartz, Erdmann Spiecker, Pierre J. Verlinden, Xueling Zhang, Martin A. Green, Anita Ho-Baillie, and Christoph J. Brabec. Balancing electrical and optical losses for efficient 4-terminal Si–perovskite solar cells with solution processed percolation electrodes. *Journal of Materials Chemistry A*, 6(8):3583–3592, 2018. doi: 10.1039/C7TA10945H. URL: http://xlink.rsc.org/?DOI=C7TA10945H. (Cited on page 13.)

[31] Dávid Forgács, Lidón Gil-Escrig, Daniel Pérez-Del-Rey, Cristina Momblona, Jérémie Werner, Bjoern Niesen, Christophe Ballif, Michele Sessolo, and Henk J. Bolink. Efficient Monolithic Perovskite/Perovskite Tandem Solar Cells. *Advanced Energy Materials*, 2016 page 1602121. doi: 10.1002/aenm.201602121. URL: http://doi.wiley.com/10.1002/aenm.201602121. (Cited on pages 13 and 36.)

[32] Dewei Zhao, Changlei Wang, Zhaoning Song, Yue Yu, Cong Chen, Xingzhong Zhao, Kai Zhu, and Yanfa Yan. Four-Terminal All-Perovskite Tandem Solar Cells Achieving Power Conversion Efficiencies Exceeding 23%. *ACS Energy Letters*, 2018 3(2):305–306. doi: 10.1021/acsenergylett.7b01287. URL: http://pubs.acs.org/doi/10.1021/acsenergylett.7b01287. (Cited on page 13.)

[33] Henning Nagel, Christopher Berge, and Armin G. Aberle. Generalized analysis of quasi-steady-state and quasi-transient measurements of carrier lifetimes in semiconductors. *Journal of Applied Physics*, 1999 86(11):6218–6221. doi: 10.1063/1.371633. URL: http://aip.scitation.org/doi/10.1063/1.371633. (Cited on page 15.)

[34] M.T. Neukom, S. Züfle, and B. Ruhstaller. Reliable extraction of organic solar cell parameters by combining steady-state and transient techniques. *Organic Electronics*, 2012 13(12):2910–2916. doi: 10.1016/j.orgel.2012.09.008. URL: http://linkinghub.elsevier.com/retrieve/pii/S1566119912004223. (Cited on pages 15, 47, 62, 66, 69, 109, 123, 141 and 167.)

[35] Henry J. Snaith, Antonio Abate, James M. Ball, Giles E. Eperon, Tomas Leijtens, Nakita K. Noel, Samuel D. Stranks, Jacob Tse-Wei Wang, Konrad Wojciechowski, and Wei Zhang. Anomalous Hysteresis in Perovskite Solar Cells. *The Journal of Physical Chemistry Letters*, 2014 5(9):1511–1515. doi: 10.1021/jz500113x. URL: http://pubs.acs.org/doi/abs/10.1021/jz500113x. (Cited on pages 16, 38, 119, 120 and 139.)

[36] Martin Thomas Neukom. Charge Carrier Dynamics of Methylammonium Lead-Iodide Perovskite Solar Cells. 2016 *arXiv:1611.06425 [cond-mat]*. URL: http://arxiv.org/abs/1611.06425. arXiv: 1611.06425. (Cited on pages 19, 47, 69, 89, 123 and 167.)

[37] A. Baumann, J. Lorrmann, D. Rauh, C. Deibel, and V. Dyakonov. A New Approach for Probing the Mobility and Lifetime of Photogenerated Charge Carriers in Organic Solar Cells Under Real Operating Conditions. *Advanced Materials*, 2012 24(32):4381–4386. doi: 10.1002/adma.201200874. URL: http://doi.wiley.com/10.1002/adma.201200874. (Cited on pages 25, 76, 80 and 92.)

[38] G. Dennler, A.J. Mozer, G. Juška, A. Pivrikas, R. Österbacka, A. Fuchsbauer, and N.S. Sariciftci. Charge carrier mobility and lifetime versus composition of conjugated polymer/fullerene bulk-heterojunction solar cells. *Organic Electronics*, 2006 7(4):229–234. doi: 10.1016/j.orgel.2006.02.004. URL: http://linkinghub.elsevier.com/retrieve/pii/S1566119906000474. (Cited on page 80.)

[39] Rick Hamilton, Christopher G. Shuttle, Brian O'Regan, Thomas C. Hammant, Jenny Nelson, and James R. Durrant. Recombination in Annealed and Nonannealed Polythiophene/Fullerene Solar Cells: Transient Photovoltage Studies versus Numerical Modeling. *The Journal of Physical Chemistry Letters*, 2010 1(9):1432–1436. doi: 10.1021/jz1001506. URL: http://pubs.acs.org/doi/abs/10.1021/jz1001506. (Cited on pages 68, 82, 83, 105 and 117.)

[40] Thomas Kirchartz and Jenny Nelson. Meaning of reaction orders in polymer:fullerene solar cells. *Physical Review B*, 2012 86(16):165201. doi: 10.1103/PhysRevB.86.165201. URL: https://link.aps.org/doi/10.1103/PhysRevB.86.165201. (Cited on pages 74, 92 and 144.)

[41] Tracey M. Clarke, Christoph Lungenschmied, Jeff Peet, Nicolas Drolet, and Attila J. Mozer. A Comparison of Five Experimental Techniques to Measure Charge Carrier Lifetime in Polymer/Fullerene Solar Cells. *Advanced Energy Materials*, 2015 5(4): 1401345. doi: 10.1002/aenm.201401345. URL: http://doi.wiley.com/10.1002/aenm.201401345. (Cited on pages 80, 83, 92 and 106.)

[42] Zhe Li, Feng Gao, Neil C. Greenham, and Christopher R. McNeill. Comparison of the Operation of Polymer/Fullerene, Polymer/Polymer, and Polymer/Nanocrystal Solar Cells: A Transient Photocurrent and Photovoltage Study. *Advanced Functional Materials*, 2011 21(8):1419–1431. doi: 10.1002/adfm.201002154. URL: http://doi.wiley.com/10.1002/adfm.201002154. (Cited on page 89.)

[43] Dan Credgington, Yoojin Kim, John Labram, Thomas D Anthopoulos, and James R Durrant. Analysis of Recombination Losses in a Pentacene/C $_{60}$ Organic Bilayer Solar Cell. *The Journal of Physical Chemistry Letters*, 2011 2(21):2759–2763. doi: 10.1021/jz201338d. URL: http://pubs.acs.org/doi/abs/10.1021/jz201338d. (Cited on page 92.)

[44] C. G. Shuttle, B. O'Regan, A. M. Ballantyne, J. Nelson, D. D. C. Bradley, J. de Mello, and J. R. Durrant. Experimental determination of the rate law for charge carrier decay in a polythiophene: Fullerene solar cell. *Applied Physics Letters*, 92(9):093311, 2008. doi: 10.1063/1.2891871. URL: http://scitation.aip.org/content/aip/journal/apl/92/9/10.1063/1.2891871. (Cited on pages 25, 82, 83, 105 and 106.)

[45] George F. A. Dibb, Mathis-Andreas Muth, Thomas Kirchartz, Sebastian Engmann, Harald Hoppe, Gerhard Gobsch, Mukundan Thelakkat, Nicolas Blouin, Steve Tierney, Miguel Carrasco-Orozco, James R. Durrant, and Jenny Nelson. Influence of doping on charge carrier collection in normal and inverted geometry polymer:fullerene solar cells. *Scientific Reports*, 3(1):3335, 2013. doi: 10.1038/srep03335. URL: http://dx.doi.org/10.1038/srep03335. (Cited on pages 25, 71 and 78.)

[46] Tomas Leijtens, Samuel D. Stranks, Giles E. Eperon, Rebecka Lindblad, Erik MJ Johansson, Ian J. McPherson, Hakan Rensmo, James M. Ball, Michael M. Lee, and Henry J. Snaith. Electronic properties of meso-superstructured and planar organometal halide perovskite films: charge trapping, photodoping, and carrier mobility. *ACS nano*, 8(7):7147–7155, 2014. URL: http://pubs.acs.org/doi/abs/10.1021/nn502115k. (Cited on pages 25, 126 and 134.)

[47] Phil Calado, Dan Burkitt, Jizhong Yao, Joel Troughton, Trystan M. Watson, Matt J. Carnie, Andrew M. Telford, Brian C. O'Regan, Jenny Nelson, and Piers R.F. Barnes. Identifying Dominant Recombination Mechanisms in Perovskite Solar Cells by Measuring the Transient Ideality Factor. *Physical Review Applied*, 2019 11 (4). doi: 10.1103/PhysRevApplied.11.044005. URL: https://link.aps.org/doi/10.1103/PhysRevApplied.11.044005. (Cited on page 29.)

[48] Annika Spies, Jeneke Reinhardt, Mathias List, Birger Zimmermann, and Uli Würfel. Impact of Charge Carrier Mobility and Electrode Selectivity on the Performance of Organic Solar Cells. In Karl Leo, editor, *Elementary Processes in Organic Photovoltaics*, volume 272, pages 401–418. Springer International Publishing, Cham, 2017. ISBN 978-3-319-28336-4 978-3-319-28338-8. doi: 10.1007/978-3-319-28338-8_17. URL: http://link.springer.com/10.1007/978-3-319-28338-8_17. (Cited on pages 32 and 72.)

[49] Akshay Kokil, Ke Yang, and Jayant Kumar. Techniques for characterization of charge carrier mobility in organic semiconductors. *Journal of Polymer Science Part B: Polymer Physics*, 2012 50(15):1130–1144. doi: 10.1002/polb.23103. URL: http://doi.wiley.com/10.1002/polb.23103. (Cited on pages 103, 105 and 106.)

[50] Tracey M. Clarke, Jeff Peet, Andrew Nattestad, Nicolas Drolet, Gilles Dennler, Christoph Lungenschmied, Mario Leclerc, and Attila J. Mozer. Charge carrier mobility, bimolecular recombination and trapping in polycarbazole copolymer:fullerene (PCDTBT:PCBM) bulk heterojunction solar cells. *Organic Electronics*, 2012 13(11): 2639–2646. doi: 10.1016/j.orgel.2012.07.037. URL: http://linkinghub.elsevier.com/retrieve/pii/S156611991200362X. (Cited on pages 32, 116, 117 and 155.)

[51] Naichia Yeh and Pulin Yeh. Organic solar cells: Their developments and potentials. *Renewable and Sustainable Energy Reviews*, 2013 21:421–431. doi: 10.1016/j.rser.2012.12.046. URL: https://linkinghub.elsevier.com/retrieve/pii/S1364032113000026. (Cited on page 32.)

[52] Harald Hoppe and Niyazi Serdar Sariciftci. Morphology of polymer/fullerene bulk heterojunction solar cells. *Journal of Materials Chemistry*, 16(1):45–61, 2006. doi: 10.1039/B510618B. URL: http://xlink.rsc.org/?DOI=B510618B. (Cited on pages 33, 66, 68 and 69.)

[53] G. Yu, J. Gao, J. C. Hummelen, F. Wudl, and A. J. Heeger. Polymer Photovoltaic Cells: Enhanced Efficiencies via a Network of Internal Donor-Acceptor Heterojunctions. *Science*, 1995 270(5243):1789–1791. doi: 10.1126/science.270.5243.1789. URL: http://www.sciencemag.org/cgi/doi/10.1126/science.270.5243.1789. (Cited on pages 33 and 69.)

[54] Baobing Fan, Lei Ying, Zhenfeng Wang, Baitian He, Xiao-Fang Jiang, Fei Huang, and Yong Cao. Optimisation of processing solvent and molecular weight for the production of green-solvent-processed all-polymer solar cells with a power conversion efficiency over 9%. *Energy & Environmental Science*, 10(5):1243–1251, 2017. doi: 10.1039/C7EE00619E. URL: http://xlink.rsc.org/?DOI=C7EE00619E. (Cited on page 33.)

[55] Jianhui Hou, Olle Inganäs, Richard H. Friend, and Feng Gao. Organic solar cells based on non-fullerene acceptors. *Nature Materials*, 2018 17(2):119–128. doi: 10.1038/nmat5063. URL: http://www.nature.com/articles/nmat5063. (Cited on page 33.)

[56] Yong Cui, Huifeng Yao, Ling Hong, Tao Zhang, Ye Xu, Kaihu Xian, Bowei Gao, Jinzhao Qin, Jianqi Zhang, Zhixiang Wei, and Jianhui Hou. Achieving Over 15% Efficiency in Organic Photovoltaic Cells via Copolymer Design. *Advanced Materials*, 2019 31(14):1808356. doi: 10.1002/adma.201808356. URL: https://onlinelibrary.wiley.com/doi/abs/10.1002/adma.201808356. (Cited on page 33.)

[57] Mark Gruber, Julia Wagner, Konrad Klein, Ulrich Hörmann, Andreas Opitz, Martin Stutzmann, and Wolfgang Brütting. Thermodynamic Efficiency Limit of Molecular Donor-Acceptor Solar Cells and its Application to Diindenoperylene/C60-Based Planar Heterojunction Devices. *Advanced Energy Materials*, 2012 2(9):1100–1108. doi: 10.1002/aenm.201200077. URL: http://doi.wiley.com/10.1002/aenm.201200077. (Cited on page 33.)

[58] Tayebeh Ameri, Parisa Khoram, Jie Min, and Christoph J. Brabec. Organic Ternary Solar Cells: A Review. *Advanced Materials*, 2013 25(31):4245–4266. doi: 10.1002/adma.201300623. URL: http://doi.wiley.com/10.1002/adma.201300623. (Cited on page 33.)

[59] Akihiro Kojima, Kenjiro Teshima, Yasuo Shirai, and Tsutomu Miyasaka. Organometal Halide Perovskites as Visible-Light Sensitizers for Photovoltaic Cells. *Journal of the American Chemical Society*, 2009 131(17):6050–6051. doi: 10.1021/ja809598r. URL: http://pubs.acs.org/doi/abs/10.1021/ja809598r. (Cited on page 35.)

[60] Jun Hong Noh, Sang Hyuk Im, Jin Hyuck Heo, Tarak N. Mandal, and Sang Il Seok. Chemical Management for Colorful, Efficient, and Stable Inorganic–Organic Hybrid Nanostructured Solar Cells. *Nano Letters*, 2013 13(4):1764–1769. doi: 10.1021/nl400349b. URL: http://pubs.acs.org/doi/10.1021/nl400349b. (Cited on page 35.)

[61] Yixin Zhao, Alexandre M. Nardes, and Kai Zhu. Mesoporous perovskite solar cells: material composition, charge-carrier dynamics, and device characteristics. *Faraday Discussions*, 176:301–312, 2014. doi: 10.1039/C4FD00128A. URL: http://xlink.rsc.org/?DOI=C4FD00128A. (Cited on pages 35 and 102.)

[62] The Duong, YiLiang Wu, Heping Shen, Jun Peng, Xiao Fu, Daniel Jacobs, Er-Chien Wang, Teng Choon Kho, Kean Chern Fong, Matthew Stocks, Evan Franklin, Andrew Blakers, Ngwe Zin, Keith McIntosh, Wei Li, Yi-Bing Cheng, Thomas P. White, Klaus Weber, and Kylie Catchpole. Rubidium Multication Perovskite with Optimized Bandgap for Perovskite-Silicon Tandem with over 26% Efficiency. *Advanced Energy Materials*, 2017 page 1700228. doi: 10.1002/aenm.201700228. URL: http://doi.wiley.com/10.1002/aenm.201700228. (Cited on page 36.)

[63] Michael Powalla, Stefan Paetel, Erik Ahlswede, Roland Wuerz, Cordula D. Wessendorf, and Theresa Magorian Friedlmeier. Thin-film solar cells exceeding 22% solar cell efficiency: An overview on CdTe-, Cu(In,Ga)Se $_2$ -, and perovskite-based materials. *Applied Physics Reviews*, 2018 5(4):041602. doi: 10.1063/1.5061809. URL: http://aip.scitation.org/doi/10.1063/1.5061809. (Cited on pages 36 and 37.)

[64] Zejiao Shi, Jia Guo, Yonghua Chen, Qi Li, Yufeng Pan, Haijuan Zhang, Yingdong Xia, and Wei Huang. Lead-free Organic-Inorganic Hybrid Perovskites for Photovoltaic Applications: Recent Advances and Perspectives. *Advanced Materials*, 2017 page 1605005. doi: 10.1002/adma.201605005. URL: http://doi.wiley.com/10.1002/adma.201605005. (Cited on page 36.)

[65] Cristina Momblona, Lidón Gil-Escrig, Enrico Bandiello, Eline M. Hutter, Michele Sessolo, Kay Lederer, Jan Blochwitz-Nimoth, and Henk J. Bolink. Efficient vacuum deposited p-i-n and n-i-p perovskite solar cells employing doped charge transport layers. *Energy Environ. Sci.*, 9(11):3456–3463, 2016. doi: 10.1039/C6EE02100J. URL: http://xlink.rsc.org/?DOI=C6EE02100J. (Cited on pages 36, 143, 148, 149, 153 and 156.)

[66] Jorge Ávila, Cristina Momblona, Pablo Boix, Michele Sessolo, Miguel Anaya, Gabriel Lozano, Koen Vandewal, Hernán Míguez, and Henk J. Bolink. High voltage vacuum-deposited CH $_3$ NH $_3$ PbI $_3$ –CH $_3$ NH $_3$ PbI $_3$ tandem solar cells. *Energy & Environmental Science*, 2018. doi: 10.1039/C8EE01936C. URL: http://xlink.rsc.org/?DOI=C8EE01936C. (Cited on page 36.)

[67] Lijian Zuo, Zhuowei Gu, Tao Ye, Weifei Fu, Gang Wu, Hanying Li, and Hongzheng Chen. Enhanced Photovoltaic Performance of CH $_3$ NH $_3$ PbI $_3$ Perovskite Solar Cells through Interfacial Engineering Using Self-Assembling Monolayer. *Journal of*

the American Chemical Society, 2015 137(7):2674–2679. doi: 10.1021/ja512518r. URL: http://pubs.acs.org/doi/abs/10.1021/ja512518r. (Cited on page 36.)

[68] Wei Zhang, Michael Saliba, David T. Moore, Sandeep K. Pathak, Maximilian T. Hörantner, Thomas Stergiopoulos, Samuel D. Stranks, Giles E. Eperon, Jack A. Alexander-Webber, Antonio Abate, Aditya Sadhanala, Shuhua Yao, Yulin Chen, Richard H. Friend, Lara A. Estroff, Ulrich Wiesner, and Henry J. Snaith. Ultrasmooth organic–inorganic perovskite thin-film formation and crystallization for efficient planar heterojunction solar cells. *Nature Communications*, 2015 6:6142. doi: 10.1038/ncomms7142. URL: http://www.nature.com/doifinder/10.1038/ncomms7142. (Cited on page 36.)

[69] Carlito S. Ponseca, Tom J. Savenije, Mohamed Abdellah, Kaibo Zheng, Arkady Yartsev, Tobjörn Pascher, Tobias Harlang, Pavel Chabera, Tonu Pullerits, Andrey Stepanov, Jean-Pierre Wolf, and Villy Sundström. Organometal Halide Perovskite Solar Cell Materials Rationalized: Ultrafast Charge Generation, High and Microsecond-Long Balanced Mobilities, and Slow Recombination. *Journal of the American Chemical Society*, 2014 136(14):5189–5192. doi: 10.1021/ja412583t. URL: http://pubs.acs.org/doi/abs/10.1021/ja412583t. (Cited on pages 36, 121, 128 and 134.)

[70] Jorge Avila, Lidon Gil-Escrig, Pablo P. Boix, Michele Sessolo, Steve Albrecht, and Henk J. Bolink. Influence of doped charge transport layers on efficient perovskite solar cells. *Sustainable Energy & Fuels*, 2018. doi: 10.1039/C8SE00218E. URL: http://xlink.rsc.org/?DOI=C8SE00218E. (Cited on page 37.)

[71] Hui-Seon Kim, In-Hyuk Jang, Namyoung Ahn, Mansoo Choi, Antonio Guerrero, Juan Bisquert, and Nam-Gyu Park. Control of $I - V$ Hysteresis in $CH_3NH_3PbI_3$ Perovskite Solar Cell. *The Journal of Physical Chemistry Letters*, 2015 6(22):4633–4639. doi: 10.1021/acs.jpclett.5b02273. URL: http://pubs.acs.org/doi/10.1021/acs.jpclett.5b02273. (Cited on pages 120 and 137.)

[72] Yi Hou, Wei Chen, Derya Baran, Tobias Stubhan, Norman A. Luechinger, Benjamin Hartmeier, Moses Richter, Jie Min, Shi Chen, Cesar Omar Ramirez Quiroz, Ning Li, Hong Zhang, Thomas Heumueller, Gebhard J. Matt, Andres Osvet, Karen Forberich, Zhi-Guo Zhang, Yongfang Li, Benjamin Winter, Peter Schweizer, Erdmann Spiecker, and Christoph J. Brabec. Overcoming the Interface Losses in Planar Heterojunction Perovskite-Based Solar Cells. *Advanced Materials*, 2016 28(25):5112–5120. doi: 10.1002/adma.201504168. URL: http://doi.wiley.com/10.1002/adma.201504168. (Cited on pages 37 and 120.)

[73] Yuchuan Shao, Zhengguo Xiao, Cheng Bi, Yongbo Yuan, and Jinsong Huang. Origin and elimination of photocurrent hysteresis by fullerene passivation in CH3nh3pbi3 planar heterojunction solar cells. *Nature Communications*, 2014 5:5784. doi: 10.1038/ncomms6784. URL: http://www.nature.com/doifinder/10.1038/ncomms6784. (Cited on pages 37 and 120.)

[74] Qian Xu, Zhen Lu, Lifeng Zhu, Chun Kou, Yahui Liu, Cuihong Li, Qingbo Meng, Wenhua Li, and Zhishan Bo. Elimination of the J–V hysteresis of planar perovskite solar cells by interfacial modification with a thermo-cleavable fullerene derivative. *Journal of Materials Chemistry A*, 4(45):17649–17654, 2016. doi: 10.1039/C6TA06143E. URL: http://xlink.rsc.org/?DOI=C6TA06143E.

[75] Yi Hou, Simon Scheiner, Xiaofeng Tang, Nicola Gasparini, Moses Richter, Ning Li, Peter Schweizer, Shi Chen, Haiwei Chen, Cesar Omar Ramirez Quiroz, Xiaoyan Du, Gebhard J. Matt, Andres Osvet, Erdmann Spiecker, Rainer H. Fink, Andreas Hirsch, Marcus Halik, and Christoph J. Brabec. Suppression of Hysteresis Effects in Organohalide Perovskite Solar Cells. *Advanced Materials Interfaces*, 2017 page 1700007. doi: 10.1002/admi.201700007. URL: http://doi.wiley.com/10.1002/admi.

201700007.

[76] Yanjun Fang, Cheng Bi, Dong Wang, and Jinsong Huang. The Functions of Fullerenes in Hybrid Perovskite Solar Cells. *ACS Energy Letters*, 2017 2(4):782–794. doi: 10.1021/acsenergylett.6b00657. URL: http://pubs.acs.org/doi/abs/10.1021/acsenergylett.6b00657. (Cited on page 37.)

[77] Stefaan De Wolf, Jakub Holovsky, Soo-Jin Moon, Philipp Löper, Bjoern Niesen, Martin Ledinsky, Franz-Josef Haug, Jun-Ho Yum, and Christophe Ballif. Organometallic Halide Perovskites: Sharp Optical Absorption Edge and Its Relation to Photovoltaic Performance. *The Journal of Physical Chemistry Letters*, 2014 5(6):1035–1039. doi: 10.1021/jz500279b. URL: http://pubs.acs.org/doi/10.1021/jz500279b. (Cited on page 38.)

[78] Wan-Jian Yin, Tingting Shi, and Yanfa Yan. Unusual defect physics in CH3nh3pbi3 perovskite solar cell absorber. *Applied Physics Letters*, 2014 104(6):063903. doi: 10.1063/1.4864778. URL: http://scitation.aip.org/content/aip/journal/apl/104/6/10.1063/1.4864778. (Cited on pages 38 and 134.)

[79] James M. Ball and Annamaria Petrozza. Defects in perovskite-halides and their effects in solar cells. *Nature Energy*, 2016 1(11):16149. doi: 10.1038/nenergy.2016.149. URL: http://www.nature.com/articles/nenergy2016149. (Cited on page 38.)

[80] Christian Wehrenfennig, Giles E. Eperon, Michael B. Johnston, Henry J. Snaith, and Laura M. Herz. High Charge Carrier Mobilities and Lifetimes in Organolead Trihalide Perovskites. *Advanced Materials*, 2014 26(10):1584–1589. doi: 10.1002/adma.201305172. URL: http://doi.wiley.com/10.1002/adma.201305172. (Cited on pages 38, 126, 128 and 134.)

[81] Igal Levine, Satyajit Gupta, Achintya Bera, Davide Ceratti, Gary Hodes, David Cahen, Dengyang Guo, Tom J. Savenije, Jorge Ávila, Henk J. Bolink, Oded Millo, Doron Azulay, and Isaac Balberg. Can we use *time-resolved* measurements to get *steady-state* transport data for halide perovskites? *Journal of Applied Physics*, 2018 124(10):103103. doi: 10.1063/1.5037637. URL: http://aip.scitation.org/doi/10.1063/1.5037637. (Cited on pages 38 and 148.)

[82] Brian Maynard, Qi Long, Eric A. Schiff, Mengjin Yang, Kai Zhu, Ranjith Kottokkaran, Hisham Abbas, and Vikram L. Dalal. Electron and hole drift mobility measurements on methylammonium lead iodide perovskite solar cells. *Applied Physics Letters*, 2016 108(17):173505. doi: 10.1063/1.4948344. URL: http://scitation.aip.org/content/aip/journal/apl/108/17/10.1063/1.4948344. (Cited on pages 38, 124 and 128.)

[83] Shuangyong Sun, Teddy Salim, Nripan Mathews, Martial Duchamp, Chris Boothroyd, Guichuan Xing, Tze Chien Sum, and Yeng Ming Lam. The origin of high efficiency in low-temperature solution-processable bilayer organometal halide hybrid solar cells. *Energy & Environmental Science*, 7(1):399–407, 2014. doi: 10.1039/C3EE43161D. URL: http://xlink.rsc.org/?DOI=C3EE43161D. (Cited on page 38.)

[84] Atsuhiko Miyata, Anatolie Mitioglu, Paulina Plochocka, Oliver Portugall, Jacob Tse-Wei Wang, Samuel D. Stranks, Henry J. Snaith, and Robin J. Nicholas. Direct Measurement of the Exciton Binding Energy and Effective Masses for Charge carriers in an Organic-Inorganic Tri-halide Perovskite. *arXiv preprint arXiv:1504.07025*, 2015. URL: http://arxiv.org/abs/1504.07025. (Cited on page 38.)

[85] Eric T. Hoke, Daniel J. Slotcavage, Emma R. Dohner, Andrea R. Bowring, Hemamala I. Karunadasa, and Michael D. McGehee. Reversible photo-induced trap formation in mixed-halide hybrid perovskites for photovoltaics. *Chemical Science*, 6(1):613–617, 2015. doi: 10.1039/C4SC03141E. URL: http://xlink.rsc.org/?DOI=

C4SC03141E. (Cited on page 38.)

[86] Holger Röhm, Tobias Leonhard, Michael J. Hoffmann, and Alexander Colsmann. Ferroelectric domains in methylammonium lead iodide perovskite thin-films. *Energy & Environmental Science*, 10(4):950–955, 2017. doi: 10.1039/C7EE00420F. URL: http://xlink.rsc.org/?DOI=C7EE00420F. (Cited on page 38.)

[87] E. L. Unger, E. T. Hoke, C. D. Bailie, W. H. Nguyen, A. R. Bowring, T. Heumüller, M. G. Christoforo, and M. D. McGehee. Hysteresis and transient behavior in current–voltage measurements of hybrid-perovskite absorber solar cells. *Energy & Environmental Science*, 2014 7(11):3690–3698. doi: 10.1039/C4EE02465F. URL: http://xlink.rsc.org/?DOI=C4EE02465F. (Cited on pages 38, 39, 119 and 120.)

[88] Eugen Zimmermann, Ka Kan Wong, Michael Müller, Hao Hu, Philipp Ehrenreich, Markus Kohlstädt, Uli Würfel, Simone Mastroianni, Gayathri Mathiazhagan, Andreas Hinsch, Tanaji P. Gujar, Mukundan Thelakkat, Thomas Pfadler, and Lukas Schmidt-Mende. Characterization of perovskite solar cells: Towards a reliable measurement protocol. *APL Materials*, 2016 4(9):091901. doi: 10.1063/1.4960759. URL: http://scitation.aip.org/content/aip/journal/aplmater/4/9/10.1063/1.4960759. (Cited on page 38.)

[89] W. Tress, N. Marinova, T. Moehl, S. M. Zakeeruddin, Mohammad Khaja Nazeeruddin, and M. Grätzel. Understanding the rate-dependent J–V hysteresis, slow time component, and aging in CH $_3$ NH $_3$ PbI $_3$ perovskite solar cells: the role of a compensated electric field. *Energy & Environmental Science*, 8(3):995–1004, 2015. doi: 10.1039/C4EE03664F. URL: http://xlink.rsc.org/?DOI=C4EE03664F. (Cited on pages 38, 39, 77, 119, 121 and 139.)

[90] Aron Walsh, David O. Scanlon, Shiyou Chen, X. G. Gong, and Su-Huai Wei. Self-Regulation Mechanism for Charged Point Defects in Hybrid Halide Perovskites. *Angew. Chem. Int. Ed.*, 2015 54(6):1791–1794. doi: 10.1002/anie.201409740. URL: http://doi.wiley.com/10.1002/anie.201409740. (Cited on pages 38, 119, 122, 127, 129, 139 and 151.)

[91] Davide Moia, Ilario Gelmetti, Phil Calado, William Fisher, Michael Stringer, Onkar Game, Yinghong Hu, Pablo Docampo, David Lidzey, Emilio Palomares, Jenny Nelson, and Piers R. F. Barnes. Ionic-to-electronic current amplification in hybrid perovskite solar cells: ionically gated transistor-interface circuit model explains hysteresis and impedance of mixed conducting devices. *Energy Environ. Sci.*, 12(4):1296–1308, 2019. doi: 10.1039/C8EE02362J. URL: http://xlink.rsc.org/?DOI=C8EE02362J. (Cited on pages 39 and 146.)

[92] Moritz H. Futscher, Ju Min Lee, Tianyi Wang, Azhar Fakharuddin, Lukas Schmidt-Mende, and Bruno Ehrler. Quantification of Ion Migration in CH3nh3pbi3 Perovskite Solar Cells by Transient Capacitance Measurements. *arXiv preprint arXiv:1801.08519*, 2018. (Cited on page 39.)

[93] Heejae Lee, Sofia Gaiaschi, Patrick Chapon, Arthur Marronnier, Heeryung Lee, Jean-Charles Vanel, Denis Tondelier, Jean-Eric Bourée, Yvan Bonnassieux, and Bernard Geffroy. Direct Experimental Evidence of Halide Ionic Migration under Bias in CH $_3$ NH $_3$ PbI $_{3-x}$ Cl $_x$ -Based Perovskite Solar Cells Using GD-OES Analysis. *ACS Energy Letters*, 2017 2(4):943–949. doi: 10.1021/acsenergylett.7b00150. URL: http://pubs.acs.org/doi/abs/10.1021/acsenergylett.7b00150. (Cited on pages 39, 77, 139 and 151.)

[94] Rebecca A. Belisle, William H. Nguyen, Andrea R. Bowring, Philip Calado, Xiaoe Li, Stuart J. C. Irvine, Michael D. McGehee, Piers R. F. Barnes, and Brian C. O'Regan. Interpretation of inverted photocurrent transients in organic lead halide perovskite

solar cells: proof of the field screening by mobile ions and determination of the space charge layer widths. *Energy & Environmental Science*, 10(1):192–204, 2017. doi: 10.1039/C6EE02914K. URL: http://xlink.rsc.org/?DOI=C6EE02914K. (Cited on pages 38 and 140.)

[95] Jarvist M. Frost and Aron Walsh. What Is Moving in Hybrid Halide Perovskite Solar Cells? *Accounts of Chemical Research*, 2016 49(3):528–535. doi: 10.1021/acs.accounts.5b00431. URL: http://pubs.acs.org/doi/abs/10.1021/acs.accounts.5b00431. (Cited on pages 38, 77, 95, 128 and 151.)

[96] Christopher Eames, Jarvist M. Frost, Piers R. F. Barnes, Brian C. O'Regan, Aron Walsh, and M. Saiful Islam. Ionic transport in hybrid lead iodide perovskite solar cells. *Nat Commun*, 2015 6(1):7497. doi: 10.1038/ncomms8497. URL: http://www.nature.com/articles/ncomms8497. (Cited on pages 39, 77, 119, 122, 126, 139 and 151.)

[97] Jun Haruyama, Keitaro Sodeyama, Liyuan Han, and Yoshitaka Tateyama. First-Principles Study of Ion Diffusion in Perovskite Solar Cell Sensitizers. *Journal of the American Chemical Society*, 2015 137(32):10048–10051. doi: 10.1021/jacs.5b03615. URL: http://pubs.acs.org/doi/abs/10.1021/jacs.5b03615. (Cited on page 39.)

[98] Stephan van Reenen, Martijn Kemerink, and Henry J. Snaith. Modeling Anomalous Hysteresis in Perovskite Solar Cells. *J. Phys. Chem. Lett.*, 2015 6(19):3808–3814. doi: 10.1021/acs.jpclett.5b01645. URL: http://pubs.acs.org/doi/10.1021/acs.jpclett.5b01645. (Cited on pages 39, 119, 120, 129, 133, 140 and 151.)

[99] Giles Richardson, Simon E. J. O'Kane, Ralf G. Niemann, Timo A. Peltola, Jamie M. Foster, Petra J. Cameron, and Alison B. Walker. Can slow-moving ions explain hysteresis in the current–voltage curves of perovskite solar cells? *Energy Environ. Sci.*, 9(4):1476–1485, 2016. doi: 10.1039/C5EE02740C. URL: http://xlink.rsc.org/?DOI=C5EE02740C. (Cited on pages 119, 120, 122, 123, 129, 133, 140 and 151.)

[100] Philip Calado, Andrew M. Telford, Daniel Bryant, Xiaoe Li, Jenny Nelson, Brian C. O'Regan, and Piers R.F. Barnes. Evidence for ion migration in hybrid perovskite solar cells with minimal hysteresis. *Nat Commun*, 2016 7(1):13831. doi: 10.1038/ncomms13831. URL: http://www.nature.com/articles/ncomms13831. (Cited on pages 39, 119, 120, 123, 129, 140, 151 and 154.)

[101] Zhen Li, Chuanxiao Xiao, Ye Yang, Steven P. Harvey, Dong Hoe Kim, Jeffrey A. Christians, Mengjin Yang, Philip Schulz, Sanjini U. Nanayakkara, Chun-Sheng Jiang, Joseph M. Luther, Joseph J. Berry, Matthew C. Beard, Mowafak M. Al-Jassim, and Kai Zhu. Extrinsic ion migration in perovskite solar cells. *Energy & Environmental Science*, 10(5):1234–1242, 2017. doi: 10.1039/C7EE00358G. URL: http://xlink.rsc.org/?DOI=C7EE00358G. (Cited on pages 39 and 156.)

[102] Yuchuan Shao, Yanjun Fang, Tao Li, Qi Wang, Qingfeng Dong, Yehao Deng, Yongbo Yuan, Haotong Wei, Meiyu Wang, Alexei Gruverman, Jeffery Shield, and Jinsong Huang. Grain boundary dominated ion migration in polycrystalline organic–inorganic halide perovskite films. *Energy & Environmental Science*, 9(5):1752–1759, 2016. doi: 10.1039/C6EE00413J. URL: http://xlink.rsc.org/?DOI=C6EE00413J. (Cited on pages 39, 137 and 156.)

[103] Ronen Gottesman, Eynav Haltzi, Laxman Gouda, Shay Tirosh, Yaniv Bouhadana, Arie Zaban, Edoardo Mosconi, and Filippo De Angelis. Extremely Slow Photoconductivity Response of $CH_3NH_3PbI_3$ Perovskites Suggesting Structural Changes under Working Conditions. *The Journal of Physical Chemistry Letters*, 2014 5(15):2662–2669. doi: 10.1021/jz501373f. URL: http://pubs.acs.org/doi/abs/10.1021/jz501373f. (Cited on page 39.)

[104] Ye Zhang, Mingzhen Liu, Giles E. Eperon, Tomas C. Leijtens, David McMeekin, Michael Saliba, Wei Zhang, Michele de Bastiani, Annamaria Petrozza, Laura M. Herz, Michael B. Johnston, Hong Lin, and Henry J. Snaith. Charge selective contacts, mobile ions and anomalous hysteresis in organic–inorganic perovskite solar cells. *Materials Horizons*, 2(3):315–322, 2015. doi: 10.1039/C4MH00238E. URL: http://xlink.rsc.org/?DOI=C4MH00238E.

[105] Bo Wu, Kunwu Fu, Natalia Yantara, Guichuan Xing, Shuangyong Sun, Tze Chien Sum, and Nripan Mathews. Charge Accumulation and Hysteresis in Perovskite-Based Solar Cells: An Electro-Optical Analysis. *Advanced Energy Materials*, 2015 5 (19):1500829. doi: 10.1002/aenm.201500829. URL: http://doi.wiley.com/10.1002/aenm.201500829.

[106] Nam-Gyu Park. Switchable photovoltaics. *Nature Materials*, 2015 14(2):140–141. doi: 10.1038/nmat4177. URL: http://www.nature.com/articles/nmat4177.

[107] Zhengguo Xiao, Yongbo Yuan, Yuchuan Shao, Qi Wang, Qingfeng Dong, Cheng Bi, Pankaj Sharma, Alexei Gruverman, and Jinsong Huang. Giant switchable photovoltaic effect in organometal trihalide perovskite devices. *Nature Materials*, 2014 14 (2):193–198. doi: 10.1038/nmat4150. URL: http://www.nature.com/doifinder/10.1038/nmat4150. (Cited on page 39.)

[108] Emilio J. Juarez-Perez, Rafael S. Sanchez, Laura Badia, Germá Garcia-Belmonte, Yong Soo Kang, Ivan Mora-Sero, and Juan Bisquert. Photoinduced Giant Dielectric Constant in Lead Halide Perovskite Solar Cells. *The Journal of Physical Chemistry Letters*, 2014 5(13):2390–2394. doi: 10.1021/jz5011169. URL: http://pubs.acs.org/doi/abs/10.1021/jz5011169. (Cited on pages 39, 139 and 146.)

[109] Daniel A. Jacobs, Heping Shen, Florian Pfeffer, Jun Peng, Thomas P. White, Fiona J. Beck, and Kylie R. Catchpole. The two faces of capacitance: New interpretations for electrical impedance measurements of perovskite solar cells and their relation to hysteresis. *Journal of Applied Physics*, 2018 124(22):225702. doi: 10.1063/1.5063259. URL: http://aip.scitation.org/doi/10.1063/1.5063259. (Cited on pages 39, 140, 143, 146 and 151.)

[110] Platform for all-in-one characterization (PAIOS) by Fluxim AG, Switzerland. URL: http://www.fluxim.com. (Cited on pages 43, 110, 121 and 141.)

[111] Semiconducting thin film optics simulator (SETFOS) by Fluxim AG, Switzerland. URL: http://www.fluxim.com. (Cited on pages 47, 57, 88, 95, 123, 127, 140 and 141.)

[112] Thomas Lanz, Beat Ruhstaller, Corsin Battaglia, and Christophe Ballif. Extended light scattering model incorporating coherence for thin-film silicon solar cells. *Journal of Applied Physics*, 110(3):033111, 2011. URL: http://scitation.aip.org/content/aip/journal/jap/110/3/10.1063/1.3622328. (Cited on page 47.)

[113] R. Häusermann, E. Knapp, M. Moos, N. A. Reinke, T. Flatz, and B. Ruhstaller. Coupled optoelectronic simulation of organic bulk-heterojunction solar cells: Parameter extraction and sensitivity analysis. *Journal of Applied Physics*, 106(10):104507, 2009. doi: 10.1063/1.3259367. URL: http://scitation.aip.org/content/aip/journal/jap/106/10/10.1063/1.3259367. (Cited on pages 47, 57, 69, 71, 109, 111 and 123.)

[114] Martin T. Neukom, Nils A. Reinke, Kai A. Brossi, and Beat Ruhstaller. Transient photocurrent response of organic bulk heterojunction solar cells. In *SPIE Photonics Europe*, pages 77220V–77220V. International Society for Optics and Photonics, 2010. URL: http://proceedings.spiedigitallibrary.org/proceeding.aspx?articleid=749468. (Cited on pages 47 and 167.)

[115] M.T. Neukom, N.A. Reinke, and B. Ruhstaller. Charge extraction with linearly increasing voltage: A numerical model for parameter extraction. *Solar Energy*,

2011 85(6):1250–1256. doi: 10.1016/j.solener.2011.02.028. URL: http://linkinghub.elsevier.com/retrieve/pii/S0038092X11000818. (Cited on pages 47, 79, 109, 157 and 167.)

[116] Simon Züfle, Martin T. Neukom, Stéphane Altazin, Marc Zinggeler, Marek Chrapa, Ton Offermans, and Beat Ruhstaller. An Effective Area Approach to Model Lateral Degradation in Organic Solar Cells. *Advanced Energy Materials*, 2015 pages 1614–6840. doi: 10.1002/aenm.201500835. URL: http://doi.wiley.com/10.1002/aenm.201500835. (Cited on pages 47, 67, 69, 98, 109 and 168.)

[117] S. Dongaonkar, J. D. Servaites, G. M. Ford, S. Loser, J. Moore, R. M. Gelfand, H. Mohseni, H. W. Hillhouse, R. Agrawal, M. A. Ratner, T. J. Marks, M. S. Lundstrom, and M. A. Alam. Universality of non-Ohmic shunt leakage in thin-film solar cells. *Journal of Applied Physics*, 2010 108(12):124509. doi: 10.1063/1.3518509. URL: http://aip.scitation.org/doi/10.1063/1.3518509. (Cited on pages 53, 68 and 72.)

[118] D.L. Scharfetter and H.K. Gummel. Large-signal analysis of a silicon Read diode oscillator. *IEEE Transactions on Electron Devices*, 1969 16(1):64–77. doi: 10.1109/T-ED.1969.16566. URL: http://ieeexplore.ieee.org/document/1475609/. (Cited on page 57.)

[119] H.K. Gummel. A self-consistent iterative scheme for one-dimensional steady state transistor calculations. *IEEE Transactions on Electron Devices*, 1964 11(10):455–465. doi: 10.1109/T-ED.1964.15364. URL: http://ieeexplore.ieee.org/document/1473752/. (Cited on page 57.)

[120] E. Knapp, R. Häusermann, H. U. Schwarzenbach, and B. Ruhstaller. Numerical simulation of charge transport in disordered organic semiconductor devices. *Journal of Applied Physics*, 2010 108(5):054504. doi: 10.1063/1.3475505. URL: http://aip.scitation.org/doi/10.1063/1.3475505. (Cited on page 57.)

[121] Evelyne Knapp and Beat Ruhstaller. Numerical analysis of steady-state and transient charge transport in organic semiconductor devices. *Optical and Quantum Electronics*, 2011 42(11-13):667–677. doi: 10.1007/s11082-011-9443-1. URL: http://link.springer.com/10.1007/s11082-011-9443-1. (Cited on pages 57 and 95.)

[122] M. Ershov, H. C. Liu, L. Li, M. Buchanan, Z. R. Wasilewski, and A. K. Jonscher. Negative capacitance effect in semiconductor devices. *IEEE Transactions on Electron Devices*, 1998 45(10):2196–2206. doi: 10.1109/16.725254. URL: http://arxiv.org/abs/cond-mat/9806145. arXiv: cond-mat/9806145. (Cited on pages 57, 58 and 142.)

[123] Kenneth Levenberg. A method for the solution of certain non-linear problems in least squares. *Quarterly of applied mathematics*, 2(2):164–168, 1944. (Cited on pages 60, 61 and 110.)

[124] Donald W. Marquardt. An Algorithm for Least-Squares Estimation of Nonlinear Parameters. *Journal of the Society for Industrial and Applied Mathematics*, 1963 11(2):431–441. doi: 10.1137/0111030. URL: http://epubs.siam.org/doi/10.1137/0111030. (Cited on pages 60, 61 and 110.)

[125] Martin Neukom, Simon Züfle, Sandra Jenatsch, and Beat Ruhstaller. Opto-electronic characterization of third-generation solar cells. *Science and Technology of Advanced Materials*, 2018 19(1):291–316. doi: 10.1080/14686996.2018.1442091. URL: https://www.tandfonline.com/doi/full/10.1080/14686996.2018.1442091. (Cited on pages 65, 67, 141, 144, 146 and 167.)

[126] Dieter K. Schroder. Carrier lifetimes in silicon. *IEEE transactions on Electron Devices*, 44(1):160–170, 1997. URL: http://ieeexplore.ieee.org/abstract/document/554806/. (Cited on pages 65 and 82.)

[127] Andres Cuevas, Mark J. Kerr, Christian Samundsett, Francesca Ferrazza, and Gianluca Coletti. Millisecond minority carrier lifetimes in n -type multicrystalline silicon. *Applied Physics Letters*, 2002 81(26):4952–4954. doi: 10.1063/1.1529089. URL: http://aip.scitation.org/doi/10.1063/1.1529089.

[128] J. Knobloch, S. W. Glunz, D. Biro, W. Warta, E. Schaffer, and W. Wettling. Solar cells with efficiencies above 21% processed from Czochralski grown silicon. In *Photovoltaic Specialists Conference, 1996., Conference Record of the Twenty Fifth IEEE*, pages 405–408. IEEE, 1996. (Cited on page 65.)

[129] Harrison Ka Hin Lee, Zhao Li, Iordania Constantinou, Franky So, Sai Wing Tsang, and Shu Kong So. Batch-to-Batch Variation of Polymeric Photovoltaic Materials: its Origin and Impacts on Charge Carrier Transport and Device Performances. *Advanced Energy Materials*, 2014 4(16):1400768. doi: 10.1002/aenm.201400768. URL: http://doi.wiley.com/10.1002/aenm.201400768. (Cited on page 66.)

[130] M. Glatthaar, M. Riede, N. Keegan, K. Sylvester-Hvid, B. Zimmermann, M. Niggemann, A. Hinsch, and A. Gombert. Efficiency limiting factors of organic bulk heterojunction solar cells identified by electrical impedance spectroscopy. *Solar Energy Materials and Solar Cells*, 2007 91(5):390–393. doi: 10.1016/j.solmat.2006.10.020. URL: http://linkinghub.elsevier.com/retrieve/pii/S0927024806004235. (Cited on pages 66, 67, 70 and 71.)

[131] Wolfgang Brütting, Stefan Berleb, and Anton G. Mückl. Device physics of organic light-emitting diodes based on molecular materials. *Organic electronics*, 2(1):1–36, 2001. (Cited on pages 66, 72 and 98.)

[132] Mingdong Wang, Fangyan Xie, Jun Du, Qin Tang, Shizhao Zheng, Qian Miao, Jian Chen, Ni Zhao, and J.B. Xu. Degradation mechanism of organic solar cells with aluminum cathode. *Solar Energy Materials and Solar Cells*, 2011 95(12):3303–3310. doi: 10.1016/j.solmat.2011.07.020. URL: http://linkinghub.elsevier.com/retrieve/pii/S0927024811004235. (Cited on pages 67, 98 and 109.)

[133] Wolfgang Tress, Karl Leo, and Moritz Riede. Influence of Hole-Transport Layers and Donor Materials on Open-Circuit Voltage and Shape of I-V Curves of Organic Solar Cells. *Advanced Functional Materials*, 2011 21(11):2140–2149. doi: 10.1002/adfm.201002669. URL: http://doi.wiley.com/10.1002/adfm.201002669. (Cited on pages 68 and 70.)

[134] Sarah R. Cowan, Wei Lin Leong, Natalie Banerji, Gilles Dennler, and Alan J. Heeger. Identifying a Threshold Impurity Level for Organic Solar Cells: Enhanced First-Order Recombination Via Well-Defined PC84bm Traps in Organic Bulk Heterojunction Solar Cells. *Advanced Functional Materials*, 2011 21(16):3083–3092. doi: 10.1002/adfm.201100514. URL: http://doi.wiley.com/10.1002/adfm.201100514. (Cited on pages 68 and 72.)

[135] Adolf Goetzberger, Joachim Knobloch, and Bernhard Voß. *The Principles of Photovoltaics*. John Wiley & Sons, Ltd, 2014 Chichester, UK. ISBN 978-1-119-03376-9 978-0-471-97144-3. doi: 10.1002/9781119033769.ch3. URL: http://doi.wiley.com/10.1002/9781119033769.ch3. (Cited on pages 68 and 70.)

[136] Jasper J Michels, A Jolt Oostra, and Paul W M Blom. Short-circuit prevention strategies in organic light-emitting diodes and solar cells. *Smart Materials and Structures*, 2016 25(8):084015. doi: 10.1088/0964-1726/25/8/084015. URL: http://stacks.iop.org/0964-1726/25/i=8/a=084015?key=crossref.a8384c9fdb33396deae23361e3fd0241. (Cited on pages 68 and 72.)

[137] Jun-Seok Yeo, Jin-Mun Yun, Seok-Soon Kim, Dong-Yu Kim, Junkyung Kim, and Seok-In Na. Variations of cell performance in ITO-free organic solar cells with

increasing cell areas. *Semiconductor Science and Technology*, 2011 26(3):034010. doi: 10.1088/0268-1242/26/3/034010. URL: http://stacks.iop.org/0268-1242/26/i=3/a=034010?key=crossref.706ec37a8fb9e6f3285ca63a7a97eb41. (Cited on pages 69 and 72.)

[138] Andrea Seemann, Tobias Sauermann, Christoph Lungenschmied, Oskar Armbruster, Siegfried Bauer, H.-J. Egelhaaf, and Jens Hauch. Reversible and irreversible degradation of organic solar cell performance by oxygen. *Solar Energy*, 2011 85(6):1238–1249. doi: 10.1016/j.solener.2010.09.007. URL: http://linkinghub.elsevier.com/retrieve/pii/S0038092X10002999. (Cited on pages 69, 78 and 109.)

[139] Davide Bartesaghi, Irene del Carmen Pérez, Juliane Kniepert, Steffen Roland, Mathieu Turbiez, Dieter Neher, and L. Jan Anton Koster. Competition between recombination and extraction of free charges determines the fill factor of organic solar cells. *Nature Communications*, 2015 6:7083. doi: 10.1038/ncomms8083. URL: http://www.nature.com/doifinder/10.1038/ncomms8083. (Cited on page 70.)

[140] Julia Wagner, Mark Gruber, Andreas Wilke, Yuya Tanaka, Katharina Topczak, Andreas Steindamm, Ulrich Hörmann, Andreas Opitz, Yasuo Nakayama, Hisao Ishii, Jens Pflaum, Norbert Koch, and Wolfgang Brütting. Identification of different origins for s-shaped current voltage characteristics in planar heterojunction organic solar cells. *Journal of Applied Physics*, 2012 111(5):054509. doi: 10.1063/1.3692050. URL: http://aip.scitation.org/doi/10.1063/1.3692050. (Cited on page 70.)

[141] Fernando De Castro, Antonino Laudani, Francesco Riganti Fulginei, and Alessandro Salvini. An in-depth analysis of the modelling of organic solar cells using multiple-diode circuits. *Solar Energy*, 2016 135:590–597. doi: 10.1016/j.solener.2016.06.033. URL: http://linkinghub.elsevier.com/retrieve/pii/S0038092X16302122. (Cited on pages 71 and 109.)

[142] W. Nie, H. Tsai, R. Asadpour, J.-C. Blancon, A. J. Neukirch, G. Gupta, J. J. Crochet, M. Chhowalla, S. Tretiak, M. A. Alam, H.-L. Wang, and A. D. Mohite. High-efficiency solution-processed perovskite solar cells with millimeter-scale grains. *Science*, 2015 347(6221):522–525. doi: 10.1126/science.aaa0472. URL: http://www.sciencemag.org/cgi/doi/10.1126/science.aaa0472. (Cited on pages 120 and 136.)

[143] Tejas S. Sherkar, Cristina Momblona, Lidón Gil-Escrig, Jorge Ávila, Michele Sessolo, Henk J. Bolink, and L. Jan Anton Koster. Recombination in Perovskite Solar Cells: Significance of Grain Boundaries, Interface Traps, and Defect Ions. *ACS Energy Letters*, 2017 2(5):1214–1222. doi: 10.1021/acsenergylett.7b00236. URL: http://pubs.acs.org/doi/abs/10.1021/acsenergylett.7b00236. (Cited on page 147.)

[144] Xingshu Sun, Reza Asadpour, Wanyi Nie, Aditya D. Mohite, and Muhammad Ashraful Alam. A Physics-Based Analytical Model for Perovskite Solar Cells. *IEEE Journal of Photovoltaics*, 2015 5(5):1389–1394. doi: 10.1109/JPHOTOV.2015.2451000. URL: http://ieeexplore.ieee.org/document/7160671/. (Cited on pages 71 and 109.)

[145] N. F. Mott and R. W. Gurney. Electronic Processes in Ionic Crystals. *Clarendon Press*, 1940. (Cited on page 72.)

[146] G. A. H. Wetzelaer, M. Kuik, M. Lenes, and P. W. M. Blom. Origin of the dark-current ideality factor in polymer: fullerene bulk heterojunction solar cells. *Applied Physics Letters*, 99(15):153506, 2011. URL: http://scitation.aip.org/content/aip/journal/apl/99/15/10.1063/1.3651752. (Cited on page 73.)

[147] Thomas Kirchartz, Florent Deledalle, Pabitra Shakya Tuladhar, James R. Durrant, and Jenny Nelson. On the Differences between Dark and Light Ideality Factor in Polymer:Fullerene Solar Cells. *The Journal of Physical Chemistry Letters*, 2013 4(14):2371–2376. doi: 10.1021/jz4012146. URL: http://pubs.acs.org/doi/abs/10.1021/

jz4012146. (Cited on pages 73, 74 and 144.)

[148] V. D. Mihailetchi, L. J. A. Koster, J. C. Hummelen, and P. W. M. Blom. Photocurrent Generation in Polymer-Fullerene Bulk Heterojunctions. *Physical Review Letters*, 2004 93(21):216601. doi: 10.1103/PhysRevLett.93.216601. URL: https://link.aps.org/doi/10.1103/PhysRevLett.93.216601. (Cited on pages 74 and 111.)

[149] L. J. A. Koster, V. D. Mihailetchi, R. Ramaker, and P. W. M. Blom. Light intensity dependence of open-circuit voltage of polymer:fullerene solar cells. *Applied Physics Letters*, 2005 86(12):123509. doi: 10.1063/1.1889240. URL: http://aip.scitation.org/doi/10.1063/1.1889240. (Cited on page 74.)

[150] G. Juška, K. Arlauskas, M. Viliūnas, and J. Kočka. Extraction current transients: new method of study of charge transport in microcrystalline silicon. *Physical review letters*, 84(21):4946, 2000. URL: http://journals.aps.org/prl/abstract/10.1103/PhysRevLett.84.4946. (Cited on pages 76 and 78.)

[151] A. J. Mozer, N. S. Sariciftci, L. Lutsen, D. Vanderzande, R. Österbacka, M. Westerling, and G. Juška. Charge transport and recombination in bulk heterojunction solar cells studied by the photoinduced charge extraction in linearly increasing voltage technique. *Applied Physics Letters*, 86(11):112104, 2005. doi: 10.1063/1.1882753. URL: http://scitation.aip.org/content/aip/journal/apl/86/11/10.1063/1.1882753. (Cited on pages 76 and 80.)

[152] Sebastian Bange, Marcel Schubert, and Dieter Neher. Charge mobility determination by current extraction under linear increasing voltages: Case of nonequilibrium charges and field-dependent mobilities. *Physical Review B*, 2010 81(3):035209. doi: 10.1103/PhysRevB.81.035209. URL: http://link.aps.org/doi/10.1103/PhysRevB.81.035209. (Cited on page 78.)

[153] Jens Lorrmann, Bekele Homa Badada, Olle Inganäs, Vladimir Dyakonov, and Carsten Deibel. Charge carrier extraction by linearly increasing voltage: Analytic framework and ambipolar transients. *Journal of Applied Physics*, 108(11):113705, 2010. URL: http://scitation.aip.org/content/aip/journal/jap/108/11/10.1063/1.3516392. (Cited on pages 76 and 78.)

[154] G. Juška, N. Nekrašas, and K. Genevičius. Investigation of charge carriers transport from extraction current transients of injected charge carriers. *Journal of Non-Crystalline Solids*, 2012 358(4):748–750. doi: 10.1016/j.jnoncrysol.2011.12.016. URL: http://linkinghub.elsevier.com/retrieve/pii/S0022309311007265. (Cited on page 77.)

[155] Ardalan Armin, Marrapan Velusamy, Paul L. Burn, Paul Meredith, and Almantas Pivrikas. Injected charge extraction by linearly increasing voltage for bimolecular recombination studies in organic solar cells. *Applied Physics Letters*, 101(8):083306, 2012. doi: 10.1063/1.4747330. URL: http://scitation.aip.org/content/aip/journal/apl/101/8/10.1063/1.4747330.

[156] Yajun Gao, Almantas Pivrikas, Bin Xu, Yang Liu, Weiqing Xu, Paul H.M. van Loosdrecht, and Wenjing Tian. Measuring electron and hole mobilities in organic systems: charge selective CELIV. *Synthetic Metals*, 2015 203:187–191. doi: 10.1016/j.synthmet.2015.02.036. URL: http://linkinghub.elsevier.com/retrieve/pii/S0379677915001034. (Cited on page 77.)

[157] Simon Züfle, Stéphane Altazin, Alexander Hofmann, Lars Jäger, Martin T. Neukom, Tobias D. Schmidt, Wolfgang Brütting, and Beat Ruhstaller. The use of charge extraction by linearly increasing voltage in polar organic light-emitting diodes. *Journal of Applied Physics*, 2017 121(17):175501. doi: 10.1063/1.4982903. URL: http://aip.scitation.org/doi/10.1063/1.4982903. (Cited on pages 77 and 168.)

[158] S. Züfle, S. Altazin, A. Hofmann, L. Jäger, M. T. Neukom, W. Brütting, and B. Ruhstaller. Determination of charge transport activation energy and injection barrier in organic semiconductor devices. *Journal of Applied Physics*, 2017 122(11):115502. doi: 10.1063/1.4992041. URL: http://aip.scitation.org/doi/10.1063/1.4992041. (Cited on pages 77, 106 and 168.)

[159] Oskar J. Sandberg, Mathias Nyman, and Ronald Österbacka. Direct determination of doping concentration and built-in voltage from extraction current transients. *Organic Electronics*, 2014 15(11):3413–3420. doi: 10.1016/j.orgel.2014.09.027. URL: http://linkinghub.elsevier.com/retrieve/pii/S1566119914004194. (Cited on page 78.)

[160] Lindsay C. C. Elliott, James I. Basham, Kurt P. Pernstich, Pragya R. Shrestha, Lee J. Richter, Dean M. DeLongchamp, and David J. Gundlach. Probing Charge Recombination Dynamics in Organic Photovoltaic Devices under Open-Circuit Conditions. *Advanced Energy Materials*, 2014 4(15):1400356. doi: 10.1002/aenm.201400356. URL: http://doi.wiley.com/10.1002/aenm.201400356. (Cited on page 81.)

[161] A. Baumann, K. Tvingstedt, M. C. Heiber, S. Väth, C. Momblona, H. J. Bolink, and V. Dyakonov. Persistent photovoltage in methylammonium lead iodide perovskite solar cells. *APL Materials*, 2014 2(8):081501. doi: 10.1063/1.4885255. URL: http://scitation.aip.org/content/aip/journal/aplmater/2/8/10.1063/1.4885255. (Cited on page 81.)

[162] Florent Deledalle, Pabitra Shakya Tuladhar, Jenny Nelson, James R. Durrant, and Thomas Kirchartz. Understanding the Apparent Charge Density Dependence of Mobility and Lifetime in Organic Bulk Heterojunction Solar Cells. *The Journal of Physical Chemistry C*, 2014 118(17):8837–8842. doi: 10.1021/jp502948y. URL: http://pubs.acs.org/doi/10.1021/jp502948y. (Cited on pages 82, 83, 84 and 85.)

[163] Brian C. O'Regan, James R. Durrant, Paul M. Sommeling, and Nicolaas J. Bakker. Influence of the $TiCl_4$ Treatment on Nanocrystalline TiO_2 Films in Dye-Sensitized Solar Cells. 2. Charge Density, Band Edge Shifts, and Quantification of Recombination Losses at Short Circuit. *The Journal of Physical Chemistry C*, 2007 111(37):14001–14010. doi: 10.1021/jp073056p. URL: http://pubs.acs.org/doi/abs/10.1021/jp073056p. (Cited on pages 83 and 106.)

[164] David Kiermasch, Andreas Baumann, Mathias Fischer, Vladimir Dyakonov, and Kristofer Tvingstedt. Revisiting lifetimes from transient electrical characterization of thin film solar cells; a capacitive concern evaluated for silicon, organic and perovskite devices. *Energy & Environmental Science*, 11(3):629–640, 2018. doi: 10.1039/C7EE03155F. URL: http://xlink.rsc.org/?DOI=C7EE03155F. (Cited on page 85.)

[165] D. V. Lang. Deep-level transient spectroscopy: A new method to characterize traps in semiconductors. *Journal of Applied Physics*, 1974 45(7):3023–3032. doi: 10.1063/1.1663719. URL: http://aip.scitation.org/doi/10.1063/1.1663719. (Cited on page 86.)

[166] Bruce W. Wessels. Determination of deep levels in Cu-doped GaP using transient-current spectroscopy. *Journal of Applied Physics*, 1976 47(3):1131–1133. doi: 10.1063/1.322695. URL: http://aip.scitation.org/doi/10.1063/1.322695.

[167] J.A. Borsuk and R.M. Swanson. Current transient spectroscopy: A high-sensitivity DLTS system. *IEEE Transactions on Electron Devices*, 1980 27(12):2217–2225. doi: 10.1109/T-ED.1980.20255. URL: http://ieeexplore.ieee.org/document/1481047/. (Cited on page 86.)

[168] B. M. Arora, S. Chakravarty, S. Subramanian, V. I. Polyakov, M. G. Ermakov, O. N. Ermakova, and P. I. Perov. Deep-level transient charge spectroscopy of Sn donors

in Al $_x$ Ga $_{1-x}$ As. *Journal of Applied Physics*, 1993 73(4):1802–1806. doi: 10.1063/1.353189. URL: http://aip.scitation.org/doi/10.1063/1.353189.

[169] Thomas R. Hanak, Richard K. Ahrenkiel, Donald J. Dunlavy, Assem M. Bakry, and Michael L. Timmons. A new method to analyze multiexponential transients for deep-level transient spectroscopy. *Journal of Applied Physics*, 1990 67(9):4126–4132. doi: 10.1063/1.344973. URL: http://aip.scitation.org/doi/10.1063/1.344973. (Cited on page 86.)

[170] Peter Stallinga, Henrique L. Gomes, H. Rost, A. B. Holmes, M. G. Harrison, and R. H. Friend. Electronic levels in MEH-PPV. *Synthetic metals*, 111:535–537, 2000. URL: http://www.sciencedirect.com/science/article/pii/S0379677999004130. (Cited on page 86.)

[171] Deniz Bozyigit, Michael Jakob, Olesya Yarema, and Vanessa Wood. Deep Level Transient Spectroscopy (DLTS) on Colloidal-Synthesized Nanocrystal Solids. *ACS Applied Materials & Interfaces*, 2013 5(8):2915–2919. doi: 10.1021/am400326t. URL: http://pubs.acs.org/doi/abs/10.1021/am400326t. (Cited on page 86.)

[172] Stefan Neugebauer, Julia Rauh, Carsten Deibel, and Vladimir Dyakonov. Investigation of electronic trap states in organic photovoltaic materials by current-based deep level transient spectroscopy. *Applied Physics Letters*, 2012 100(26):263304. doi: 10.1063/1.4731637. URL: http://aip.scitation.org/doi/10.1063/1.4731637. (Cited on page 86.)

[173] Woon Seok Yang, Byung-Wook Park, Eui Hyuk Jung, Nam Joong Jeon, Young Chan Kim, Dong Uk Lee, Seong Sik Shin, Jangwon Seo, Eun Kyu Kim, Jun Hong Noh, and others. Iodide management in formamidinium-lead-halide–based perovskite layers for efficient solar cells. *Science*, 356(6345):1376–1379, 2017. URL: http://science.sciencemag.org/content/356/6345/1376.abstract. (Cited on page 86.)

[174] K. I. Kirov and K. B. Radev. A simple charge-based DLTS technique. *physica status solidi (a)*, 63(2):711–716, 1981. URL: http://onlinelibrary.wiley.com/doi/10.1002/pssa.2210630241/full. (Cited on page 86.)

[175] R. A. Street. Localized state distribution and its effect on recombination in organic solar cells. *Physical Review B*, 2011 84(7):075208. doi: 10.1103/PhysRevB.84.075208. URL: https://link.aps.org/doi/10.1103/PhysRevB.84.075208. (Cited on pages 87, 89 and 102.)

[176] Christopher R. McNeill, Inchan Hwang, and Neil C. Greenham. Photocurrent transients in all-polymer solar cells: Trapping and detrapping effects. *Journal of Applied Physics*, 2009 106(2):024507. doi: 10.1063/1.3177337. URL: http://aip.scitation.org/doi/10.1063/1.3177337. (Cited on pages 89 and 90.)

[177] Inchan Hwang, Christopher R. McNeill, and Neil C. Greenham. Drift-diffusion modeling of photocurrent transients in bulk heterojunction solar cells. *Journal of Applied Physics*, 2009 106(9):094506. doi: 10.1063/1.3247547. URL: http://aip.scitation.org/doi/10.1063/1.3247547. (Cited on page 89.)

[178] N. W. Duffy, L. M. Peter, R. M. G. Rajapakse, and K. G. U. Wijayantha. A novel charge extraction method for the study of electron transport and interfacial transfer in dye sensitised nanocrystalline solar cells. *Electrochemistry Communications*, 2(9):658–662, 2000. (Cited on page 92.)

[179] C. G. Shuttle, A. Maurano, R. Hamilton, B. O'Regan, J. C. de Mello, and J. R. Durrant. Charge extraction analysis of charge carrier densities in a polythiophene/fullerene solar cell: Analysis of the origin of the device dark current. *Applied Physics Letters*, 2008 93(18):183501. doi: 10.1063/1.3006316. URL: http://aip.scitation.org/doi/10.1063/1.3006316. (Cited on page 92.)

[180] Brian C. O'Regan, Piers R. F. Barnes, Xiaoe Li, Chunhung Law, Emilio Palomares, and Jose M. Marin-Beloqui. Optoelectronic Studies of Methylammonium Lead Iodide Perovskite Solar Cells with Mesoporous TiO $_2$: Separation of Electronic and Chemical Charge Storage, Understanding Two Recombination Lifetimes, and the Evolution of Band Offsets during $J - V$ Hysteresis. *Journal of the American Chemical Society*, 2015 137(15):5087–5099. doi: 10.1021/jacs.5b00761. URL: http://pubs.acs.org/doi/abs/10.1021/jacs.5b00761. (Cited on page 92.)

[181] Ilja Lange, Juliane Kniepert, Patrick Pingel, Ines Dumsch, Sybille Allard, Silvia Janietz, Ullrich Scherf, and Dieter Neher. Correlation between the Open Circuit Voltage and the Energetics of Organic Bulk Heterojunction Solar Cells. *The Journal of Physical Chemistry Letters*, 2013 4(22):3865–3871. doi: 10.1021/jz401971e. URL: http://pubs.acs.org/doi/10.1021/jz401971e. (Cited on pages 92 and 93.)

[182] Brendan Wright, Yukihiro Nakajima, Tracey M. Clarke, Kouichi Okuda, Heikki Paananen, Attila J. Mozer, and Shogo Mori. Quantifying Recombination Losses during Charge Extraction in Bulk Heterojunction Solar Cells Using a Modified Charge Extraction Technique. *Advanced Energy Materials*, 2017 7(11):1602026. doi: 10.1002/aenm.201602026. URL: http://doi.wiley.com/10.1002/aenm.201602026. (Cited on pages 92 and 93.)

[183] James I. Basham, Thomas N. Jackson, and David J. Gundlach. Predicting the J - V Curve in Organic Photovoltaics Using Impedance Spectroscopy. *Advanced Energy Materials*, 2014 4(15):1400499. doi: 10.1002/aenm.201400499. URL: http://doi.wiley.com/10.1002/aenm.201400499. (Cited on page 95.)

[184] Germà Garcia-Belmonte, Antoni Munar, Eva M. Barea, Juan Bisquert, Irati Ugarte, and Roberto Pacios. Charge carrier mobility and lifetime of organic bulk heterojunctions analyzed by impedance spectroscopy. *Organic Electronics*, 2008 9(5):847–851. doi: 10.1016/j.orgel.2008.06.007. URL: http://linkinghub.elsevier.com/retrieve/pii/S1566119908001122.

[185] Mohammed F. Al-Mudhaffer, Matthew J. Griffith, Krishna Feron, Nicolas C. Nicolaidis, Nathan A. Cooling, Xiaojing Zhou, John Holdsworth, Warwick J. Belcher, and Paul C. Dastoor. The origin of performance limitations in miniemulsion nanoparticulate organic photovoltaic devices. *Solar Energy Materials and Solar Cells*, 2018 175:77–88. doi: 10.1016/j.solmat.2017.09.007. URL: http://linkinghub.elsevier.com/retrieve/pii/S0927024817304968.

[186] Nasim Mohammadian, Ahmad Moshaii, Amirhossein Alizadeh, Saba Gharibzadeh, and Raheleh Mohammadpour. Influence of Perovskite Morphology on Slow and Fast Charge Transport and Hysteresis in the Perovskite Solar Cells. *The Journal of Physical Chemistry Letters*, 2016 7(22):4614–4621. doi: 10.1021/acs.jpclett.6b01909. URL: http://pubs.acs.org/doi/abs/10.1021/acs.jpclett.6b01909. (Cited on pages 95, 136 and 137.)

[187] Amalie Dualeh, Thomas Moehl, Nicolas Tétreault, Joël Teuscher, Peng Gao, Mohammad Khaja Nazeeruddin, and Michael Grätzel. Impedance Spectroscopic Analysis of Lead Iodide Perovskite-Sensitized Solid-State Solar Cells. *ACS Nano*, 2014 8(1):362–373. doi: 10.1021/nn404323g. URL: http://pubs.acs.org/doi/abs/10.1021/nn404323g. (Cited on page 95.)

[188] Evelyne Knapp and Beat Ruhstaller. The role of shallow traps in dynamic characterization of organic semiconductor devices. *Journal of Applied Physics*, 112(2):024519, 2012. doi: 10.1063/1.4739303. URL: http://scitation.aip.org/content/aip/journal/jap/112/2/10.1063/1.4739303. (Cited on page 95.)

[189] Deniz Bozyigit, Sebastian Volk, Olesya Yarema, and Vanessa Wood. Quantification of Deep Traps in Nanocrystal Solids, Their Electronic Properties, and Their Influence on Device Behavior. *Nano Letters*, 2013 13(11):5284–5288. doi: 10.1021/nl402803h. URL: http://pubs.acs.org/doi/10.1021/nl402803h. (Cited on pages 95, 106 and 112.)

[190] Evelyne Knapp and Beat Ruhstaller. Analysis of negative capacitance and self-heating in organic semiconductor devices. *Journal of Applied Physics*, 2015 117(13): 135501. doi: 10.1063/1.4916981. URL: http://scitation.aip.org/content/aip/journal/jap/117/13/10.1063/1.4916981. (Cited on pages 95 and 98.)

[191] Durgesh C. Tripathi and Y. N. Mohapatra. Diffusive capacitance in space charge limited organic diodes: Analysis of peak in capacitance-voltage characteristics. *Applied Physics Letters*, 102(25):253303, 2013. doi: 10.1063/1.4812487. URL: http://scitation.aip.org/content/aip/journal/apl/102/25/10.1063/1.4812487. (Cited on pages 98 and 99.)

[192] S. L. M. van Mensfoort and R. Coehoorn. Determination of Injection Barriers in Organic Semiconductor Devices from Capacitance Measurements. *Physical Review Letters*, 2008 100(8):086802. doi: 10.1103/PhysRevLett.100.086802. URL: http://link.aps.org/doi/10.1103/PhysRevLett.100.086802. (Cited on page 98.)

[193] W. Chr. Germs, J. J. M. van der Holst, S. L. M. van Mensfoort, P. A. Bobbert, and R. Coehoorn. Modeling of the transient mobility in disordered organic semiconductors with a Gaussian density of states. *Physical Review B*, 2011 84(16):165210. doi: 10.1103/PhysRevB.84.165210. URL: http://link.aps.org/doi/10.1103/PhysRevB.84.165210. (Cited on page 98.)

[194] Sandra Jenatsch, Roland Hany, Anna C. Véron, Martin Neukom, Simon Züfle, Andreas Borgschulte, Beat Ruhstaller, and Frank Nüesch. Influence of Molybdenum Oxide Interface Solvent Sensitivity on Charge Trapping in Bilayer Cyanine Solar Cells. *The Journal of Physical Chemistry C*, 2014 118(30):17036–17045. doi: 10.1021/jp5005314. URL: http://pubs.acs.org/doi/abs/10.1021/jp5005314. (Cited on pages 98 and 168.)

[195] Tobias D. Schmidt, Lars Jäger, Yutaka Noguchi, Hisao Ishii, and Wolfgang Brütting. Analyzing degradation effects of organic light-emitting diodes via transient optical and electrical measurements. *Journal of Applied Physics*, 2015 117(21):215502. doi: 10.1063/1.4921829. URL: http://scitation.aip.org/content/aip/journal/jap/117/21/10.1063/1.4921829. (Cited on pages 98 and 105.)

[196] Stefan Nowy, Wei Ren, Andreas Elschner, Wilfried Lövenich, and Wolfgang Brütting. Impedance spectroscopy as a probe for the degradation of organic light-emitting diodes. *Journal of Applied Physics*, 107(5):054501, 2010. doi: 10.1063/1.3294642. URL: http://scitation.aip.org/content/aip/journal/jap/107/5/10.1063/1.3294642. (Cited on page 98.)

[197] S. Altazin, S. Züfle, E. Knapp, C. Kirsch, T.D. Schmidt, L. Jäger, Y. Noguchi, W. Brütting, and B. Ruhstaller. Simulation of OLEDs with a polar electron transport layer. *Organic Electronics*, 2016 39:244–249. doi: 10.1016/j.orgel.2016.10.014. URL: http://linkinghub.elsevier.com/retrieve/pii/S1566119916304414. (Cited on page 98.)

[198] Thomas Kirchartz, Wei Gong, Steven A. Hawks, Tiziano Agostinelli, Roderick C. I. MacKenzie, Yang Yang, and Jenny Nelson. Sensitivity of the Mott–Schottky Analysis in Organic Solar Cells. *The Journal of Physical Chemistry C*, 2012 116(14):7672–7680. doi: 10.1021/jp300397f. URL: http://pubs.acs.org/doi/abs/10.1021/jp300397f. (Cited on pages 99 and 109.)

[199] M. Mingebach, C. Deibel, and V. Dyakonov. Built-in potential and validity of the Mott-Schottky analysis in organic bulk heterojunction solar cells. *Physical Review B*, 2011 84(15):153201. doi: 10.1103/PhysRevB.84.153201. URL: https://link.aps.org/doi/10.1103/PhysRevB.84.153201. (Cited on pages 99, 104 and 109.)

[200] J. Li and L. M. Peter. Surface recombination at semiconductor electrodes: Part III. Steady-state and intensity modulated photocurrent response. *Journal of electroanalytical chemistry and interfacial electrochemistry*, 193(1-2):27–47, 1985. URL: http://www.sciencedirect.com/science/article/pii/0022072885850506. (Cited on pages 100 and 146.)

[201] E. A. Ponomarev and L. M. Peter. A generalized theory of intensity modulated photocurrent spectroscopy (IMPS). *Journal of Electroanalytical Chemistry*, 396 (1-2):219–226, 1995. URL: http://www.sciencedirect.com/science/article/pii/0022072895041155. (Cited on page 100.)

[202] Jessica Krüger, Robert Plass, Michael Grätzel, Petra J. Cameron, and Laurence M. Peter. Charge Transport and Back Reaction in Solid-State Dye-Sensitized Solar Cells: A Study Using Intensity-Modulated Photovoltage and Photocurrent Spectroscopy. *The Journal of Physical Chemistry B*, 2003 107(31):7536–7539. doi: 10.1021/jp0348777. URL: http://pubs.acs.org/doi/abs/10.1021/jp0348777.

[203] Arthur J. Frank, Nikos Kopidakis, and Jao van de Lagemaat. Electrons in nanostructured TiO2 solar cells: transport, recombination and photovoltaic properties. *Coordination Chemistry Reviews*, 2004 248(13-14):1165–1179. doi: 10.1016/j.ccr.2004.03.015. URL: http://linkinghub.elsevier.com/retrieve/pii/S0010854504000621. (Cited on page 100.)

[204] Gyeong-Ok Kim and Kwang-Sun Ryu. Dynamic Response of Charge Transfer and Recombination at Various Electrodes in Dye-sensitized Solar Cells Investigated Using Intensity Modulated Photocurrent and Photovoltage Spectroscopy. *Bulletin of the Korean Chemical Society*, 2012 33(2):469–472. doi: 10.5012/bkcs.2012.33.2.469. URL: http://koreascience.or.kr/journal/view.jsp?kj=JCGMCS&py=2012&vnc=v33n2&sp=469. (Cited on pages 100 and 102.)

[205] Ying Ting Set, Marc Daniel Heinemann, Erik Birgersson, and Joachim Luther. On the Origin of the Quadrant I Semicircle in Intensity-Modulated Photocurrent Spectra of P3ht:PCBM Bulk Heterojunction Solar Cells: Evidence of Degradation-Related Trap-Assisted Recombination. *The Journal of Physical Chemistry C*, 2013 117(16):7993–8000. doi: 10.1021/jp310841v. URL: http://pubs.acs.org/doi/abs/10.1021/jp310841v. (Cited on page 100.)

[206] Yongqian Gao, Adam J. Wise, Alan K. Thomas, and John K. Grey. Spectroscopic and Intensity Modulated Photocurrent Imaging of Polymer/Fullerene Solar Cells. *ACS Applied Materials & Interfaces*, 2016 8(1):285–293. doi: 10.1021/acsami.5b08724. URL: http://pubs.acs.org/doi/abs/10.1021/acsami.5b08724. (Cited on page 101.)

[207] Juan-Pablo Correa-Baena, Miguel Anaya, Gabriel Lozano, Wolfgang Tress, Konrad Domanski, Michael Saliba, Taisuke Matsui, Tor Jesper Jacobsson, Mauricio E. Calvo, Antonio Abate, Michael Grätzel, Hernán Míguez, and Anders Hagfeldt. Unbroken Perovskite: Interplay of Morphology, Electro-optical Properties, and Ionic Movement. *Advanced Materials*, 2016 28:5031–5037. doi: 10.1002/adma.201600624. URL: http://doi.wiley.com/10.1002/adma.201600624. (Cited on pages 101, 120 and 146.)

[208] Joshua C. Byers, Scott Ballantyne, Konstantin Rodionov, Alex Mann, and O. A. Semenikhin. Mechanism of Recombination Losses in Bulk Heterojunction P3ht:PCBM Solar Cells Studied Using Intensity Modulated Photocurrent Spectroscopy. *ACS*

Applied Materials & Interfaces, 2011 3(2):392–401. doi: 10.1021/am100998t. URL: http://pubs.acs.org/doi/abs/10.1021/am100998t. (Cited on pages 102 and 146.)

[209] A. Pivrikas, N. S. Sariciftci, G. Juška, and R. Österbacka. A review of charge transport and recombination in polymer/fullerene organic solar cells. *Progress in Photovoltaics: Research and Applications*, 2007 15(8):677–696. doi: 10.1002/pip.791. URL: http://doi.wiley.com/10.1002/pip.791. (Cited on pages 103, 106 and 117.)

[210] Kevin K.H. Chan, S.W. Tsang, Harrison K.H. Lee, Franky So, and S.K. So. Charge injection and transport studies of poly(2,7-carbazole) copolymer PCDTBT and their relationship to solar cell performance. *Organic Electronics*, 2012 13(5):850–855. doi: 10.1016/j.orgel.2012.01.030. URL: http://linkinghub.elsevier.com/retrieve/pii/S1566119912000596. (Cited on pages 105, 117 and 155.)

[211] Dirk Hertel, Ed Vin Soh, Heinz Bässler, and Lewis J. Rothberg. Electric field dependent generation of geminate electron–hole pairs in a ladder-type -conjugated polymer probed by fluorescence quenching and delayed field collection of charge carriers. *Chemical Physics Letters*, 2002 361(1-2):99–105. doi: 10.1016/S0009-2614(02)00898-9. URL: http://linkinghub.elsevier.com/retrieve/pii/S0009261402008989. (Cited on pages 105 and 111.)

[212] Juliane Kniepert, Marcel Schubert, James C. Blakesley, and Dieter Neher. Photogeneration and Recombination in P3ht/PCBM Solar Cells Probed by Time-Delayed Collection Field Experiments. *The Journal of Physical Chemistry Letters*, 2011 2(7):700–705. doi: 10.1021/jz200155b. URL: http://pubs.acs.org/doi/abs/10.1021/jz200155b. (Cited on page 105.)

[213] Andreas Baumann, Stefan Väth, Philipp Rieder, Michael C. Heiber, Kristofer Tvingstedt, and Vladimir Dyakonov. Identification of Trap States in Perovskite Solar Cells. *The Journal of Physical Chemistry Letters*, 2015 6(12):2350–2354. doi: 10.1021/acs.jpclett.5b00953. URL: http://pubs.acs.org/doi/abs/10.1021/acs.jpclett.5b00953. (Cited on pages 105 and 148.)

[214] Xu Han, Monojit Bag, Timothy S. Gehan, Dhandapani Venkataraman, and Dimitrios Maroudas. Analysis of hole transport in thin films and nanoparticle assemblies of poly(3-hexylthiophene). *Chemical Physics Letters*, 2014 610-611:273–277. doi: 10.1016/j.cplett.2014.07.022. URL: http://linkinghub.elsevier.com/retrieve/pii/S0009261414006009. (Cited on page 106.)

[215] Ying Ting Set, Teng Zhang, Erik Birgersson, and Joachim Luther. What parameters can be reliably deduced from the current-voltage characteristics of an organic bulk-heterojunction solar cell? *Journal of Applied Physics*, 2015 117(8):084503. doi: 10.1063/1.4913674. URL: http://aip.scitation.org/doi/10.1063/1.4913674. (Cited on page 109.)

[216] Rickard Hansson. *Materials and Device Engineering for Efficient and Stable Polymer Solar Cells*. PhD thesis, Karlstads universitet, 2017. (Cited on pages 109 and 110.)

[217] Gon Namkoong, Jaemin Kong, Matthew Samson, In-Wook Hwang, and Kwanghee Lee. Active layer thickness effect on the recombination process of PCDTBT:PC71bm organic solar cells. *Organic Electronics*, 2013 14(1):74–79. doi: 10.1016/j.orgel.2012.10.025. URL: http://linkinghub.elsevier.com/retrieve/pii/S1566119912004910. (Cited on page 111.)

[218] Zhe Li and Christopher R. McNeill. Transient photocurrent measurements of PCDTBT:PC $_{70}$ BM and PCPDTBT:PC $_{70}$ BM Solar Cells: Evidence for charge trapping in efficient polymer/fullerene blends. *Journal of Applied Physics*, 2011 109(7):074513. doi: 10.1063/1.3573394. URL: http://aip.scitation.org/doi/10.1063/1.3573394. (Cited on page 117.)

[219] Martin Thomas Neukom, Simon Züfle, Evelyne Knapp, Mohammed Makha, Roland Hany, and Beat Ruhstaller. Why perovskite solar cells with high efficiency show small IV-curve hysteresis. *Solar Energy Materials and Solar Cells*, 2017 169:159–166. doi: 10.1016/j.solmat.2017.05.021. URL: https://linkinghub.elsevier.com/retrieve/pii/S0927024817302386. (Cited on pages 119, 157 and 167.)

[220] Dane W. deQuilettes, Wei Zhang, Victor M. Burlakov, Daniel J. Graham, Tomas Leijtens, Anna Osherov, Vladimir Bulović, Henry J. Snaith, David S. Ginger, and Samuel D. Stranks. Photo-induced halide redistribution in organic–inorganic perovskite films. *Nature Communications*, 2016 7:11683. doi: 10.1038/ncomms11683. URL: http://www.nature.com/doifinder/10.1038/ncomms11683. (Cited on pages 119 and 151.)

[221] Konrad Domanski, Juan-Pablo Correa-Baena, Nicolas Mine, Mohammad Khaja Nazeeruddin, Antonio Abate, Michael Saliba, Wolfgang Tress, Anders Hagfeldt, and Michael Grätzel. Not All That Glitters Is Gold: Metal-Migration-Induced Degradation in Perovskite Solar Cells. *ACS Nano*, 2016 10(6):6306–6314. doi: 10.1021/acsnano.6b02613. URL: http://pubs.acs.org/doi/abs/10.1021/acsnano.6b02613. (Cited on pages 119 and 156.)

[222] David A. Egger, Leeor Kronik, and Andrew M. Rappe. Theory of Hydrogen Migration in Organic-Inorganic Halide Perovskites. *Angewandte Chemie International Edition*, 2015 54(42):12437–12441. doi: 10.1002/anie.201502544. URL: http://doi.wiley.com/10.1002/anie.201502544. (Cited on page 119.)

[223] Somayeh Gholipour, Juan-Pablo Correa-Baena, Konrad Domanski, Taisuke Matsui, Ludmilla Steier, Fabrizio Giordano, Fariba Tajabadi, Wolfgang Tress, Michael Saliba, Antonio Abate, Abdollah Morteza Ali, Nima Taghavinia, Michael Grätzel, and Anders Hagfeldt. Highly Efficient and Stable Perovskite Solar Cells based on a Low-Cost Carbon Cloth. *Advanced Energy Materials*, 2016 page 1601116. doi: 10.1002/aenm.201601116. URL: http://doi.wiley.com/10.1002/aenm.201601116. (Cited on page 120.)

[224] Dong Yang, Xin Zhou, Ruixia Yang, Zhou Yang, Wei Yu, Xiuli Wang, Can Li, Shengzhong (Frank) Liu, and Robert P. H. Chang. Surface optimization to eliminate hysteresis for record efficiency planar perovskite solar cells. *Energy & Environmental Science*, 9(10):3071–3078, 2016. doi: 10.1039/C6EE02139E. URL: http://xlink.rsc.org/?DOI=C6EE02139E. (Cited on page 120.)

[225] Jin Hyuck Heo, Hye Ji Han, Dasom Kim, Tae Kyu Ahn, and Sang Hyuk Im. Hysteresis-less inverted CH $_3$ NH $_3$ PbI $_3$ planar perovskite hybrid solar cells with 18.1% power conversion efficiency. *Energy & Environmental Science*, 8(5):1602–1608, 2015. doi: 10.1039/C5EE00120J. URL: http://xlink.rsc.org/?DOI=C5EE00120J. (Cited on page 120.)

[226] Juan Pablo Correa Baena, Ludmilla Steier, Wolfgang Tress, Michael Saliba, Stefanie Neutzner, Taisuke Matsui, Fabrizio Giordano, T. Jesper Jacobsson, Ajay Ram Srimath Kandada, Shaik M. Zakeeruddin, Annamaria Petrozza, Antonio Abate, Mohammad Khaja Nazeeruddin, Michael Grätzel, and Anders Hagfeldt. Highly efficient planar perovskite solar cells through band alignment engineering. *Energy & Environmental Science*, 2015. doi: 10.1039/C5EE02608C. URL: http://xlink.rsc.org/?DOI=C5EE02608C. (Cited on page 120.)

[227] Namyoung Ahn, Dae-Yong Son, In-Hyuk Jang, Seong Min Kang, Mansoo Choi, and Nam-Gyu Park. Highly Reproducible Perovskite Solar Cells with Average Efficiency of 18.3% and Best Efficiency of 19.7% Fabricated via Lewis Base Adduct of Lead(II) Iodide. *Journal of the American Chemical Society*, 2015 137(27):8696–8699. doi: 10.1021/jacs.5b04930. URL: http://pubs.acs.org/doi/abs/10.1021/jacs.5b04930. (Cited

on page 120.)

[228] Yongzhen Wu, Xudong Yang, Wei Chen, Youfeng Yue, Molang Cai, Fengxian Xie, Enbing Bi, Ashraful Islam, and Liyuan Han. Perovskite solar cells with 18.21% efficiency and area over 1 cm2 fabricated by heterojunction engineering. *Nature Energy*, 2016 1:16148. doi: 10.1038/nenergy.2016.148. URL: http://www.nature.com/articles/nenergy2016148. (Cited on page 120.)

[229] Daniel A. Jacobs, Yiliang Wu, Heping Shen, Chog Barugkin, Fiona J. Beck, Thomas P. White, Klaus Weber, and Kylie R. Catchpole. Hysteresis phenomena in perovskite solar cells: the many and varied effects of ionic accumulation. *Phys. Chem. Chem. Phys.*, 19(4):3094–3103, 2017. doi: 10.1039/C6CP06989D. URL: http://xlink.rsc.org/?DOI=C6CP06989D. (Cited on page 121.)

[230] S. Altazin, L. Stepanova, K. Lapagna, P. Losio, J. Werner, B. Niesen, A. Dabirian, M. Morales Masis, S. de Wolf, C. Ballif, and B. Ruhstaller. Design of Perovskite/Crystalline-Silicon Tandem Solar Cells. 2016. doi: 10.4229/EUPVSEC20162016-3DV.2.2. URL: https://doi.org/10.4229/EUPVSEC20162016-3DV.2.2. (Cited on page 123.)

[231] Julian Burschka, Norman Pellet, Soo-Jin Moon, Robin Humphry-Baker, Peng Gao, Mohammad K. Nazeeruddin, and Michael Grätzel. Sequential deposition as a route to high-performance perovskite-sensitized solar cells. *Nature*, 2013 499(7458):316–319. doi: 10.1038/nature12340. URL: http://www.nature.com/doifinder/10.1038/nature12340. (Cited on page 124.)

[232] Mohammed Makha, Silvia Letícia Fernandes, Sandra Jenatsch, Ton Offermans, Jürg Schleuniger, Jean-Nicolas Tisserant, Anna C. Véron, and Roland Hany. A transparent, solvent-free laminated top electrode for perovskite solar cells. *Science and Technology of Advanced Materials*, 2016 17(1):260–266. doi: 10.1080/14686996.2016.1176512. URL: https://www.tandfonline.com/doi/full/10.1080/14686996.2016.1176512. (Cited on page 126.)

[233] Stéphane Altazin, Lieven Penninck, and Beat Ruhstaller. Outcoupling Technologies: Concepts, Simulation, and Implementation. In Chihaya Adachi, Reiji Hattori, Hironori Kaji, and Takatoshi Tsujimura, editors, *Handbook of Organic Light-Emitting Diodes*, pages 1–22. Springer Japan, Tokyo, 2018. ISBN 978-4-431-55761-6. doi: 10.1007/978-4-431-55761-6_21-1. URL: http://link.springer.com/10.1007/978-4-431-55761-6_21-1. (Cited on page 128.)

[234] E. Hendry, M. Koeberg, B. O'Regan, and M. Bonn. Local Field Effects on Electron Transport in Nanostructured TiO_2 Revealed by Terahertz Spectroscopy. *Nano Letters*, 2006 6(4):755–759. doi: 10.1021/nl0600225. URL: http://pubs.acs.org/doi/abs/10.1021/nl0600225. (Cited on page 128.)

[235] Andreas Paulke, Samuel D. Stranks, Juliane Kniepert, Jona Kurpiers, Christian M. Wolff, Natalie Schön, Henry J. Snaith, Thomas J. K. Brenner, and Dieter Neher. Charge carrier recombination dynamics in perovskite and polymer solar cells. *Applied Physics Letters*, 2016 108(11):113505. doi: 10.1063/1.4944044. URL: http://scitation.aip.org/content/aip/journal/apl/108/11/10.1063/1.4944044. (Cited on pages 128, 134 and 148.)

[236] Almantas Pivrikas, Bronson Philippa, Ronald D. White, and Gytis Juska. Photocarrier lifetime and recombination losses in photovoltaic systems. *Nature Photonics*, 10(5):282–283, 2016. URL: http://www.nature.com/nphoton/journal/v10/n5/full/nphoton.2016.78.html. (Cited on page 132.)

[237] Almantas Pivrikas, Bronson Philippa, Ronald D. White, and Gytis Juška. Reply to 'Revisiting photocarrier lifetimes in photovoltaics'. *Nature Photonics*, 2016 10(9):563–

563. doi: 10.1038/nphoton.2016.165. URL: http://www.nature.com/doifinder/10.1038/nphoton.2016.165. (Cited on page 132.)

[238] Martin T. Neukom, Andreas Schiller, Simon Züfle, Evelyne Knapp, Jorge Ávila, Daniel Pérez-del Rey, Chris Dreessen, Kassio P.S. Zanoni, Michele Sessolo, Henk J. Bolink, and Beat Ruhstaller. Consistent Device Simulation Model Describing Perovskite Solar Cells in Steady-State, Transient, and Frequency Domain. *ACS Applied Materials & Interfaces*, 2019 11(26):23320–23328. doi: 10.1021/acsami.9b04991. URL: http://pubs.acs.org/doi/10.1021/acsami.9b04991. (Cited on pages 139 and 167.)

[239] Simon E. J. O'Kane, Giles Richardson, Adam Pockett, Ralf G. Niemann, James M. Cave, Nobuya Sakai, Giles E. Eperon, Henry J. Snaith, Jamie M. Foster, Petra J. Cameron, and Alison B. Walker. Measurement and modelling of dark current decay transients in perovskite solar cells. *J. Mater. Chem. C*, 5(2):452–462, 2017. doi: 10.1039/C6TC04964H. URL: http://xlink.rsc.org/?DOI=C6TC04964H. (Cited on pages 140, 145 and 151.)

[240] Daniel Walter, Andreas Fell, Yiliang Wu, The Duong, Chog Barugkin, Nandi Wu, Thomas White, and Klaus Weber. Transient Photovoltage in Perovskite Solar Cells: Interaction of Trap-Mediated Recombination and Migration of Multiple Ionic Species. *The Journal of Physical Chemistry C*, 2018 122(21):11270–11281. doi: 10.1021/acs.jpcc.8b02529. URL: http://pubs.acs.org/doi/10.1021/acs.jpcc.8b02529. (Cited on pages 140 and 151.)

[241] Nir Tessler and Yana Vaynzof. Preventing Hysteresis in Perovskite Solar Cells by Undoped Charge Blocking Layers. *ACS Applied Energy Materials*, 2018 1(2):676–683. doi: 10.1021/acsaem.7b00176. URL: http://pubs.acs.org/doi/10.1021/acsaem.7b00176. (Cited on pages 142 and 148.)

[242] Jacob N. Wilson, Jarvist M. Frost, Suzanne K. Wallace, and Aron Walsh. Perspective: Dielectric and Ferroic Properties of Halide Perovskite Solar Cells. 2018 *arXiv:1811.01832 [cond-mat]*. URL: http://arxiv.org/abs/1811.01832. arXiv: 1811.01832. (Cited on page 147.)

[243] Jaesang Lee, Hsiao-Fan Chen, Thilini Batagoda, Caleb Coburn, Peter I. Djurovich, Mark E. Thompson, and Stephen R. Forrest. Deep blue phosphorescent organic light-emitting diodes with very high brightness and efficiency. *Nature Materials*, 2016 15(1):92–98. doi: 10.1038/nmat4446. URL: http://www.nature.com/articles/nmat4446. (Cited on page 148.)

[244] Michael Eck, Chuyen Van Pham, Simon Züfle, Martin Neukom, Martin Sessler, Dorothea Scheunemann, Emre Erdem, Stefan Weber, Holger Borchert, Beat Ruhstaller, and Michael Krüger. Improved efficiency of bulk heterojunction hybrid solar cells by utilizing CdSe quantum dot–graphene nanocomposites. *Phys. Chem. Chem. Phys.*, 2014 16(24):12251–12260. doi: 10.1039/C4CP01566E. URL: http://xlink.rsc.org/?DOI=C4CP01566E. (Cited on page 167.)

[245] S. Jenatsch, S. Altazin, P.-A. Will, M. T. Neukom, E. Knapp, S. Züfle, S. Lenk, S. Reineke, and B. Ruhstaller. Quantitative analysis of charge transport in intrinsic and doped organic semiconductors combining steady-state and frequency-domain data. *Journal of Applied Physics*, 2018 124(10):105501. doi: 10.1063/1.5044494. URL: http://aip.scitation.org/doi/10.1063/1.5044494. (Cited on page 168.)

[246] Alfian F. Madsuha, Chuyen Van Pham, Michael Eck, Martin Neukom, and Michael Krueger. Improved Hole Injection in Bulk Heterojunction (BHJ) Hybrid Solar Cells by Applying a Thermally Reduced Graphene Oxide Buffer Layer. *Journal of Nanomaterials*, 2019 2019:1–10. doi: 10.1155/2019/6095863. URL: https://www.hindawi.com/journals/jnm/2019/6095863/. (Cited on page 168.)